School of Molecular and Life Sciences

Structural and Photophysical Investigation of Lanthanoid Complexes of Calixarene-Based Antenna Ligands

Chao Shen

This thesis is presented for the Degree of
Doctor of Philosophy
of
Curtin University

November 2021

Declaration

To the best of my knowledge and belief this thesis contains no material previously published by any other person except where due acknowledgment has been made.
This thesis contains no material with has been accepted for the award of any other degree or diploma in any unidersity.

Signature:

Date: 07/11/2021

Abstract

Lanthanoid complexes with calixarene derivatives are well studied. These macrocyclic polyphenol ligands not only have preorganized donor sites but are also readily functionalised using well-established chemistry. Here the aim was to use the calixarene framework as a receptor to bring lanthanoid cations and "antenna" functional group together. An antenna moiety provides a pathway to transfer the energy to the lanthanoid, overcoming the low absorption cross-section of the lanthanoid cation. Naphthalenetetracarboxylic diimide (NDI) was selected as the antenna moiety. Although the photophysical properties of NDI itself and its d-block metal complex have been widely studied, lanthanoid complexes with NDI have rarely been reported. Therefore, the aim of this project is to fill this gap and investigate the structural and photophysical properties of NDI-functionalised calixarenes, the NDI radical anion reduced species, and their corresponding lanthanoid complexes. The energy transfer process will also be proposed in some cases.

The syntheses of six new calixarene ligands were carried out using established methodologies with the structures confirmed using ^{1}H and ^{13}C NMR spectroscopy, including 2D NMR spectroscopy. All ligands were further characterized by high-resolution mass spectrometry and elemental analysis. Some ligands and lanthanoid complexes were also characterized by single crystal X-ray crystallography. Photophysical investigations of lanthanoid complexes were studied in solution and solid state at room temperature, and at 77K, to understand the energy transfer mechanism from the NDI to the lanthanoid. Electrochemistry and spectroelectrochemistry studies of the NDI-functionalised calixarenes showed the expected reduction to anion and then dianion, and also provided the spectroscopic information needed to confirm the successful bulk chemical reduction of neutral NDI to NDI radical anion. This was critical to be able to study the NDI radical anion as an antenna to sensitise the Ln^{3+} complex.

Chapter 1 presents an overview of lanthanoid chemistry, development of calixarenes and recently developed lanthanoid complexes with calixarenes. Fundamental photophysics is also included in this chapter. The basic photophysical and electrochemical properties of NDI are described, as well as progress in the field of lanthanoid complexes with NDI.
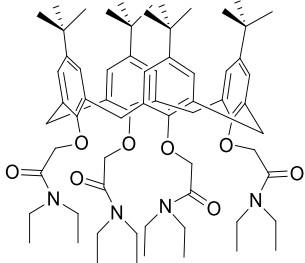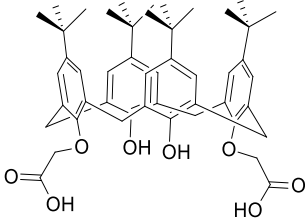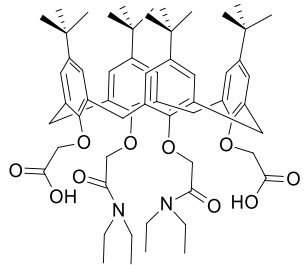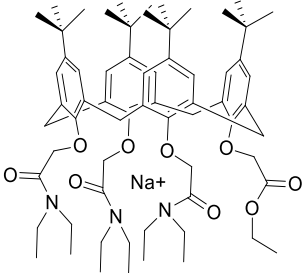
Three new bis-NDI functionalized calixarenes are reported in Chapter 2. The aim of determining the structural properties of all ligands in this chapter was achieved. The structural properties of bis-NDI substituted ligands were studied by ^{1}H, ^{13}C NMR spectroscopy, and single crystal X-ray crystallography. Bis-NDI substituted ligand **L1** can not form the complex with the secondary amide linkages inhibiting lanthanoid binding. Methylation of the secondary amide (**L1**) to tertiary amide (**L2**) was used to break the hydrogen bond, and the resulting ligand was capable of binding lanthanoid ions. Alternatively, alkylation of the two unsubstituted phenol groups in ligand **L1** to form a calixarenetetramide (**L3**) also achieved lanthanoid complexation. The photophysical properties of all ligands was also investigated, and the attempt to selectively sensitise the lanthanoid via the NDI on the lower rim of the calixarene was successful in the case of lanthanoid complexes of ligand **L2** and **L3**. It has been found that the NDI antenna moiety of ligand **L2** can only sensitise Yb^{3+} luminescence. In contrast, Eu^{3+}, Nd^{3+} and Yb^{3+} luminescence can be induced by energy transfer from the NDI of ligand **L3**, although more studies will be needed to fully understand these different behaviours. The hydrodynamic size of the solution phase
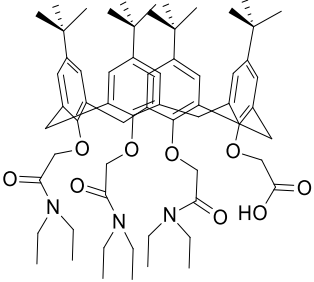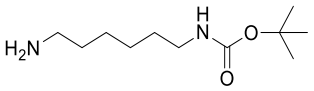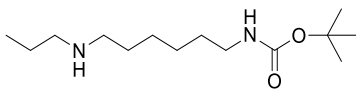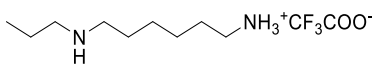
species was increased upon complexation, leading to emission presumed to be from an aggregate. However, energy transfer between the aggregate and Ln^{3+} does not take place.
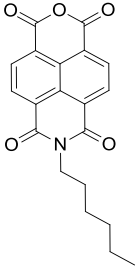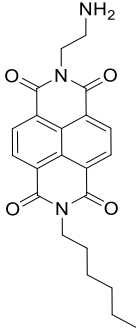
Chapter 3 extended the ligands to mono-NDI substituted calixarenetetramide ligands. The sequence of ligands extended the alkyl linking group of the NDI antenna. The structural properties of the mono-NDI substituted ligands were studied by ^{1}H and ^{13}C NMR spectroscopy. The photophysical properties of these ligands and their corresponding lanthanoid complexes were also investigated by absorption and emission spectroscopy. The energy transfer processes was also proposed in some cases. In particular, the NDI of these ligands can sensitise Eu^{3+} metal-centred emission, and the energy transfer to Eu^{3+} is from the excited singlet state of NDI. Sensitisation of Yb^{3+} ion was achievable via the calixarene aromatic backbone in all cases, whereas the NDI antenna only sensitised the Yb^{3+} luminescence in the case of Yb(**L4**) and Yb(**L5**), albeit with the poor sensitisation efficiency. Only the ligand **L6** was found to form aggregates in the absence of metals. Ligand **L6** had the NDI moiety most distant from the coordination centre, and in this case, sensitisation was achieved for Nd^{3+}, but not for Yb^{3+}. Spectrophotometric titration experiments were used to confirm that these calixarenes form 1:1 lanthanoid complexes, as expected from the literature.
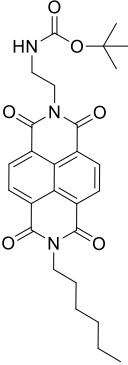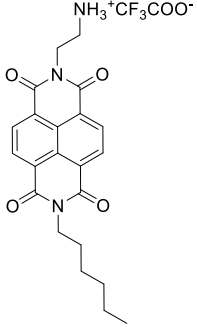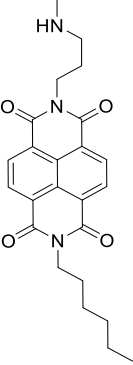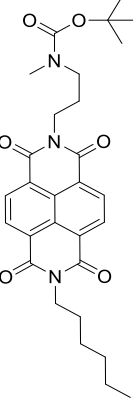
Chapter 4 focuses on synthesis and study of the photophysical properties of NDI radical anion containing species and its Yb^{3+} complex. Spectroelectrochemical results confirmed that TDAE could be used to reduce ligand **L5** from the neutral NDI to NDI radical anion species. The attempt to investigate emission properties and energy transfer process was also successful. The NDI radical anion is emissive in the NIR region. Upon complexation to Yb^{3+}, the NDI radical anion successfully sensitised Yb^{3+} luminescence via energy transfer from the excited doublet state. This is, to our knowledge, the first example of lanthanoid excitation via a doublet state.
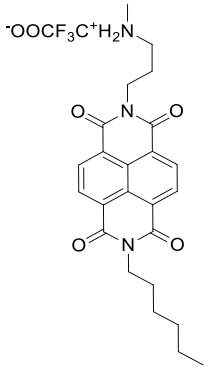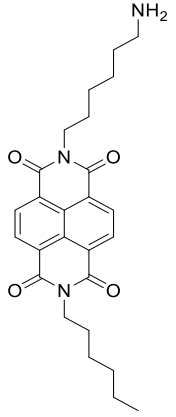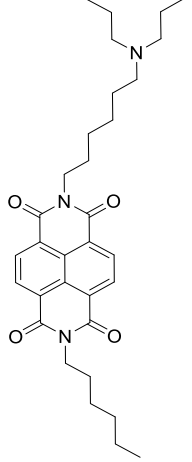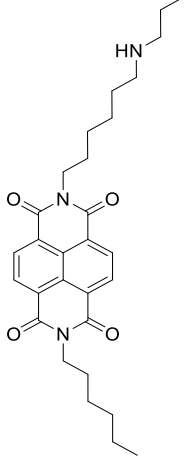
List of Compounds

Structure	Calixarene Compound Number Intermediate Compound Number
	Compound **R1**
	Compound **C1**
	Compound **C2**
	Compound **C3**

Structure	
	Compound **C4**
	Compound **I1**
	Compound **I2**
	Compound **I3**
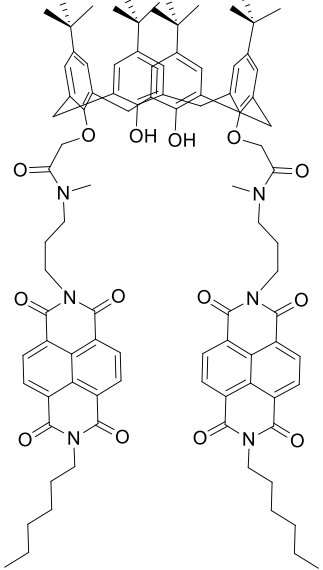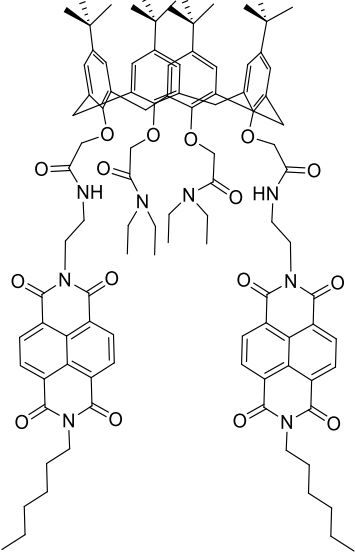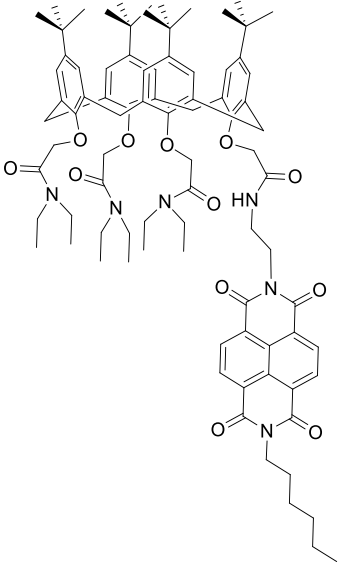
Structure	NDI Compound Number
	Compound **X**
	Compound **NDI1**

	Compound **NDI2**
	Compound **NDI3**
	Compound **NDI4**
	Compound **NDI5**

⁻OOCF₃C⁺H₂N—CH₃ chemical structure	Compound **NDI6**
NH₂ chemical structure	Compound **NDI7**
N chemical structure	Compound **NDI8**
HN chemical structure	Compound **NDI9**

Structure	
	Compound **NDI10**
	Compound **NDI11**

Structure	Ligand Number
	Ligand **L1**

	Ligand **L2**
	Ligand **L3**
	Ligand **L4**

	Ligand **L5**
	Ligand **L6**

Acknowledgements

There are a lot of people I want to express my gratitude and appreciation to. Guide and help me not just in terms of research.

My deepest gratitude goes first to three supervisors: Prof. Mauro Mocerino, Prof. Massimiliano (Max) Massi and Prof. Mark I. Ogden for guiding me professionally in the journal of doctoral studies. I want to thank Mauro for his idea of synthesis of the functionalized calixarenes. I want to thank Max for training me to use all instruments related to phophysics and very useful discussion about the data. I want to thank Mark for all your help and contribution to the scholarship application, milestone applications and thesis submission. I would like to express my sincere gratitude for the discussion, meeting, my talk practice, etc. I really appreciate the grammar and logical corrections in my written works.

Big thank you to our collaborator, Dr. Evan Moore. My thanks go to Prof. Paul Bernhardt for collecting data of cyclic voltammetry and spectroelectrochemistry and analysis of the spectra.
My thanks also go to Prof. Stephen Moggach and Dr. Alexandre N. Sobolev at the University of Western Australia for the crystal structures.

I would like to thank the "Lanthanoid team". Dr. Laura Abad Galan who helped me collect the photophysical data at the early stage of my PhD studies and shared the basic knowledge about lanthanoid. Dr.Anna Ranieri who contributed her knowledge to my study on photophysics. Dr. Rene Phe who guided me to synthesize my first calixarene. Mr Chris Driscoll who shared his synthetic skills and makes synthesis and purification in my project much more straightforward. Mr. Lee Cameron for the useful discussion on photophysics and crystal structures. I also want to thank Chiara Caporale for the elemental analysis.

Special thank you to my close friends in Perth: Fei Wang, DC Chan and Wei Hu.

Last but not least, I thank the China Scholarship Council and Curtin University for the scholarship. Without this financial support, I would not have the opportunity to come to Australia.

Table of Content

1 Introduction

The photophysical properties of the lanthanoids have been widely studied and have found a wide range of applications. Despite this, there remains aspects of their fundamental behaviour that are not fully characterised, particularly in terms of how energy is transferred from ligands to the metal centres. The aim of this project is to design new lanthanoid ionophores that will enable systematic study of energy transfer, both from excited states that are known to result in light emission, and also excited state types that have never been studied.

1.1 Luminescent Lanthanoids

The term "lanthanoids" refers to the *f*-block elements of atomic number 57-71, although they are often referred to as lanthanides or "rare earth elements". This latter term typically includes yttrium and scandium. The first lanthanoid to be isolated as an element was cerium which was achieved almost two hundred years ago. Although they are called rare earth elements, they are more abundant than some d-block metals, especially lanthanum, cerium and neodymium. Lanthanoids are categorised into two groups: light lanthanoids (from lanthanum to europium) and heavy lanthanoids (from gadolinium to lutetium), although europium is sometimes included in the heavy group.[1] This distinction reflects how the elements tend to separate during the challenging process of purification from mineral ores.

Technically speaking, lanthanum should be excluded from the family of lanthanoids because of the lack of 4*f* electrons. Although yttrium(III) is not a member of the lanthanoids, it is always found together with lanthanoids in nature. Its chemical behaviour is very similar to the lanthanoids, and the ionic radius of the yttrium(III) is similar to that of holmium(III). This is due to the lanthanoid contraction. Therefore, yttrium(III) is often included in studies of lanthanoids, particularly as it is diamagnetic which can simplify studies using NMR spectroscopy.

The general electronic configuration of the lanthanoid elements is $[Xe]4f^n6s^2$, but with the exceptions of lanthanum, cerium, gadolinium and lutetium following the electronic configuration of $[Xe]4f^{n-1}5d^16s^2$.[2] The dominant oxidation state of the lanthanoids is +3 with electronic configuration $[Xe]4f^n$(n=0-14). Some lanthanoid ions in the doubly charged state are also stable, such as $Eu^{2+}[Xe]4f^7$, $Yb^{2+}[Xe]4f^{14}$ and $Sm^{2+}[Xe]4f^6$.[3] Most trivalent lanthanoid ions are paramagnetic due to the unpaired electrons, while yttrium (III), lanthanum (III) and lutetium (III) are diamagnetic, and are commonly used for NMR studies.

One of the most discussed features of this metal ion series is the lanthanoid contraction.[4] This phenomenon describes the steady decrease in the ionic radius with increasing atomic number. The 4*f* electrons are poorly shielded from the nuclear charge. In other words, the increasing positive nuclear charge increases the electrostatic attraction force between the nucleus and the outer 4*f* electrons.

The 4*f* orbital referred to as "inner core", although they are valence orbitals. This causes lanthanoids to have very limited interaction with the ligand orbital and tend to form bonds with strong ionic character and weak directionality. As a result, the lanthanoids exhibit dramatically different coordination behaviours to d-block metals which tends to have well-defined coordination numbers and coordination geometries. The coordination geometry of a lanthanoid complex is generally determined by the bulkiness of ligands, the ionic radius and coordinated solvent molecules. Coordination numbers

are more commonly in the range of 8 to 10, but known to extend from 4 - 12.[3] The coordination number is affected by the ionic radius of lanthanoids as well, with a change in structure often observed across the series. For example for the DMSO solvates of the lanthanoid nitrates from lanthanum(III) to samarium(III), the composition is $Ln(DMSO)_4(NO_3)_3$, whereas from europium(III) to lutetium(III) the coordination number is reduced by one giving $Ln(DMSO)_3(NO_3)_3$.[5]

Table 1: The element, atomic number, electronic configuration and ionic radius of lanthanoids.[2]

Element	Atomic number	Ln atomic electron configuration	Ln^{3+} electronic configuration	Ln^{3+} ionic radius (ppm)
La	57	$[Xe]4f^05d^16s^2$	$[Xe]4f^0$	103
Ce	58	$[Xe]4f^26s^2$	$[Xe]4f^1$	102
Pr	59	$[Xe]4f^36s^2$	$[Xe]4f^2$	99
Nd	60	$[Xe]4f^46s^2$	$[Xe]4f^3$	98.3
Pm	61	$[Xe]4f^56s^2$	$[Xe]4f^4$	97
Sm	62	$[Xe]4f^66s^2$	$[Xe]4f^5$	95.8
Eu	63	$[Xe]4f^76s^2$	$[Xe]4f^6$	94.7
Gd	64	$[Xe]4f^75d^16s^2$	$[Xe]4f^7$	93.8
Tb	65	$[Xe]4f^96s^2$	$[Xe]4f^8$	92.3
Dy	66	$[Xe]4f^{10}6s^2$	$[Xe]4f^9$	91.2
Ho	67	$[Xe]4f^{11}6s^2$	$[Xe]4f^{10}$	90.1
Er	68	$[Xe]4f^{12}6s^2$	$[Xe]4f^{11}$	89
Tm	69	$[Xe]4f^{13}6s^2$	$[Xe]4f^{12}$	88
Yb	70	$[Xe]4f^{14}6s^2$	$[Xe]4f^{13}$	86.8
Lu	71	$[Xe]4f^{14}5d^16s^2$	$[Xe]4f^{14}$	86.1

The useful properties of lanthanoid-containing materials, most often magnetic or photophysical phenomena, are related to the electronic structure of these elements.

The electronic configuration of lanthanoids is characterised by term symbols, which are indicated as $^{2S+1}L_J$, where "2S+1" is the spin multiplicity. L is total orbital quantum number represented by S, P, D, F, G for 0, 1, 2, 3, 4 depending on the value of L. The ^{2S+1}L state can further be separated into $^{2S+1}L_J$ states by the spin-orbital interaction, where J is the total angular number. The value of the "J" lies in the range of |L-S| to L+S.

Hund's law is used to determine lowest ground state.[6]

1) The lowest in energy is the largest value of spin multiplicity.

2) Based on rule 1, the total orbital quantum number should be largest, which is the lowest in energy.

3) If electrons are filled in more than half shell, the largest J value is the lowest in energy; if electrons are filled in less than half shell, the smallest J value is the lowest in energy.

The sharp line-like emissions from *f-f* transitions are relatively unperturbed by the ligand environment and cover a useful range of wavelengths for many applications. Lanthanum(III) and lutetium(III) do not have any photoluminescent properties related to *f*-electron electronic transitions due

to their $4f^0$ and $4f^{14}$ configurations respectively. The emission of Gd^{3+} is in the ultra-violet region. The emission of Sm^{3+}, Eu^{3+}, Tb^{3+}, Dy^{3+} covers the visible region. The emission of Nd^{3+}, Er^{3+} and Yb^{3+} covers the near-infrared region. Lanthanoids, such as Tm^{3+}, Pr^{3+} and Ho^{3+}, are emissive both in the visible and the near-infrared region.[7-8]
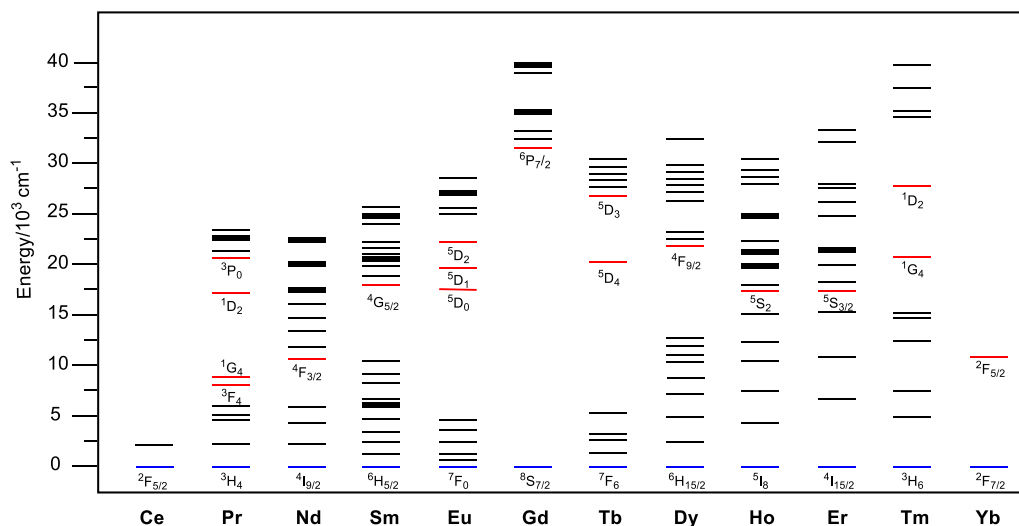
Figure 1: The energy level of lanthanoids. The ground state is highlighted in blue. Excited states are highlighted in red.[7] Figure reproduced from reference with the permission of the Royal Society of Chemistry.

The luminescence is attributed to radiative decay from the emissive state (red) to the ground state (blue). They are shown in Figure 1. In the case of Ln(III) aqua ions, some lanthanoids, such as Nd^{3+} and Yb^{3+}, have a luminescent type of fluorescence (Figure 2) because the $\Delta S = 0$. While others, such as Eu^{3+} and Gd^{3+}, have a luminescent type of phosphorescence in the radiative decay process because the $\Delta S \neq 0$. The Pr^{3+} luminescence is phosphorescent in the transition of $^1G_4$ to ^3H_J (J = 4 - 6) and $^1D_2$ to ^3F_J (J = 2 - 4) as well as fluorescent in the transition of $^3P_0$ to ^3H_J (J = 4 - 6). As mentioned above, these emission properties of lanthanoid are not significantly affected by the chemical environment even if they form complexes with ligands because of the inner orbital character of 4f electrons.

Ln	Excited state	τ_{Rad}/ms	End state		Lumin. type	λ/nm	Emission color
Pr	$^1G_4$	n.a.	^3H_J	4–6	P	1300	NIR
	$^1D_2$	n.a.	^3F_J	2–4	P	890, 1060	NIR
	$^3P_0$	n.a.	^3H_J	4–6	F	525–680	Orange
Nd	$^4F_{3/2}$	0.42	^4I_J	9/2–15/2	F	1060	NIR
Sm	$^4G_{5/2}$	6.26	^6H_J	5/2–15/2	P	590	Orange
Eu	$^5D_0$	9.67	^7F_J	0–6	P	620	Red
Gd	$^6P_{7/2}$	10.9	$^8S_{7/2}$		P	312	UV
Tb	$^5D_4$	9.02	^7F_J	6–0	P	550	Green
Dy	$^4F_{9/2}$	1.85	^6H_J	15/2–5/2	P	570	Yellow-orange
Ho	$^5F_5$	n.a.	^5I_J	8–4	F	970, 1450	NIR
	$^5S_2$	0.37	^5I_J	8–4	F	540	Green
Er	$^4S_{3/2}$	0.66	^4I_J	15/2–9/2	F		
	$^4I_{13/2}$	n.a.	$^4I_{15/2}$		F	1530	NIR
Tm	$^1G_4$	n.a.	^3H_J	6–4	P		
Yb	$^2F_{5/2}$	1.2^f	$^2F_{7/2}$		F	980	NIR

Figure 2: Summary of excited state and end state properties of the Ln(III) aqua ions.[7] Figure reproduced from reference with the permission of the Royal Society of Chemistry.

1.2 Fundamentals of Photophysics

1.2.1 Absorption of Light

Light absorption in this context describes the process where a photon is absorbed by a molecule, and a molecule is excited from the ground state to the excited state before emission occurs. The absorption of light follows the Beer-Lambert law[9]:

$$A = \varepsilon bc \qquad\qquad \textbf{Eqn 1}$$

ε is the molar absorptivity. It is a constant for a specific substance and has the unit of L mol $^{-1}$ cm $^{-1}$; b is the optical path length of the sample and has the value of 1 for a standard cuvette; c is the concentration (mol/L).

In theory, when the light interacts with the 4f electron of the lanthanoid, the lanthanoid is excited from the ground state to excited state. However, absorption of light by lanthanoids is weak as it occurs via forbidden transitions governed by spin and symmetry selection rules.

1.2.2 Selection rules

The spin selection rule states total spin quantum number must not change (S = total spin quantum number, $\Delta S = 0$). In other words, the transition from the ground state to the excited singlet state does not involve a change in spin orientation. Theoretically, this electronic transition is forbidden. However, the spin selection rule can be relaxed if the singlet state and triplet state are mixed due to the spin orbit coupling of the metal centre.

The Laporte selection rule is another rule to determine if the electronic transition is allowed. The Laporte selection rule only applies to molecules or atoms which have an inversion centre, and a change of parity should be involved ($\Delta l = \pm 1$, where l is the azimuthal quantum number). For example, the parity does not change in the *f-f* transition, so it is not allowed. However, the Laporte selection rule can also be relaxed for those complexes that have low symmetry.

1.2.3 Antenna Effect

The lanthanoids have a low molar absorptivity due to the forbidden f-f transition, making the direct excitation of the lanthanoid centre inefficient. In order to solve this problem, an organic chromophore can be used to transfer energy to the lanthanoid centre upon excitation. This well-established approach was firstly employed by Weissman in 1942 (Figure 3).[10] The coordinated chromophore with excellent capability for harvesting light is excited from the ground state to the excited state. The energy is further transferred to the lanthanoid and populates the excited state of the lanthanoid centre resulting in line-like characteristic emission. This phenomenon is known as the "antenna effect" discovered in 1942 by Weissman,[10] and these coordinated chromophores are known as antenna ligands.
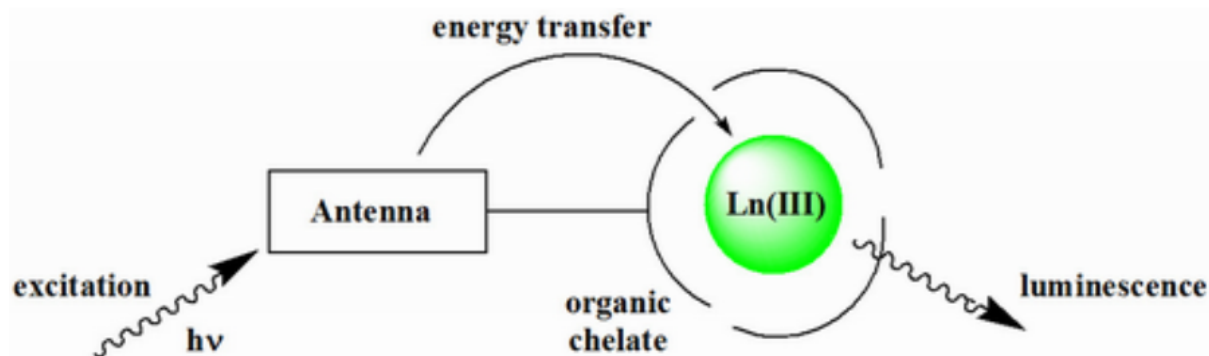
Figure 3: Schematic representation of lanthanoid luminescence via the antenna effect.[10]

The energy transfer to the metal centre is proposed to be a non-radiative decay process following the Dexter[11] or Förster mechanism[12]. The detailed sensitisation mechanism and antenna effect are illustrated in the Jablonski diagram (Figure 4). Upon excitation, the molecule is excited from the ground state to the excited singlet state without a change in spin multiplicity. The molecule can relax via the internal conversion process. The internal conversion describes non-radiative relaxation from the higher excited singlet state to the lower excited singlet state with same spin multiplicity. Kasha's rule states the emission is independent of the excitation wavelength, and luminescence occurs from the lowest vibrational level of the excited singlet state.[13] Following Kasha's rule, the excited molecules can further relax to the ground state radiatively. This radiative decay is known as fluorescence. The excited molecule can also lose the energy and relax to the ground state non-radiatively. Non-radiative decay refers to heat loss or any relaxation pathway without the emission of light.

Alternatively, population of the excited triplet state can occur via an intersystem crossing process (ISC). The ISC is a spin forbidden transition and is not allowed by selection rules. The spin-orbit coupling effect is increased in the presence of a heavy atom (such as lanthanoids, or other heavy atoms such as Br and I introduced in the solvent used), and the ISC process becomes more efficient. Therefore, the excited molecule can relax to the ground state with the different spin multiplicity in a process known as phosphorescence.

The triplet state can undergo an energy transfer process to populate the emissive state of the lanthanoid, which is the most crucial process of the antenna effect. The complex will finally relax to the ground state, resulting in luminescence characteristic of the specific lanthanoid. It is notable that the energy gap between the triplet state and the excited state of the lanthanoid should be ≥ 2500 cm^{-1}.[14] Otherwise, an unfavourable back energy transfer process may take place. The energy transfer from the triplet state is common, but sensitisation of lanthanoid emission from the excited singlet state of the antenna moiety has also been reported.[15-16] All these electron transition processes are illustrated in the Jablonski diagram (Figure 4).
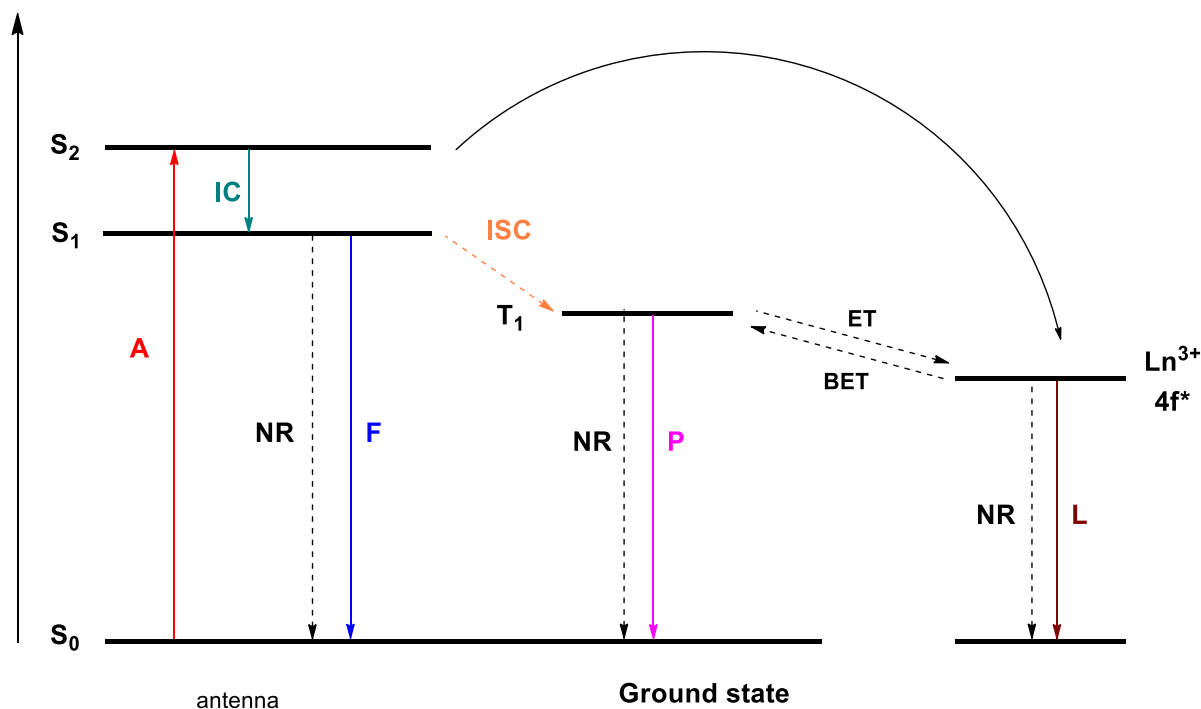
Figure 4: Jablonski diagram of the antenna effect and possible energy transfer (ET) pathways: singlet state(S), triplet state (T), absorption (A); non-radiative decay (NR): radiative decay including fluorescence (F), phosphorescence (P), luminescence (L); non-radiative decay: internal conversion (IC), intersystem crossing (ISC), back energy transfer (BET).

1.2.4 Efficiency of Energy Transfer Process

There are two important parameters to characterise the sensitisation process. The first parameter is the observed lifetime.

The observed lifetime is defined as the time that molecules spend in the excited state before they relax back to the ground state. The time which the intensity decays to 36.8% (1/e) of the original value corresponds to the observed lifetime.[17] The equation below shows how to calculate the lifetime.

$$I(t) = I_0 e^{-t/\tau}$$ **Eqn 2**

Where I_0 is the initial intensity; I_t is the intensity at t time; τ is the observed lifetime; t is the given time. More commonly, the lifetime is estimated based on decay functions. The experimental data is fitted to the well-established decay model, and the fitting should have a reasonable χ_R^2 value(the goodness of fit) and weighted residuals (the difference between calculated data and experimental data).[18]

The second parameter is the overall photoluminescence quantum yield ϕ_{Ln}^L which is defined as the ratio of the number of emitted photons to the number of the photons absorbed by the antenna. It describes the whole efficiency of the energy transfer process. The integrating sphere is more commonly employed to measure quantum yield if the lanthanoid complex has a high QY value, such as typical

europium (III) complexes. Otherwise, the optically diluted method (reference method) proposed by Crosby and Demas[19] is used to calculate QY. This method is commonly used for complexes with lower QY, such as ytterbium(III) complexes.

$$\phi_{Ln}^{L} = \phi_{ref}(\frac{I_{Ln}}{I_{ref}})(\frac{A_{ref}}{A_{Ln}})(\frac{n_{Ln}^{2}}{n_{ref}^{2}})$$ **Eqn 3**

Where ϕ_{ref} is the quantum yield of a standard. A is the absorbance. n is the refractive index of the solvent.

1.2.5 Non-radiative Processes

1.2.5.1 Back Energy Transfer

As stated above, the triplet state of the sensitising ligand plays a vital role in transferring the energy and populating the excited state of the lanthanoid. The energy gap between the triplet state and the excited state of the lanthanoid, along with the energy gap between the triplet and singlet state, is key to the energy transfer process. If the energy gap is not big enough, the efficient energy transfer process does not take place. The optimal energy gap required for the intersystem crossing should be above 5000 cm^{-1}. In order to avoid the back energy transfer and efficiently sensitise the lanthanoid, the energy of the triplet state should be ≥2500 cm^{-1} above the energy of the emissive state of the lanthanoid.[14] Otherwise, the BET process can repopulate the triplet state. It has been reported that even if the energy gap is less than 2500 cm^{-1}, it is still possible that the excited lanthanoid relaxes to its ground state radiatively at reduced temperature, typically 77 K.[20-21] The reason behind this phenomenon is that low temperature reduces the extent of thermal back energy transfer, making the energy transfer process more efficient.

There are two methods to estimate the energy of the triplet state of the ligand. The first method is to freeze the ligand in a glass solution at 77 K. By freezing samples in a glass, the non-radiative processes are slowed, and the radiative phosphorescence has a chance to compete. As a result, the phosphorescence from the triplet state is increased. Alternatively, the addition of a heavy atom, such as iodine and bromine, can increase the rate of the intersystem crossing process and induce the emission from the triplet state. In lanthanoid chemistry, one of the most commonly used heavy atoms is the gadolinium(III) ion. The advantage of using Gd^{3+} is its higher accepting energy level of its emissive state in comparison to the triplet state of the ligand. The energy of the triplet state can be estimated from the phosphorescence of the ligand attributed to the 0-phonon transition.

1.2.5.2 Multiphonon Relaxation

Multiphonon relaxation is one of the main quenching processes when the lanthanoid ions are surrounded by coordinated ligands containing CH, NH and OH oscillators. In particular, these functional groups have vibrational overtones, which can efficiently quench the lanthanoid emission. The quenching effect depends on the energy gap between the emissive state of lanthanoids and its highest vibrational

level of the ground state. The less vibrational quanta of oscillators required to bridge the energy gap, the more effectively the quenching process will take place. The quenching effect can be minimised by using deuterated ligands or solvents, which lowers the energy of the oscillators.

One relevant example of trivalent terbium is given in Figure 5. The energy gap between the emissive state ($^5D_4$) and the ground state ($^7F_6$) is around 14800 cm^{-1}. The vibrational energy of the O-H bond is around 3650 cm^{-1}. The four vibrational quanta of the OH group can quench the emissive state. In comparison, the O-D groups (2200 cm^{-1}) needs at least six vibrational quanta.
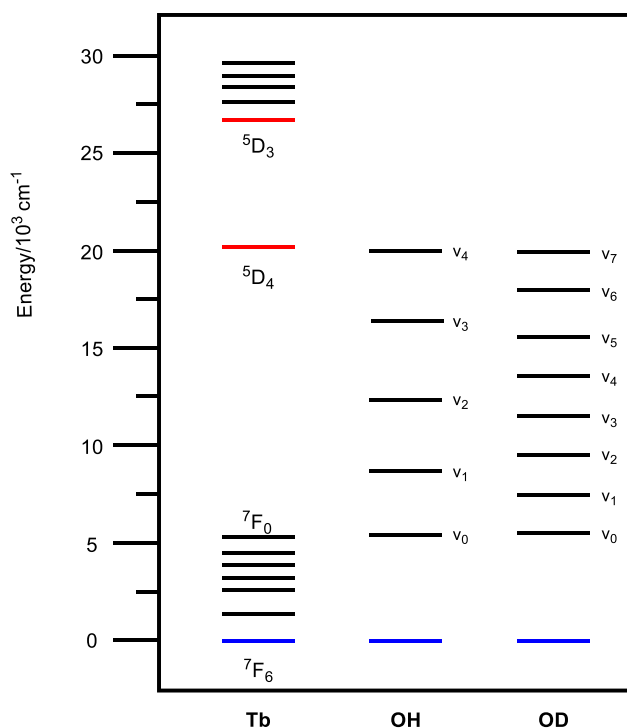
Figure 5: Quenching effect of OH and OD in multiphonon relaxation in the case of terbium $^5D_4$ emissive state.

The multiphonon relaxation also contributes to the short lifetime when the lanthanoid complex is coordinated with the solvent molecules such as water or alcohol. The excited-state lifetime of lanthanoid significantly increases when deuterated solvent is used. For example, the Tb^{3+} complex of p-allylcalix[4]arene tetraamide has methanol molecules in the first coordination sphere.[22] The value of the lifetime was 1.707 ms in a MeOH solution and 2.234 ms in a MeOD solution. Taking advantage of the different lifetime in deuterated and nondeuterated solutions, the number of coordinated water or alcohol molecules can be calculated by the equation established by Horrocks.[23-24]

$$q = A(k_{MeOD} - K_{MeOH}) - B \qquad \textbf{Eqn 4}$$

The "A" describes a constant reflecting quenching sensitivity. For example, 4.2 and 8.4 are used for the Tb(III) complex in the water and methanol. The coefficient "B" represents the contribution of the quenching effect by solvent molecules in the second coordination sphere, and it is constant. The Δ_k is the difference between the decay rate calculated by the inverse value of the observed lifetime in a

nondeuterated solvent and deuterated solvent. Normally, the calculated value is rounded to an integer referring to the number of coordinated solvent molecules. If the value is much less than one, that means the solvent molecules are not in the first coordination sphere, which means they are more than 4Å away from the coordination centre.

1.2.5.3 Charge Transfer States

The emissive state can also be quenched by a ligand to metal charge transfer LMCT state in the quenching process of the lanthanoid complex. The LMCT is the transition of an electron from the occupied orbital in the ligand to the unoccupied orbital in the metal centre. The energy of the charge transfer state is dependent on the character of the ligand. Taking a europium(III) complex of a phenolate for example, the phenolate acts as an electron donor and europium(III) as an electron acceptor. Where there is a low-lying LMCT state in the lanthanoid complex, it will be competitive with the population of the emissive state of Eu^{3+} (see Figure 6).[25] If the energy of LMCT is high enough, the efficiency of quenching will be reduced, and favourable photophysical properties may be found.[26] The LMCT is a dark state, and the lanthanoid can be deactivated to the ground state via a non-radiative relaxation pathway. The energy transfer process to the light emitting state is not efficient, and the quantum yield is significantly reduced as a consequence of the presence of the LMCT state. However, it is still likely the LMCT as an intermediate state plays an important role in sensitising ytterbium luminescence.[27-29]
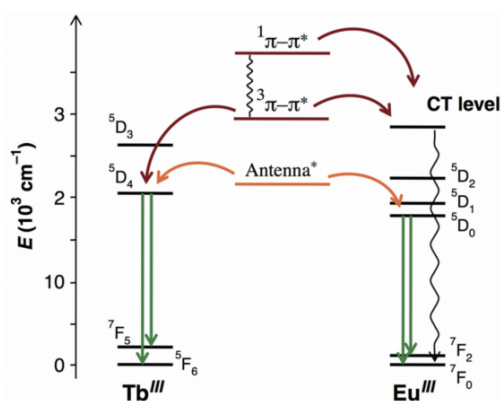
Figure 6: Jablonski program for energy transfer process showing the role of CT level in the Europium complex.[30] Figure reproduced from reference with the permission of the Taylor & Francis Ltd.

1.3 Calixarene

The term calixarene results from combination of two features of these macrocycles: 1) Calix or calic derives from the Latin for the cup-like shape; 2) arene captures the fact the macrocycles comprise of linked aromatic rings. The calixarene can be divided into three moieties: upper-rim functional groups, phenolic rings and methylene bridges. All groups can be replaced with other functional groups, including the methylene bridges. Inspired by the ready access to a range of macrocycle ring sizes, and easy

functionalisation on the lower and upper rims, researchers continue exploring their potential applications in the field including the biological drugs,[31-32] electrochemical sensors,[33-34] chromatography,[35-36] catalyst,[37-38] and luminescent materials.[22, 30]
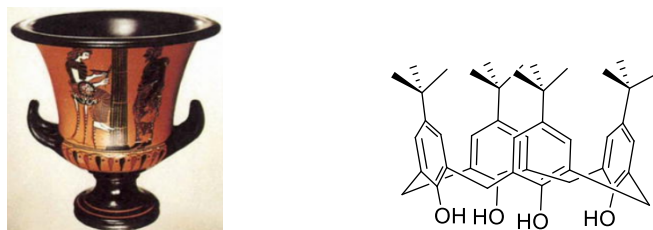
Figure 7: Left, calyx crater; Right: *p-tert*-butylcalix[4]arene.[39] Figure reproduced from reference with the permission of the Royal Society of Chemistry.

1.3.1 History of Calixarenes

Calixarene chemistry can be dated back to 1941. It was first reported by Zinke, who observed a polymer mixing *p-tert*-butylphenol with formaldehyde in the condensation reaction. But he did not propose the structure of the product.[40] It was not until 1944 that the reaction conditions were optimised, and more details were revealed in his new paper.[41] The product was characterised by the melting point which was above 300 °C, which was consistent with that reported in his previous paper. Analytical techniques were very limited at that time, but the subunit of the polymer or tetramer was confirmed to have the formula of $C_{11}H_{14}O$. By referring to the structure of the resorcinol-aldehyde product,[42] the structure of calix[4]arene as a cyclic tetramer was proposed by Zinke in the same year (Figure 8). In the coming years, more structures of calixarene derivatives with different functional groups on the *para*-substituted position were synthesised and reported.
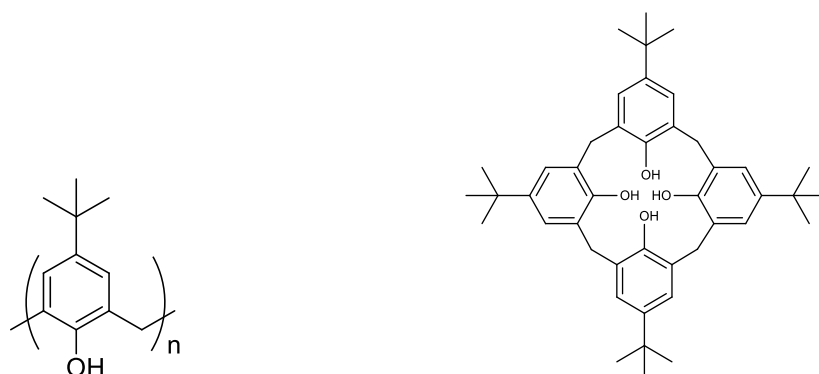
Figure 8: Structure of the subunit of the product proposed by Zinke in 1941[40] and cyclic tetramer (calixarene) in 1944.[41]

The proposed structure of cyclic tetramer known today was further confirmed by Hayes and his coworkers in 1956.[43] The rational and stepwise synthesis is based on a ten-step reaction by introducing

a bromine atom as a blocking group at the *ortho*-position of the hydroxylphenol to protect one reactive site and selectively opening another reactive site to link a neighbouring phenol (Scheme 1). Repetition of these steps three times, followed by catalytic hydrogenation to remove the bromine, affords mono-hydroxymethylated linear tetramer. The acid-catalysed cyclisation reaction in a diluted solution is performed to yield the cyclic tetramer, which was characterised by infrared analysis and elemental analysis. Based on the crystallographic data, the structure of cyclic tetramer was also confirmed by Cornforth.[44] He also stated the potential for four rotational diastereoisomers known as conformers today, with the isolation of the diastereoisomer requiring the hindered rotation of the aromatic rings. The characterisation of cyclic tetramer was a huge milestone in phenol-formaldehyde chemistry and paved the way for further studies on calixarenes.
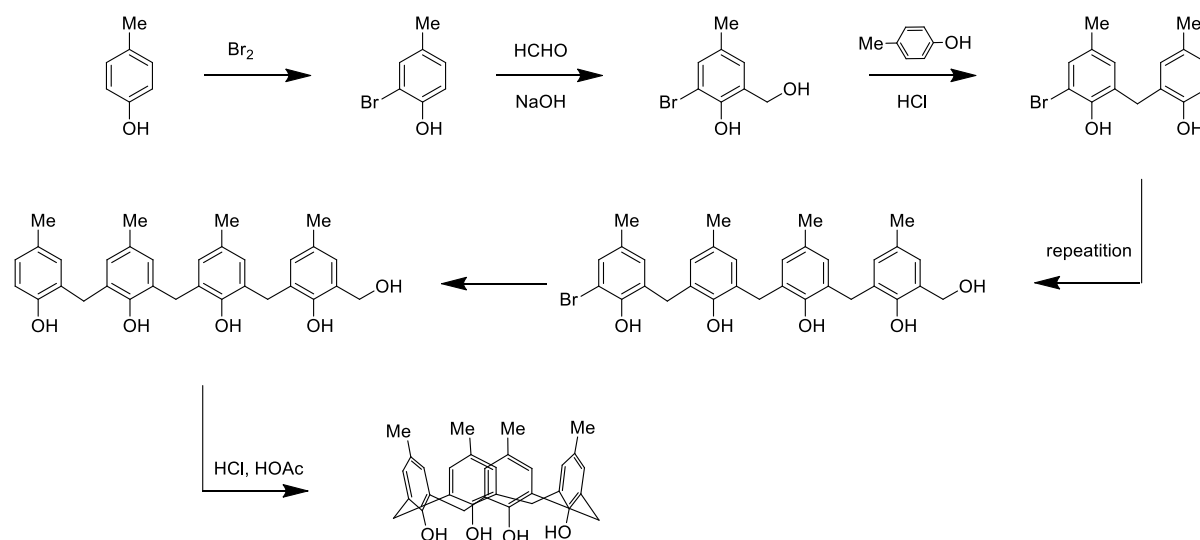
Scheme 1: Synthesis of *para*-methylcalix[4]arene from the linear tetramer.[43]

In 1975, David Gutsche reported some cyclic tetramers functionalised with different *para*-substituents in a symposium. In 1978, it was Gutsche that named this cyclic tetramer as the calixarene known today.[45] Experimental observations were well-established, and reaction conditions were further optimised. Since then, calixarene researchers have been using the term calixarene to name this cyclic tetramer, and related macrocycles, synthesising the parent calixarenes following the procedure reported in this paper.

1.3.2 Nomenclature of Calixarene

Before 1978, the International Union of Pure and Applied Chemistry nomenclature for the calixarene was not well-established. Therefore, the nomenclature of calixarene depended on the language researchers speak and functional groups on the lower rim and upper rim of the calixarene. Researchers from different countries used different names. Since Zinke proposed the structure of cyclic tetramer, he called it "Mehrkernmethylenephenol verbindungen".[46] Hayes named them "cyclic tetramer novolaks".[43] The cyclic tetramer was called tetrahydroxycyclotetra-m-benzylene by Cornforth.[44] A more official nomenclature, pentacyclo[19.3.1.1^{3,7}1^{9,13}1^{15,19}]octacosa-1(25),3,5,7(28),9,11,13(27),

15,17,19(26),21,23-dodecaene, was introduced by the Chemical Abstract Service with a registry number of 60705-62-6.[47] However, this nomenclature was too long and complicated when functionalised groups were introduced on the upper and lower rim. In order to simplify nomenclature, Gutsche coined the name calix[4]arene in the paper published in the Journal of Organic Chemistry in 1978.[45] If functional groups were at the *para*-position on the upper rim, it was called *p*-substituent calixarene, such as *p-tert*-butyl calix[4]arene. Although this terminology was not initially accepted by IUPAC and Chemical Abstracts, it finally became a legitimate name. The symbol "n" in the bracket (calix[n]arene) represents the number of repeating aromatic rings in the cyclic array. Recently, a giant calixarene containing up to 90 repeating phenolic units has been reported.[48]

The CAS numbering system is also accepted in literature. The nomenclature follows the rules of giving different groups different numbers. Taking *p-tert*-butylcalix[4]arene as an example, 5,11,17,13 represents quaternary carbon of aromatic rings linking to the *p-tert*-butyl group on the upper rim, and 25,26,27,28 represents quaternary carbon of opposite aromatic ring linking to the hydroxyl group at the lower rim. Therefore, the systematic name is 5,11,17,23-tetra-*tert*-butyl-25,26,27,28-tetrahydroxylcalix[4]arene.
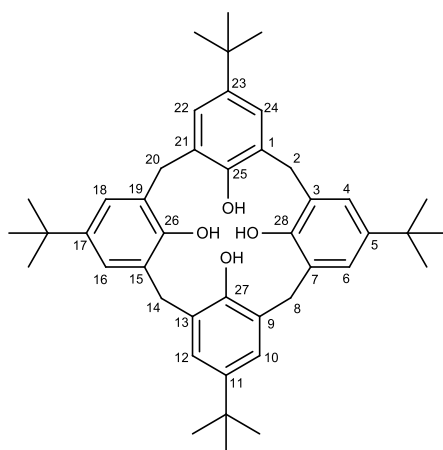
Figure 9: Structure and numbering of calix[4]arene.

In this project, all ligands containing calixarene are based on *p-tert*-butylcalix[4]arene. Even if the simplified nomenclature or CAS number systems are employed, the nomenclature is still rather complicated due to one or more different kinds of substituents at the lower rim. Therefore, in this thesis all calixarene derivatives are named as number + ligand or compound + number with a graphical representation to clarify the full structure.

1.3.3 Graphical Representation of Calixarene

There are four typically graphical representations of calixarene in literature: 1) bracketed aromatic unit with methylene bridge; 2) bracketed aromatic unit with methylene bridge and a loop; 3) three-dimensional structure; 4) flattened structure (Figure 10). The first two structural representations were used in older literature. While the 3D structure and flattened structure are much more common in today's

literature mainly because it is more intuitive for readers to understand structure if more than one different functional group are attached to the lower and upper rim.
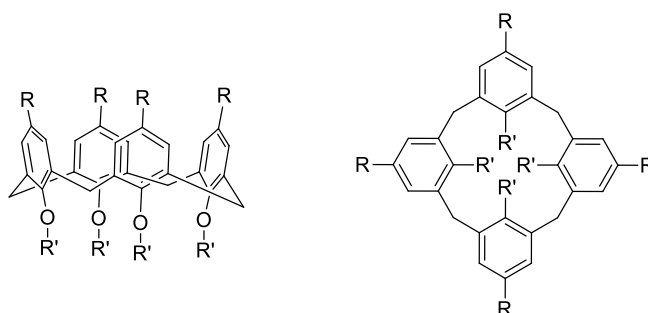
Figure 10: Left: 3D structure; Right: flattened structure. R and R' are substituents.

The more complicated functional groups and chromophores will be attached to the lower rim in this project. Therefore, the 3D structure is used to illustrate all calix[4]arene derivatives.

The calixarene can be viewed as a 3D basket, bowl or cup with a wider upper rim pointing upward (exo), and a narrower lower rim pointing downward (endo). The hydrogen atoms of the methylene bridge do not have the same environment. One hydrogen atom is closer to the aryl ring, and the term "equatorial" is used. The other is closer to the hydroxyl group, and the term "axial" is used (Figure 11). There is a cavity that is capable of trapping small solvent molecules with an appreciable size, such as dichloromethane, DMF, THF, EtOH and so on.[49-51]
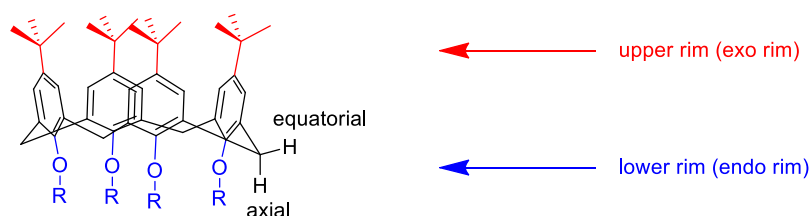
Figure 11: Upper rim (exo rim) in red; Lower rim (endo rim) in blue.

1.3.4 Conformational Isomers

Cornforth was the first researcher who recognised the four condensation products with the same chemical formula and stated the presence of these conformers attributed to the steric hindrance.[44] The four conformation isomers were named by Gutsche in 1983 as cone, partial, 1,3-alternate and 1,2-alternate (Figure 12).[52]

13
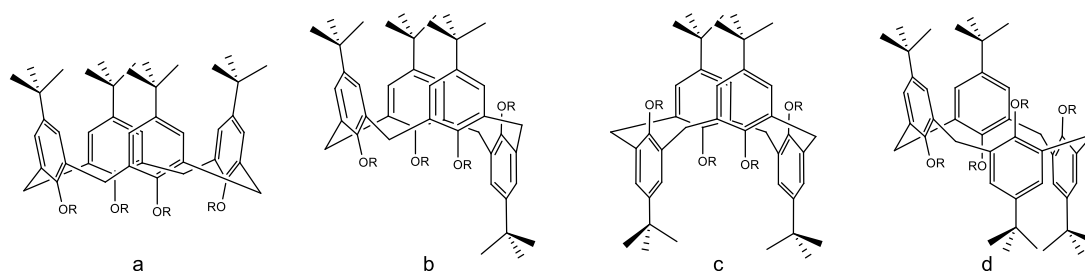
Figure 12: Conformation of calixarene: a) cone; b) partial cone; c) 1,3-alternate; d)1,2-alternate.[52]

For the unsubstituted calixarene, the most stable conformational isomer is the cone conformer due to the more intramolecular hydrogen bonds formed on the lower rim. The stability is followed by partial cone, 1,2-alternate and 1,3-alternate. The ranking is also confirmed by computational calculations based on dipole moment.[53] The existence of conformers has been confirmed by ^{1}H NMR spectroscopy (Figure 13, left).[54] In particular, the authors studies equatorial and axial protons of the methylene bridge of *p-tert*-butyl calixarene at variable temperature and measures the conformational mobility. The splitting pattern of ArC**H₂**Ar peaks is doublet for each proton at room temperature, indicating the non-equivalent chemical environment of equatorial and axial protons. While the two doublet peaks coalesce into one sharp singlet peak with the temperature increasing to 89 degrees in CDCl₃, indicating that absorption of the energy leads to the increased rate of interconversion of cone conformer on the NMR time-scale in comparison to that observed at room temperature.

This investigation was extended to study the conformational mobility in pyridine-d₅ (Figure 13, right).[54] Compared with the calixarene in CDCl₃, the faster interconversion rate occurs at relatively low temperature. This finding confirms that the pyridine plays an important role in lowering the energy barrier and weakens the intramolecular hydrogen bonds between phenolic units. The effect is similar to the decreasing number of hydrogen bonds. Calixarene researchers also confirmed that the replacement of *para*-substituent groups on the upper rim has limited influence on the rate of conformational inversion.[39, 55]
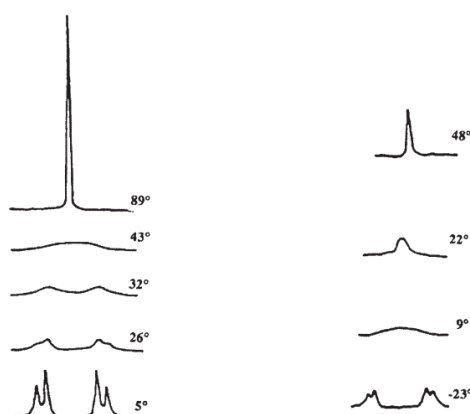
Figure 13: Variable temperature ^{1}H NMR spectra of the aromatic region of *p-tert*-butyl calix[4]arene.[54] **Left: CDCl₃ solution. Right: pyridine-d₅ solution. Figure reproduced from reference with the permission of the Royal Society of Chemistry.**

For the substituted calixarene, the phenolic group can flip from an endo rim to an exo rim through the annulus and around the methylene bridges. The occurrence of isomerisation depends on the stability of hydrogen bonds on the lower rim of the substituted calixarene or the steric bulkiness of the attached groups. The group which is larger than the ethyl group should be bulky enough to restrict the rotation, allowing the isolation of each conformer. In this project, the calixarenes are fully alkylated or bis-O-alkylated. Therefore, the bulkier group, such as amide group, on the lower rim will be used to isolate the desired conformer. The potential for conformers impacting on the coordination chemistry remains for the bis-substituted calixarenes, so it is important to be aware of the potential impact of conformational mobility.

1.3.5 Functionalisation of Calix[4]arenes

Functional groups can be introduced on the lower rim and upper rim. In this project, all ligands are based on the parent *p-tert*-butylcalixarene. Therefore, the discussion will focus on the functionalisation on the lower rim via nucleophilic substitution. The phenolic groups of calixarene are nucleophiles after deprotonation, and alkyl halides are excellent electrophiles. The extent of deprotonation of the calixarene determines the number of substituents on the lower rim. Understanding of the pK_a values, therefore, plays a vital role in selectively deprotonating phenolic groups which then enables selective functionalisation of the calixarene (Table 2). The determination of the pK_a value is straightforward by acid-base titration,[56] photometric titration[57] and theoretical calculation.[58] There are four intramolecular hydrogen bonds on the lower rim. The higher the pK_a value is, the stronger the base is needed. For example, the first proton is very acidic. A weak base, CsF, is used to deprotonate the first phenolic group to form a mono-dissociated species.[59] There are still three hydrogen bonds among the OR group and three phenolic groups. The second proton dissociation has a pK_a value of 9.1-11.8 and requires a moderate base, such as potassium carbonate.[60] The bis-substituted product has a pair of hydrogen bonds between OR groups and its adjacent phenolic hydroxyl groups. The stronger base, barium oxide, is used to deprotonate the third one.[61] Sodium hydride is required to deprotonate the last phenol group.[62]

Table 2: The pK_a value for each deprotonation reaction of the calixarene on the lower rim.

Deprotonation of phenol	pK_a value
First	1.8 ~ 3.3 [63-64]
Second	9.7 ~ 11.8 [64-66]
Third	12.3 ~ 12.8 [64-66]
Fourth	12.5 ~ 14 [64-66]

Selective nucleophilic substitution can generally be achieved based on the discussion above, but the reaction sometimes does not abide by these rules. For example, unsubstituted and bis-substituted byproducts are always found in monosubstitution reaction using CsF as a base even if the stoichiometry of starting materials to the base to the alkylating reagent is 1:1:1.[67] Themoderate base, K_2CO_3, is capable of completing tri- or tetra-alkylation at high temperature if both of the base and alkylating

reagent are in excess.[68-69] All these factors contribute to the extent of alkylation achieved: the reaction temperature, the reaction time, the amount of alkylating reagent and base strength. Therefore, the reaction conditions should be optimised and well-controlled in order to yield the majority of the desired product.

1.3.6 Lanthanoid Complexes of Calixarene Diamides

There is a significant literature on the lanthanoid complexes of calixarenes. Here we will focus on some exemplar systems that are of most relevance to this project, lower rim amide substituted calixarenes, that are di-, tri-, and tetra-alkylated. Considering first the dialkylated system, there are two structural isomers that can be obtained, the 1,2- and 1,3-substituted bisamide calixarenes.

The 1,2-bisamide structural isomer is less common in the literature and was reported as a byproduct from the tris-amide calixarene synthesis. One example reported by the Ogden group showed the single crystal of the lanthanum(III) complex of 1,2-bisamide calixarene (Figure 14).[70] The crystal structure reveals a ten-coordinate complex: two oxygen atoms from amide groups, three phenolate oxygen atoms, one oxygen atom from the intact phenolic group. Each picrate ligand coordinates to the lanthanum(III) in a bidentate mode where the oxygen atom is from a nitro group and the phenolate group. The picrate ligands display different orientations when coordinated to the lanthanum(III). One of the crystal structures is showed below.
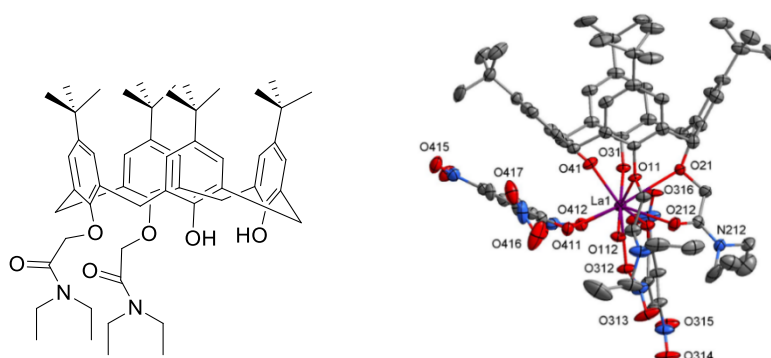
Figure 14: Left, 1,2-bis-amide functionalised calixarene; Right, crystal structure of lanthanum(III) complex.[70] Figure reproduced from reference with the permission of the Springer Nature.

The 1,3-bis-substituted calixarene has been widely studied because it is relatively easy to synthesise and purify. The 1,3-bisamide calixarene (Figure 15, left) can be synthesised from the nucleophilic substitution between the diacylchloride-functionalised calixarene and diethylamine in the presence of triethylamine or more directly by alkylation of the calixarene using 2-chloro-N,N-diethylacetamide.[71] The purification is straightforward via recrystallisation. A series of lanthanoid complexes of calixarenediamide are also characterised by x-ray crystallography, giving the general formulation [Ln(L-2H)(picrate)]•xH_2O (Figure 15).[72] The crystals are grown by slow evaporation of the mixture of the DCM/EtOH in the presence of triethylamine. The lanthanoid is eight-coordinate. The lanthanum(III) complex is taken as an example for comparison. Six oxygen atoms of calixarene on the

lower rim participate in coordination. Unlike 1,2-bisamide isomer, both of the phenolic rings are fully deprotonated. The water molecule is bound to the metal. The picrate ligand is found to coordinate the lanthanum(III) in a monodentate fashion. For those lanthanoids with smaller ionic radius, although the coordination number is still eight, coordination sphere is completed by a picrate ligand coordinating in a bidentate fashion without the water molecule.
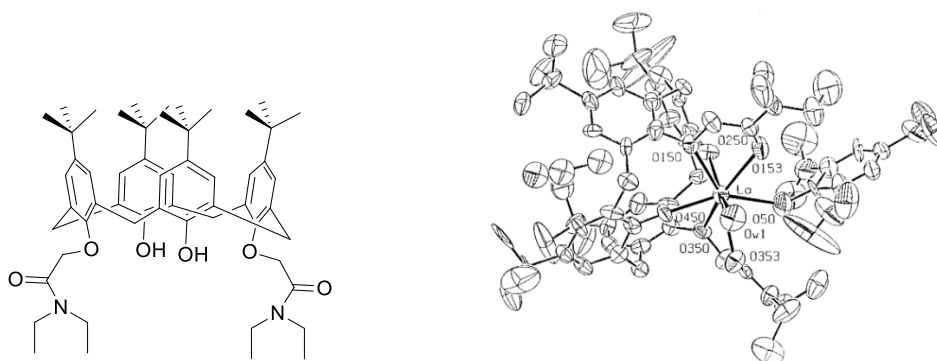
Figure 15: Left, 1,3-bis-amide functionalised calixarene; Right, crystal structure of lanthanum(III) complex.[72] **Figure reproduced from reference with the permission of the American Chemical Society.**

It is notable that the complexation of the praseodymium(III) picrate with 1,3-bis-amide functionalised calixarene also takes place in the absence of a base (Figure 16).[73] The praseodymium complex is eight-coordinated by three picrate groups in a bidentate fashion, two amide oxygen atoms and one oxygen atom of the phenolic group of calixarene.
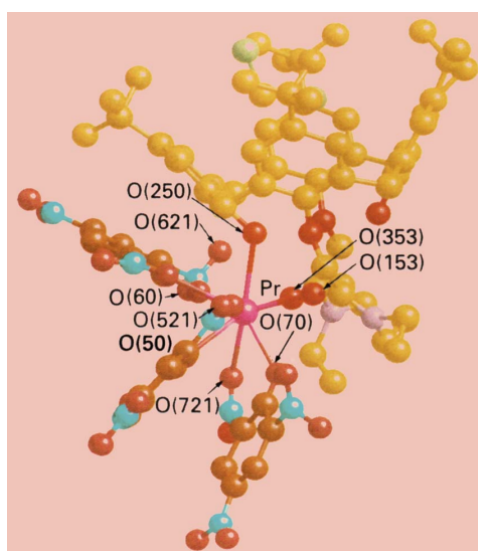
Figure 16: Crystal structure of praseodymium(III) complex of 1,3-bis-amide functionalised calixarene in the absence of a base.[73] **Figure reproduced from reference with the permission of the Royal Society of Chemistry.**

The research into the complexation properties of lanthanoid complex of 1,3-substituted calixarene diamide using proton NMR titration has demonstrated that this ligand has a strong affinity toward lanthanoid ions. If there are no extra binding sites on the lower rim, the complexation properties would not be affected. In an example of the NMR titration experiment performed by Marco group,[74] the morpholide group is attached to calixarene diamide (Figure 17), and it is titrated with La^{3+} ion in a mixture of CDCl3/MeOD. The symmetry of calixarene diamide is verified by the two hydrogen environments of *tert*-butyl group and aromatic rings. After addition of 0.5 equivalent of La^{3+} salts, the NMR peaks become broad and shifted. Continuous addition of La^{3+} salts to one equivalent leads to sharp peaks. But the variation in chemical shift experienced by all protons is slight ($\Delta_{chemical\ shift} \leq 0.1$ ppm, Table 3). Further spectral changes are not observed after addition of more La^{3+} salts, and the 1:1 complex is formed. The formation of the 1:1 complex is also studied by computational calculation and give some insights into the La^{3+} complex.
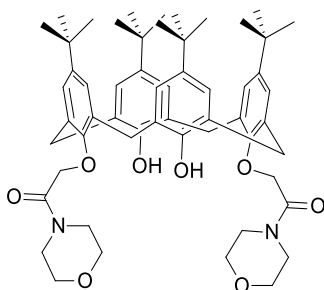
Figure 17: Structure of bis-morpholide substituted calixarenediamide.[74]

Table 3: The proton chemical shift (ppm) of ligand and La^{3+} complex.[74]

	t-Bu	ArCH2Ar		OCH2CO	ArH
		Eq	Ax		
Ligand	0.94, 1.26	3.32	4.32	4.73	6.77, 7.01
Ligand + La^{3+}	0.87, 1.31	3.36	4.22	4.81	6.69, 7.11

The group of Hamdi reported two examples of 2-furanylmethyl- and 2-thienylmethyl-amide functionalised calixarene diamide (Figure 18).[75] The target molecule is synthesized by reacting calixarene diester with excess amine precursors, and the ester group can be converted to the amide group by an aminolysis reaction. This binding is assessed by UV-visible spectrophotometric experiment (Figure 19). The ligand is titrated with lanthanide ion in acetonitrile in the presence of 10^{-2} MEt4NClO4, but the base is not used. Upon addition of the Ln[3+], the intensity of the absorption peak attributed to the ${}^{1}\pi\pi^{*}$ transition of calixarene decreases with increasing intensity of shoulder around 310 nm. Two isosbestic points are found, indicative of single equilibrium. The stability constant for each complex (La^{3+}, Nd[3+], Gd^{3+} and Yb[3+]) was log K > 8, although the data is best fitted to the ML2 species.
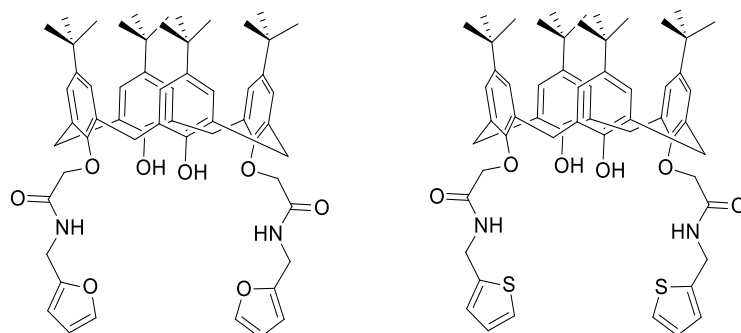
Figure 18: Structure of 2-furanylmethyl- and 2-thienylmethyl-amide functionalised calixarene diamide.[75]
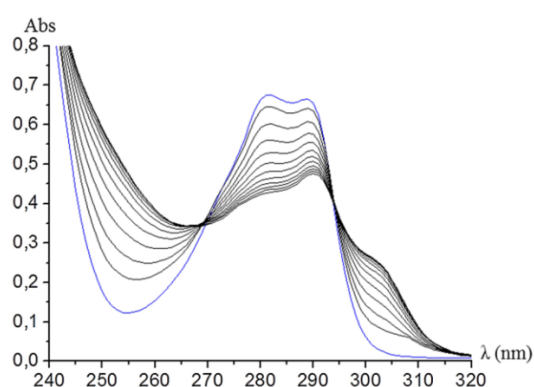
Figure 19: Spectrophotometric titration of of furanyl ligand with the Yb^{3+} in the acetonitrile solution.[75] **Figure reproduced from reference with the permission of the Springer Nature.**

Regardless of 1,3-bisamide and 1,2-bisamide structural isomers, both bis-amide functionalised calixarenes form the stable lanthanoid complex generally in a ratio of 1:1 metal to ligand. It is notable that these calixarenes provide the preorganised donor sites for lanthanoids and are not reported to form a complex with alkali metals in the purification process.

1.3.7 Lanthanoid Complexes of Calixarene Triamide

There are two synthetic paths to produce tris-amide functionalised calixarenes (Scheme 2): 1) monoalkylated calixarene with benzyl ether group on the lower rim is synthesised first, followed by alkylation of the rest of phenols via the ether group using 2-chloro-*N,N*-diethylacetamide as an alkylating reagent. The tris-amide calixarene is formed from the addition of Pd(OH)$_2$/C to debenzylate the calixarene;[76] 2) Alternatively, the parent calixarene is directly reacted with the alkylating reagent using a mixture of barium oxide and hydroxide as a base. The synthetic route is more straightforward, but the purification to separate from the bis and tetra-substituted by-products is not easy, and the yield is modest (23%).[61]
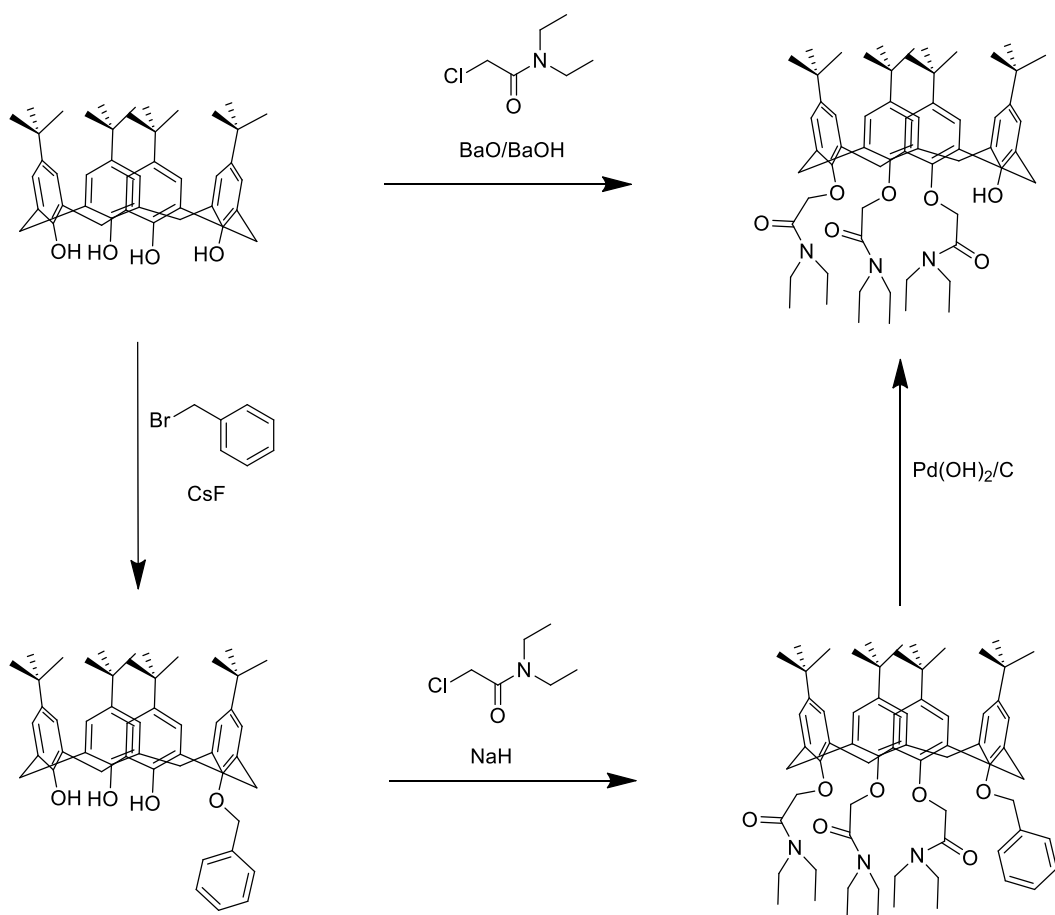
Scheme 2: Synthesis of the tris-amide calixarene.[61, 76]

The corresponding gadolinium(III) complex is characterised by X-ray crystallography (Figure 20). The single crystal was grown by slow evaporation of the mixture of DCM and EtOH. The gadolinium(III) complex of the tris-amide calixarene has a molecular formula of [(pic-*O*)Gd(L–H)(EtOH)](pic)·2EtOH.[77] All seven oxygen atoms of calixarene coordinate to the Gd^{3+} complex, including the oxygen atom of the phenolate group and amide oxygen atoms. One picrate ligand is bound to the Gd(III) in a bidentate fashion, while the other negatively charged picrate anion balances out with the one positively charged complex in the outer coordination sphere. The research also reveals that the Gd^{3+} complex can form without adding triethylamine. The deprotonation could be readily induced by Gd^{3+} ion upon complexation.
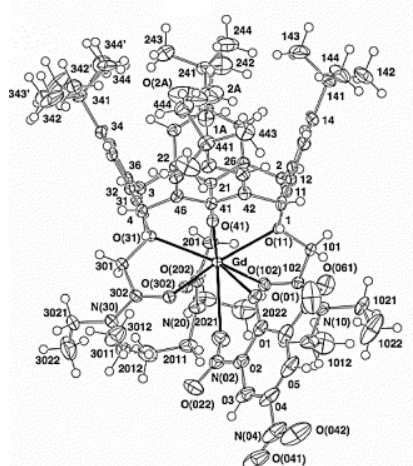
Figure 20: Gd³⁺ complex of the tris-amide functionalised calixarene.[77] Figure reproduced from Reference with the permission of Elsevier.

1.3.8 Lanthanoid Complexes of Calixarene Tetraamides

Calixarene tetraamides are well-established ligands as they bind strongly to metal cations including the lanthanoids. The procedure for synthesis has been well-established:1) if all attached amide groups are the same, the synthesis is achieved via the reaction of parent calixarene with a suitable alkylating reagent and a strong base heated to reflux; 2) if there are two or more different kinds of amide groups or different functional groups attached to the calixarene via the amide linker, calixarene bisamide or calixarene trisamide has to be made first followed by reacting with alkylating reagents. The calixarene tetraamide, especially with the diethyl amide functional group on the lower rim, has been well-studied in terms of synthesis, coordination properties and photophysical properties.

The pioneering work done by the groups of Ungaro and Ugozzoli group reported synthesis of this calixarene tetraamide.[78] The reaction between the parent *p-tert*-butylcalixarene and 2-chloro-*N,N*-diethylacetamide using excess NaH as a base yielded the tetra-amide functionalised calixarene (Figure 21, left). The purification is straightforward by recrystallisation due to the relatively low solubility of the product in comparison to the alkylating reagent. The resulting product, however, is the alkali metal complex as this tetra-substituted calixarene is a strong alkali metal receptor. The free ligand can be obtained by stirring the Na⁺ complex in an aqueous acid solution, and then it is extracted with dichloromethane.[79] Alternatively, the removal of the metal can be done by heating the complex in a mixture of methanol and water, followed by removal of the organic solvent and filtration.[22]
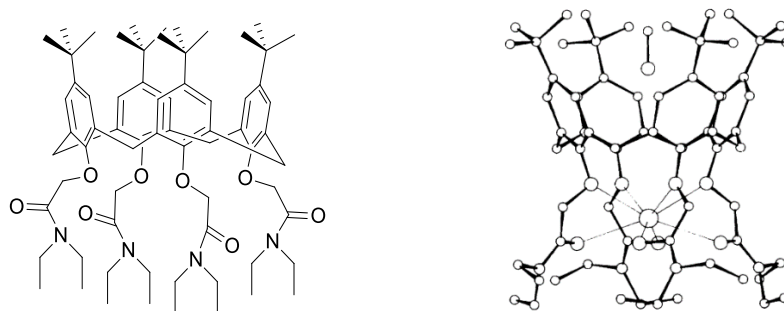
Figure 21: Structure of calixarene tetraamide and its corresponding potassium complex.[78]**Figure reproduced from reference with the permission of the Royal Society of Chemistry.**

A few years later, the group of Sabbatini reported photophysical properties of lanthanoid complexes of the same ligand. In terms of the photophysics, the peak at 420 nm corresponding to phosphorescence of can be observed at 77K with/without Gd^{3+} ion in the emission spectra. The energy of the triplet state is calculated to be 23800 cm^{-1}, making energy transfer to terbium ions accessible. The absorption and excitation spectra are closely matched, and this confirms calixarene tetraamide can work as an antenna to sensitise the terbium luminescence. The luminescence quantum yield is 0.2% in water, and the lifetime is 1.5 ms (Table 4). The value of the observed lifetime of the Tb^{3+} complex in D_2O can be improved to 2.6 ms due to the presence of one coordinated water molecule. Not surprisingly, the poor quantum yield and lifetime value are detected in the case of the europium complex even if the deuteration technique is used. This is due to the presence of a LMCT process, which is confirmed by the observation of a shoulder around 300 nm in the absorption spectrum. The quenching of the excited state of Eu^{3+} by LMCT and schematic energy level diagram for Eu^{3+} and Tb^{3+} complex have been discussed in the above section.

Table 4: Luminescent properties of Eu^{3+} and Tb^{3+} complex in H_2O and D_2O.[80]

	Lifetime/ms		Quantum yield
Compound	$\tau(H_2O)$	$\tau(D_2O)$	$\Phi(H_2O)$
$[Eu(\mathbf{L})]^{3+}$	0.65	1.9	2.0×10^{-4}
$[Tb(\mathbf{L})]^{3+}$	1.5	2.6	2.0×10^{-1}

Marcos reported an investigation of lanthanoid binding properties of *p-tert*-butyl[4]arene-tetra-acetamide.[81] The ionophoric properties of this ligand toward lanthanoid is evaluated by NMR titration in $CDCl_3/CD_3OD$ (Table 5). They use lanthanum for the study due to its diamagnetic nature. When the ratio of Ln/Ligand is less than 1, peaks corresponding to free ligand and complex are both observed, indicating the slow ligand exchange occurring at room temperature. When the ratio is increased to 1:1, the complete loss of ligand NMR signal supports the formation of 1:1 metal to ligand complex. Upon complexation, only the proton chemical shifts of *tert*-butyl group and $N(CH_2CH_3)_2$ are not strongly affected. Equatorial protons of $Ar-CH_2-Ar$ move downfield, while axial protons experience an upfield shift. By an in depth analysis of the difference of proton signals between axial and equatorial protons

before and after complexation, the more flattened and symmetrical cone conformation is formed in comparison to the ligand. Phenolic oxygen atoms participate in interaction with La^{3+}, leading to the deshielding effect on the aromatic protons. In the case of the Eu^{3+} and Yb^{3+}, the peaks shift in different directions upon complexation. The assignment of peaks is not achievable due to the distorted and broadened signals.

Table 5: Chemical shift (ppm) of peaks before and after complexation.[81]

	t-Bu	ArCH$_2$Ar		OCH$_2$CO	ArH
		Eq	Ax		
Ligand	1.07	3.19	5.29	5.02	6.78
Ligand + La^{3+}	1.19	3.79	4.30	5.34	7.34

The group of de Namor also reported a similar investigation of the same ligand with trivalent ions in CD$_3$CN by NMR spectroscopy.[82] The lanthanoid they use to form a 1:1 complex is extended to Sc^{3+} and Y^{3+}.[83] They further investigated the stability constant of a series of lanthanoid complexes using competitive potentiometric titration and microcalorimetric titration in acetonitrile and DMF solutions (Table 6). The discussion on these two techniques is beyond the scope of this thesis, but the large binding constants show calixarene tetraamide is tightly bound to lanthanoid ions.

Table 6: The binding constant of selected lanthanoid complexes in acetonitrile and DMF.[82]

Cation	Log K	
	MeCN	DMF
Y(III)	4.86 ± 0.02	4.78 ± 0.05
La(III)	4.80 ± 0.04	4.53 ± 0.04
Nd(III)	5.83 ± 0.03	4.99 ± 0.05
Eu(III)	5.54 ± 0.04	5.00 ± 0.02
Gd(III)	6.13 ± 0.04	5.12 ± 0.01
Yb(III)	4.91 ± 0.04	4.67 ± 0.05

The research on tetra-amide functionalised calixarene is also extended to study the binding constant and stoichiometry of the lanthanoid-ligand complex by UV-visible spectroscopic titration.[84] The UV-visible spectrum of spectroscopic titration of the lanthanum(III) nitrate to calixarene tetraamide in an acetonitrile solution is recorded (Figure 22). The peak in the absorption spectrum corresponds to the $^1\pi\pi^*$ transition of the aromatic rings of calixarene. The spectroscopic titration curve reveals that both secondary tetra-amide and tertiary tetra-amide functionalised calixarene form 1:1 metal to ligand complexes. The binding constant of the secondary tetra-amide functionalised lanthanum(III) complex was calculated to be log K = 5.104 ± 0.008.
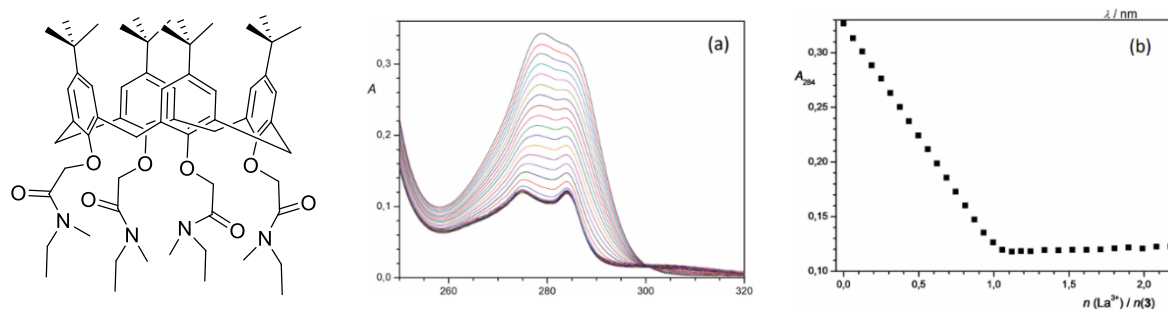
Figure 22: Left: structure of the tertiary tetra-amide functionalised calixarene; middle, spectrophotometric titration of the calixarene with the La(NO₃)₃·xH₂O; Right: the dependence of absorbance at 284 nm versus the La³⁺/ligand molar ratio.[84]**Figure reproduced from reference with the permission of the Croatian Chemical Society.**

The stoichiometry of lanthanoid complex of calixarene tetraamide can also be investigated by emission spectroscopic studies. One of the examples, debutylated calixarenetetramide (Figure 23, NR_2 = 1), was reported by the Gunnlaugsson group.[85] The piperidyl-functionalised caliaxarene tetraamide was titrated with $Tb(ClO_4)_3$ in methanol (Figure 24). Without Tb^{3+} ions, the broad and weak emission from the calixarene scaffold is observed at 416 nm at room temperature. Upon addition of the Tb^{3+} ions, the absorption peak corresponding to the calixarene decreases. The hydrochromic behavior of the calixarene in the complex is displayed, evidenced by the blue shift of the absorption maxima at 271 nm. As is discussed above, the calixarene can sensitise the Tb^{3+} via the antenna effect. The Tb^{3+} luminescence is switched on upon addition of $0 \rightarrow 1$ equivalent of Tb^{3+}. The emission intensity does not further increase after one equivalent of Tb^{3+}. The nonlinear regression analysis SPECFIT confirms the formation of 1:1 complex with a binding constant value of log K = 8.2 ± 0.8.
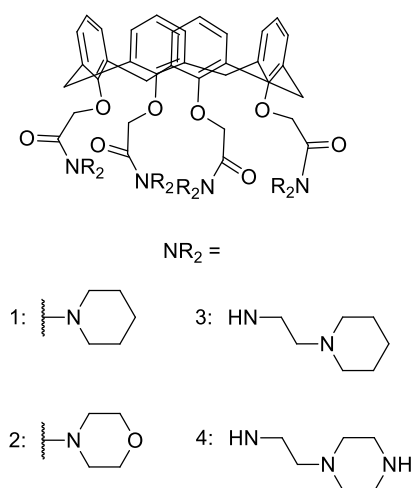
Figure 23: Structure of debutylated calixarenetetramide.[85]
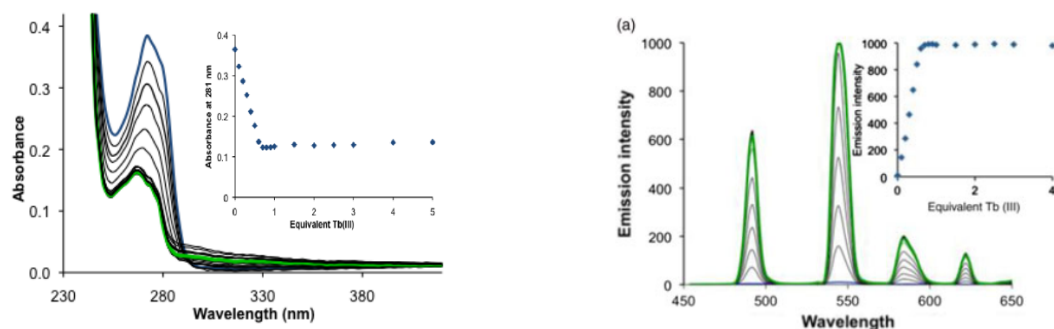
Figure 24 : Absorption (left) and Emission (right) spectra of ligand upon the addition of Tb(ClO$_4$)$_3$ in methanol.[85] **Figure reproduced from reference with the permission of the Taylor & Francis Ltd.**

In this report, the influences of the additional functional groups (such as piperazine and morpholine) attached to the secondary or tertiary amide group are also studied. Different non-coordinating functional groups (NR$_2$ = 2, 3, 4) still result in a 1:1 complex with the value of binding constant log K > 5. However, increasing the length of CH$_2$ chain or converting to the secondary amide group can lead to a shorter lifetime and poorer overall quantum yield.

Table 7: Summary of photophysical properties of Tb^{3+} complexes.[85]

Complex	Tb(**1**)	Tb(**2**)	Tb(**3**)	Tb(**4**)
$\Phi(\%)$	19.0	18.6	0.5	0.2
τ_{MeOD}(ms)	2.325	2.593	1.759	1.457
τ_{MeOH}(ms)	1.566	2.500	1.322	1.337
Binding constant (log K)	8.2 ± 0.8	5.5 ± 0.3	7.8 ± 0.3	5.3 ± 0.1

The group of Roundhill developed a Tb^{3+} complex of carbamoyloxy/primary amide-functionalised calixarene tetraamide (Figure 25).[86] The Tb^{3+} ion is expected in its coordination site, and its characteristic luminescence is sensitised via calixarene. The lifetime of this complex in methanol falls in the microsecond range, and the lifetime is shortened after addition of the water. This is due to the complexation of water to the Tb^{3+} centre, and the water in the first coordination sphere is a more efficient quencher of the lanthanoid luminescence than methanol. Furthermore, the lifetime is significantly shorter in comparison to that observed in tertiary amide-functionalised calixarene reported by Sabbatini group[80] and Gunnlaugsson group[85]. The NH vibration quenching which can relax the Tb^{3+} excited state is responsible for this result.
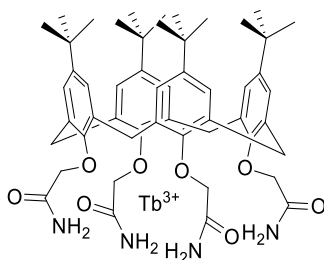
Figure 25: Structure of Tb³⁺ complex of primary amide-functionalised calixarene.[86]

The research on the tetra-amide functionalised calixarene with *p*-allyl groups on the upper rim further extends the investigation of lanthanoid complexes (Figure 26). Similar to the debutylated calixarene, the change of the substituent to *p*-allyl on the upper rim does not prevent the formation of a 1:1 lanthanoid complex. The *p*-allyl calixarene tetraamide also can work as an antenna for lanthanoid sensitisation. It is also found by X-ray crystallography that the solvent molecule accommodates inside the calixarene cavity coordinated directly to the lanthanoid centre. The presence of a solvent molecule which has a OH oscillator, may significantly affect the photophysical properties of lanthanoid complexes. Unlike the bis-amide or tri-amide functionalised calixarene, the addition of a base is not necessary for growing crystals due to the absence of OH groups. All oxygen atoms of the calixarene, including the oxygen atoms of amide groups, participate in lanthanoid coordination. In the crystal structure, the neodymium cation is nine-coordinate: four oxygen atoms from calixarene, four oxygen atoms from amide groups plus one oxygen atom from water molecules situating in the cavity of the calixarene. The complexation results in a positively charged complex which was balanced out with three nitrate ions from the $Nd(NO_3)_n(solvent)_n$ complexes.
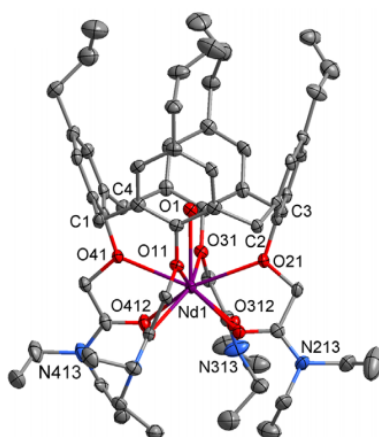
Figure 26: Complexes of tetra-amide functionalised calixarene. Left: potassium(I) complex of *p-tert*-butylcalix[4]arene;[78] **Right, neodymium(III) complex of tetra-amide functionalised calix[4]arene with *para*-allyl groups on the upper rim.**[22] **Figure reproduced from reference with the permission of the Taylor & Francis Ltd.**

Researchers have made use of the well-established chemistry of the calixarene to design systems that will bind Ln cations in the vicinity of a range of potential antenna moieties. Particularly for the

tetraamide system, the antenna moiety can be attached to the lower rim of the calixarene via the amide linker and successfully sensitise lanthanoid luminescence. The group of Reinhoudt reported an isothiocyanate-functionalised fluorescein moiety as a sensitizer (Figure 27).[87] The authors propose the energy transfer from the excited triplet state to the emissive state of Nd^{3+} and Er^{3+}, but the singlet state might also be involved. As well as considering the impact of coordinated solvent molecules, the authors also mention another factor that some solvent molecules, such as water and methanol, are high vibrational energy groups resulting in a shorter lifetime and lower luminescence intensity. The authors also mention that another factor needed to be taken into consideration is the spacers between the lanthanoid centre and antenna. The external heavy metal effect (intersystem crossing) is less effective after the length of spacer is increased from C_3 to C_6. Although the spacers do not shorten the luminescent lifetime, it significantly reduces the fluorescein intensity due to the different energy transfer efficiency.
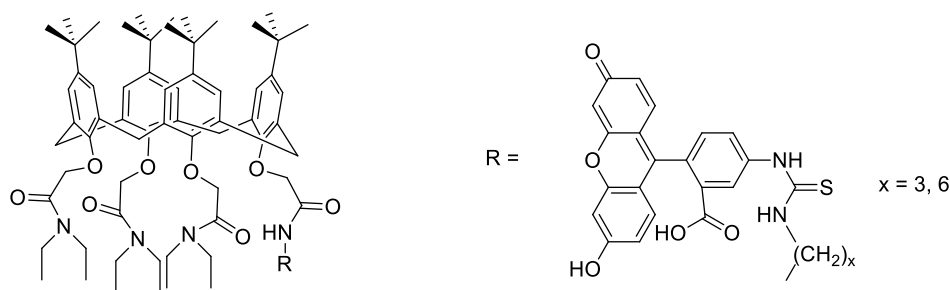
Figure 27: Tetrasubstituted calixarene derivatives.[87]

1.4 Naphthalenetetracarboxylic Diimide

1.4.1 Naphthalenetetracarboxylic Dianhydride (NDA)

The naphthalenetetracarboxylic diimide (NDI) is a member in the family of rylene diimide. The naphthalene tetracarboxylic anhydride is the precursor of NDI. The naphthalene tetracarboxylic anhydride (NDA) consists of six oxygen atoms, four hydrogen atoms and fourteen carbon atoms. The NDA is a centrosymmetric molecule with all atoms in the same plane. It is commercially available, but the synthesis of NDA is not straightforward. It has been reported that the synthesis of NDA can be achieved starting from the pyrene via a three-step reaction (Scheme 3).[88] The first step is the chlorination to introduce the chlorine at 1, 3, 6 and 8 positions. The tetrachlorinated pyrene is further hydrolysed to the enol, followed by tautomerising to the bis-dione. The desired product is obtained by the further oxidative process using chromic acid or chlorine.
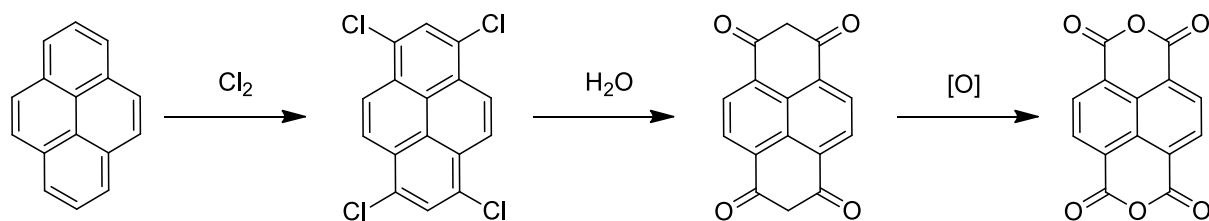
An alternative synthetic path for NDA is achieved by a reaction of commercially available 1,4,5,8-naphthalenetetracarboxylic acid with SF$_4$ (Scheme 4).[89] Due to the production of harmful by-products (SO$_2$ and HF) in the reaction, sulphur tetrafluoride is no longer used for the preparation of NDA. The use of acetic acid as the solvent of the reaction not only avoided the formation of by-products, but it also improved the yield and has an easy workup procedure.[90]
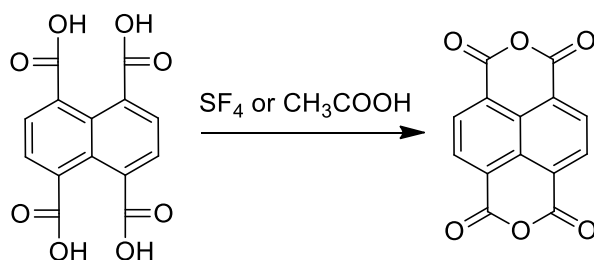
Scheme 4: Synthesis of the NDA from 1,4,5,8-Naphthalenetetracarboxylic acid.[89-90]

1.4.2 Naphthalenetetracarboxylic Diimide (NDI)

The NDI is synthesised from NDA and can be functionalised at the axial position, shoulder position and core position for different properties and applications.
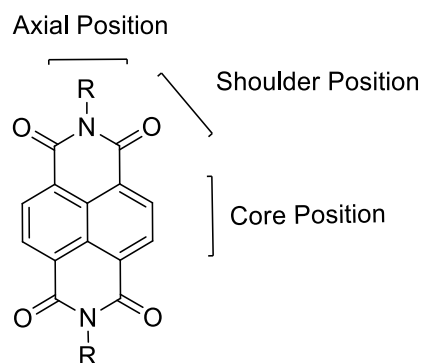
Figure 28: Structure of NDI. "R" is the functionalised group.

The condensation reaction of NDA with alkyl/aromatic amines at the axial position produces NDI derivatives, which are more soluble than NDA. A wide range of functional groups attached to the amine can be introduced at the axial position for various purposes and potential applications. For example, alkyl chain functionalisation improves solubility in organic solvents.[91] Polypyridyl groups,[92] phosphonate groups[93] and carboxylate groups[94] can offer extra coordination sites to bind metals. Aromatic rings at the axial position may impact photophysical properties.[95]

The synthesis and purification of a mono-imide mono-anhydride functionalised molecule is not straightforward because the reactivity of the two anhydride groups is the same, and the byproduct (diimide) has a similar polarity to the one observed for the desired product, making separation by

chromatography difficult. In contrast, the synthesis and purification of diimides with the same substituent is much easier because the excess amine is much polar than the NDA product. Nevertheless, if two different functional groups need to be attached to the diimide, stepwise functionalisation of NDA can be achieved (Scheme 5).
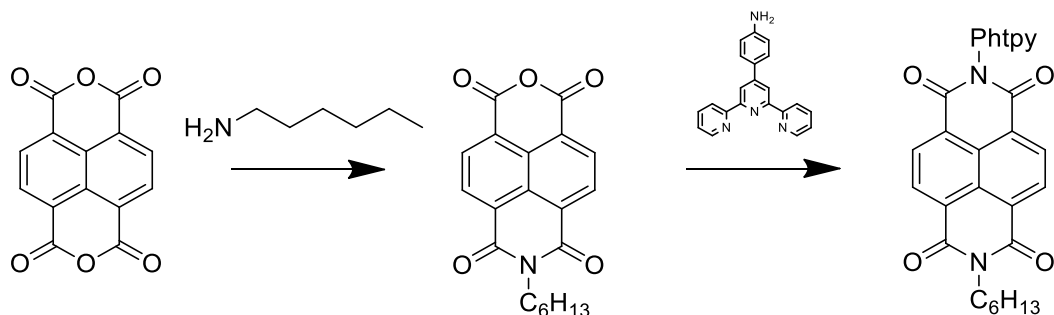
Scheme 5: Synthesis of polypyridyl NDI.[96]

The synthesis of core-functionalised NDI requires three steps (Scheme 6)[97]: 1) the first step is to synthesise the brominated NDA using bromine/iodine oleum at the core position. The stoichiometry of the NDA to bromine, reaction time and temperature should be well-controlled to yield the desired mono-, di-, tri- and tetra-substituted products; 2) The second step is the condensation reaction of the brominated NDA with the required amine; 3) The desired functional groups can then be attached to the core of NDI via nucleophilic aromatic substitution reactions. The example of core-cyanated naphthalene diimide is shown below.
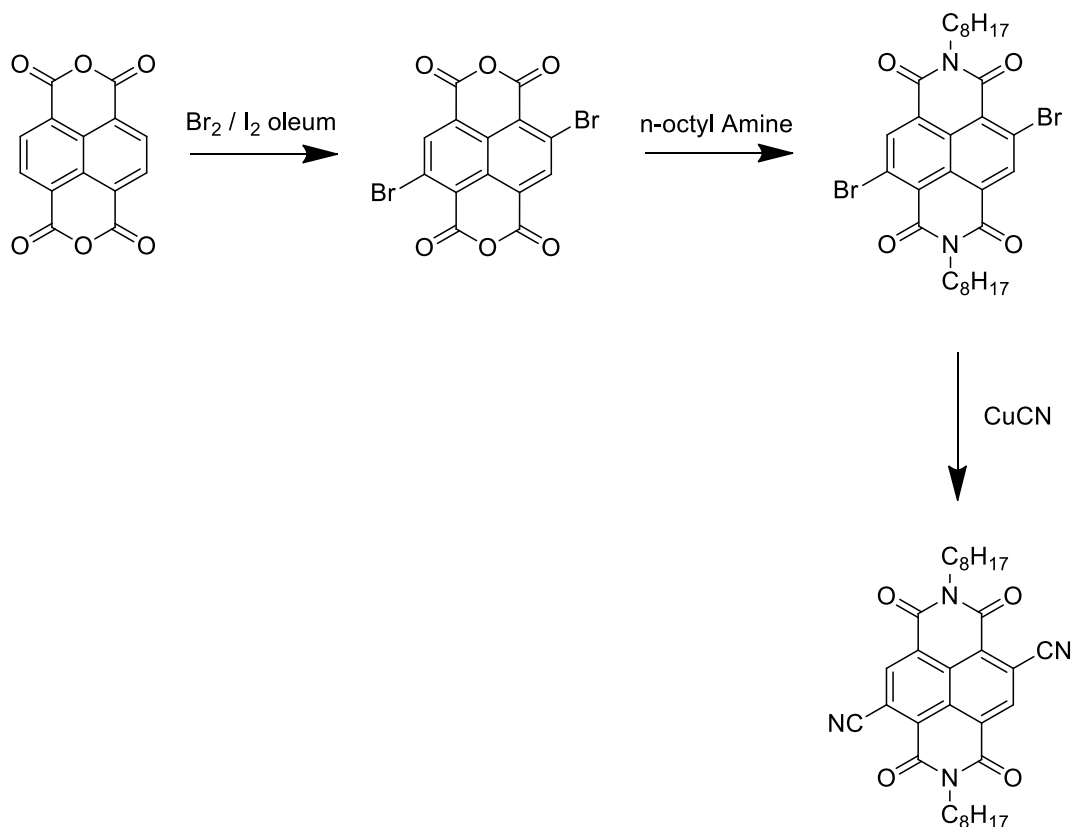
Scheme 6: Synthesis of core-cyanated naphthalene diimide.[97]

The shoulder functionalisation is less common in comparison to functionalisation at axial and core positions. It has been reported that this can be achieved by utilising the anhydride group of the NDA to react with arylene diamine at high temperature in the presence of zinc acetate as a catalyst (Scheme 7).[98]. Another example reported by the group of Pritam shows the oxygen of the anhydride can be replaced with the dithiafulvalene moiety via a $P(OEt)_3$-mediated cross-coupling reaction in toluene.[99] The further reaction to produce the imide derivative is achieved by reacting with amines.
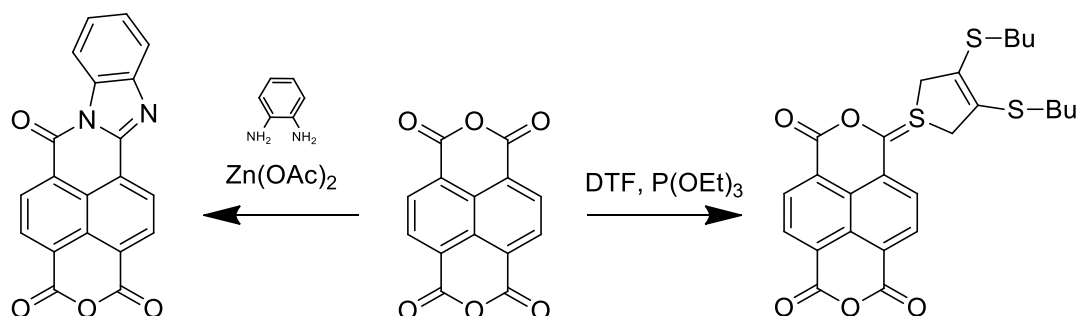
Scheme 7: Synthesis of NDA derivatives functionalised at the shoulder position.[99]

The functionalisation of NDI at different positions makes NDI have different physical and chemical properties, allowing versatile applications of the NDI. These will be discussed in the following section.

1.4.3 Photophysical Properties of NDI

Core–substituted NDI derivatives are most widely studied because c-NDI derivatives exhibit various chemical-physical, photophysical and electronic properties. From the photophysical perspective, the absorption profile of core-substituted NDI not only has a band around 400 nm corresponding to the π-π* transition of NDI core, but it also has a substituent-dependent charge transfer band in the lower energy range. In this project, we are interested in photophysical properties and their interaction with lanthanoids. As discussed above, however, the charge transfer state is not preferable for lanthanoids. Therefore, the discussion will mainly focus on the axially functionalised NDI without any aromatic substituents as these are most relevant to this thesis.

The steady-state absorption spectrum of the alkyl NDI-functionalised at axial position shows an intense band around 400 nm with vibronic progression, indicating S_0 - S_1 transition (Figure 29).[100] The band below 250 nm is associated with the π-π* transition. Upon excitation, the mirror image fluorescent emission with a 7 nm Stokes shift is observed. The excited-state lifetime of the peak around 400 nm is less than 20 ps, corresponding to the fluorescent emission.[95] The intersection point of absorption and emission spectra at room temperature is used to estimate the energy of the excited singlet state of alkyl-substituted NDIs lying around 25800 cm^{-1}. Phosphorescence is not observed at room temperature. The addition of organic solvents with heavy atoms, such as MeI, facilitates the intersystem crossing process to produce more efficiently populate the triplet state, making it possible to see phosphorescence. The long-lived emission indicating the energy of the lowest triplet state is observed only in the presence of methyl iodide at 77K. However, it is ambiguous as to whether the phosphorescence is from the NDI monomer or aggregates.
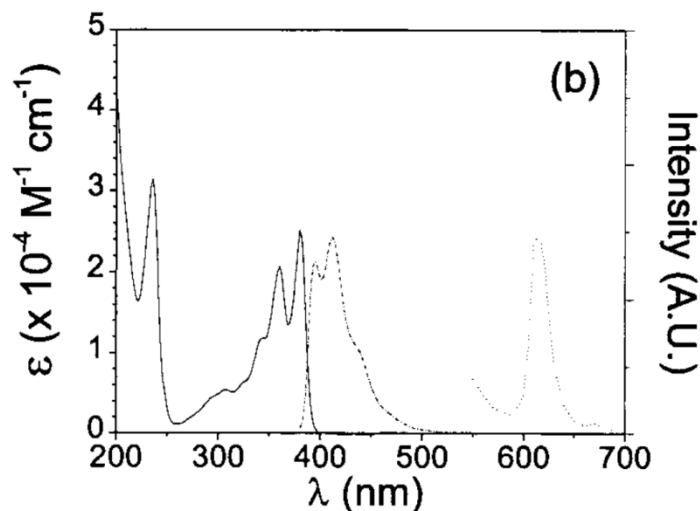
Figure 29: UV-visible spectrum (room temperature, dash trace), fluorescence (room temperature, dashed trace), phosphorescence (77K, dotted trace).[100] Figure reproduced from reference with the permission of the American Chemical Society.

1.4.4 NDI Aggregates

Due to the planar nature of the molecule, the naphthalenetetracarboxylic diimides tend to form an aggregate in concentrated organic solutions and de-aggregate in a diluted solution. For example, the NDI functionalised with propyl groups at the axial position (Figure 30, left) was found to aggregate in acetonitrile solution. It has been reported that aggregate species dominate the emission spectrum in a water solution.[101] As long as the aggregate forms, a structureless and broad band is observed around 500 nm along with the peak around 400 nm corresponding to the fluorescence of monomer in the emission spectrum (Figure 30). The lifetime of the aggregate peak is estimated to be around 19 ns.[102] But the lifetime can be variable when NDI is functionalised in a way leading to differently structured aggregates.[103-104] Although the absorption and excitation spectra of NDI in a concentrated acetonitrile solution are not recorded, the authors propose the NDI self-associates to form the aggregates in the ground state due to the lower probability of occurrence of the diffusional process upon excitation. Supported by many crystal structures,[105-107] the aggregation also occurs in the solid state due to intermolecular π-πstacking interactions. In the photophysical investigation of NDI in toluene or hydrocarbon functionalised NDI, a broad peak around 500 nm is also observed.[95, 107] However, this peak can be either the aggregate peak or the peak attributed to the charge transfer state.
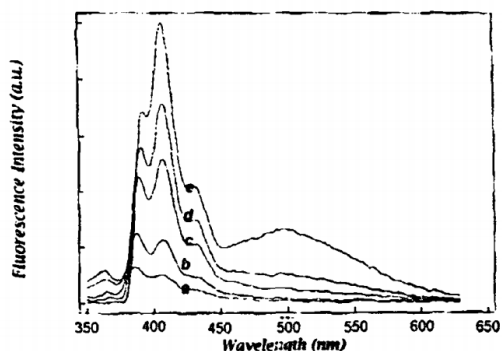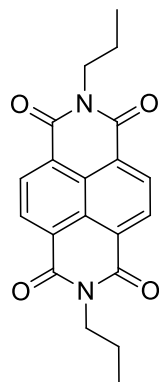
Figure 30: Emission spectra of the dibutyl-functionalised NDI in acetonitrile solutions at different concentrations. Concentration from a to e: 4.6 x 10^{-6} M to 1.5 x 10^{-4} M. Excitation wavelength: 340 nm.[101] **Figure reproduced from reference with the permission of the American Chemical Society.**

The aggregation properties of NDI are unpredictable. The formation of aggregate depends on many factors: the functional groups of NDI, the concentration of a solution, different solvents, media, etc. Incorporation of the NDI into the metal complex extends the application of NDI, but it makes the understanding of the formation of aggregate more difficult. Therefore, a carefully designed NDI ligand with the consideration mentioned above is a challenge in this project.

1.4.5 NDI Dimers and Trimers

Over the past two decades, there are some reports on the construction of dimeric and trimeric NDIs. The group of Howard reported the synthesis and characterisation of a NDI dimer (Figure 31).[108] The condensation reaction between naphthalenetetracarboxylic dianhydride and 2,2-(ethylenedioxy)bis(ethylamine) yields the dimeric NDI molecule linked via the ethylenedioxy group. The papers only describe structural characterisation by X-ray crystallography. They show the electron-deficient NDI has a host-guest interaction with the electron-rich pyrene via the intermolecular π-πstacking to afford a supramolecular polymer.
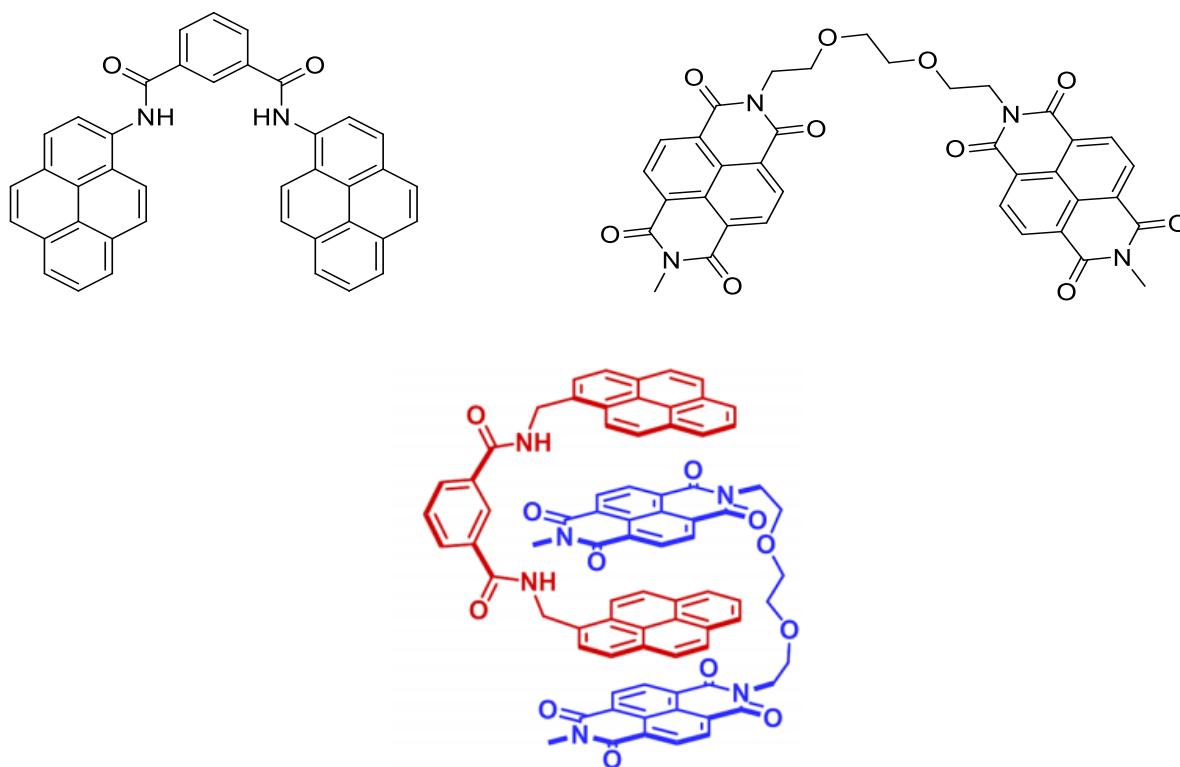
Figure 31: Left, bis-pyrenyl molecule; middle, bis-NDI molecule; right, subunit of polymer driven by π-π* stacking interaction.[108] **Figure reproduced from reference with the permission of the American Chemical Society**

The Stoddart and Wasielewski group reported the synthesis and characterisation of the cyclic NDI dimer which was linked by two cyclohexanes (Figure 32).[102] The one equivalent of 1,2-cyclohexanediamine is reacted with one equivalent of NDA to produce the NDI dimer. Regardless of diamine enantiomers, the reaction yield is only 10%. The X-ray crystallography show there is an intramolecular π-π stacking interaction between these two NDI units with a distance of 3.5 Å and an intermolecular π-π stacking interaction between them with a distance of 3.3 Å.
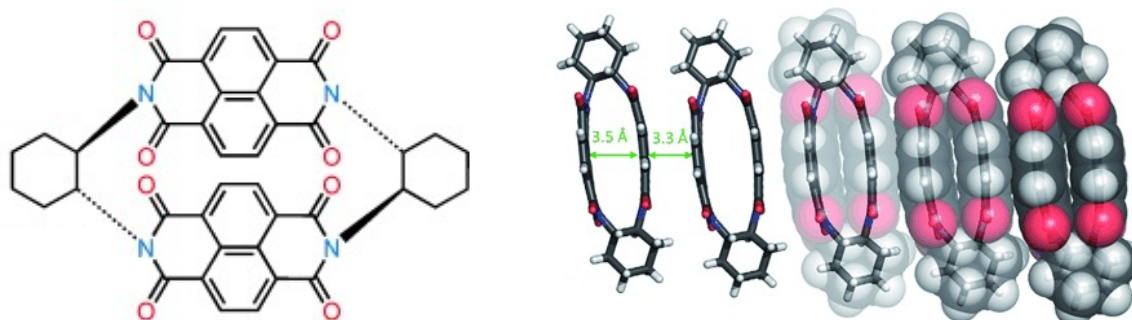
Figure 32: Rigid cyclophane dimer and its crystal structure.[102] **Figure reproduced from reference with the permission of the John Wiley and Sons.**

33

The close distance between two NDI rings leads to through-space electronic interaction. Therefore, some photophysical (Figure 33) and electrochemical (Figure 34) properties of monomer are not observed. From a photophysical perspective, the UV-visible spectrum of NDI dimer in a dichloromethane solution shows the visible blue-shifted peak in comparison to dicyclohexyl NDI and a shoulder around 400 nm attributed to the H aggregation that molecules stack predominantly face-to-face. One broad and structureless band around 500 nm is observed in the emission spectrum of the dimer. The lack of a peak around 410 nm and the vibronic progression commonly observed in the case of monomer indicates the formation of aggregate. The excimer-like emission is attributed to the dimeric molecule in the solution. The decay is fitted to monoexponential decay, and its lifetime is 20 ns.
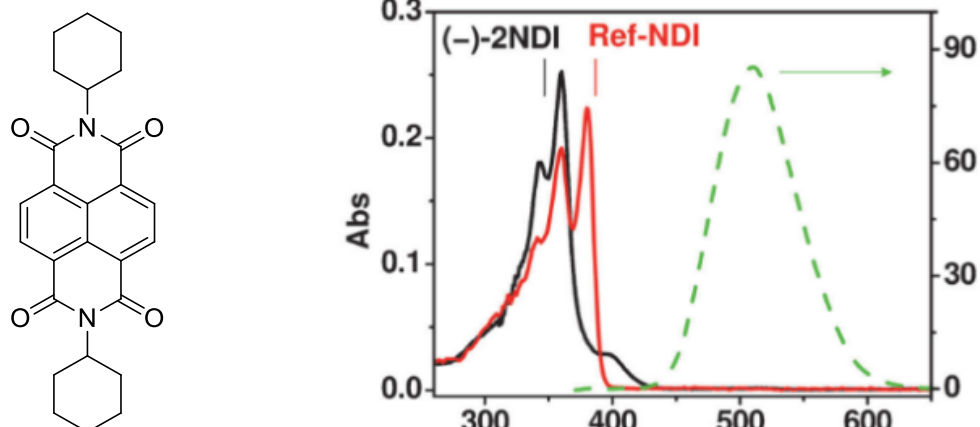
Figure 33: Dihexyl-functionalised NDI (reference); b) UV-visible absorption spectrum of the dimer (in black) and NDI dimer (in red), emission spectra of NDI dimer (in green).[102]Figure reproduced from reference with the permission of the John Wiley and Sons.

From the electrochemical perspective, four separate redox couples are resolved. The first cathodic wave and second wave correspond to the reduction of neutral NDI to NDI radical anion, both of which shift more positively in comparison to the reference. While the third and fourth cathodic waves correspond to NDI radical anion to NDI dianions, both of which shift more negatively. The splitting of the reduction potentials reveals electronic communication between the two NDI units in the NDI dimers units when it is reduced.
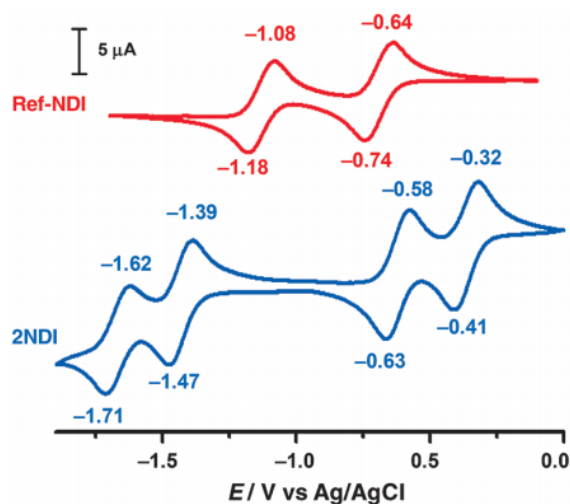
Figure 34: Cyclic voltammogram of reference (red trace) and NDI dimer (blue trace).[102] **Figure reproduced from reference with the permission of the** John Wiley and Sons.

The through-space electronic interaction can be extended to a molecular triangular prism consisting of three NDI units linked by three cyclohexanes. Similar phenomena with six well-separated redox couples appeared in the cyclic voltammogram.[109]
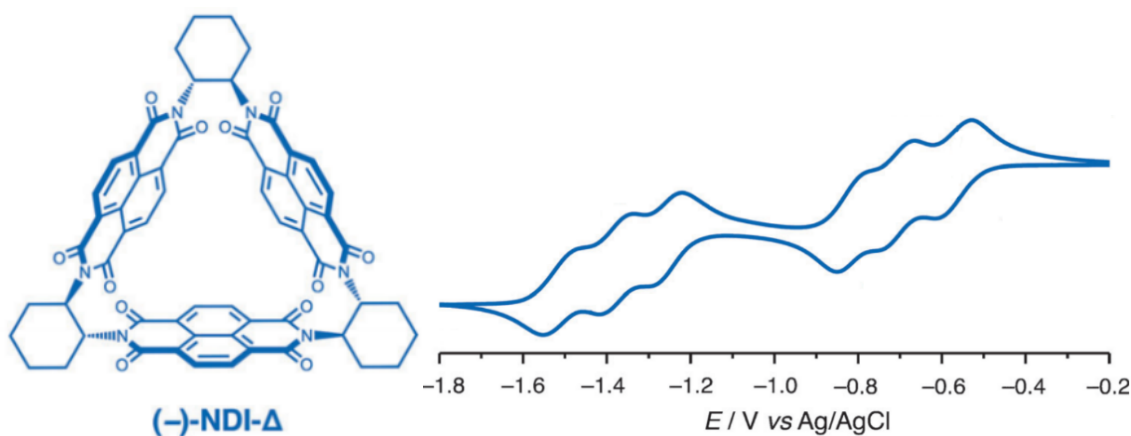
Figure 35: Structure of NDI triangle and its cyclic voltammogram.[109] **Figure reproduced from reference with the permission of the** John Wiley and Sons.

1.4.6 NDI Radical Monoanion and Dianion

The discovery of NDI radical anions and dianions is from the pioneering work of Stephen Nelsen who observed the redox peak in the spectrum of cyclic voltammetry and characterised it by EPR experiments *in situ*.[110] The most common way to synthesise the NDI radical anion and dianion is based on the chemical reduction of neutral NDI. Reactions are carried out by employing some reducing reagents, such as sodium dithionite,[111] $CoCp_2$,[109, 112] hydrazine,[113-114] etc. The neutral ligand can be recovered by adding mild oxidant, such as chloranil,[131] and nitrosonium tetrafluoroborate.[115]
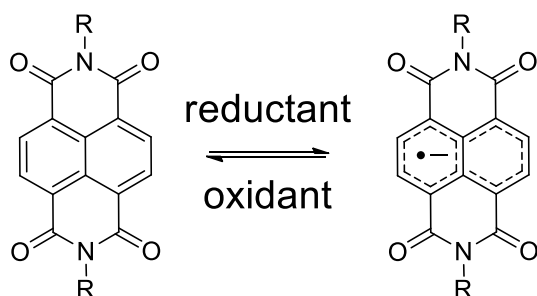
Scheme 8: The illustration of generating radical anion and recovering the neutral NDI.

Some other ways to generate the NDI radical anion include photoinduced energy transfer process and thermal energy transfer[116]: 1) A strong Lewis basic anion, such as F^- or OH^-, can generate the radical anion via thermal energy transfer process utilising the electron-accepting abilities of NDI. The excess F^- anion can further reduce the NDI radical anion to its dianion form. Therefore, the NDI can also work as a fluorescent sensor for sensing F^- ion; 2) A weak Lewis base, such as CH_3COO^- and Cl^-, can generate the radical upon photoexcitation.

Bulk electrolysis experiment can also be employed to reduce the neutral NDI (Scheme 9).[106] Compared with reduction by adding an excess amount of reducing reagents or photogenerating process, the reduction reaction can achieve excellent yield. It also offers the advantages of a selective generation of radical anion and dianions as the working electrode is held at the required constant potential.
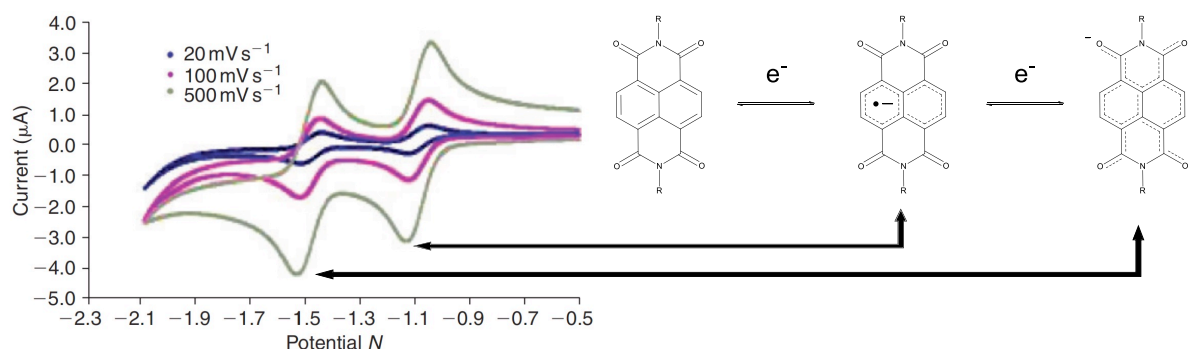
Scheme 9: Cyclic voltammetry of alkyl NDI and potential needed to generate reduced NDI species.[106] (NDI: E_{1red} = –1.10 V, E_{2red} = –1.50 vs. Fc/Fc$^+$ in CH_2Cl_2). Figure reproduced from reference with the permission of the CSIRO.

The absorption profile of NDI functionalised with pentyl groups at the axial position exhibits an absorption band around 360 nm corresponding to the S_0 to S_1 transition (Figure 36). In contrast to the neutral species, the absorption spectrum of the radical monoanion shows four lower energy bands for the NDI radical anion attributed to D_0 to D_n electronic transitions.[106, 117] The absorbance of neutral NDI decreases but does not disappear after bulk electrolysis in this system.
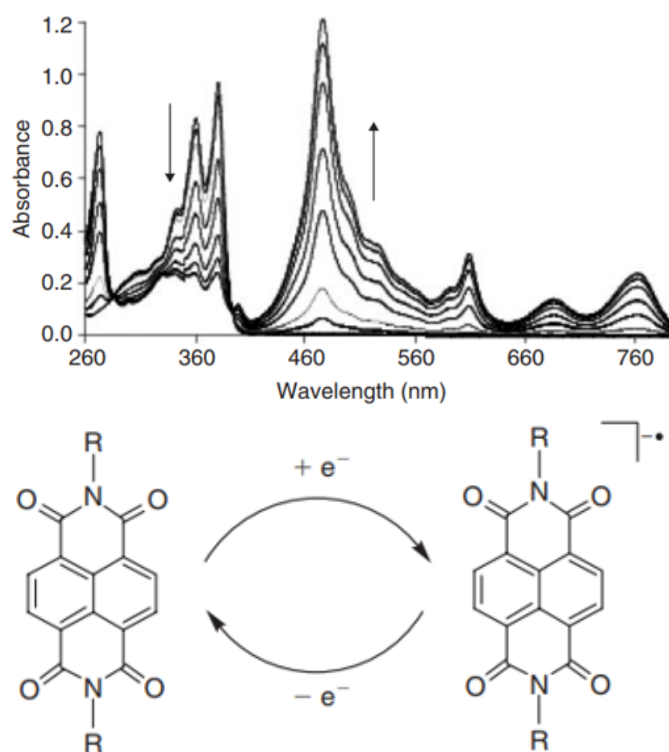
Figure 36: Absorbance spectra at constant electrolysis potential.[106] "R" group is $CH_2(CH_2)_3CH_3$. Figure reproduced from reference with the permission of the CSIRO.

However, the radical monoanion is still not stable with respect to oxidation. The deep colour always fades immediately if the reduction potential is removed or the mixture is exposed to the air. It was not until 2018 that the first stable NDI radical anion core-functionalised with tetracyano groups was isolated (Figure 37).[115] The NDI radical anion with phosphonium counter ion is isolated and characterised by ESI-MS and X-ray crystallography. This NDI radical anion has unprecedented stability at room temperature, and it can even be purified by column chromatography. Neutral molecules can be recovered by using $NOBF_4$ as an oxidant. The reversibility of neutral NDI to NDI radical anion is further supported by X-ray crystallography and UV-visible studies.

There was another example of diphosphonium-substituted cNDI radical anion reported by the same group showing similar stability, spectroscopic properties and electronic properties.[117] The lifetime of the doublet state is estimated to be 260 ps by transient absorption experiments.[118]
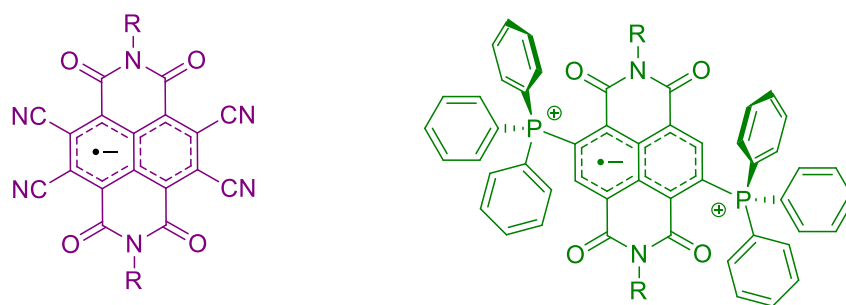
Figure 37: Structure of tetracyano-NDI radical anion (left)[115] and bis-phosphonium functionalised NDI radical anion (right).[117]

1.4.7 NDI Applications

The NDI finds application as anion, cation and pH sensors. An example of the anion sensor is based on its interaction with the fluoride anion.[119] As a fluoride sensor, the advantage of NDI is that the colour change is visible to the naked eye. The sensing ability of NDI can be improved by introducing electron donor groups at the core position.[120] NDI is also a promising candidate for cation sensing after the introduction of a coordinating group, regardless of where it is functionalised. The addition of the metal usually leads to changes in the absorption spectrum and emission spectrum. The detection limit of the trace amount of a selective metal can be as low as 10^{-7} M for metals, such as Hg^{2+} (Figure 38).[121] The pH sensor has also been widely studied when the pH-sensitive group is introduced, such as pyridine[122] and amine[123]. The NDI sensor is stable under basic and acidic conditions. The spectra are usually reversible in response to pH after the addition of a base to acid or acid to base.
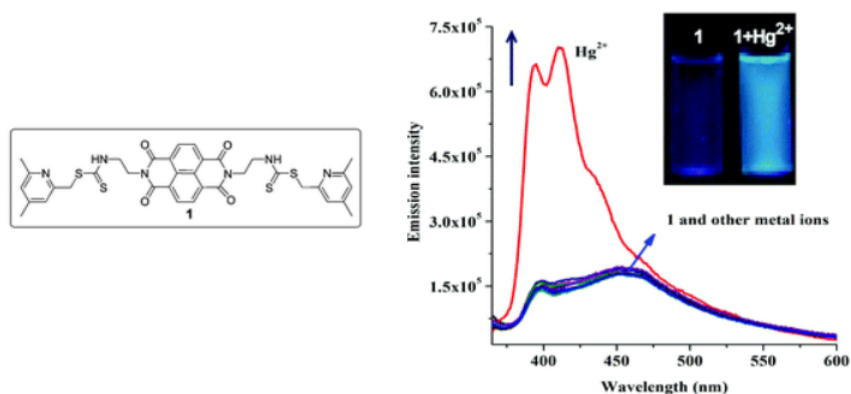
Figure 38 : NDI derivative used as a cation sensor for the detection of Hg^+ ion.[121] **Figure reproduced from reference with the permission of the Royal Society of Chemistry.**

NDI has been extensively studied with respect to its interaction with DNA. The NDI derivatives can intercalate with DNA because of its planar core. The introduction of ferrocenyl moieties at the axial position is used to sense single-strand DNA and double-stranded DNA with the assistance of electrochemical analysis.[124] Moreover, well-designed amine-functionalised NDI derivatives can selectively bind the quadruplex, regulate the telomerase activity and finally inhibit the cell growth (Figure 39).[125-126]
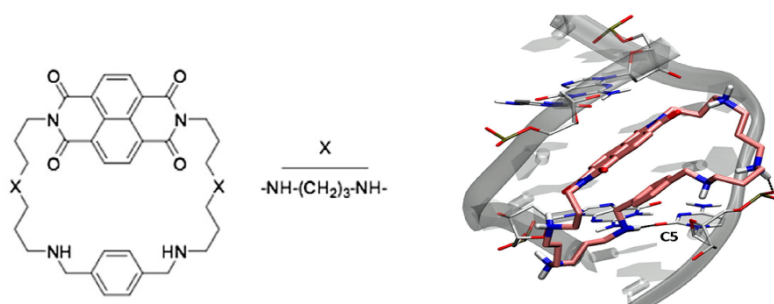
Figure 39: Binding mode of NDI derivatives with duplex DNA.[126] **Figure reproduced from Reference with the permission of Elsevier.**

The surface of the NDI core is π-acidic and can be used as an organocatalyst. It can not only catalyse enolate addition, but it also can stabilise the intermediate and transition state. For example, phenoxyethanol-functionalised NDI can stabilise the enolate and the transition state via anion–π interactions on the surface of the NDI core.[127] It opens up a new pathway to develop and catalyse the reactions, such as aldol reaction, Claisen condensation, Mannich reaction, etc. NDI derivatives can also catalyse photosynthesis by using its photoexcited charge-transfer state upon irradiation. For example, amine-functionalised C-NDI derivatives have an electron-deficient core and an electron-rich donor, increasing the character of the charge-transfer state.[128] The excited state reduction potential is estimated to be approximately +1.0 V (vs SCE) which is sufficient to photocatalyse typical organic reactions.

The unique properties of NDI also contribute to the development in the field of ion channels in the lipid membrane,[129-130] optoelectronics,[131-132] field-effect transistor,[97, 133] gas adsorption,[134-135] and so on.

1.4.8 Lanthanoid Complexes of NDI

NDI ligands with d-block metals have been extensively investigated over the last couple of decades in the field of photoredox chemistry as an electron acceptor[136-138] and coordination chemistry as a building block[112, 139-140] for constructing large structures. However, the NDI derivatives with rare earth elements are relatively unexplored.

Lanthanoids tend to coordinate to oxygen atoms and have a wide range of coordination number depending on the cationic radii and coordinated ligands. 1,4,7,10-The tetraazacyclododecane-1,4,7,10-tetraacetic acid (DOTA),[141] ethylenediaminetetraacetic acid (EDTA)[142] and diethylenetriaminepentaacetic acid (DTPA)[143] are widely used ligands functionalised with carboxylic acid groups for binding lanthanoids. However, carboxylate ligands can coordinate to the metal in many ways: monodentate, bidentate, bridging, μ_2-η^2,η^1 ligands, etc (Figure 40).[144] Regardless of the coordination mode, oxygen atoms of coordinating carboxylate groups have a high affinity for lanthanoids. Therefore, the carboxylic acid groups can be introduced through diimide nitrogen, and reported lanthanoid complexes containing NDIs heavily rely on the introduction of carboxylic acid groups for binding.

Figure 40: Coordination mode of carboxylate (from left to right): monodentate; bidentate; bridging;μ₂-η²,η¹.

Hui Li and his coworkers reported the successful synthesis of a well-ordered coordination polymer containing the lanthanum(III) complex of carboxylate-functionalised NDI (Figure 41).[145] The carboxylate groups can be fully deprotonated and coordinate to lanthanoid without the addition of base. The lanthanum(III) ion in a monomeric unit was nine-coordinate: two chloride atoms, an oxygen atom from DMF and six oxygen atoms from carboxylate groups coordinating in a μ₂-η²,η¹fashion: two μ-O4 atoms and two O3 atoms are from two carboxylate groups; the other two μ-O4 atoms are from the two neighbouring carboxylate groups. Two μ-O4 atoms with one μ-Cl atoms bridge to the neighbouring lanthanum(III) ions. Intermolecular π-π* stacking interactions contribute to the formation of 3D coordination architecture as well.
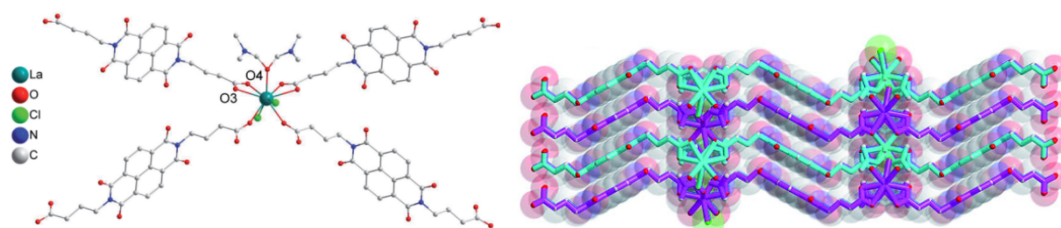
Figure 41: Lanthanoid complex of carboxylate-functionalised NDI in the subunit (left); polymeric structure (right).[145] Figure reproduced from reference with the permission of the John Wiley and Sons.

The polymer was investigated in the solid state by absorption and emission spectroscopy (Figure 42). Both spectra display the broad peak and loss of vibronic structure. No significant difference between the ligand and complex is observed in the absorption spectrum. Upon excitation, the complex displays a blue-shift emission in comparison to the ligand. The ligand to metal charge transfer state probably contributes to this emission spectrum. The photophysical investigation is also extended to other lanthanoids. It is notable that the small spike corresponding to Eu^{3+} luminescence is observed around 620 nm in the emission spectrum, attributed to the $^5D_0{\rightarrow}^7F_2$ transition. But further evidence is not found to show that the energy transfer is from the NDI.
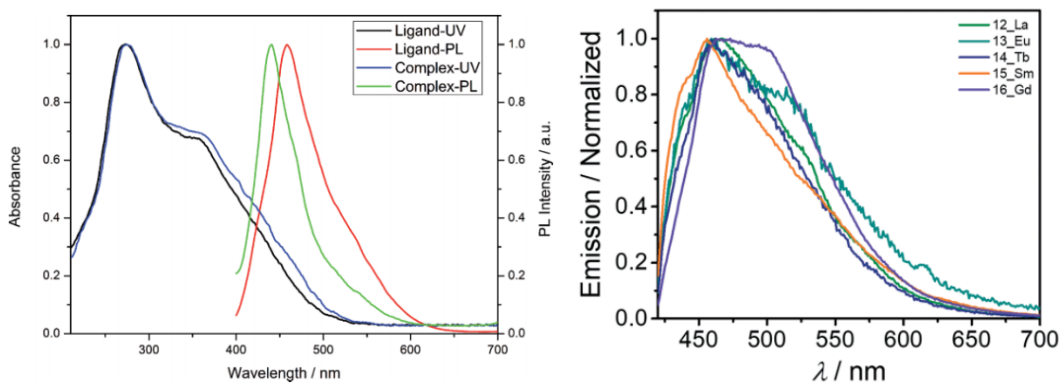
Figure 42: UV-visible spectra and emission spectra of the ligand and coordination polymer in the solid state.[145-146] **Figures reproduced from reference with the permission of the John Wiley and Sons.**

Another example of the NDI-lanthanoid coordination polymer is based on the introduction of two pendant pyridine N-oxide groups at the axial position of the NDI (Figure 43).[147] Erbium(III) ions coordinate to oxygen atoms of N-oxydic pyridine rather than the pyridine or oxygen atoms of the diimide group. Upon complexation, *cis-* and *trans-*NDI isomers are bound to the erbium(III) ions in a bidentate mode. The formation of a coordination polymer occurs as a consequence of a complexation reaction between erbium(III) ions and *trans* ligands. In the subunit, both of the Er^{3+} ions are octacoordinate in a dinuclear cyclic ring. Three nitrate anions are bound to each Ln^{3+} ion in a bidentate fashion, two oxygen atoms from the *cis* ligand and one oxygen atom from the *trans* ligand bridging to neighbouring Ln^{3+} ions to form the polymeric structure.
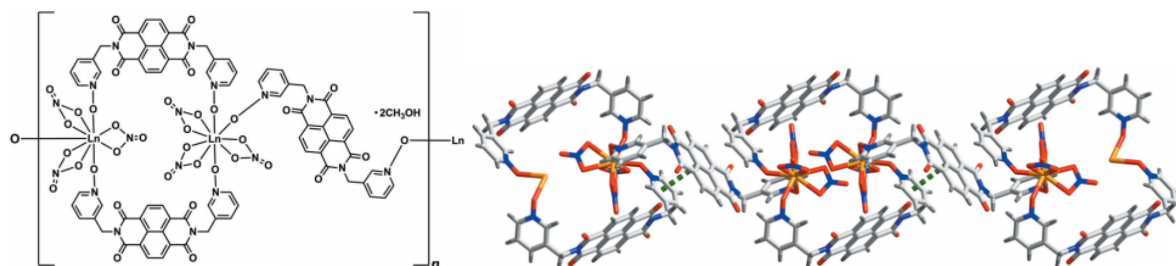
Figure 43: Structure of the subunit (left) and one-dimensional chain coordination polymer (right).[147] **Figure reproduced from reference with the permission of the International Union of Crystallography.**

The solid state photophysical study is investigated by diffuse reflection spectroscopic technique. The optical spectrum shows the optical band gap was 3.02 eV (410 nm) according to the absorption edge (Figure 44). A small red-shifted absorption edge is observed in comparison to the ligand, which further confirms the interaction between the metal and the ligand.
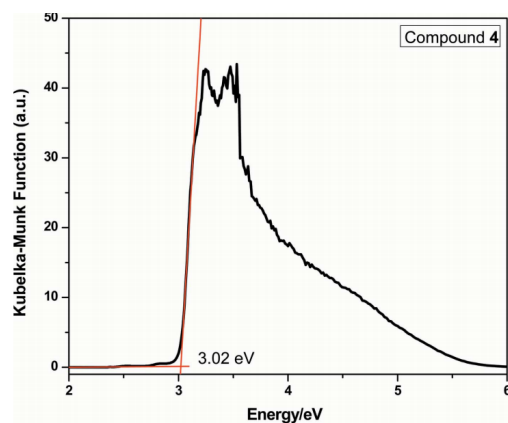
Figure 44: Optical diffusion reflection spectrum of the coordination polymer.[147] **Figure reproduced from reference with the permission of the International Union of Crystallography.**

Europium complexes of poly(diketone)-functionalised naphthalene diimide are used to detect DNA hybridization as a fluorescent intercalator (Figure 45).[148] The diketone is well known for its lanthanoid-binding property and sensitisation of lanthanoid luminescence. The europium fluorescence is observed after the intercalation with the double-stranded DNA, and the intensity of the Eu^{3+} fluorescence is proportional to the amount of Eu^{3+} complexes intercalated into DNA. The multidentate ligand consists of more than two antennas, and the energy transfer process is complicated to study. Further optical properties are not investigated in this paper.
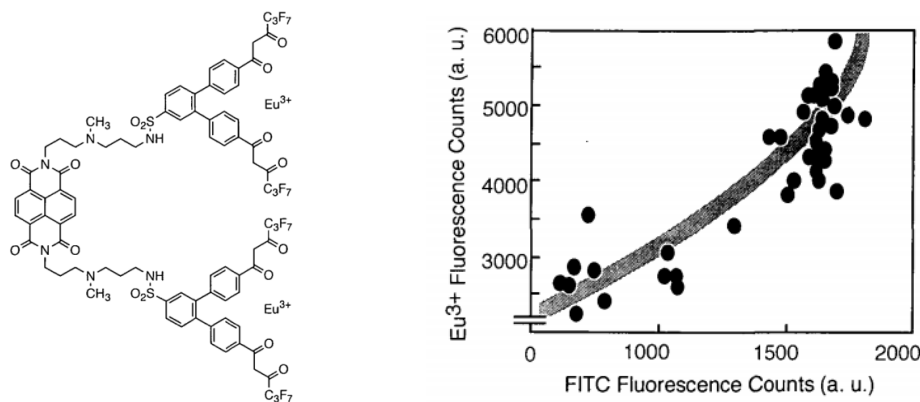
Figure 45: Structure of europium complex with diketone-functionalised naphthalene (left); the graph shows fluorescence intensity as a function of the amount of DNA.[148] **Figure reproduced from reference with the permission of the Oxford University Press.**

During the course of this project, the group of Hao reported the first example of naphthlenetetracarboxylic diimide as an antenna to sensitise the lanthanoid luminescence.[149] The benzenedicarboxylic acid-functionalised NDI (benzo-imide-phenanthroline tetracarboxylic acid, H₄BIPA-TC) is used for the construction of europium-based metal-organic frameworks (Figure 46). The Eu-MOF is prepared by heating the mixture of H₄BIPA-TC and $Eu(NO_3)_3$ hydrate at 100 °C for 36 hours. The crystal was obtained by slowly cooling the mixture to room temperature. The monomeric unit is a dinuclear europium(III) complex. The metal centre is bridged by carboxylates from four different ligands.

Each europium(III) ion is nine-coordinated by the two oxygen atoms from two DMA molecules, one nitrate ion coordinating in bidentate fashion and five oxygens from four different carboxylate groups: one oxygen atom and two μ-O atoms were from two different carboxylate groups coordinating in a μ_2-η^2,η^1 mode, two oxygen atoms are from two different carboxylate groups coordinating in a bridging mode.
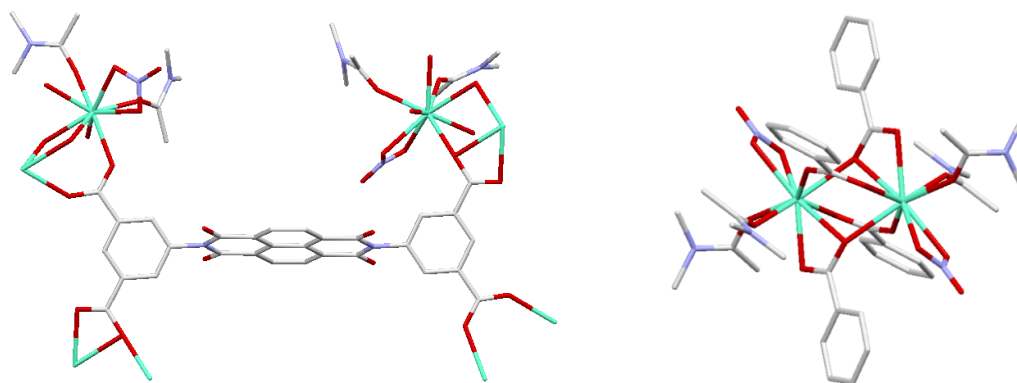
Figure 46: Coordination environment of the H4BIPA-TC ligand (left); Structure of the monomeric unit of Eu-MOF (right).[149]Figure reproduced from reference with the permission of the Royal Society of Chemistry.

The H4BIPA-TC ligand and Eu-MOF are characterised by the emission in the solid state and dispersed phase (Figure 47). Upon excitation, the emission spectrum of the free ligand in the solid state displays a peak around 440 nm. The emission band of Eu-MOF is red-shifted to around 450 nm with a shoulder around 550 nm. More importantly, the Eu^{3+} spike around 617 nm corresponding to the $^5D_0\rightarrow{}^7F_2$ transition is observed. When the Eu-MOF is dispersed in different organic solvents, both of the spikes at 593 nm and 617 nm are also observed, which is attributed to the $^5D_0\rightarrow{}^7F_1$ and $^5D_0\rightarrow{}^7F_2$ transitions. Unfortunately, the absorption and excitation spectrum are not recorded. But this is, to our knowledge, the first example of lanthanoid sensitisation via NDI as an antenna.
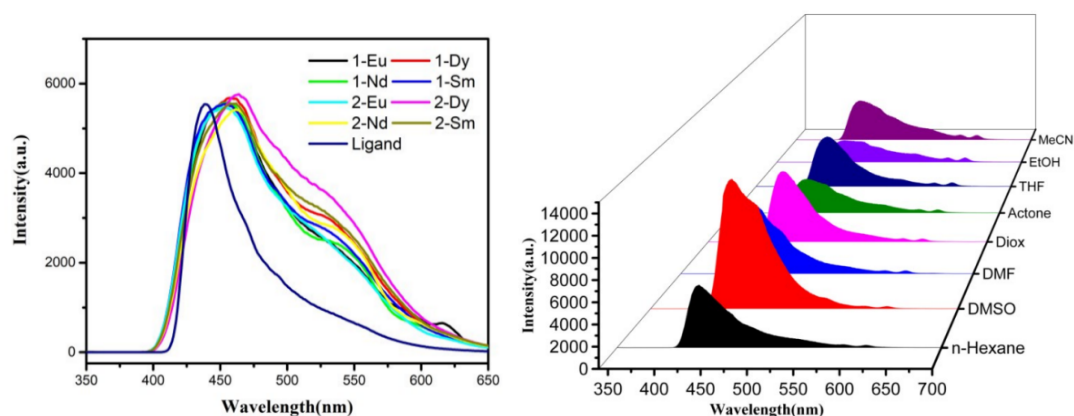
Figure 47: Left: Emission spectra of the ligand and Ln-MOFs in the solid state. Right: emission spectra of Eu-MOF dispersed in different organic solvents.[149]Figure reproduced from reference with the permission of the Royal Society of Chemistry.

There are other examples of Ln-MOF containing NDI derivatives. Most of the lanthanoid MOF focused on structural characterization and catalytic properties. None of these reported detailed lanthanoids photoluminescence in the UV-Visible and the near-infrared region. This inspired us to synthesise and investigate some lanthanoid complexes of well-designed NDI ligands.

1.5 Aim and Scope

The naphthalenetetracarboxylic diimide(NDI) incorporated into the d-block metal complexes has been well studied. The f-block metal complexes of NDI are relatively unexplored. This research will focus on the synthesis of lanthanoid complexes containing NDI as an antenna and investigate their structural, electrochemical and photophysical properties.

The photophysical investigation of previously reported lanthanoid complexes of NDI is very limited. In a review of the lanthanoid coordination complex containing NDI, the formation of the complex heavily relied on the extra aromatic donors, such as pyridine,[150-152] and carboxylic acid-functionalised benzene,[145-146, 149, 153] for example. These systems tend to form coordination polymers, making it difficult or impossible to study the solution phase photophysics. The calixarene has preorganized donor sites and a well-known metal-binding properties. The bisamide and tetraamide-functionalised calixarene derivatives bind strongly to lanthanoid ions, and the functionalisaion is relatively simple to introduce the NDI on the lower rim. Therefore, the synthesis and characterisation of these new ligands will be a major component of this research.

The second objective is to investigate the photophysical properties of lanthanoid complexes of NDI-functionalised calixarenes in the solution phase and solid state. This project also seeks to develop the NDI as an antenna to allow the possibility of sensitisation of lanthanoid luminescence as the detailed energy transfer process has not been reported. This is intended to lead to discrete soluble complexes which can be more readily studied in solution, although the tendency towards aggregation is also in scope for the studies. The studies of lanthanoid complexes will focus on Eu^{3+}, Nd^{3+} and Yb^{3+} to investigate the possibility of the antenna effect via the NDI and compare the visible emitter with NIR emitters.
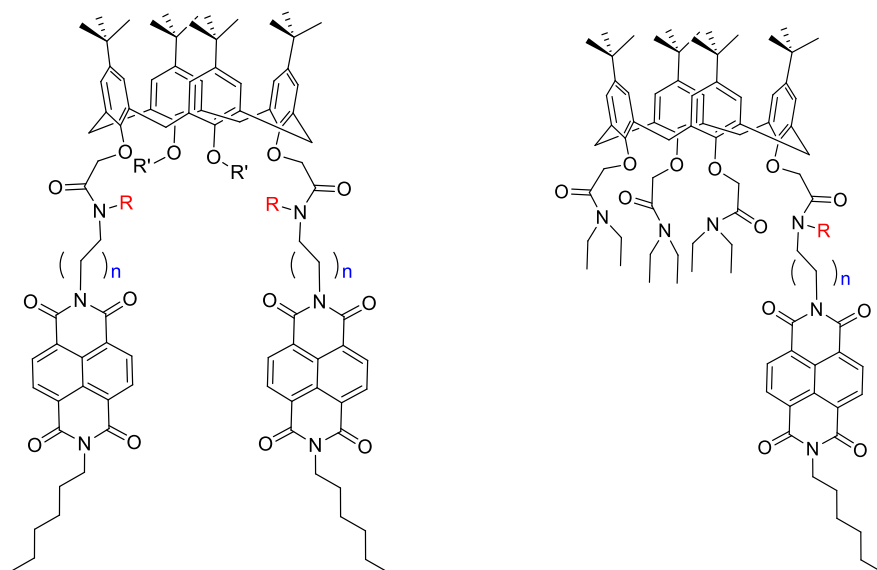
Figure 48: Some target molecules. Left: bis-amide functionalised calixarene. Right: tetra-amide functionalised calixarene. R and R' are functional groups. The "n" is the number of methylene groups.

To further expand the knowledge of NDI derivatives, study of the reduced systems is of particular interest as the neutral NDI can be chemically or electrochemically reduced to the NDI radical anion. The major component of this part of the research is to synthesize stable NDI radical anion containing species and their corresponding lanthanoid complexes. The absorption properties of the radical anion have been well-studied, but the emission properties are unexplored so the photophysical properties of the new ligands will be studied. Most importantly, the NDI radical anion has not been studied as an antenna moiety for any lanthanoid complexes. Of particular interest is the excited doublet state of the monoanion as, to our knowledge, no examples of energy transfer from a doublet state of any ligand to a lanthanoid have been reported. Therefore, the research will extend to study of lanthanoid sensitisation via the excited doublet state of NDI.

2 Lanthanoid Complexes of Bis-NDI Substituted Calixarene

2.1 Introduction

One of the major components of this project is to synthesise NDI-substituted calixarenes. Therefore, chapter 2 mainly focuses on the synthesis of bis-NDI substituted calixarene ligands (**L1**, **L2** and **L3**), along with their corresponding Ln(**L2**-2H)NO$_3$ where Ln = Eu^{3+} and Yb^{3+} and Ln(**L3**) complexes where Ln = Nd^{3+}, Yb^{3+} and Eu^{3+}. The structural properties of these ligands were studied by ^{1}H NMR spectroscopy, ^{13}C NMR spectroscopy and single crystal X-ray crystallography. The ligands were also characterised by elemental analysis and high-resolution mass spectrometry. These three ligands have similar structures with minor changes of the functional groups. While minor in terms of functional groups, these changes may have significant effects on lanthanoid binding and photophysical properties. The ligand **L1** is a calixarenediamide with two secondary amide groups and two methylene groups linking the NDIs to the calixarene. In the case of the ligand **L2,** the linkers are the tertiary amide groups with three methylene linkers. The core structure of ligand **L3** is similar to ligand **L1**, but it is fully alkylated by CH$_2$CON(CH$_2$CH$_3$)$_2$ moieties. This calixarenetetramide was expected to bind strongly to lanthanoid cations. In order to know if the lanthanoid interacts with the bis-substituted **L1** and **L2** ligands, the impact of addition of Y(DMSO)$_3$(NO$_3$)$_3$ to **L1** and **L2** ligands in deuterated solvents was analysed via ^{1}H NMR spectroscopy.

The second aim is to investigate photophysical properties of ligands and their lanthanoid complexes. Based on their photophysical properties, the energy transfer process will be proposed. All ligands were studied by absorption and emission spectroscopies. In addition, spectrophotometric titrations were conducted to quantitatively analyse ligand **L2** to lanthanoid interaction. Photophysical properties of **L2** and **L3** ligands and their corresponding monomeric lanthanoid complexes were investigated in 10^{-4} M and 10^{-5} M solutions and solid state. . Cyclic voltammetry, along with spectroelectrochemistry, was used to investigate some of the electrochemical properties.The overall aim was to synthesise the ligands and explore whether the NDI as an antenna at the lower rim of calixarene is suitable for sensitizing the lanthanoid luminescence.

Ligand	R	R	n
L1	⁃ξ—H	⁃ξ—H	2
L2	⁃ξ—CH$_3$	⁃ξ—H	3
L3	⁃ξ—H	⁃ξ—CH$_2$CON(CH$_2$CH$_3$)$_2$	2
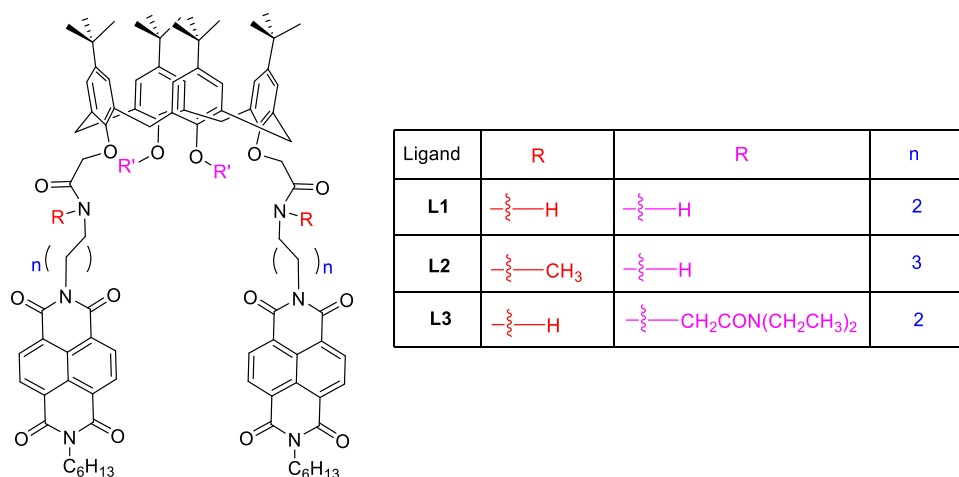
Figure 49: Target tetraamide calixarene derivatives, L1, L2 and L3.

2.2 Synthesis

In Chapter 1, we have discussed that the use of carboxylic acid-functionalised calixarenes as a starting point to attach desired moieties using an amide linkage is a well-established strategy. The formation of amide bonds can be either via the nucleophilic substitution between the acyl chloride-functionalized calixarene and amines or the amide coupling reaction between carboxylic acids and amines. Hence the first step was to make amine-functionalised NDIs which are essential intermediates for the synthesis of the desired ligands.

2.2.1 Amine-Functionalised NDI Derivatives

Compound **NDI1** was selected as an appropriately functionalised NDI derivative for the purposes of this project.

Compound **X**   Compound **NDI1**

Compound **X**   Compound **NDI2**   Compound **NDI3**
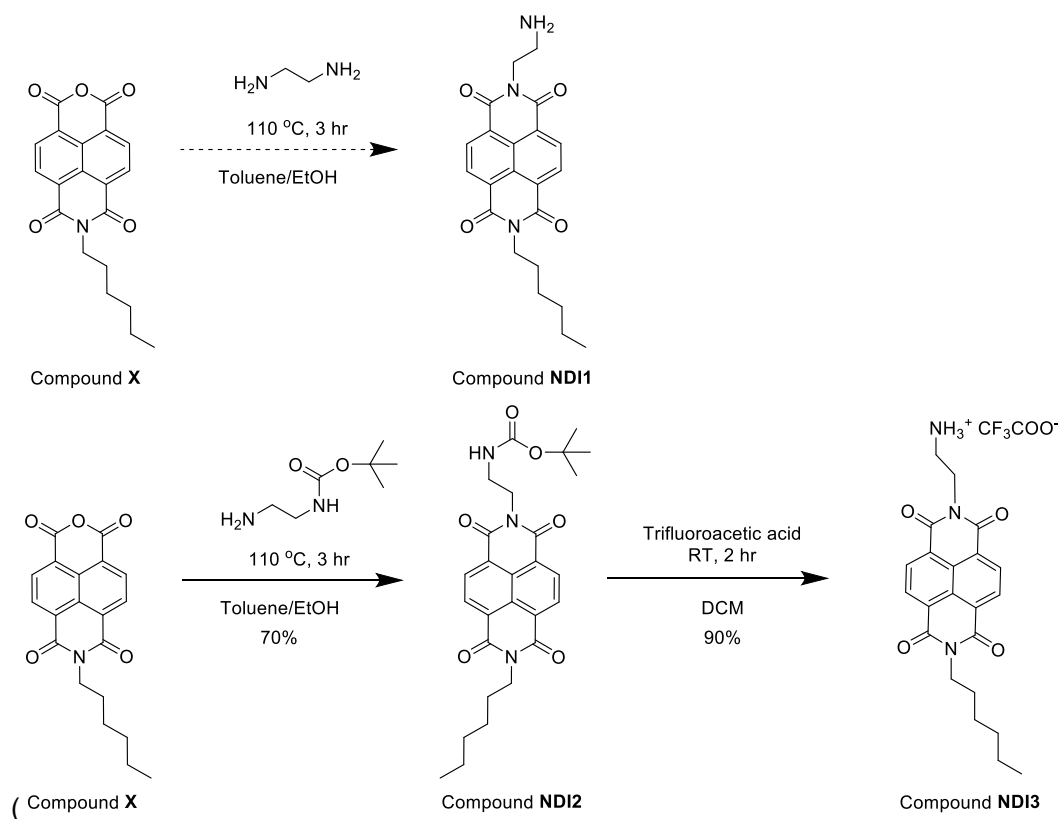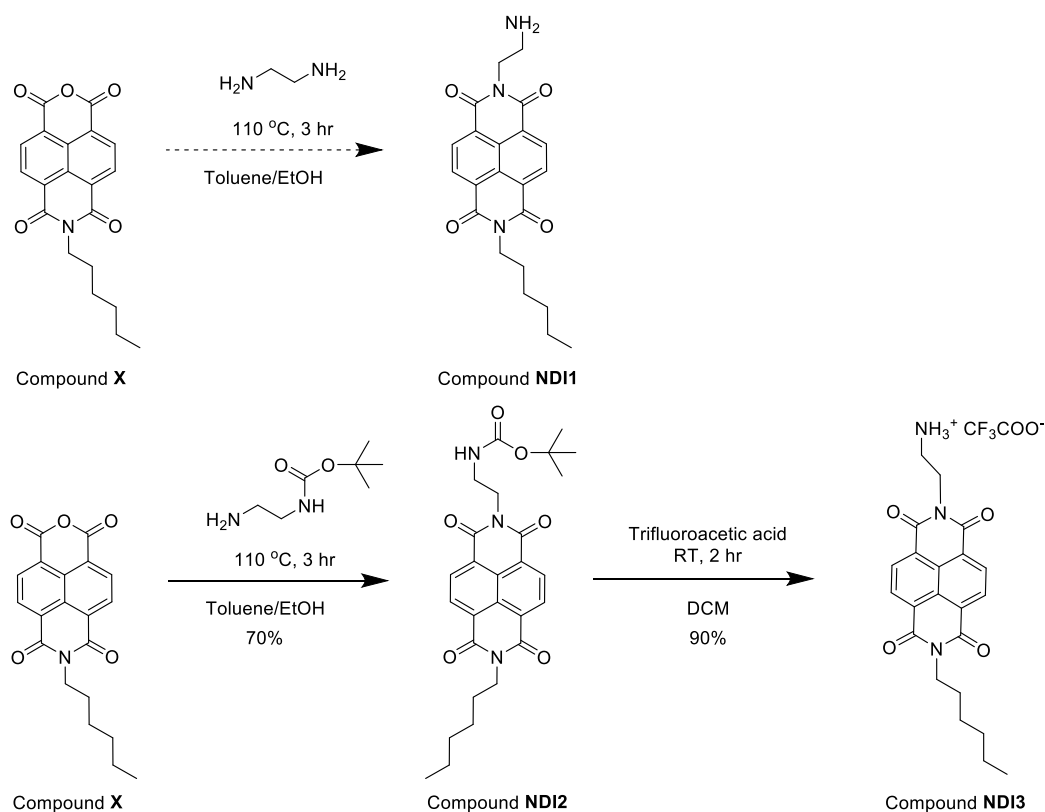
(Scheme *10*).

Scheme 10: Synthesis of the primary amine-functionalised naphthalenetetracarboxylic diimide (Compound NDI1 and NDI3)

The compound **X**, which was the precursor for all NDI compounds in this project, was prepared according to a literature procedure.[96] There were two synthetic paths explored to synthesise the amine-functionalised NDI. The first attempt involved heating the compound **X** and excess ethylenediamine in a mixture of toluene and ethanol. Although the TLC plate showed the starting material was consumed, the resulting products were insoluble in all common organic solvents. There was no evidence that the resulting product was the compound **NDI1**. As a result, the Boc-protected amine (compound **NDI2**) was synthesised for use in the condensation reaction. Subsequent removal of the Boc protecting group using trifluoroacetic acid in dichloromethane afforded compound **NDI3** as a pale yellow solid in 63% overall yield. The structure of compound **NDI3** was confirmed by NMR spectroscopy in DMSO-d_6 (Figure 50).[154] The protection-deprotection steps enabled isolation and characterization of this important intermediate. After adding K_2CO_3 solid to compound **NDI3** dissolved in DMSO-d_6, a white precipitate immediately formed and all proton signals disappeared in the spectrum, suggesting poor solubility of the compound **NDI3** in the neutral amine form.

48
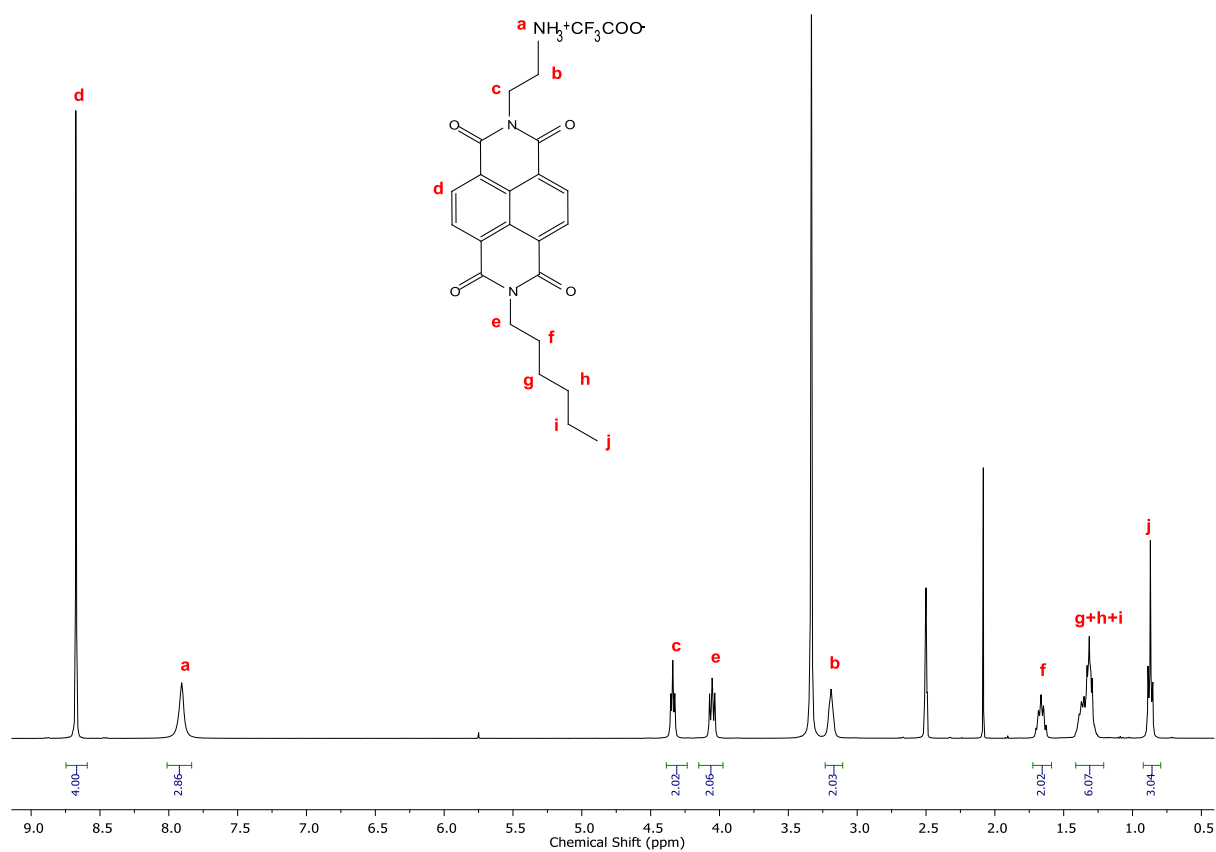
Figure 50: ^{1}H NMR spectra of compound NDI3 in DMSO-d_6 recorded at 400 MHz.

The secondary amine-functionalised NDI (compound **NDI6)** was prepared following Scheme 11 shown below. The aim of using a secondary amine in addition to the primary amine was to allow a comparison of secondary and tertiary amide linkages in the calixarene receptors.
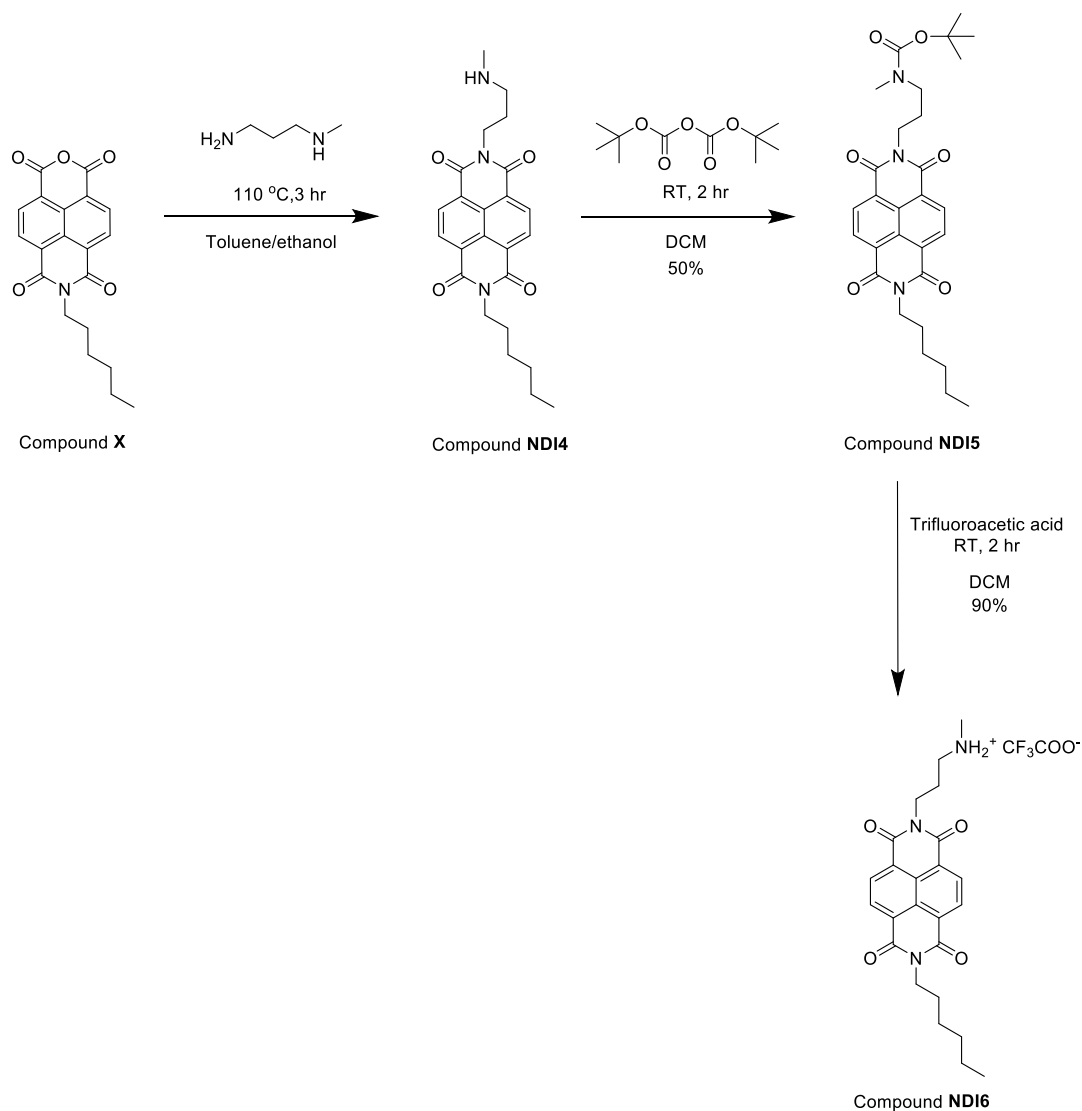
Scheme 11: Synthesis of the secondary amine-functionalised naphthalenetetra-carboxylicdiimide (compound NDI6)

The synthesis started from compound **X**. The condensation reaction between compound **X** and N-methyl-1,3-diaminopropane was carried out. The reaction mixture was stirred under reflux at 110 °C for three hours in a mixture of toluene and ethanol. Although the isolated product displayed one spot on silica and alumina TLC plates, the presence of impurities was confirmed by NMR. In contrast to the compound **NDI1**, the compound **NDI4** has a higher solubility in organic solvents, including dichloromethane, which allows for *N*-Boc protection. The Boc-protected secondary amine is much less polar than impurities and starting materials and so can be readily purified by chromatography. Removal of the *N*-Boc protecting group using trifluoroacetic acid afforded the pure compound **NDI6** as a yellow solid. The NMR spectrum (Figure 51) is in agreement with similar derivatives found in the literature.[155]
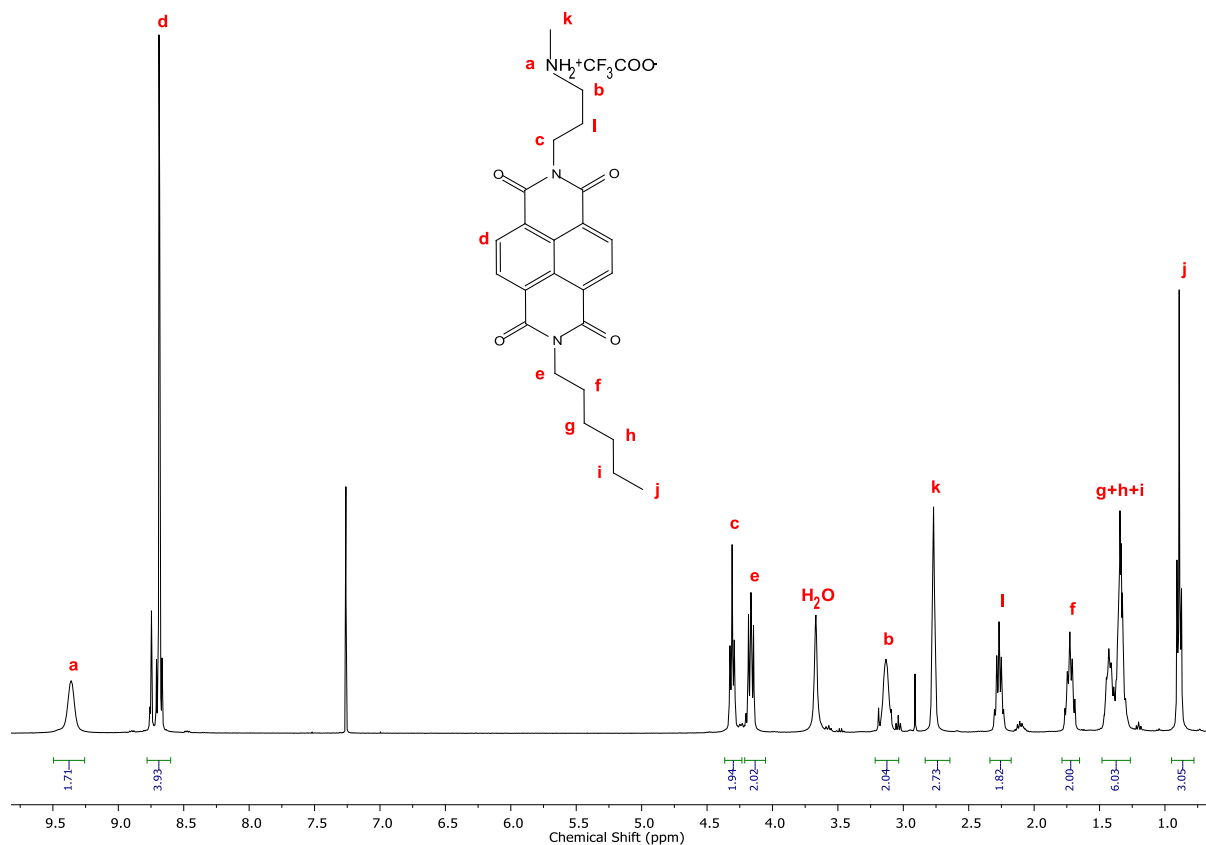
Figure 51: ¹H NMR spectra of compound NDI6 in CDCl₃ recorded at 400 MHz.

2.2.2 Synthesis of Bis-NDI Substituted Ligands

2.2.2.1 Bis-Substituted Calixarene

Synthesis of the parent *p-tert*-butylcalix[4]arene has been well-established by the pioneering work of Gutsche (Figure 52).[156] The reaction was performed in this project. All calixarene derivatives in this project were based on the calix[4]arene framework. The synthesis could be split into two parts. More specifically, 37% paraformaldehyde and *p-tert*-butylphenol were heated at 120 °C in the presence of sodium hydroxide as a catalyst for two hours. In the second step, diphenyl ether was added, and the mixture was further heated to reflux for three hours under a nitrogen atmosphere. The resulting dark brown solid was precipitated by adding ethyl acetate, followed by filtration. The pure product was obtained by recrystallisation from hot toluene.
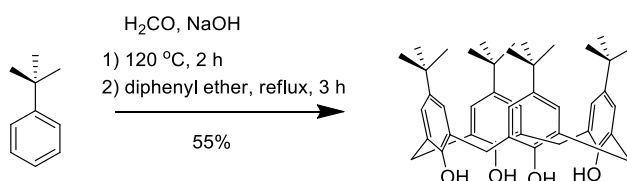
Figure 52: Synthesis of the *p-tert*-butylcalix[4]arene.[156]
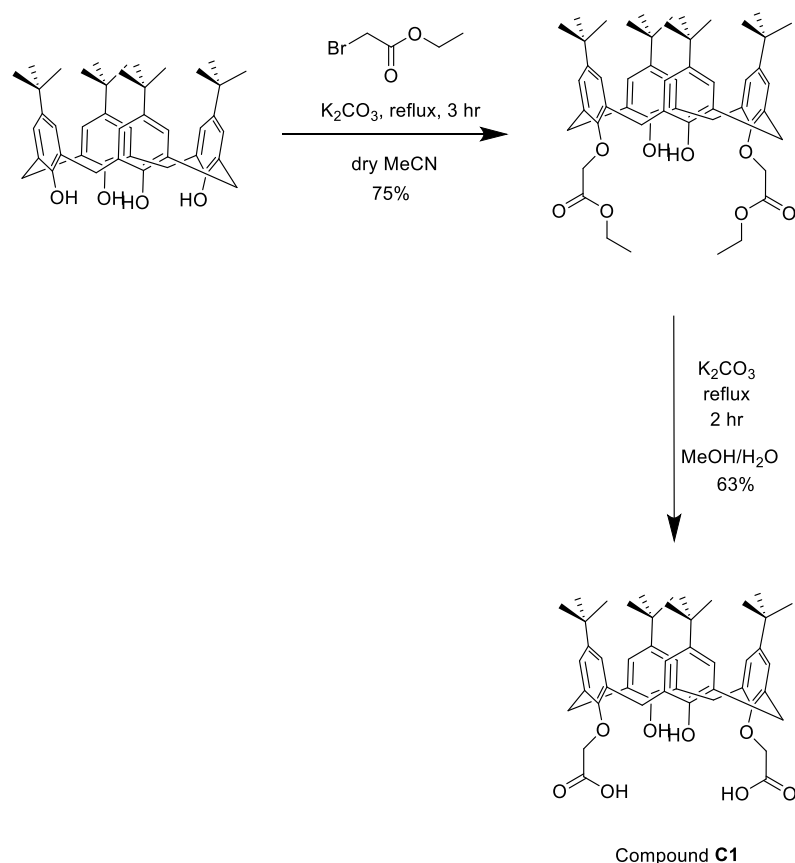
Scheme 12: Synthesis of the compound C1.[157]

The compound **C1** was an essential intermediate for bis-NDI substituted ligands and was prepared following the method outlined by Boyd[157] (Scheme 12). The NMR spectrum was consistent with the literature. A literature search revealed that the most common way to form the amide bond on the lower rim of the calixarene was to convert the carboxylic acid to the acyl chloride first, followed by a nucleophilic reaction. Although the ligand **L1** was successfully synthesised by this method, the yield was very low. It was also difficult to purify because impurities did not separate well by chromatography, as shown by significant streaking on the TLC. The formation of the acid chloride was confirmed by adding methanol to form the ester and comparing the TLC with the starting carboxylic acid, but efforts to improve the yield were unsuccessful. As an alternative approach, hydroxybenzotriazole (HOBT) as a coupling reagent and (3-dimethylaminopropyl)-*N'*-ethylcarbodiimide hydrochloride (EDCI) as an activating reagent were used to synthesise the ligand **L1** (Scheme 13). These two synthetic steps achieved a fair yield (44%), and it was straightforward to purify the product by column chromatography. HR-LC-MS was used to characterize the ligand **L1**. The peak corresponding to the Na complex was observed. Therefore, these reaction conditions were used for the rest of the amide coupling reactions.
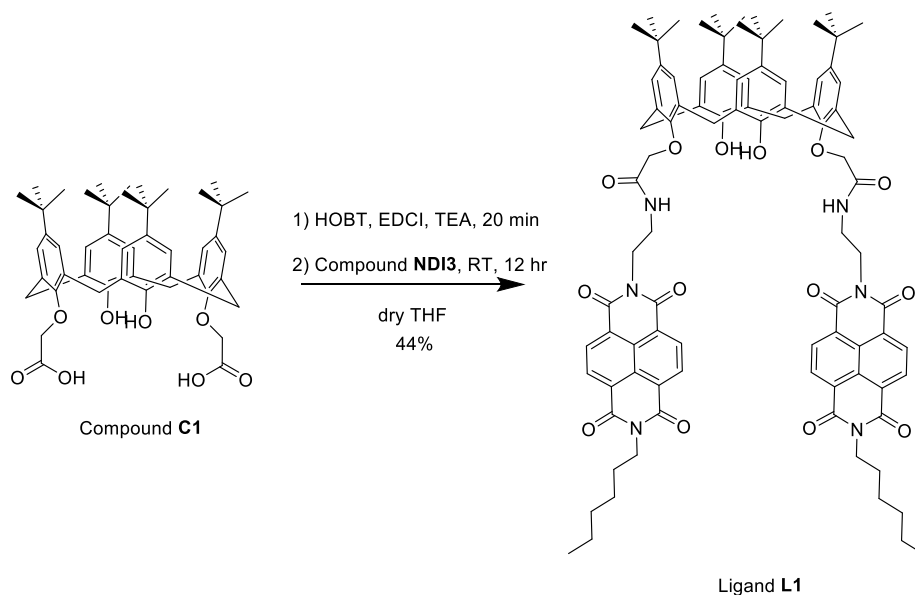
Scheme 13: **Synthesis of ligand L1.**

The ligand **L1** was characterised by ^{1}H NMR spectroscopy (Figure 53). Since it is the first NDI-functionalized calixarene reported in this thesis, detailed characterisation will be presented for clarity. The ^{1}H NMR spectrum displays the presence of secondary amide protons at 8.74 ppm. In contrast to the singlet peak corresponding to NDI in the aromatic region in the NMR spectrum of compound **NDI3**, the splitting pattern of the hydrogens of NDI moieties appears as a pair of doublets (peaks *H* and *G*). The hydrogen peak at 7.5 ppm attributed to OH protons is only observed in a concentrated solution. Due to the symmetry of the ligand **L1**, there are two aromatic hydrogen environments of phenolic units appearing as two singlet peaks at 6.74 ppm and 6.60 ppm (peak *1* and *2*). By referring to the assignment of compound **NDI3**, the peak *F* around 4.20 ppm is assigned to methylene protons attached to the NDI. The COSY NMR spectroscopy was used to assign the peaks of $CONHC\textbf{H}_2CH_2N(CO)_2$ via the cross peak appearing at(8.74 ppm, 4.00 ppm)/(peak *NH*, peak *J*). The lack of the cross peak indicates the peak *I* at 4.48 ppm corresponds to $CONHCH_2C\textbf{H}_2N(CO)_2$. The symmetry of the ligand is also supported by the other splitting pattern of hydrogen environments and the expected integration ratio: 4 protons of OCH_2 (singlet peak *5* at 4.40 ppm), 4 protons of axial Ar-C$\textbf{H}_2$-Ar (doublet peak *4a* at 3.64 ppm), 4 protons of equatorial Ar-C$\textbf{H}_2$-Ar (doublet peak *3e* at 2.98 ppm), 18 protons of *tert*-butyl groups (singlet peak at 1.10 pm) and 18 protons of the *tert*-butyl group (singlet peak at 0.94 pm). The rest of peaks (peak *E* and peak A, *B*, *C*, *D*) correspond to the hexyl chain. The spectrum is in agreement with the proposed structure.

Figure 53: ^{1}H NMR spectrum of the ligand L1 in CDCl$_3$ recorded at 400 MHz.
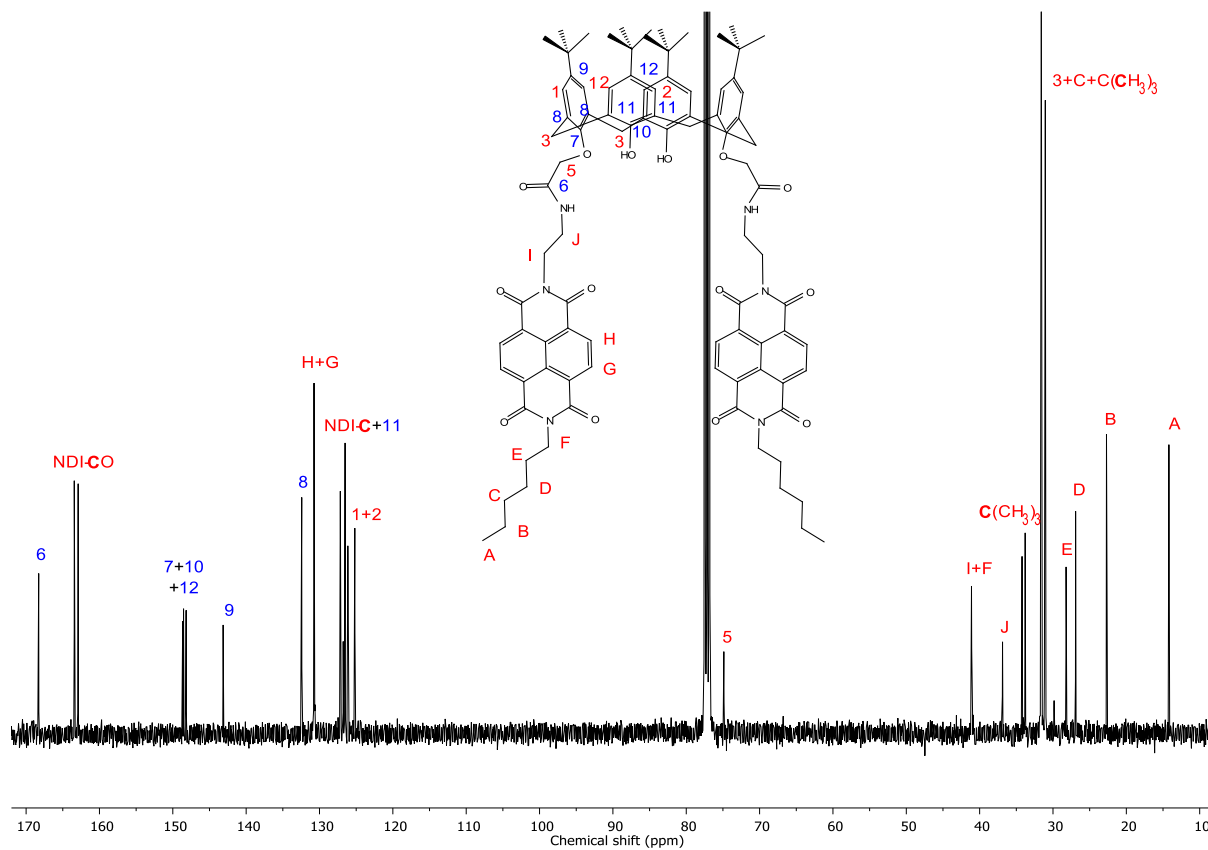
Figure 54: ^{13}C NMR spectrum of the ligand L1 in CDCl$_3$ recorded at 100 MHz.

The ligand **L1** was also characterised by ^{13}C NMR spectroscopy (Figure 54) with assistance from 2D HSQC and HMBC spectroscopy techniques. The carbon peaks are assigned by referring to hexyl-functionalised NDI (compound **NDI3**) and dicarboxylic acid-functionalized calixarene (compound **C1**). The peak at 168.28 ppm (peak *6*) is assigned to the carbonyl carbon of amide group. The symmetry of NDI gives two peaks associated with carbonyl carbon atoms of NDI-**C**O (163.43 ppm and 162.90 ppm). The resonance of quaternary carbon atoms linking to the lower rim (peak *7* and peak *10*) around 149 ppm are together with the one of the quaternary carbon linking to the *tert*-butyl group (peak *12*). The other one (peak *9*) resonates at 143.14 ppm. The assignment of quaternary carbon *11* around 126 ppm is based on the presence of a cross peak between H^{OH} andC^{11} in the HMBC spectrum, and the specific peak *11* shared by two quaternary carbon atoms of two rings is overlapped with the peak corresponding to NDI-**C** carbons. The absence of cross peak indicates the peak *8* at 132.42 ppm. The rest of the phenol carbons appear at 126.14 ppm and 125.19 ppm (peak *1* and *2*). The symmetry gives one carbon environment of OCH$_2$ (peak *5*). Carbons linking to the nitrogen atoms have a chemical shift of 41.11ppm (peak *I+F*) and 36.88 ppm (peak *J*). There are two carbon environments of **C**(CH$_3$)$_3$ with peaks around 35 ppm. The peak *3*, peak *C* and peak C(**C**H$_3$)$_3$ are overlapped and have a chemical shift around 31 ppm. The rest of peaks (peak *A*, *B*, *D* and *E*) in the further upfield are associated with the carbon atoms of hexyl carbons. The total number of discrete carbon environments is lower than expected, presumably due to the overlapping peaks. All carbon peaks have their expected chemical shift.

The ligand **L2** was synthesised using the same reaction conditions developed for ligand **L1** (see Scheme 14). The pure ligand **L2** was obtained by crystallisation from a hot toluene solution after the standard workup. The TLC plate showed one spot. The ligand was also characterized by HRLCMS, which confirmed a pure single product.
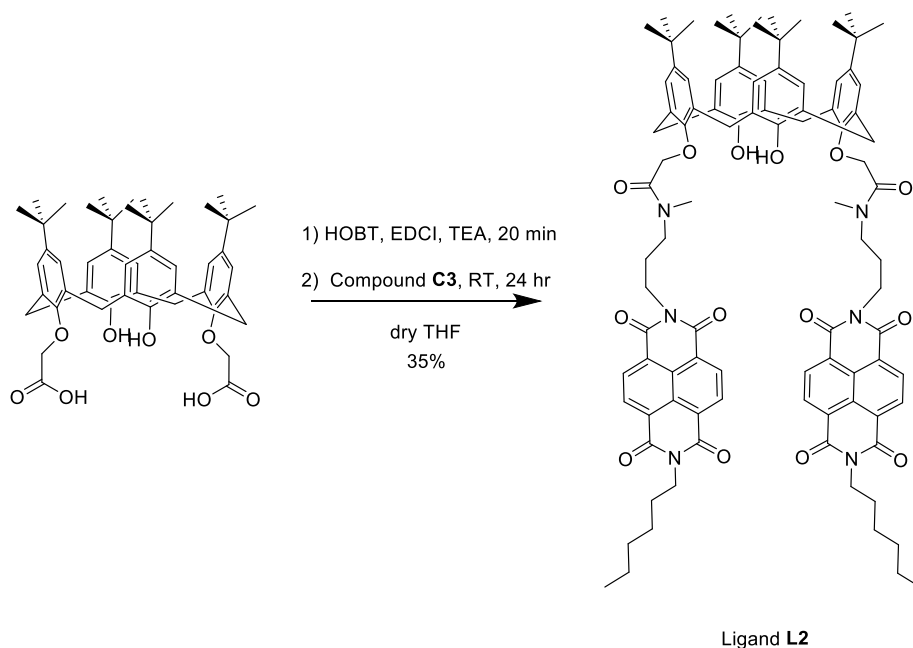
Scheme 14: Synthesis of the ligand L2.

55

The ligand **L2** was characterised by ^{1}H NMR in CDCl$_3$ (Figure 55). However, ^{1}H NMR analysis of the ligand **L2** in CDCl$_3$ showed an unexpectedly complex spectrum. Using other deuterated solvents was of no help in simplifying the spectrum. The attempt to add one drop of MeOD to break hydrogen bonds or raising temperature was also unsuccessful (Figures in appendix). Therefore, there are probably a mixture of three amide rotamers: (*E*, *E*), (*E*, *Z*) and (*Z*, *Z*). These rotamers could be stabilised by hydrogen bonding to the phenolic OH.

The ^{1}H NMR spectrum reveals two sets of peaks corresponding to protons of NDIs around 8.6 ppm with an overall integration of 8 (peak *H* + *G*). Three peaks around 7.60 ppm correspond to OH protons of phenolic units, and one singlet peak and one doublet peak (or two singlet peaks) at 4.80 ppm correspond to OCH$_2$ protons (peak *5*). The loss of symmetry again suggests the presence of amide rotamers. The presence of amide rotamers is also supported by the increased number of singlet peaks associated with aromatic rings around 6.7 ppm in comparison to these peaks observed in the ligand **L1**(peak *1* + *2*). The spectrum in the range of 5.00 ~ 2.80 ppm is more complicated. Some small peaks were initially considered to be impurities. However, the total integration ratio (26H) matches well with the structure of calixarene, and the chemical shift of functionalized groups is in the expected range. These peaks correspond to N(CO)$_2$C**H$_2$**CH$_2$(CH$_2$)$_3$CH$_3$ (peak *F*), CON(C**H$_3$**)C**H$_2$**CH$_2$C**H$_2$**N(CO)$_2$ (peak *I* + *L* + *K*), Ar-C**H$_2$**-Ar groups (peak *4a* + *4e*). The hydrogen of the *tert*-butyl group*s* also split into multiplet peaks around 1.1 ppm, indicating the presence of amide rotamers.

In order to confirm the purity of the ligand **L2**, the elemental analysis and mass spectroscopy was done. The elemental analysis data have reasonable discrepancies between calculated value (C, 73.35; H, 7.05; N, 5.35%) and experimental value (C, 73.40; H, 7.12; N, 5.58%). The pure product was also characterised by ESI-MS, and the spectrum also shows the expected major peaks and the absence of other peaks (see experimental section and appendix). Overall, there is strong evidence that the target compound was made with acceptable purity.
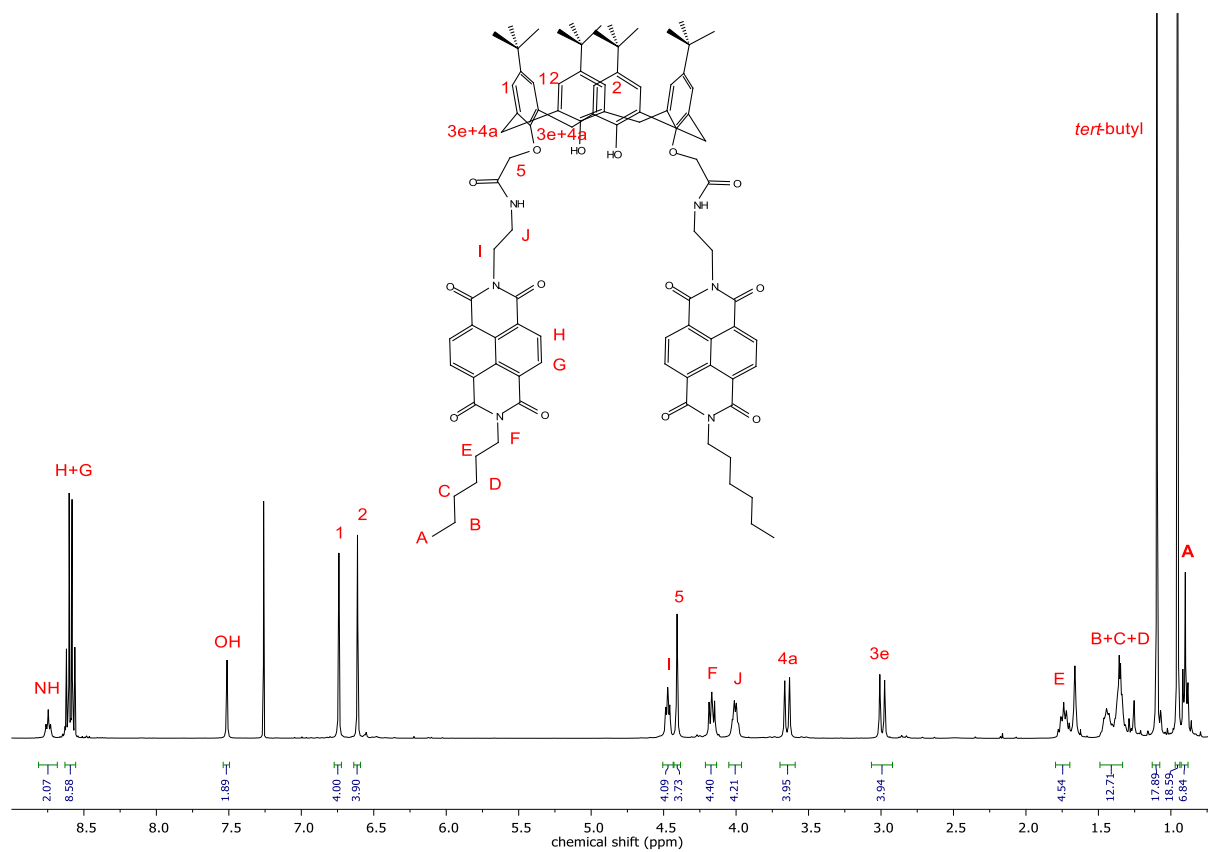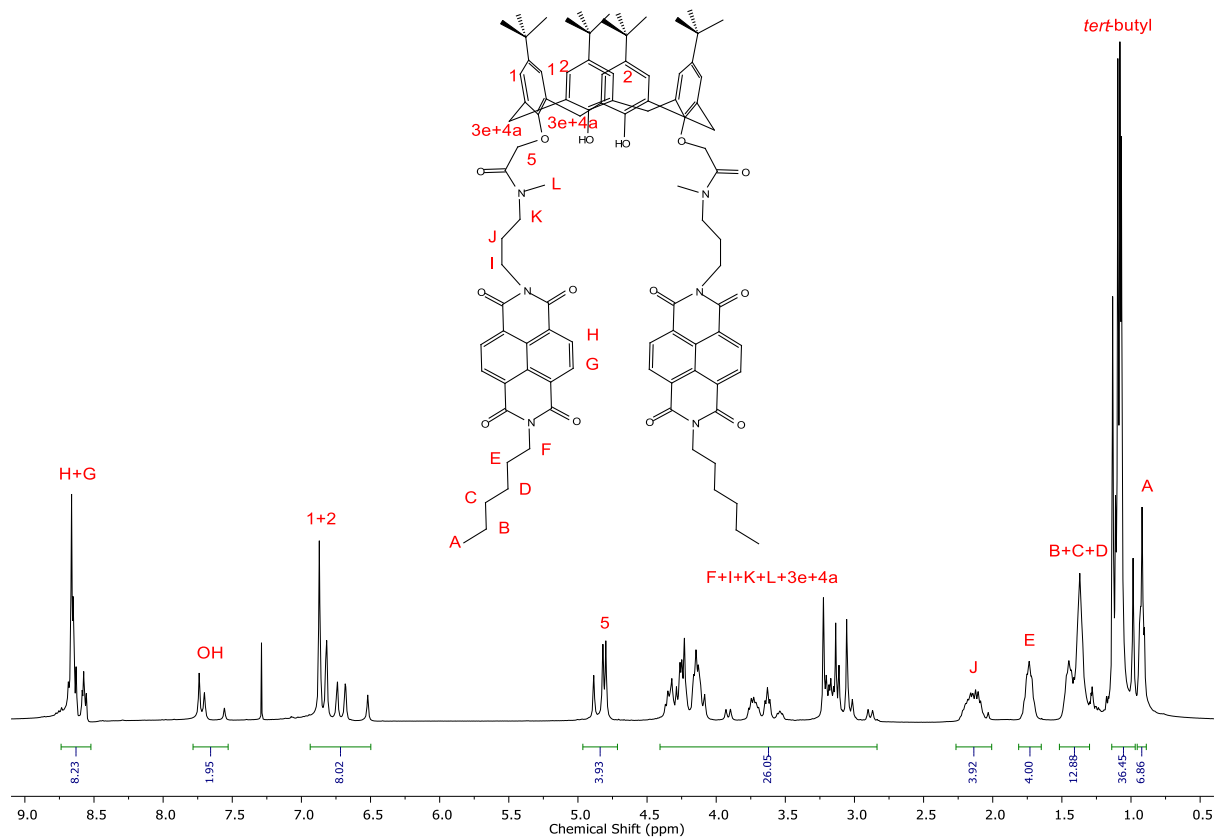
Figure 55: ^{1}H NMR spectrum of the ligand L2 in CDCl$_3$ recorded at 400 MHz.
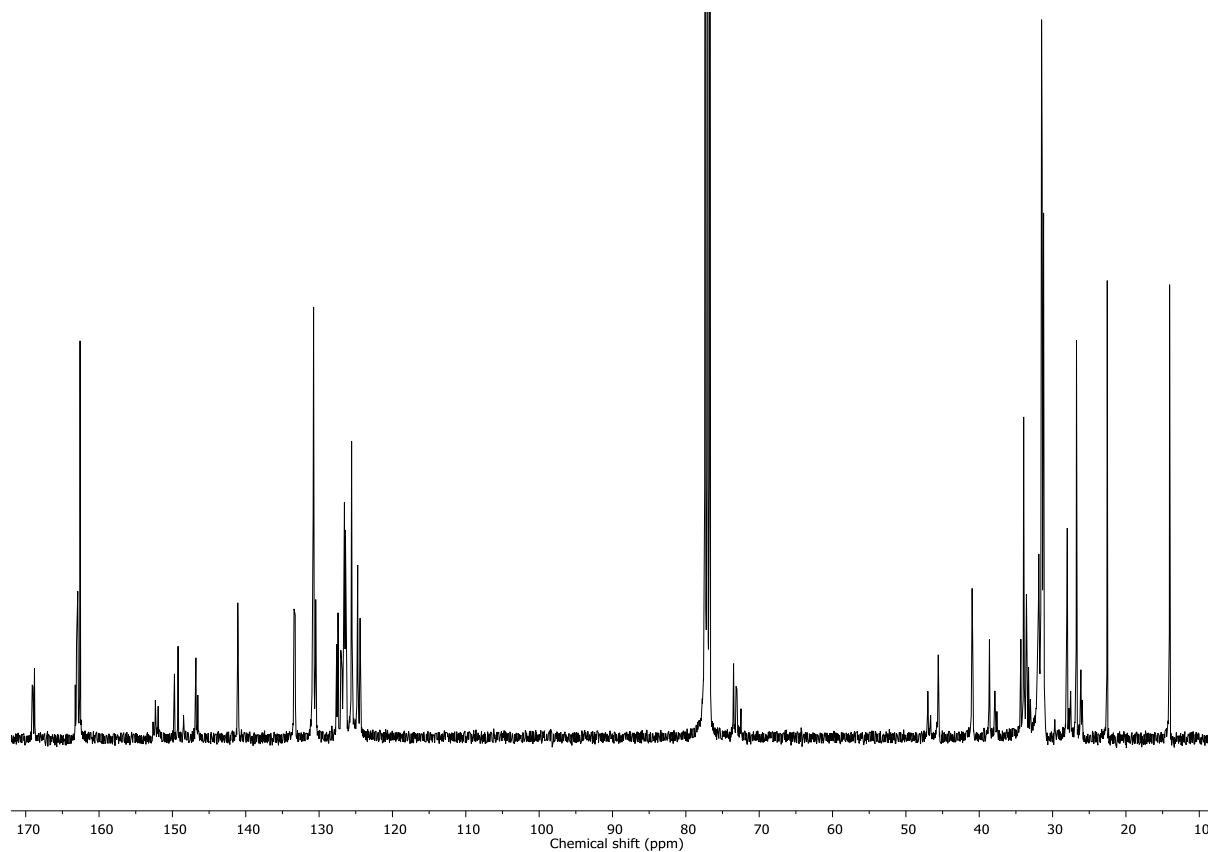
Figure 56: ^{13}C NMR spectrum of the ligand L2 in CDCl$_3$ recorded at 100 MHz.

The ^{13}C NMR spectrum was also recorded (Figure 56). However, the ligand cannot be characterised in detail by ^{13}C NMR spectroscopy due to the insufficient resolution of the Bruker Avance 100 MHz and multiplicity of peaks, presumably again due to the presence of amide rotamers. Despite these complexities in terms of characterisation using NMR spectroscopy, evidence for the purity of L2 was mentioned above, and the structure of the ligand was confirmed using single crystal X-ray crystallography of lanthanoid complexes described in Section 2.4.

2.2.2.2 Tetra-Substituted Calixarenes

Tetra-substituted calixarene receptors are likely to form more stable metal complexes, and also avoid complications of ligand deprotonation. The intermediate compound **C2** was needed to be synthesised before the amide coupling reaction to synthesise the ligand **L3**.
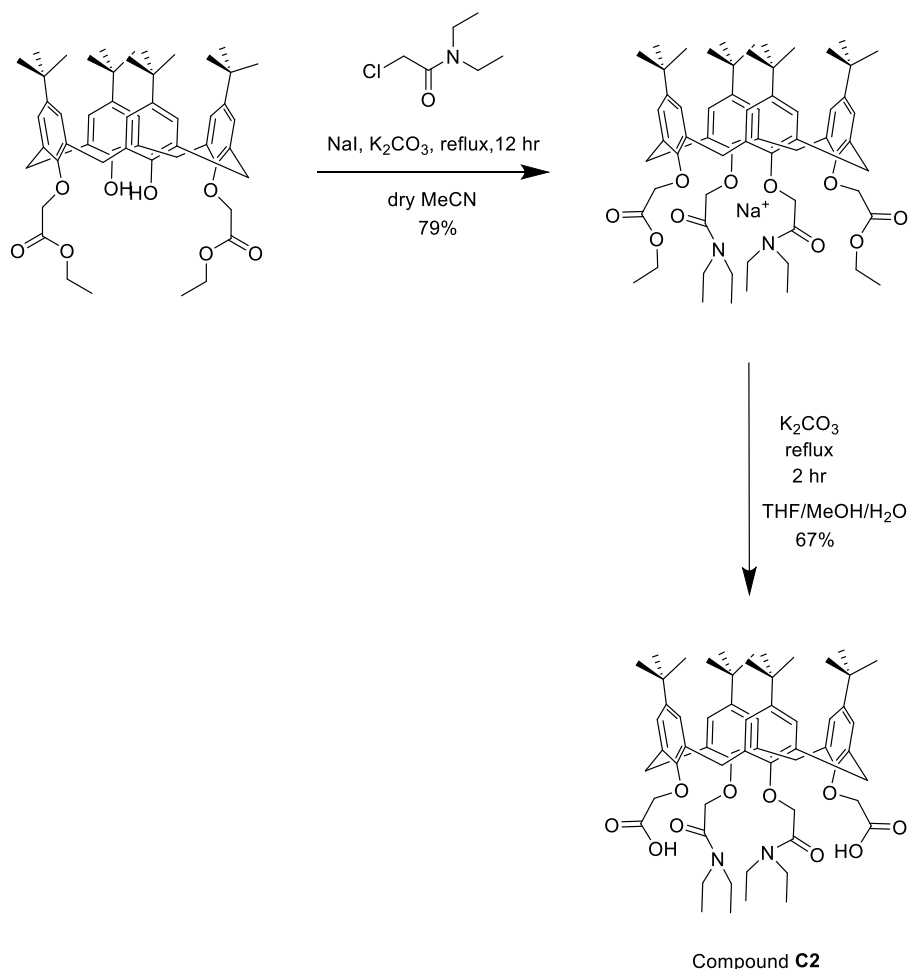
Compound **C2**

Scheme 15: Synthesis of the compound C2.[158]

The bis-carboxylic acid-functionalised calixarenediamide (compound **C2**) was prepared according to a modified literature procedure (Scheme 15), and the NMR data were consistent with that reported in the literature.[158] The reaction started from the calixarenediester. The 2-bromo-N,N-diethylacetamide

was not commercially available, so the chloro-functionalized alkylating reagent was used instead. Sodium iodide was used to achieve an *in situ* Finkelstein reaction to form the iodo-functionalized alkylating reagent first, followed by a nucleophilic substitution. Using NaI also resulted in the formation of sodium(I) complex of diester-functionalised calixarenediamide as the initial product. The hydrolysis of diester group to dicarboxylic acid group was successful using potassium carbonate as a base. In order to obtain the compound **C2**, the Na$^+$ complex was dissolved in the minimum amount of THF and added dropwise to a mixture of THF/MeOH/H$_2$O. The mixture was stirred at 50 ^{o}C for one hour. After removal of organic solvents, the compound **C2** was collected by filtration.

Compound **C2**

1) HOBT, EDCI, TEA, 20 min

2) Compound **NDI3**, RT, 24 hr

dry THF

57%
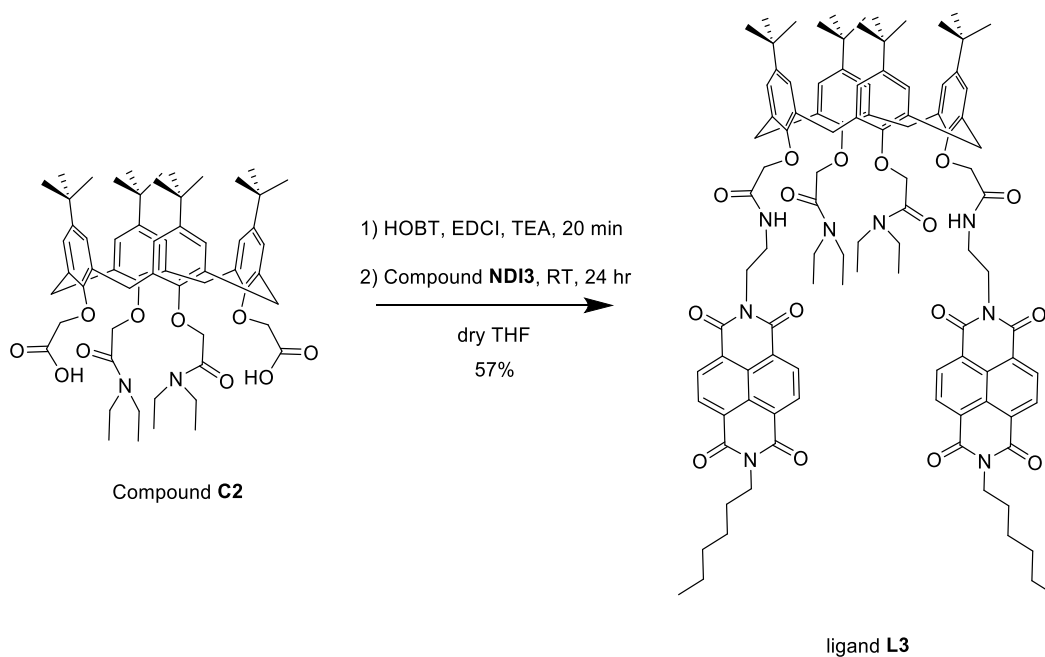
ligand **L3**

Scheme 16: Synthesis of the L3 ligand.

The ligand **L3** was synthesized following the same procedure for the **L1** and **L2** ligands (Scheme 16). Purification of ligand **L3** involved trituration with acetone, ethanol and ether. The ^{1}H NMR spectrum showed a trace amount of acid in deuterated chloroform significantly affects the proton chemical shift of some peaks. Therefore, the desired product was dissolved in CDCl$_3$ pretreated with basic alumina, and a more consistent ^{1}H NMR spectrum was obtained (Figure 57).

By referring to the assignment of peaks for the ligand **L1**, it is relatively easy to assign all peaks in the case of the ligand **L3**. No proton signals of OH groups indicate the complete alkylation of the lower rim by 2-chloro-*N,N*-diethylacetamide. The peaks of the axial of the Ar-C**H₂**-Ar protons shift downfield to around 4.60 ppm (peak *4a*) in comparison to those observed in the ligand **L1**. The peak of CONH**CH₂**CH₂N(CO)₂ shifts upfield from 4.00 ppm to 3.78 ppm (peak *J*). The CON(C**H₂**CH₃)₂ quartet peak appears at 3.22 ppm (peak *7*), integrating to 4 protons. The other peak around 3.1 ppm with an integration ratio of 8 is attributed to the CON(C**H₂**CH₃)₂ and equatorial of the Ar-C**H₂**-Ar protons (peak *7' + 3e*). The observation of two CON(C**H₂**CH₃)₂ peaks is due to resonance of the nitrogen lone pair with the carbonyl group. The broad peak at 2.90 ppm is assigned as a water peak because no cross-peaks were found in the 2D NMR spectra. The chemical shift and hydrogen environments of hexyl-

functionalized NDI unit are independent of the different substitution of the calixarene unit as insignificant changes in chemical shift and splitting pattern are observed (peak *A*, *B*, *C*, *D*, *E* and *F*). The multiple peaks corresponding to CON(CH$_2$C**H$_3$**)$_2$ (peak *8*) are overlapped with that of the *tert*-butyl group. The proton assignment is shown below. The ^{1}H spectrum is in agreement with the proposed structure.
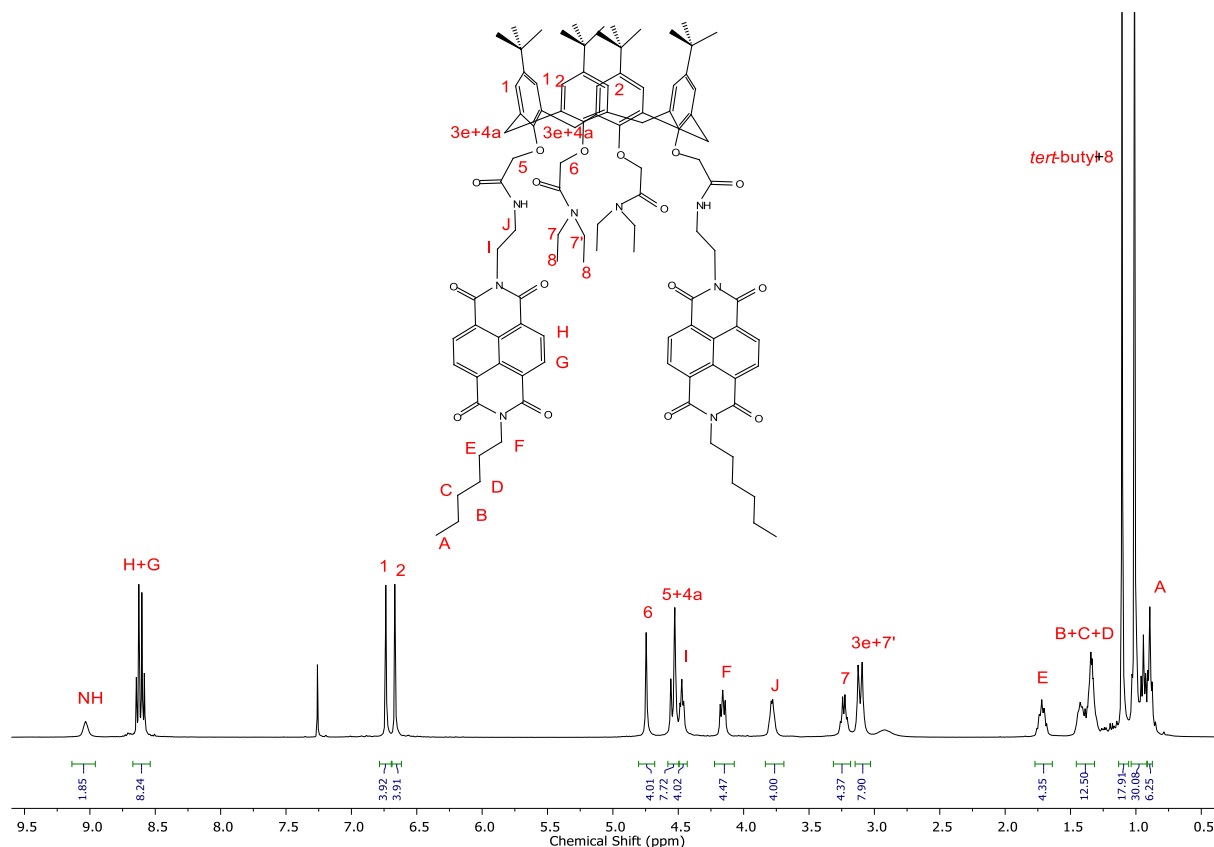
Figure 57: ^{1}H NMR spectrum of the ligand L3 in CDCl$_3$ recorded at 400 MHz.

The ^{13}C NMR assignment was made using 2D NMR spectroscopy, including HSQC and HMBC (Figure 58). Compared with the ^{13}C spectrum of ligand **L1**, the peak *9* and *12* are not overlapped with peak *11* and *14* (around 155 ppm) and shift upfield to around 145 ppm. The symmetry gives the two separate peaks at 74.04 ppm and 71.53 ppm, corresponding to OC**H$_2$** carbons (peak *5* and *6*). The peak *I* and *F* shift upfield and have a similar chemical shift around 41 ppm with the peak 7 corresponding to CON(**C**H$_2$CH$_3$)$_2$ carbons. One more additional peak is found at 14.33 ppm further upfield, indicating the CON(CH$_2$**C**H$_3$)$_2$ carbons (peak *8*). The change in chemical shift of carbon peaks in the aromatic region and aliphatic region is not significant. The total number of carbon environments is lower than expected due to the overlapping peaks. All peaks are in their expected range.
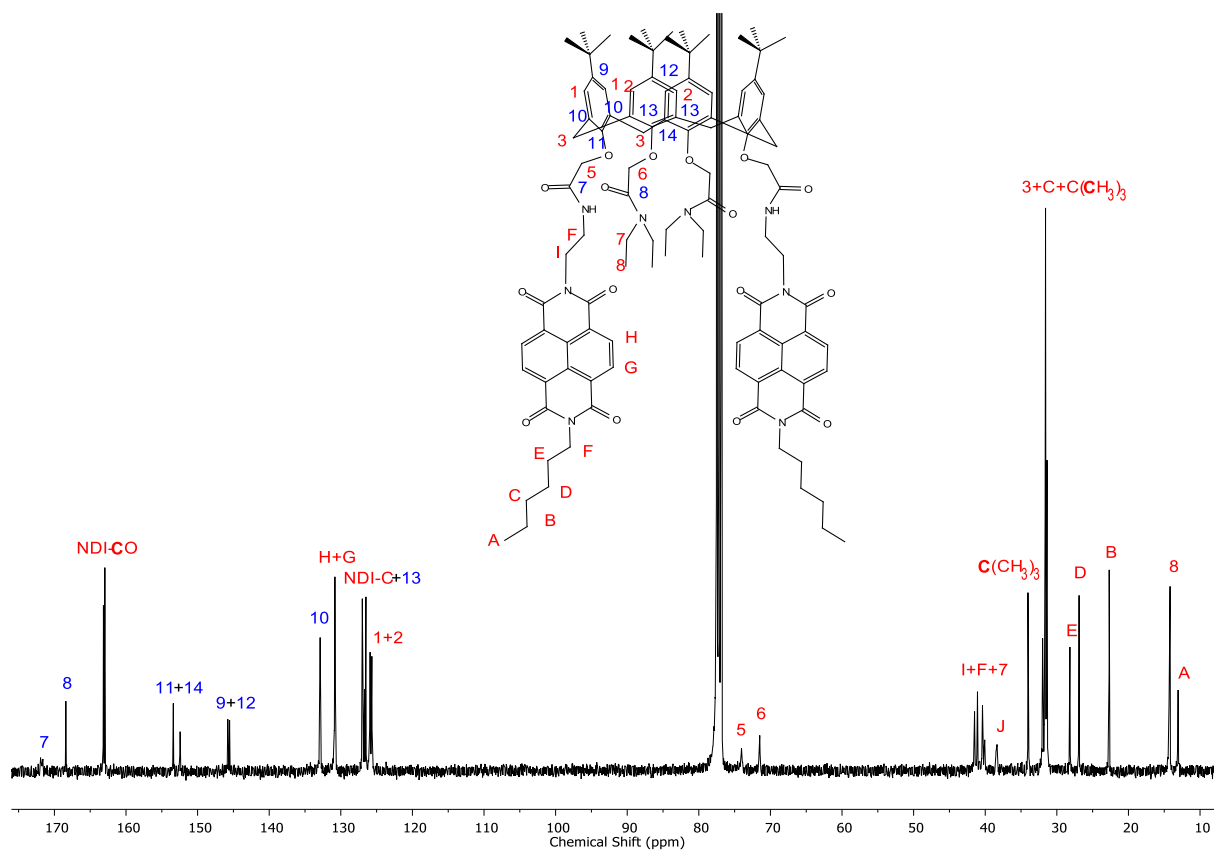
Figure 58: ^{13}C NMR spectrum of the ligand L3 in CDCl$_3$ recorded at 100 MHz.

2.3 NMR Studies of Sodium and Yttrium Complexes

In the case of ligand **L1**, the ^{1}H NMR spectrum (Figure 59) reveals that no significant peak shifts after adding Y(DMSO)$_3$(NO$_3$)$_3$ **(>20 eq.)** in the presence of triethylamine **(>20 eq.)**, suggesting no interaction between the ligand **L1** and yttrium (III) precursor. It is proposed that this may be due to hydrogen bonds between the two amide groups on the lower rim, as is often observed in similarly functionalised calixarenes.[159-161] This proposal will be given some support by the crystal structure described in section 2.4.
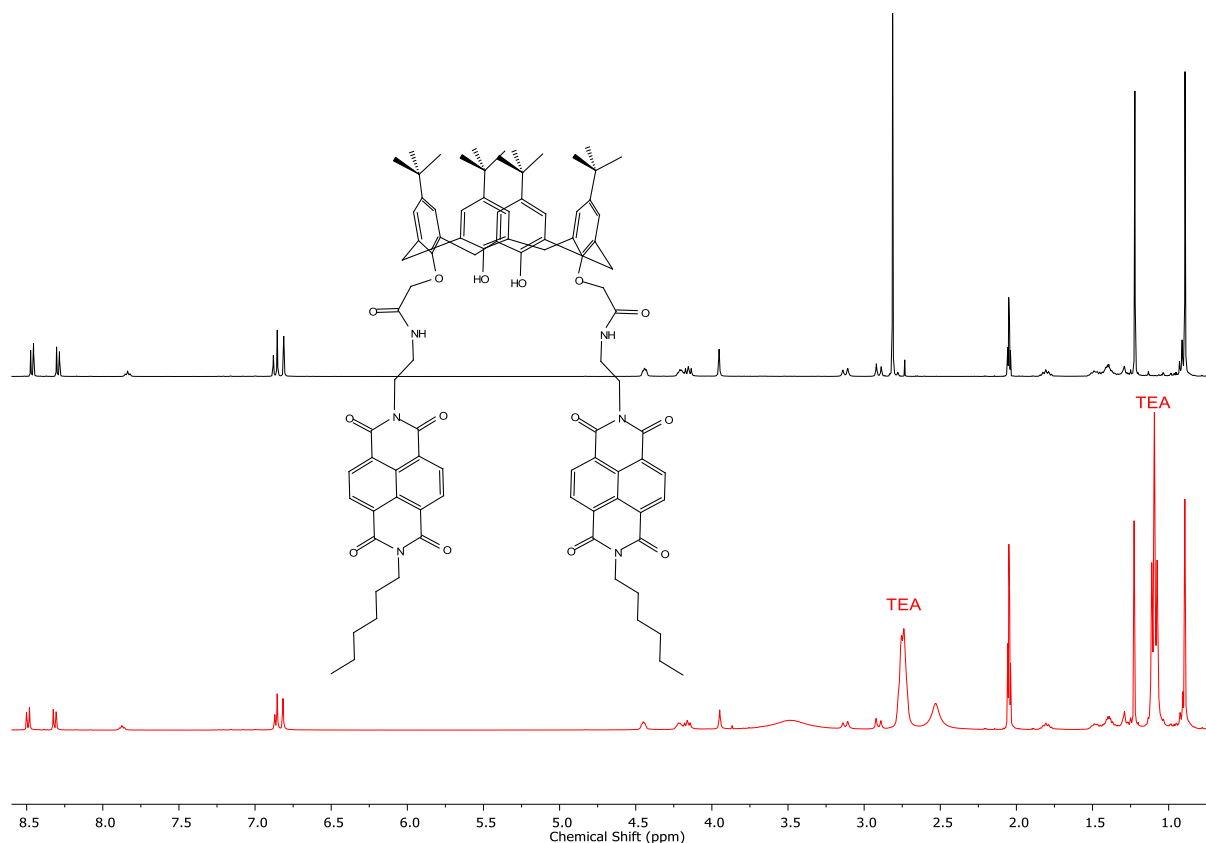
Figure 59: ^{1}H NMR spectra of the free ligand L1 in acetone-d$_6$(top spectrum) and addition of excess triethylamine (＞20 eq.) and Y(DMSO)$_3$(NO$_3$)$_3$ (＞20 eq.) to free ligand L1 in acetone-d$_6$(bottom spectrum) recorded at 400 MHz.

The H NMR spectrum shows that there is no dramatic difference between the free ligand **L2** and the ligand after column chromatography with the exception of the concentration-dependent OH peak (Figure 60). After adding the NaBF$_4$, the solution became cloudy and significant changes in the ^{1}H NMR spectrum were observed. These observations are consistent with the formation of a sodium(I) complex. It is also evidenced by the broadening and different splitting pattern of *tert*-butyl groups which are distant from the sodium centre. Phenolic units are not fully deprotonated, and the reaction between sodium precursor and ligand **L2** is probably not completed.

The CDCl$_3$ was still used as the solvent for analysis of the yttrium complex because the NMR spectrum is significantly different if the solvent was changed. It is relatively easy to compare proton signals if the solvent remained the same. After the addition of diamagnetic yttrium(III) precursors into the ligand **L2** in CDCl$_3$, a white solid rapidly precipitated. We cannot draw any detailed conclusion based on this preliminary NMR result, but it is notable that the NMR spectrum of the residual in solution is significantly changed, consistent with interaction with yttrium(III). Inspired by the apparent interaction between the ligand and Y(DMSO)$_3$(NO$_3$)$_3$, an investigation of the photophysical properties of lanthanoid complexes of ligand **L2** was initiated.
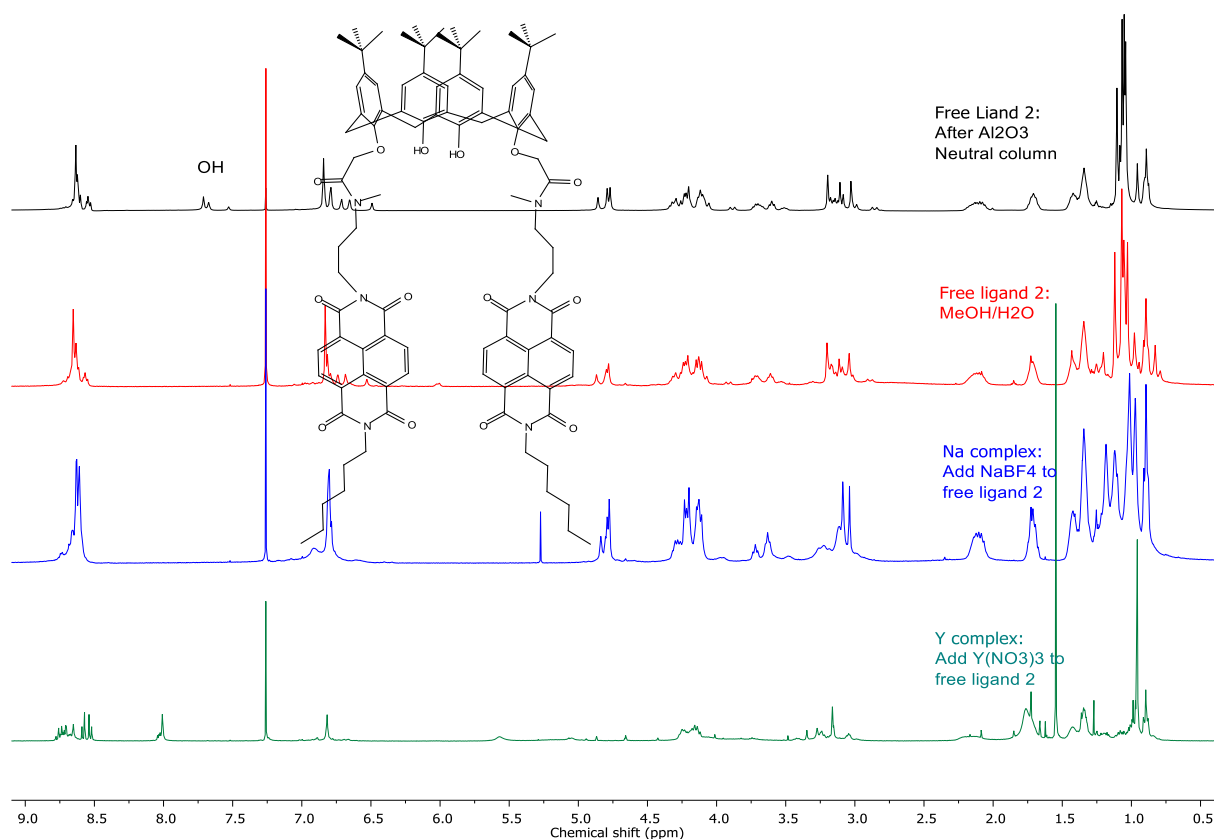
Figure 60: ^{1}H NMR spectra of the ligand L2 after column (in black), free ligand L2(in red), Na complex of ligand L2(in blue) and the soluble material remaining after the addition of Y(III) into ligand L2 (in green) in CDCl$_3$ recorded at 400 MHz.

2.4 X-Ray Crystallography

The ligand **L1** was crystallised from DMF solvent in a sealed vial and crystallized as the solvate **L1**·3DMF in a triclinic structure in the $P\overline{1}$ space group (Figure 61). The calixarene assumes the cone conformation, consistent with the solution phase analyses. As is typical of bis-substituted calixarenes, the cone conformation is stabilized by phenol O…O hydrogen bonds (O(101)…O(401), 2.776(2); O(201)…O(301), 2.850(2) Å). Unlike the secondary amide calixarene derivatives referred to above, in this case there are no hydrogen bonds between the amide H atoms and the phenol O atoms. Instead, there is a hydrogen bond between the two amide groups (N(619)…O(520), 3.073(2) Å), with the second amide NH forming a hydrogen bond with the O atom of a DMF solvent molecule (N(519)…O(20), 3.000(2) Å). These intramolecular hydrogen bonds are presumably sufficiently stable to inhibit metal binding by this ligand. The DMF(1) solvent molecule is situated in the calixarene cavity disordered over two positions, with a methyl group directed into the cavity. The conformation of the substituent groups are such that both NDI groups are aligned approximately parallel to the neighbouring unsubstituted phenol aromatic ring of the macrocycle, and with interplanar angles and centroid to centroid distances consistent with π - π stacking interactions (Phenol(2), 3.6˚, 3.63 Å; Phenol(4), 3.2˚, 3.78 Å).

Neighbouring NDI units generated about inversion centres are parallel with interplanar distances of 3.35 and 3.42 Å in the crystal leading to a linear stacking of the molecules.

a)

b)
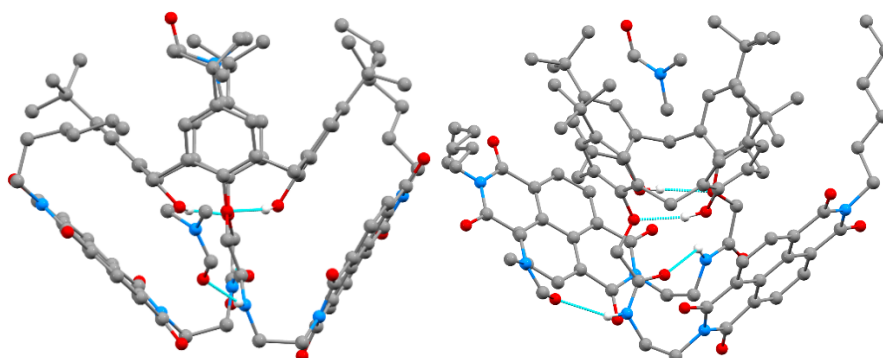
c)
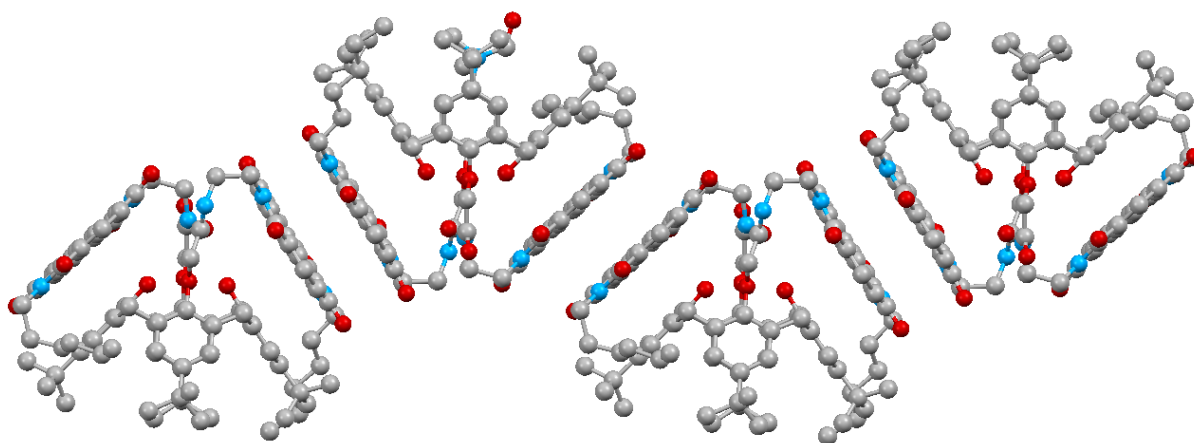
Figure 61: Crystal structure of the ligand L1. Intramolecular hydrogen bonds on the lower rim are highlighted in blue. (a) Side view. (b) Oblique view. (c) Crystal packing and intermolecular stacking interactions

While attempts to grow single crystals of ligand **L2** were unsuccessful, single crystals of Ln(**L2**-2H)NO$_3$ complex (Ln^{3+} = Eu^{3+}, Yb^{3+}) were successfully grown by evaporation of a 1:1 mixture of the ligand and the metal salt in a MeCN solution in the presence of triethylamine. The europium and ytterbium complexes are isomorphous, formulated as [Ln(**L2**-2H)NO$_3$]·6CH$_3$CN. The mononuclear complex is an eight-coordinate neutral species with the coordination sphere comprising of two deprotonated phenol O atoms, two phenol ether O atoms, the two calixarene amide O atoms, and two oxygen atoms completing the coordination sphere from the bidentate nitrate anion. The calixarene assumes the cone conformation as expected, although the conformation is significantly distorted with the angles between the phenol rings and the methylene C4 plane being: ring 1, 69.5; ring 2, 54.8; ring 3, 74.2; ring 4, 143.1°. The significant difference for ring 4 is presumably a distortion related to accommodation of the bidentate nitrate anion in the coordination sphere. The disposition of the NDI substituents is different to that observed for **L1**, now positioned away from the calixarene cavity and

stacked with an interplanar angle of 10.1° and centroid-centroid distance of 3.92 Å. In the absence of a crystal structure of the ligand **L2**, it is not possible to conclude if this change is due to the methylation of the amide groups, or the presence of the metal ion. In the crystal, there is once again an interaction between an NDI moiety and phenol ring 2, but here this is an intermolecular interaction resulting in a dimeric structure about an inversion centre (Figure 62). The intermolecular stacking interaction forms with an angle of 9.4°, and NDI centroid-centroid distance of 3.76 Å (nearest Ar centroid-centroid distance is 3.70 Å). The shortest contact is between carbon atom of the phenol ring 2 and carbon atom of the imide ring, and the distance is 3.40 Å. The complex has one acetonitrile solvent molecule embedded in the calixarene cavity, with the methyl group directed into the cavity.
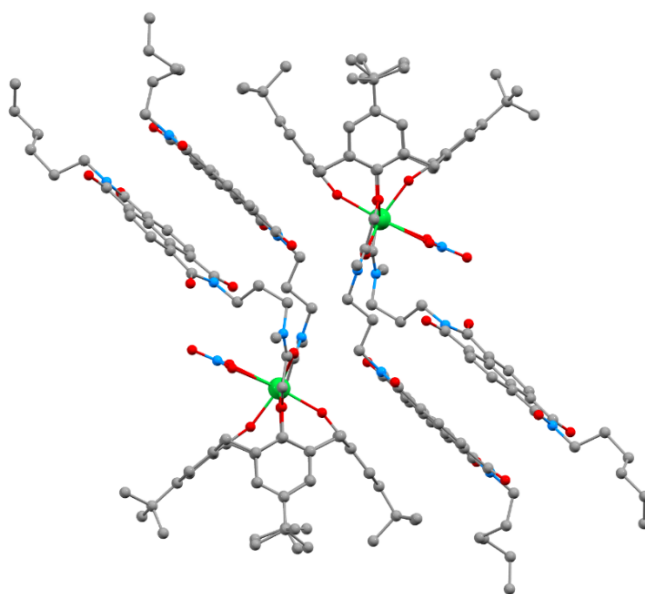
Figure 62: X-ray crystal dimeric structure of [Yb(L2-2H)NO₃]₂. Hydrogen atoms omitted for clarity.

A single clear light orange block crystal of the ligand **L3** was grown by evaporation of a DMF solution. The calixarene here exhibits a relatively symmetrical "pinched" cone conformation, where two opposing phenolic units are close to vertical, while the other are splayed out. The angles of the phenol rings relative to the methylene C4 plane are ring 1, 88.2; ring 2, 40.4; ring 3, 88.1; ring 4, 40.9°. The cavity is solvent-free as typically found for a pinched conformation. Intramolecular hydrogen bonds are observed between the NH amide groups and neighboring amide O atoms (N(719)…O(520), 2.815(5); N(819)…O(620), 2.821(4) Å). The NDI moieties are again positioned directed away from the calixarene cavity. Here the angle between the two NDI planes is 2.3°, and the distance between the NDI centroids is 4.75 Å, with the closest Ar centroid-centroid distance being 3.62 Å. A dimeric intermolecular stacking interaction is found between two NDI groups (Figure 63), where the planes of the molecule are parallel and at a distance of 3.34 Å. The intermolecular stacking interaction is present between the adjacent and offset naphthalene of NDI with the centroid-centroid distance being 3.58 Å.

a)   b)
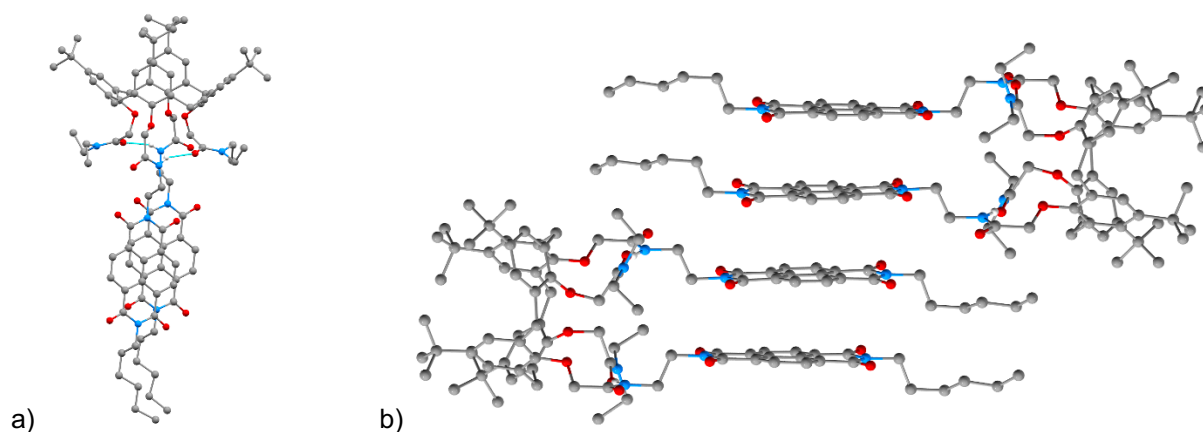
Figure 63 :X-ray crystal structure of the ligand L3. (a)Monomeric structure and intramolecular hydrogen bonds highlighted in blue. (b) Dimeric structure.

2.5 Photophysical Properties of Bis-NDI Substituted Ligands

2.5.1 Absorption and Emission Results

As was mentioned in the Introduction, NDI derivatives can exhibit aggregation properties in some solvents, and the energy transfer between aggregate and lanthanoid was also to be investigated. Therefore, the solvent is important. Water is also excluded because both calixarene and alkyl-functionalised NDI have poor solubility in that solvent. The attempt to dissolve these ligands in acetonitrile was not successful. However, using dichloromethane/acetonitrile (1:1) significantly improved their solubilities, and provided a system where the impact of aggregation could potentially be explored.

In order to assess the antenna effect, the first step was to measure the UV-visible spectra of ligands (Figure 64). The measured solution was also verified to follow the Beer's law between the concentration of 0.5×10^{-5} to 1.2×10^{-4} M (See appendix).
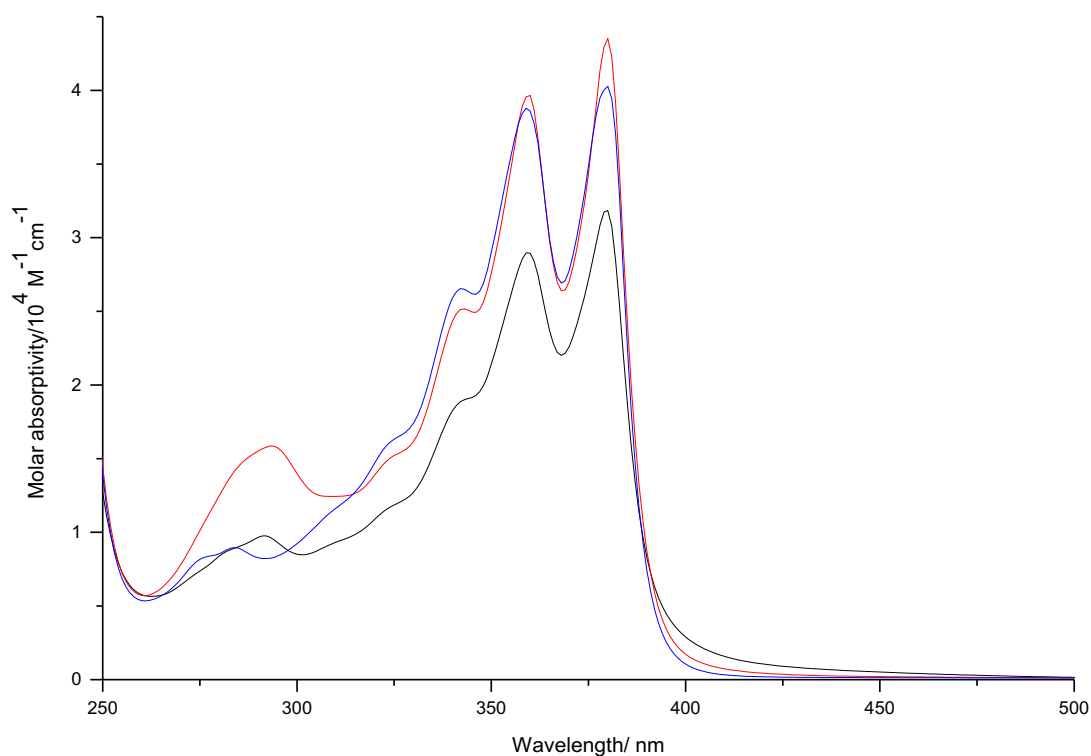
Figure 64: Absorption spectra for 10^{-4} M DCM/MeCN (1:1) solutions of ligand L1 (black), ligand L2 (red) and ligand L3 (blue).

The UV-Visible spectra of the ligand **L1,** ligand **L2** and ligand **L3** were obtained from a 10^{-4} M dichloromethane/acetonitrile (1:1 v/v) solution at room temperature. The UV-visible spectra of the three ligands are similar as expected due to the similarity of their structures. The spectra show two prominent intense bands. The absorption peak in the region of 250 nm to 300 nm is assigned to the $\pi \rightarrow \pi^*$ transition of aromatic rings of calixarene. According to previously photophysical studies on NDI,[100-101] the lower energy band from 340 nm to 400 nm represents S_0 to S_1 vibronic progression of NDI with a shoulder centred at 340 nm. (See Table 8).

Table 8: Summary of the absorption and emission data of the L1, L2 and L3 ligands in a 10^{-4} M acetonitrile/dichloromethane (1:1) solution.

Ligand	λ_{abs} [nm] (10^4 ε [M^{-1} cm^{-1}])	λ_{em} [nm]
1	283 (0.88), 292 (0.98), 324 (1.17), 342 (1.88), 360 (2.89), 380 (3.18)	407, 432
2	294 (1.58), 325 (1.52), 343 (2.52), 360 (3.97), 380 (4.35)	408, 432
3	276 (0.83), 285 (0.89), 322 (1.55), 343 (2.65), 360 (3.85), 380 (4.02)	408, 432
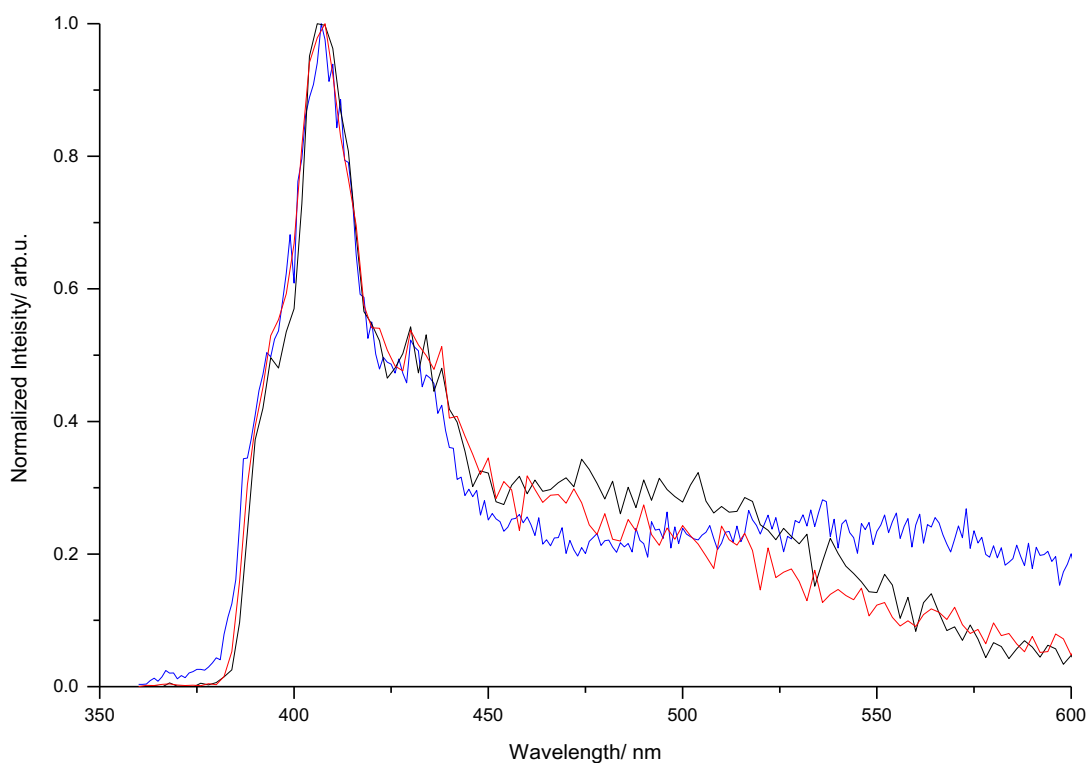
Figure 65: Emission spectra for 10^{-4} M DCM/MeCN (1:1) solution of the ligand L1 (black), ligand L2 (red) and ligand L3 (blue). Excitation wavelength: 340 nm.

The **L1**, **L2** and **L3** ligands exhibit similar emission properties to the monomer in a 10^{-4} M solution (DCM/MeCN 1:1 v/v) at room temperature (Figure 65). The emission spectrum shows a prominent peak at 410 nm with a shoulder tailing offer to 600 nm. This peak is attributed to the emission from the $^1\pi\pi^*$ state of the NDI.[100]

2.5.2 Spectrophotometric Titrations

The stoichiometry of lanthanoid complexes formed in solution was determined by stepwise addition of commercially available europium(III) nitrate hydrate to a solution containing the ligand at room temperature, until no further changes were observed. The ionic strength was maintained using a 10^{-2} M NBu$_4$PF$_6$ solution. Because of the low solubility of ligand **L2** in a MeCN solution, the ligand **L2** was dissolved in a mixture of 1:1 DCM/MeCN. The titration was initially carried out in the presence of excess base (five equivalents of triethylamine) to ensure the calixarene was fully deprotonated. Five equivalents of triethylamine were used. However, after adding 0.3 eq Eu^{3+} ions, precipitation occurred preventing further measurements.

The experiment was therefore carried out in the absence of triethylamine. Titration curves show the value of the molar absorptivity decreases steadily with increasing molar ratio of the Eu^{3+} to ligand **L2** (Figure 66). A sharp inflection point at the 1:1 ratio is observed for the ligand **L2** with Eu(III), suggesting complexation is occurring with a high effective association constant. The maximum molar absorptivity of calixarene at 294 nm is expectedly red-shifted to 310 nm upon coordination.[75]
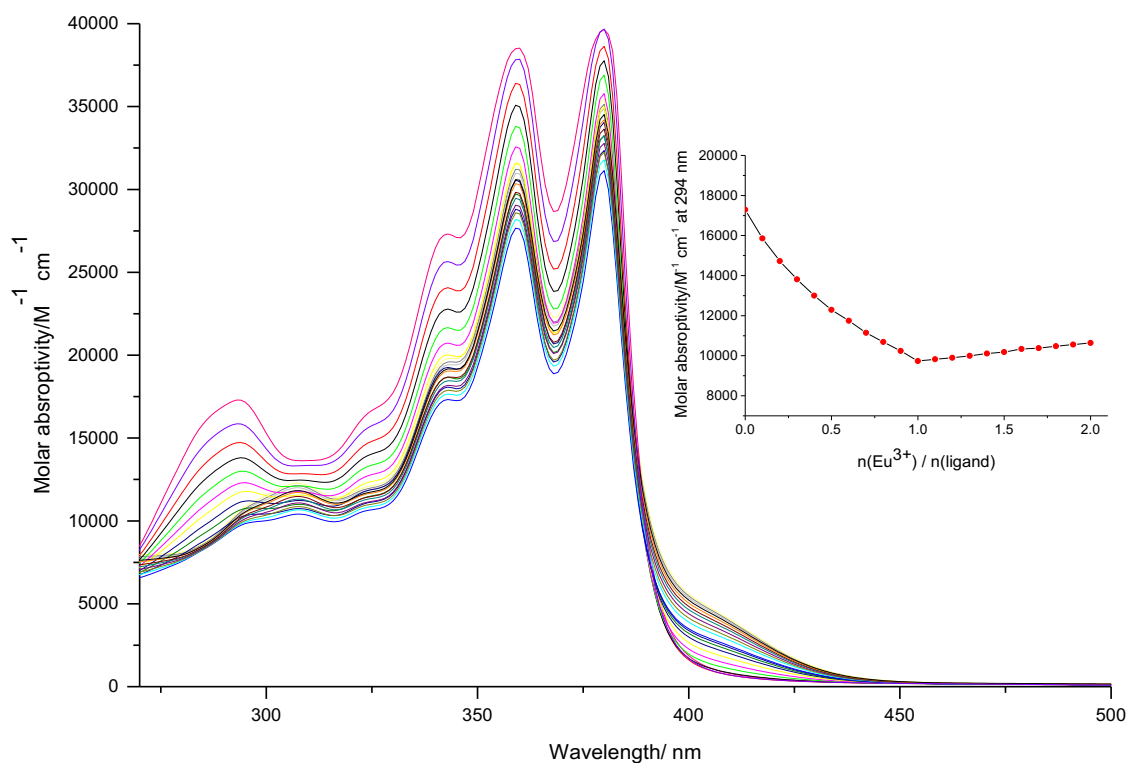
Figure 66: Spectrophotometric titration of ligand L2 with the Eu(NO₃)₃·6H₂O in DCM/MeCN (1:1) at constant ionic strength (10⁻² M NBu₄PF₆) in the absence of triethylamine at room temperature. Inset shows the dependence of absorbance at 294 nm versus the Eu³⁺/L2 molar ratio.

In an attempt to prevent byproducts from precipitating in the presence of triethylamine and to lower the effective stability constant into a range that would allow quantification, DMF was employed as a solvent. Another reason for using the DMF is its wide potential window in cyclic voltammetry. The spectrophotometric titration of the ligand **L2** with europium(III) nitrate hydrate in dimethylformamide was performed in the presence of triethylamine and 10⁻² M NBu₄PF₆ solution (Figure 67). However, there is no observable inflection point for up to four equivalents of Eu³⁺ ions. Only gradual dilution is observed based on the similar molar absorptivity, suggesting that the complex does not form in DMF. Therefore, photophysical studies were carried out in a mixture of DCM/MeCN (1:1).
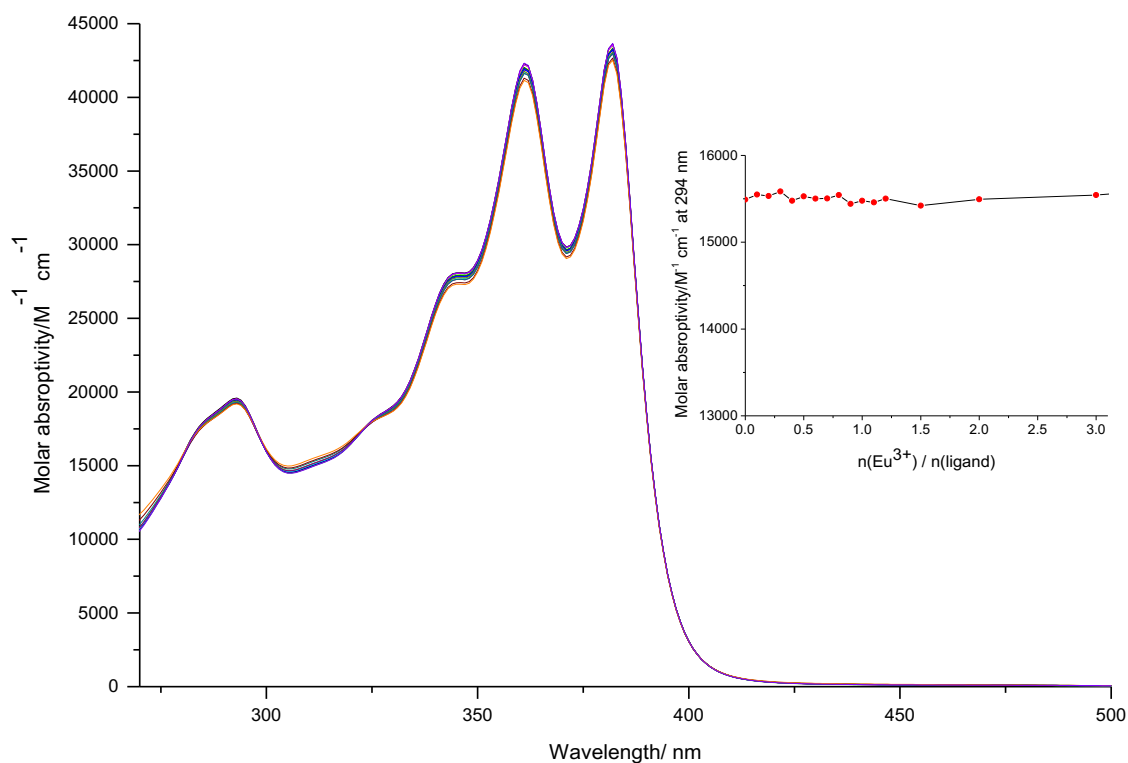
Figure 67: Spectrophotometric titration of ligand L2 with Eu(NO₃)₃·6H₂O in DMF at constant ionic strength (10^{-2} M NBu₄PF₆) in the presence of five equivalents of triethylamine at room temperature. Inset shows dependence of molar absorptivity at 294 nm versus the Eu³⁺/L2 molar ratio

2.5.3 Energy of Triplet State

The Gd^{3+} complex is used to find the energy of the triplet state of a ligand and through this assess the possibility of the energy transfer to lanthanoid ions. The experimental details of synthesis of these Gd^{3+} complexes in the solution phase and solid state, as well as the Eu^{3+}, Nd^{3+} and Yb^{3+} complexes, are given in the experimental section.

The absorption spectrum of the Gd(**L3**) complex in a mixture of 10^{-4} M DCM/MeCN (1:1**)** was recorded (Figure 68). A comparison between ligand **L3** and its Gd^{3+} complex shows the molar absorptivity of phenyl rings significantly decreases. This indicates that addition of Gd^{3+} ions results in formation of the complex. This result is in agreement with the literature.[84-85]
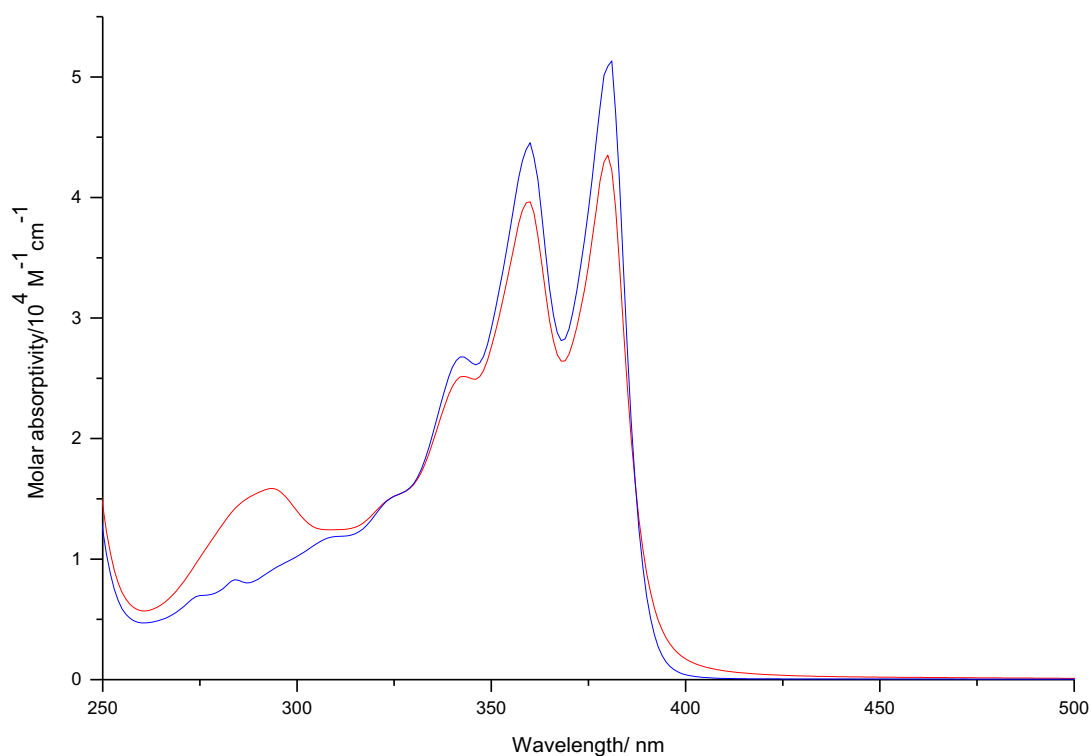
Figure 68: Absorption spectra for 10^{-4} M DCM/MeCN (1:1) solutions of ligand L3(red) and its corresponding Gd^{3+} complex in the presence of trimethylamine (blue).

The emission spectrum of **L3** displays a vibronically structured emission around 410 nm from the NDI monomer (Figure 69), and the observed lifetime of NDI functionalised at the axial position has been reported to be less than 20 ps[95, 101]. Excitation of the Gd(**L3**) complex in a 10^{-5} M MeCN/DCM (1:1) solution at 340 nm at room temperature results in a broader and structureless band spanning from 430 nm to 700 nm, which is tentatively assigned to emission from the aggregate.[12] The observed lifetime decay was fitted to the monoexponential decay, giving the value of 19 ns. This value is consistent with those reported for aggregated NDI.[102]
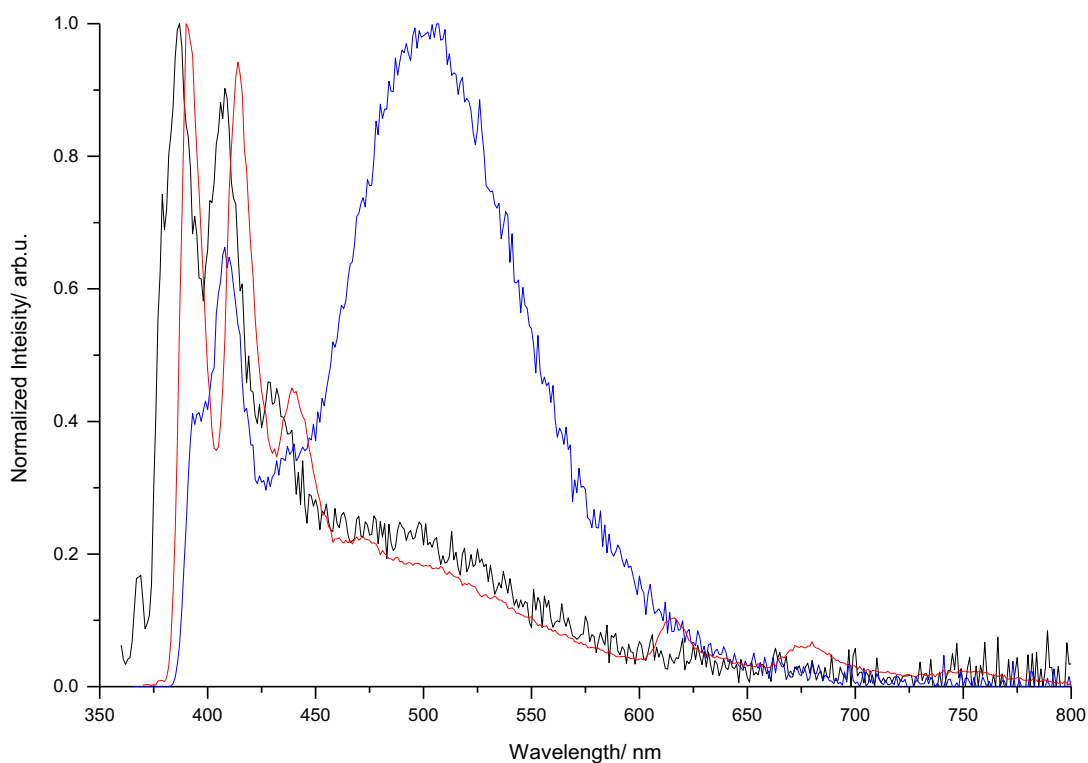
Figure 69: Emission spectra for 10^{-5} M DCM/MeCN (1:1) solution of the ligand L3(black), Gd(L3) complex at room temperature (blue) and Gd(L5) complex at 77K (red). Excitation wavelength: 340 nm.

It was hypothesised that the aggregate forms as a result of the addition of Gd^{3+} ions. To investigate this, Dynamic Light Scattering (DLS) measurements were carried out to provide some information about the size of the ligand alone and Gd(**L3**) complex in a DCM/MeCN solution (Figure 70).
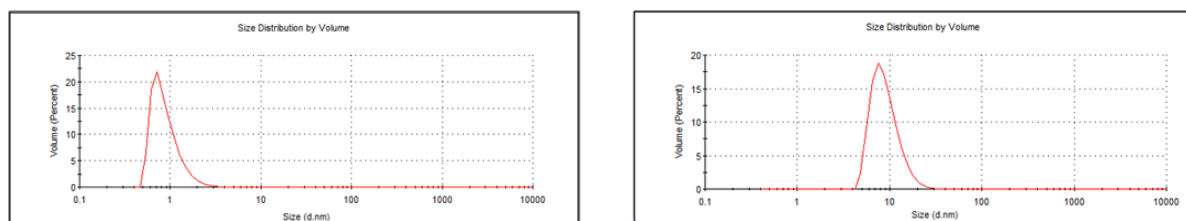
Figure 70: DLS spectra of ligand L3 (left) and Gd(L3) complex (right) in DCM/MeCN (1:1) at 10^{-5} M.

The average hydrodynamic radius measurement clearly shows the significant size difference between ligand **L3** and Gd(**L3**) complex. The average size of the ligand **L3** is 0.9 nm, while the average size of the Gd(**L3**) complex is 9.2 nm consistent with the formation of an aggregated structure. Therefore, we can conclude that the aggregate is formed due to the addition of Gd^{3+} ions, and the structureless band around 500 nm is assigned to emission from the aggregate.

The emission spectra of ligand **L3** in a DCM/MeCN (1:1) solution at room temperature follow a similar trend to that observed in the spectrum of Gd(**L2**-2H)NO$_3$ complex at room temperature (Figure

71). In this case, however, emission consistent with an aggregate is not observed. The prominent peak at 410 nm is attributed to the emission from the excited singlet state of NDI.
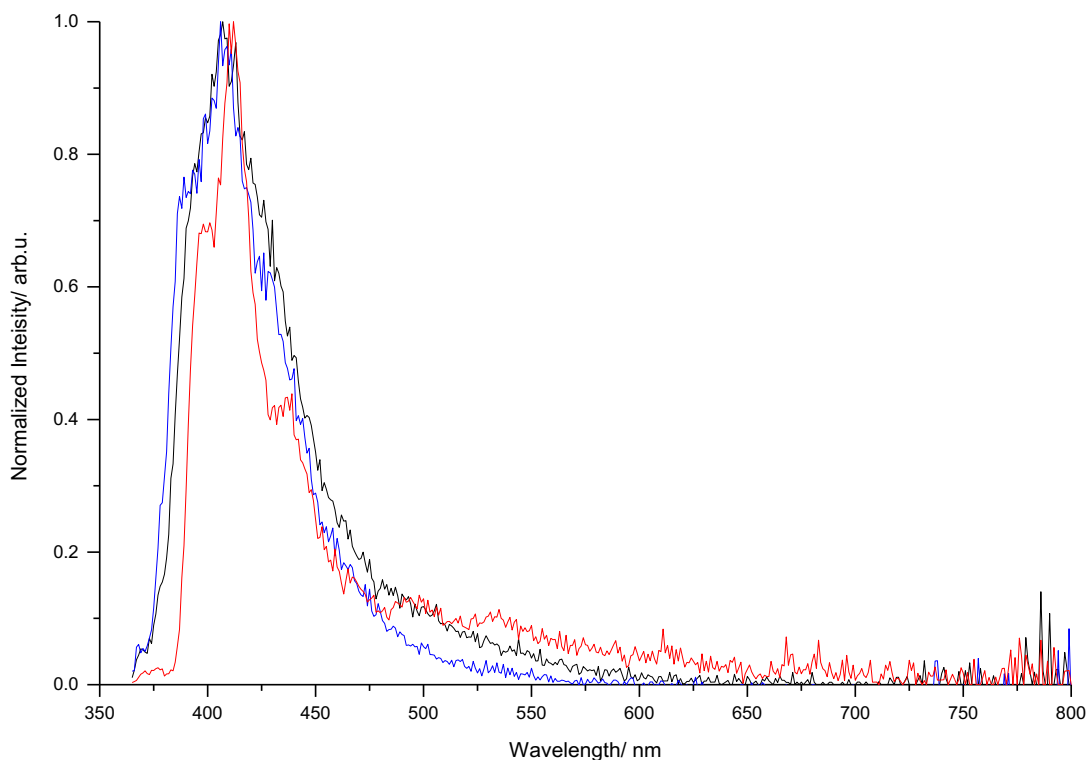
Figure 71: Emission spectra for 10^{-5} M DCM/MeCN (1:1) solution of the ligand L2(black) and its corresponding Gd^{3+} complex at room temperature (blue) and 77K (red). Excitation wavelength: 340 nm.

The phosphorescence peaks can only be observed in the Gd(**L3**)complex in the region of 600 - 800 nm at 77K (Figure 69, red trace). The lifetime can not be calculated due to the weakness of emission. However, these peaks are not observed in the case of Gd(**L2**-2H) even if excess Gd^{3+} ions are used (Figure 71, red trace). This is probably because the NDI is far away from the Gd^{3+}, and the intersystem crossing process is not favoured.

It has been reported that the phosphorescence of NDI can be induced in the presence of ethyl iodide.[100] Therefore, we confirmed the phosphorescent peak following the literature and measured the emission spectra of **L2** and **L3** in a frozen mixture of DCM/MeCN/10%EtI at 77K (Figure 72). The emission spectra of **L2** and **L3** are similar, both of which show the broad and structureless peak spanning from 350 nm to 600 nm. This phosphorescence peak from the NDI is more visible under these conditions. This result is in agreement with the literature.[100] The excited state lifetime decay was fitted to a biexponential model with components of 830.0 μs (16%) and 3.6 ms (84%) for ligand **L3**, and 874.6 μs (11%) 3.8 ms (89%) for ligand **L2**. This major component might be assigned to the decay from the triplet state of NDI monomer, and the minor component might be assigned to the decay from the triplet state of aggregate.
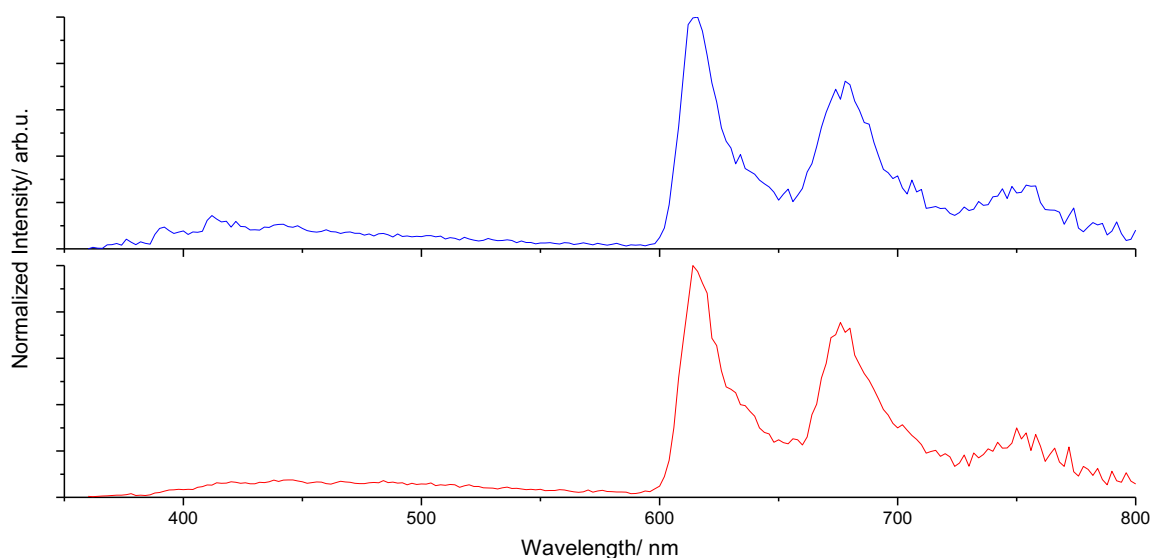
Figure 72: Emission spectra of ligand L2 (blue) and ligand L3 (red) in a mixture of DCM/MeCN/10%EtI at 77K (10^{-5} M). Excitation wavelength: 340 nm.

It is noticeable that Gd^{3+} ions can provide limited external heavy metal effect and induce weak phosphorescence in the case of Gd(**L3**) complex. When the number of methylene spacers increases from C$_2$ to C$_3$, no phosphorescence is observed in the case of Gd(**L2**-2H) complex. In the presence of 10% EtI, the peak corresponding to the phosphorescence is more visible. This observation suggests that the population of the triplet state depends on the distance between the heavy atoms and NDI. Therefore, the energy of the triplet state can be calculated to be around 16233 cm^{-1} (616 nm). The energy of the triplet state is high enough ($\geq$ 2500 cm^{-1}) to sensitise Nd^{3+} ($^4F_{3/2}$, ~11260 cm^{-1}) and Yb^{3+} ($^2F_{5/2}$, ~10200 cm^{-1}) luminescence, but it is lower than the energy of the emissive state of Eu^{3+}($^5D_0$, ~17200 cm^{-1}).

2.6 Photophysical Properties of Lanthanoid Complexes

The lanthanoid complexes for photophysical measurements in solution were formed *in situ*. The details for the preparation are shown in the experimental section. As mentioned above, the ligand **L1** does not form a complex with lanthanoids based on the lack of changes in the NMR spectra of ligand **L1** and its corresponding yttrium(III) complex in the presence of triethylamine. Therefore, its emission properties were not studied for this ligand.

The aim of the photophysical studies of the lanthanoid complexes was to investigate the antenna of energy transfer from NDI. Both the NDI and calixarene aromatic rings can work as an antenna ligand, but the NDI should be able to be selectively excited. First of all, any spectral overlap in the absorption spectrum needs to be understood. Therefore, NDI-free calixarenetetramide (**R1**) was used as a reference compound, and its absorption spectra of R1 and Eu(**R1**) complex were recorded (Figure 73).
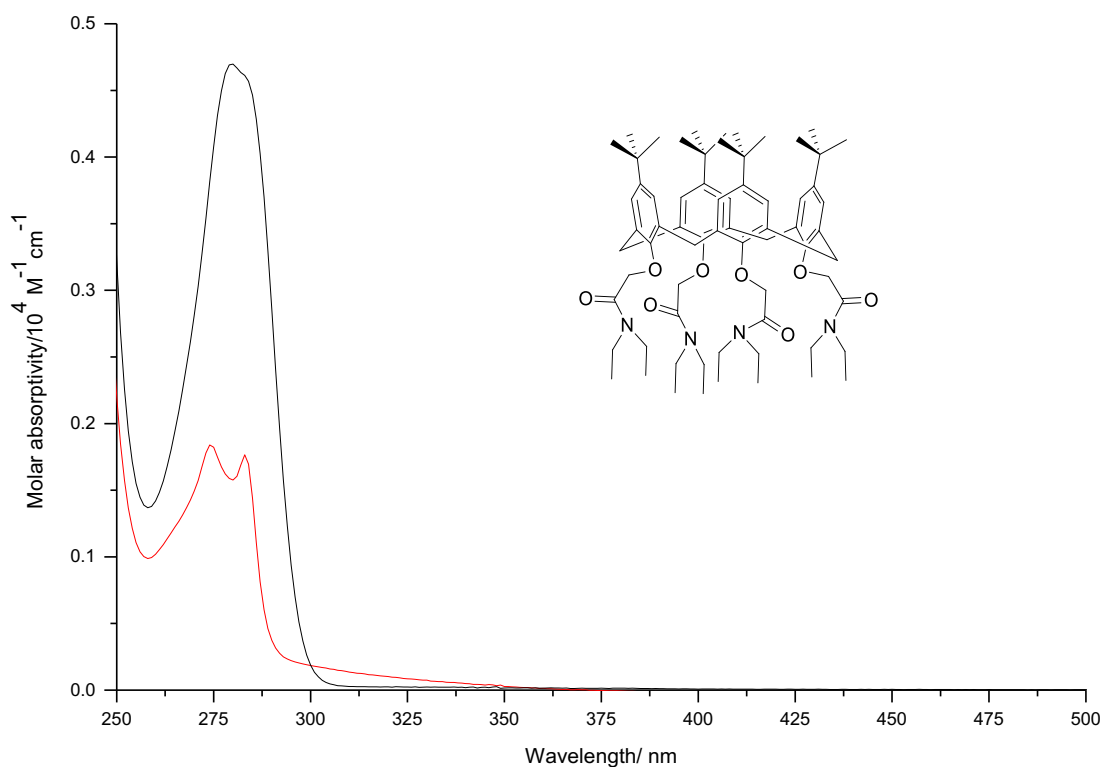
Figure 73: Absorption spectra for 10^{-4} M DCM/MeCN (1:1) solutions of tetradiethyl amide calixarene R1 (black) and its corresponding Eu(R1) complex (red).

The band is attributed to the $^1\pi\pi^*$ transition of phenyl rings, which is not overlapped with the absorption band of NDI. Therefore, using the wavelength at 340 nm can selectively excite the NDI.

2.6.1 Ytterbium(III) Complexes

We attempted to investigate the photophysical properties of Yb(**L2**-2H)NO$_3$ complex in the phase and solid state. UV-visible spectra show molar absorptivity of the ligand **L2** and its corresponding Yb^{3+} complex in Figure 74. Upon addition of one equivalent of Yb(DMSO)$_3$(NO$_3$)$_3$, the peak at 294 nm corresponding to the phenol of calixarene is red-shifted. It is evident that the Yb^{3+} complex forms in the solvent mixture.
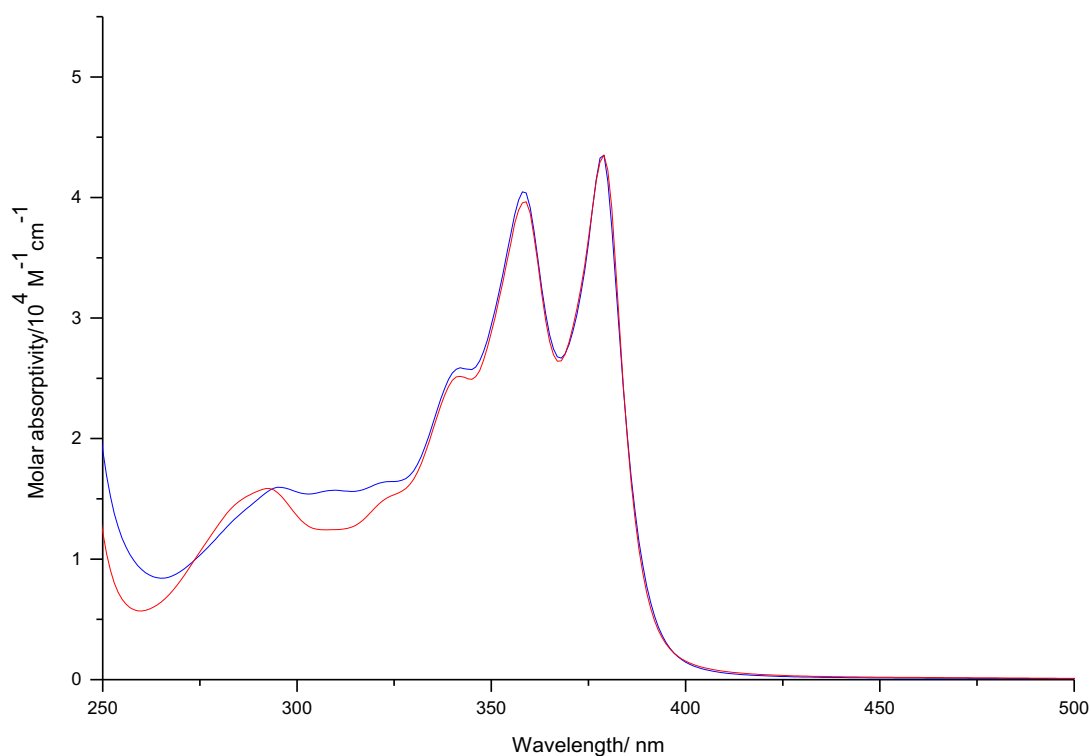
Figure 74: Absorption spectra for 10^{-4} M DCM/MeCN (1:1) solutions of ligand L2 in the presence of trimethylamine (red) and its corresponding Yb^{3+} complex (blue).

It has been reported that the calixarenes can act as an antenna ligand for lanthanoid emission.[162-163] To avoid the lanthanoid sensitization via the calixarene aromatic groups, we need to selectively excite the NDI using the wavelength at 340 nm. Upon excitation at 340 nm, the emission spectra of Yb(**L2**-2H)NO_3 complex in solution and solid state show characteristic Yb^{3+} emission resulting from $^2F_{5/2}$ to $^2F_{7/2}$ transitions in the near-infrared region (Figure 75). Three peaks are observed at 983 nm, 1016 nm and 1064 nm. The emission profiles show similar fine structures. In a 10^{-5} M solution, the emission from NDI monomer is also observed. The excitation spectrum of Yb(**L2**-2H)NO_3 complex is analogous to the absorption spectrum of the ligand **L2**, indicating Yb^{3+} luminescence is induced by the NDI monomer via the antenna effect. In a 10^{-4} M solution, a sharp peak around 400 nm is also observed in the excitation spectrum. The observation of this peak might be linked to two factors that arise from the aggregates or inner filter effect.[164-165] Due to the limited time of the course of this project, we can not further investigate this photophysical phenomenon and draw the definitive conclusion. In the solid state, an extra broad peak ranging from 500 nm to 750 nm is observed. The presence of this peak suggests an aggregate may form and transfer the energy to Yb^{3+} ion. The excited-state lifetime decay was found to be monoexponential, with values of lifetime measured to be 8.6 μs in 10^{-5} M, 8.4 μs in 10^{-4} M solutions and 9.7 μs in solid (Figure 76). Also shown is the instrumental response function (IRF). Where the lifetime of the sample is too close to the IRF, then they need to be both considered and the IRF must be deconvoluted to obtain a better fit. The overall quantum yield of the emission in the acetonitrile at room temperature was calculated using the reference method,[19] giving values of 0.2% (λ_{ex} = 285 nm) and 0.1% (λ_{ex} = 340 nm).

Figure 75: Blue trace is the normalized absorption spectrum of the ligand L2. Black trace is the excitation spectrum, and the red trace is the emission spectrum of the Yb(L2-2H)NO₃ complex. Excitation wavelength: 340 nm. Top: 10^{-5} M DCM/MeCN (1:1) solution; middle: 10^{-4} M DCM/MeCN (1:1) solution; bottom: solid state.
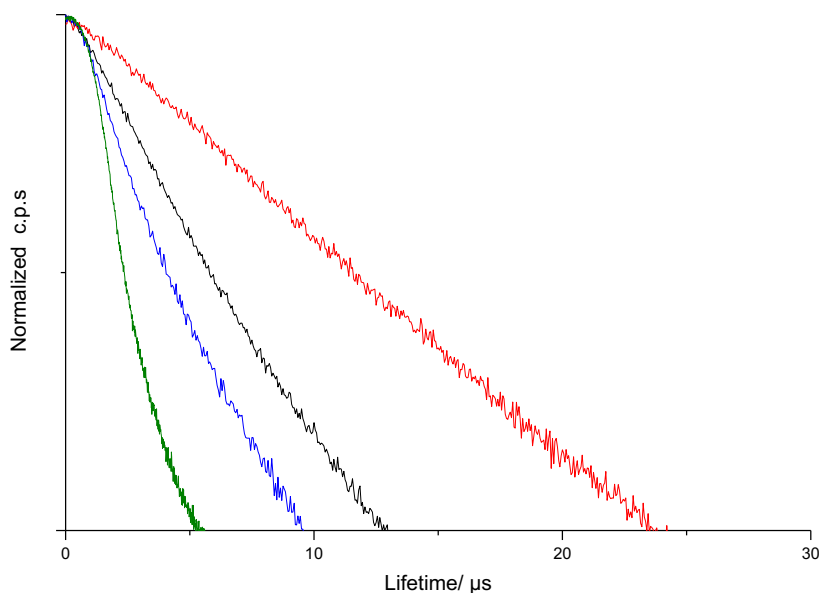
Figure 76: Lifetime decay of Yb(L2-2H)NO₃ complex in the 10^{-4} M DCM/MeCN (1:1) (blue trace), 10^{-5} M DCM/MeCN (1:1) (black trace) and the solid state (red trace) at room temperature. The green trace is the instrument response function (the response of the instrument to the blank 1:1 DCM/MeCN solution).

The emission spectra of the Yb(**L3**) complex were analysed in a mixture of dichloromethane and acetonitrile at room temperature. The emission spectra of Yb(**L3**) species display characteristic fluorescence attributed to $^2F_{5/2} \rightarrow {}^2F_{7/2}$ transition (Figure 77) in all cases. The emission from singlet O_2 is also observed around 1280 nm in solutions, indicating that the triplet states of NDI and aggregates are populated. This could also suggest that the energy transfer from the triplet state to the emissive state of Yb^{3+} is slow or does not occur. In the UV-visible region, the emissions from NDI monomer and aggregate were observed. The excitation spectra of Yb(**L3**) complex are visibly different in different concentration. In a 10^{-5} M acetonitrile solution, the excitation spectrum of the Yb^{3+} complex illustrates a sharp peak below 300 nm and a band spanning from 300 nm to 400 nm, which are assigned to the electronic transition of the phenyl moieties of calixarene and NDI monomer. In a 10^{-4} M acetonitrile solution, the peaks with relatively low intensity span from 400 nm to 500 nm, corresponding to the aggregate. The excitation spectrum shows the disappearance of the absorption of NDI monomer. In the solid state, and there are no observable peaks in the range from 250 to 400 nm. Only the aggregate peak spanning from 400 to 600 nm is observed.
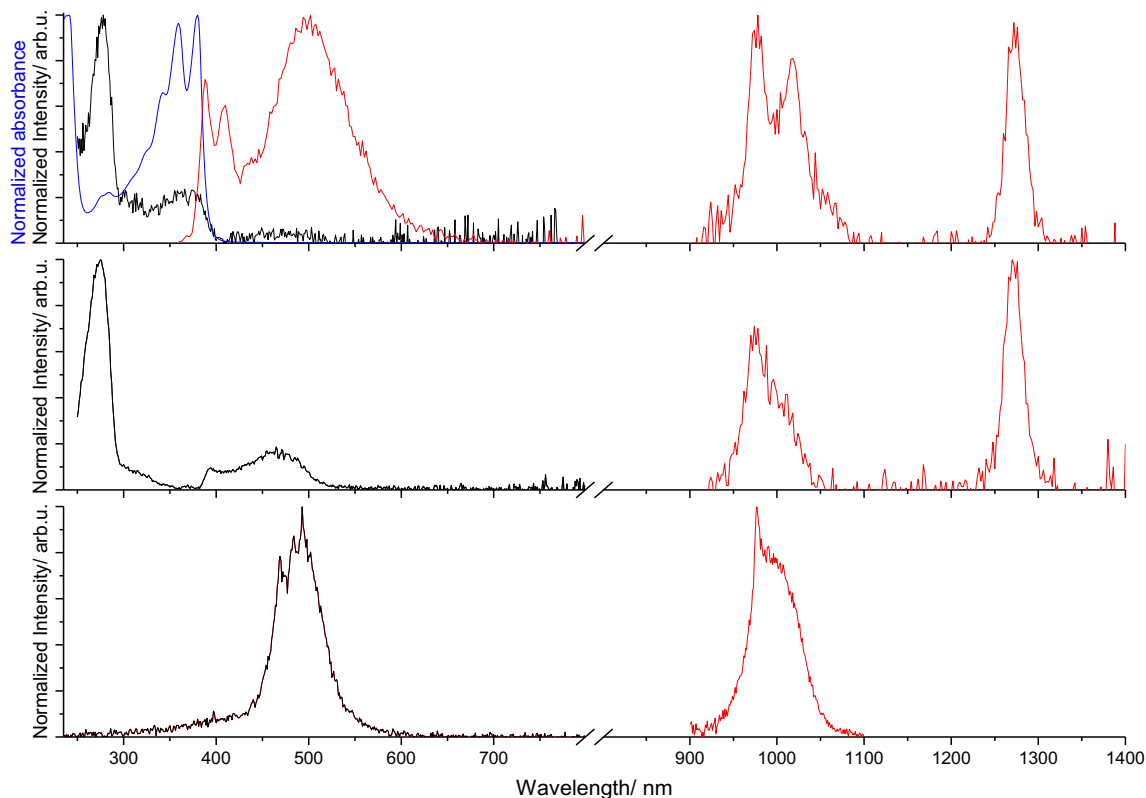
Figure 77: Blue trace is the normalized absorption spectrum of the ligand L3. Black trace is the excitation spectra, and the red trace is the emission spectra of the Yb(L3) complex. Excitation wavelength: 340 nm. Top: 10^{-5} M DCM/MeCN (1:1) solution; middle: 10^{-4} M DCM/MeCN (1:1) solution; bottom: solid state.

The excited-state lifetime decay curve of Yb(**L3**) complex was fitted to a monoexponential decay function in all cases when the emission wavelength was selected at 980 nm (Figure 78). The observed

lifetime was estimated to be 8.9 µs in a 10^{-5} M solution, 9.3 µs in a 10^{-4} M solution, and 10.7 µs in the solid state (χ^2= 1.082). The quantum yield of the emission in the acetonitrile at room temperature was calculated using the reference method, giving a value of 0.2% after excitation.

Figure 78: Lifetime decay of Yb(L3) complex in the 10^{-4} M DCM/MeCN (1:1) (blue trace), 10^{-5} M DCM/MeCN (1:1) (black trace) and the solid state (red trace) at room temperature. The green trace is the instrument response function.

2.6.2 Neodymium(III) Complexes

Before the measurement of the emission spectra, the absorption spectra of ligand **L2** and its corresponding Nd^{3+} complex were recorded in order to confirm that the complexation took place. According to the absorption spectrum of Nd^{3+} complex, the absorption band at 294 nm is red-shifted in comparison to the one observed in the ligand (Figure 79). These results suggest formation of the complex. However, the attempt to sensitise neodymium(III) luminescence via the NDI of the ligand **L2** was not successful in our hands.
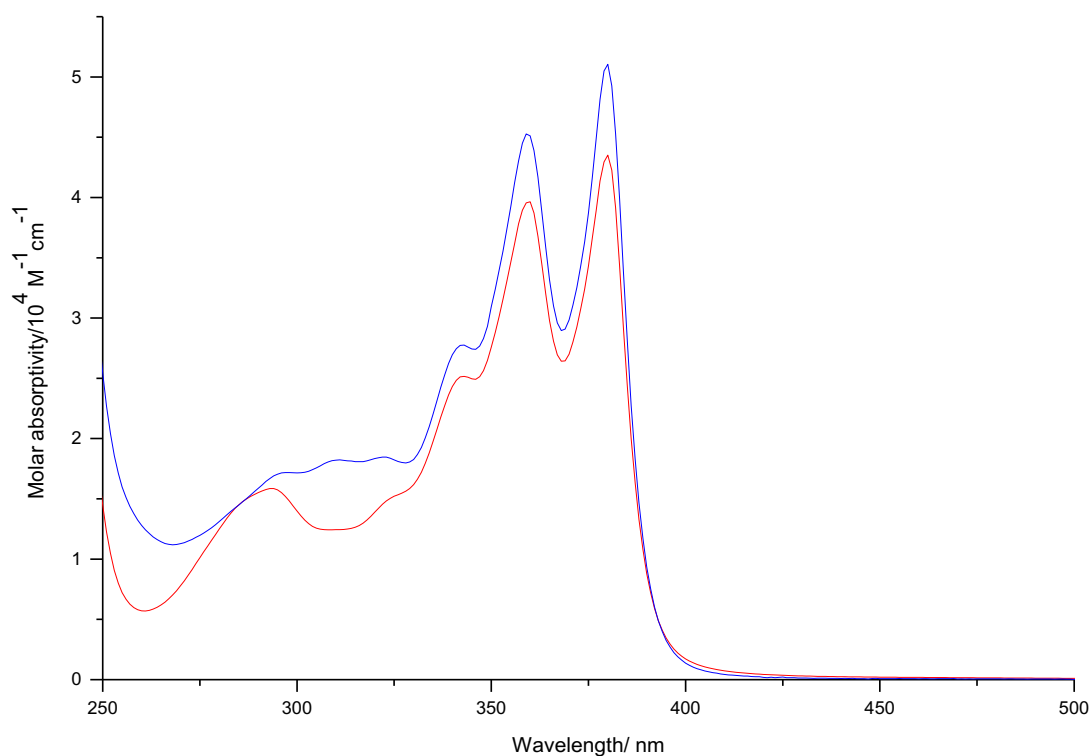
Figure 79: Absorption spectra for 10^{-4} M DCM/MeCN (1:1) solutions of ligand L2(red) and its corresponding Nd^{3+} complex (blue).

The emission spectra of the Nd^{3+} complex of **L3** in a 10^{-5} M solution show emission from NDI monomer and aggregate in the UV-visible region and the characteristic Nd^{3+} emission in the NIR region (Figure 80). These peaks correspond to the spin-allowed $^{4}F_{3/2} \rightarrow {}^{4}I_{9/2}$, $^{4}F_{3/2} \rightarrow {}^{4}I_{11/2}$ and $^{4}F_{3/2} \rightarrow {}^{4}I_{13/2}$ transitions. The peak at 1270 nm corresponding to the emission from the singlet O_2 is also observed in an air-equilibrated solution, while the emission is quenched in a degassed solution. As is mentioned in photophysics of related Gd^{3+} complex, the triplet state of NDI is populated. Therefore, triplet state of NDI is responsible for the generation of $^{1}O_2$ luminescence. The peak in the excitation spectrum is similar to the absorption spectrum, indicating that the energy transfer to Nd^{3+} ion is from the NDI monomer.

In a 10^{-4} M solution, the prominent peak at 400 nm is observed in the excitation spectrum, which is probably caused by the inner filter effect or aggregates. [164-165] The two lower energy bands correspond to the absorption of aggregate and direct excitation of Nd^{3+}. The lifetime and quantum yield in the solution phase could not be measured probably due to the poor emissive properties and self-quenching process.

In the solid state, the emission from the singlet oxygen was not observed. The aggregate peak spanning from 400 – 550 nm is observed in the excitation spectrum. The peak at 580 nm is more visible, corresponding to the direct excitation of Nd^{3+}.
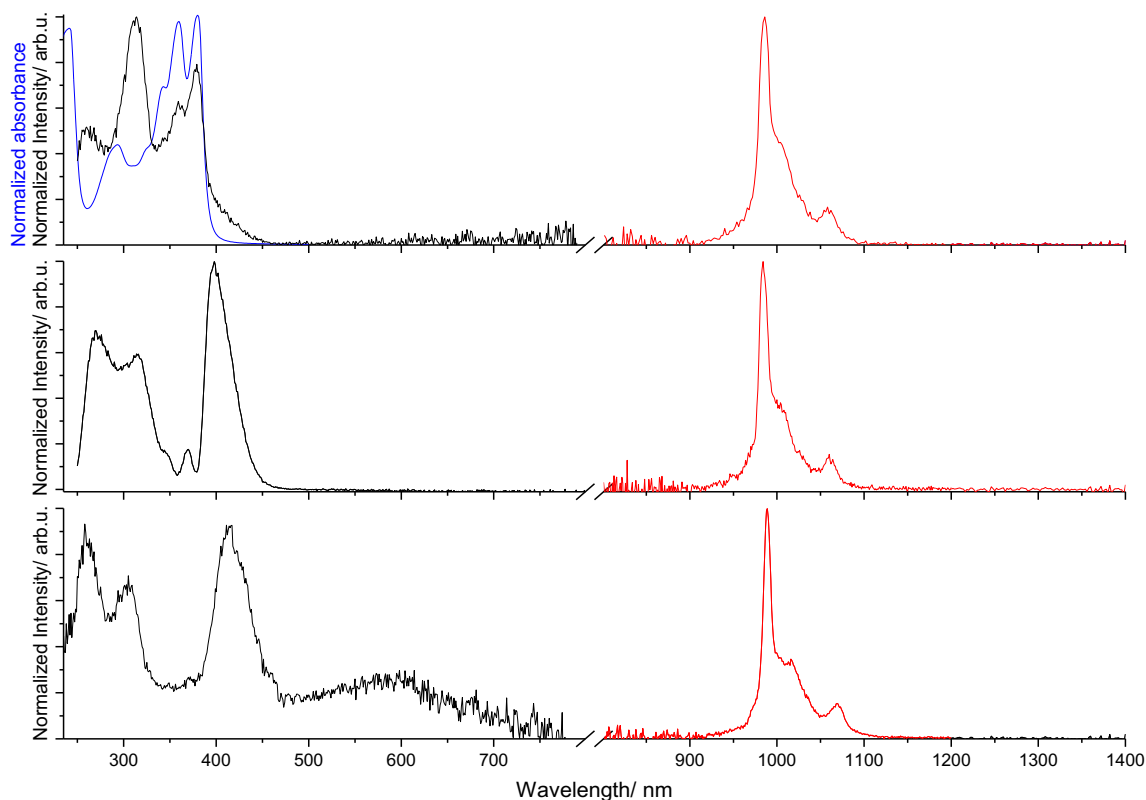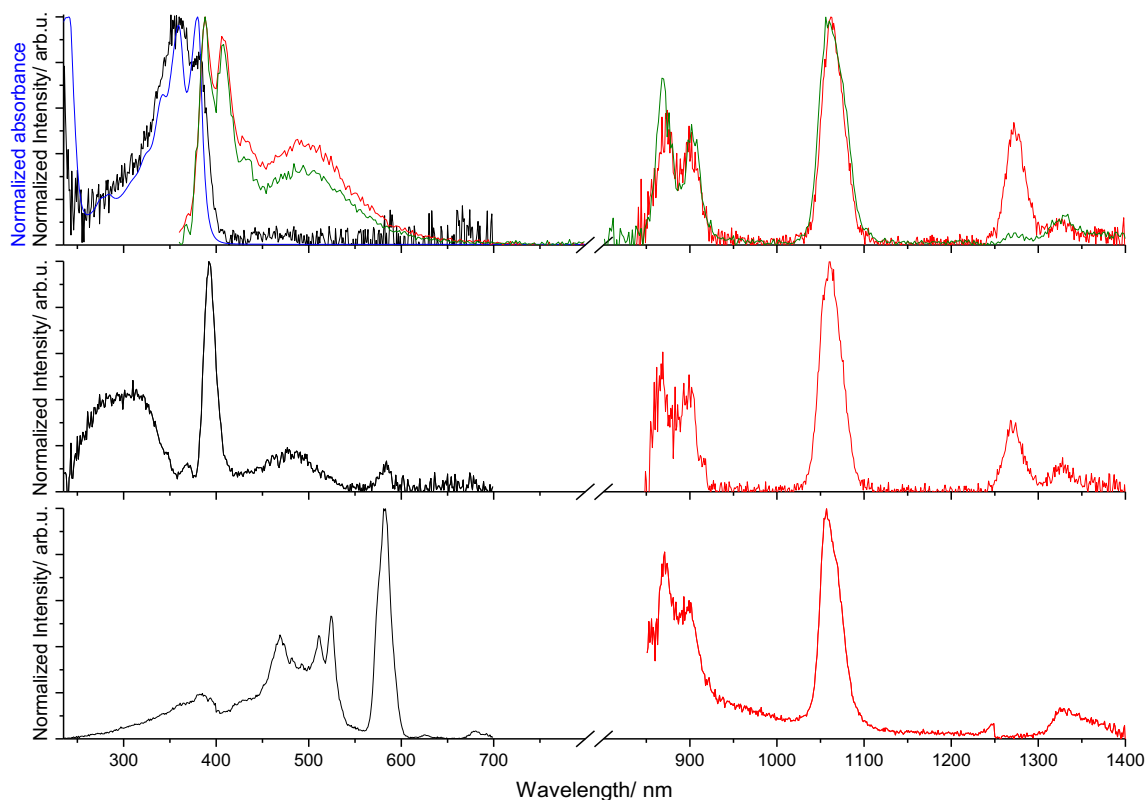
Figure 80: Blue trace is the normalized absorption spectrum of L3 ligand. Black trace is the excitation spectra, and red trace is the emission spectra of Nd(L3) complex. Green trace is the emission spectrum of Nd(L3) complex in a N$_2$–equilibrated solution. Excitation wavelength: 340 nm. Top: 10^{-5} M DCM/MeCN (1:1) solution; middle: 10^{-4} M DCM/MeCN (1:1) solution; bottom: solid state.

## 2.6.3 Europium(III) Complexes

Although the energy of the triplet state is lower than the emissive state of Eu^{3+}, the excitation of Eu^{3+} is still possible by energy transfer from the singlet state of the antenna.[166-167] Therefore, these studies were extended to Eu(III) complexes. The emission spectrum of Eu(**L2**-2H)NO$_3$ complex in a 10^{-5} M solution is not shown due to the weakness of emission. Upon excitation at 340 nm, the emission spectrum of Eu(**L2**-2H)NO$_3$ complex in a 10^{-4} M solution displays two prominent bands (Figure 81): 1) the band from 400 to 600 nm corresponding to the fluorescence from monomer and aggregate; 2) the structureless emission band in the range from 600 nm to 800 might be assigned to phosphorescence from the triplet state of NDI and Eu^{3+}.[100] The weakness of Eu^{3+} emission is due to the fact that the Eu^{3+} is easy to be reduced by phenolate in the excited state, giving rise to a low-lying LMCT state (phenolate to Eu^{3+}) which causes the non-radiative decay in solution.[168-169] It is also possible that energy transfer from the NDI to Eu^{3+} is rather inefficient. As the intersystem crossing is not favoured which has been discussed in the Gd(**L2**-2H)NO$_3$ complex, the observation of the phosphorescence from NDI might be due to the back energy transfer from the emissive state of Eu^{3+}.
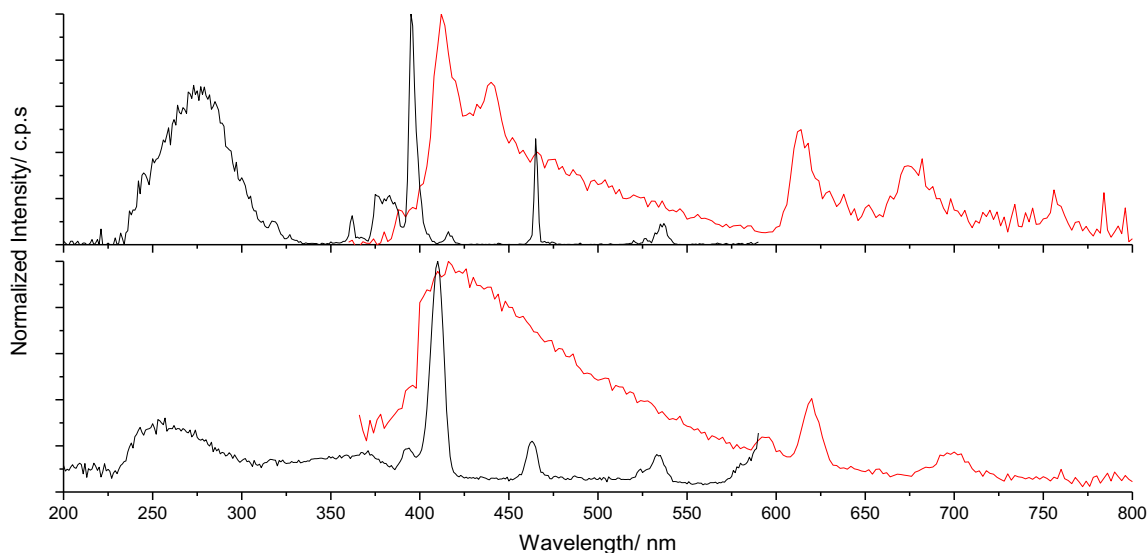
Figure 81: Black trace: the excitation spectra, $\lambda_{emission}$ = 690 nm; red trace: the emission spectra of the Eu(L2-2H)NO$_3$ complex, $\lambda_{excitation}$ = 340 nm. Top: 10^{-4} M MeCN solution; bottom: solid state.

Upon excitation at 340 nm, the emission spectrum of the Eu(**L2**-2H)NO$_3$ complex in the solid state presents a broad band spanning from 400 nm to 550 nm with europium(III) spike at 580 nm and a long tail which extends up to 730 nm. The excited-state lifetime was fitted to monoexponential decay when the emission wavelength is selected at 612 nm (Figure 82), giving a value of 203.3 µs (χ^2= 1.654).
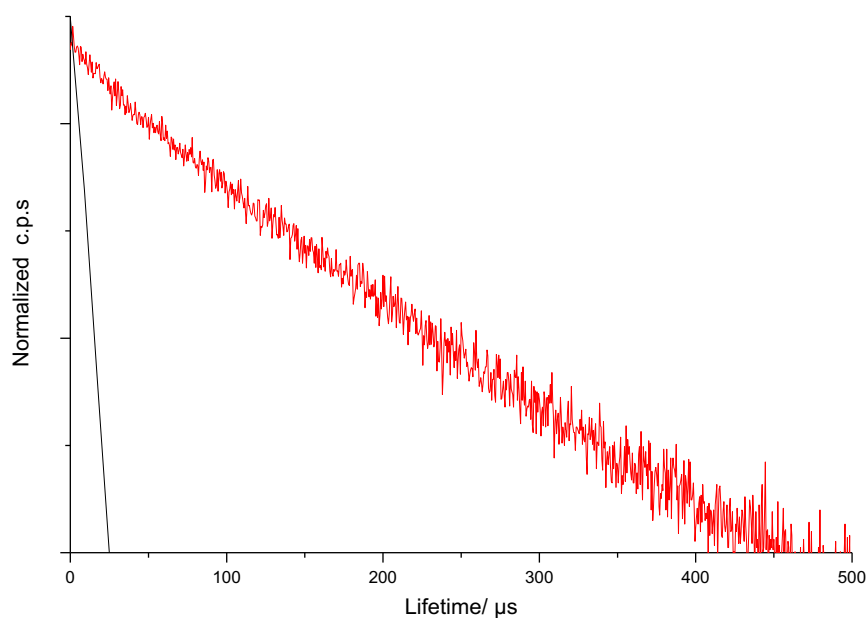
Figure 82: Lifetime decay of Eu(L2-2H)NO$_3$ complex in the solid state (red trace) and the instrument response function (black trace) at room temperature.

Upon excitation at 340 nm, the emission spectra of Eu(**L3**) complex in a mixture of DCM/MeCN(1:1)at room temperature show spikes at 580 nm, 615 nm and 690 nm in different media

(Figure 83). These peaks correspond to the $^5D_0 \rightarrow {}^7F_1$, $^5D_0 \rightarrow {}^7F_2$, and $^5D_0 \rightarrow {}^7F_4$ transitions of Eu^{3+}. Although the LMCT state has a strong quenching effect, the weak emission is still observed, probably due to the relatively high LMCT state of the europium complex of calixarenetetramide ligand **R1** (29400 cm^{-1}).[25]

The excitation spectra in the solution phase were recorded using the emission wavelength at 690 nm to avoid simultaneous excitation of aggregate. Interestingly, the excitation spectrum and normalised absorption spectrum show the same trend, suggesting that the energy transfer to the europium(III) is from NDI monomer. However, in the excitation spectrum of 10^{-4} M solution, the prominent peak at 400 nm is observed, probably caused by the inner filter effect or aggregates. [164-165]
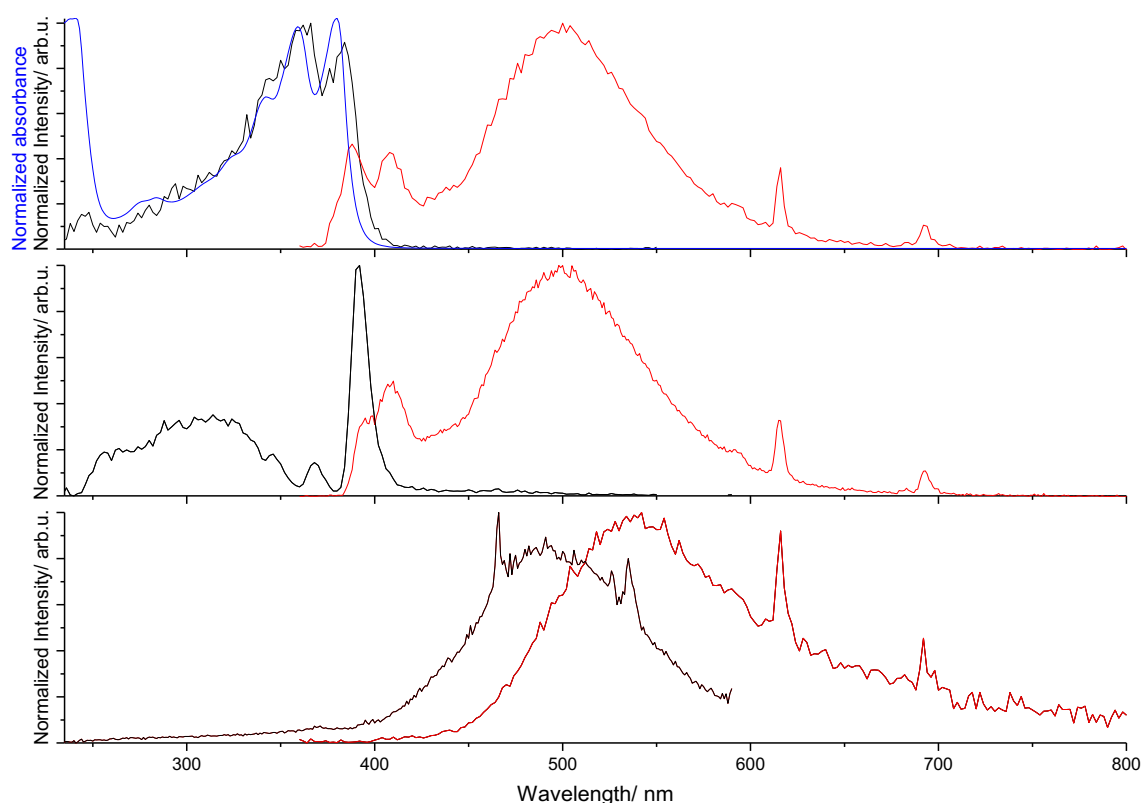
Figure 83: Black trace: the excitation spectra, $\lambda_{emission}$ = 690 nm; red trace: the emission spectra of the Eu(L3) complex, $\lambda_{excitation}$ = 340 nm; blue trace: the normalized absorption spectrum. Top: 10^{-5} M DCM/MeCN solution; middle: 10^{-4} M DCM/MeCN solution; bottom: solid state.

The excited-state lifetime decay of Eu(**L3**) complex under all conditions was fitted to monoexponential decay when the emission wavelength was selected at 690 nm (Figure 84). The observed lifetime was measured to be 50.1 μs in a 10^{-4} M solution at room temperature (χ^2= 1.431), 47.2 μs in a 10^{-5} M solution at room temperature (χ^2= 1.577), 663.4 μs in a 10^{-5} M solution at 77K (χ^2= 1.615) and 303.8 μs in the solid state (χ^2= 1.671). The residuals are provided in the appendix.
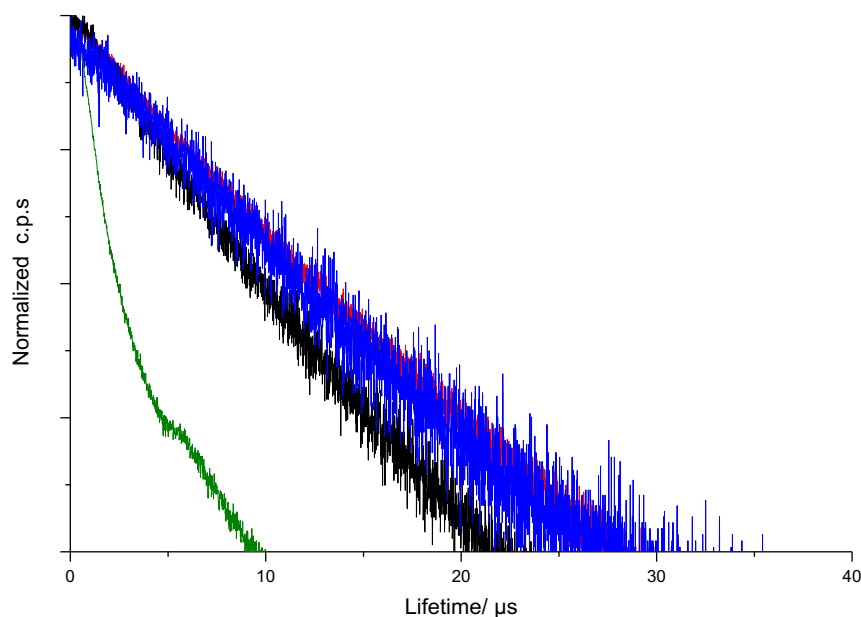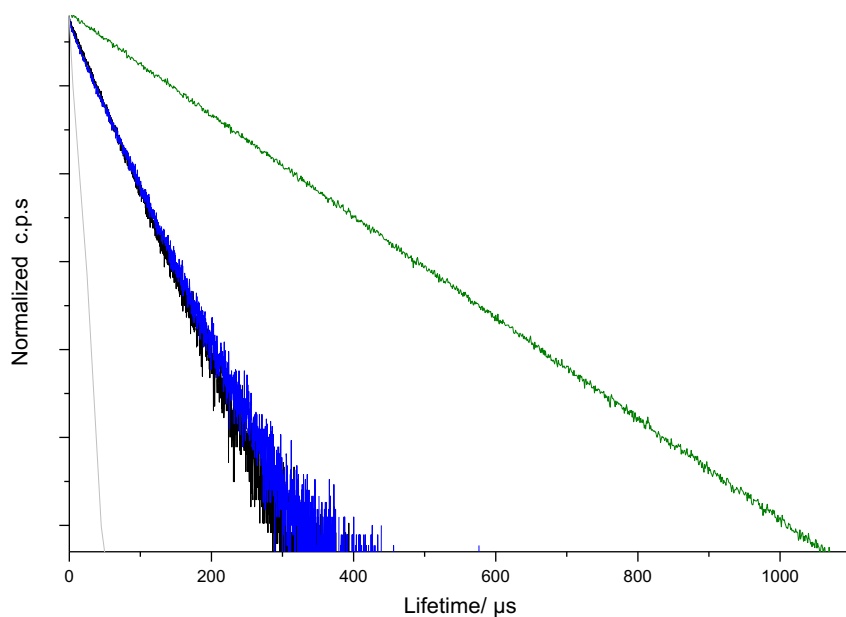
Figure 84: Lifetime decay of Eu(L3) complex in the 10^{-4} M DCM/MeCN (1:1), (black trace); 10^{-5} M DCM/MeCN (1:1), (blue trace); solid state (green trace) at room temperature. The grey trace is the instrument response function.

Table 9: A summary of the photophysical properties of Eu(III), Yb(III) and Nd(III) complexes.

Ligand/Complex	Concentration/Media	T_{obs} (µs)		ϕ_{Ln}^{L} (%)	
	λ			λ_{Ex} = 285 nm	λ_{Ex} = 340 nm
Yb(**L2**-2H)NO$_3$	DCM/MeCN 10^{-5} M (RT)	8.6	λ_{em} = 980 nm	0.2[a]	0.1[a]
	DCM/MeCN 10^{-4} M (RT)	8.4		-	-
	powder	9.7		-	-
Eu(**L2**-2H)NO$_3$	powder	203.3	λ_{em} = 690 nm	-	-
Yb(**L3**)	DCM/MeCN 10^{-5} M (RT)	8.9	λ_{em} = 980 nm	-	-
	DCM/MeCN 10^{-4} M (RT)	9.3		0.2 (MeCN)	-
	powder	10.7		-	-
Nd(**L3**)	DCM/MeCN 10^{-5} M (RT)	-	λ_{em} = 1060 nm	-	-
	DCM/MeCN 10^{-4} M (RT)	-		-	-
	powder	-		-	-
Eu(**L3**)	DCM/MeCN 10^{-5} M (RT)	50.1	λ_{em} = 690 nm	-	-
	DCM/MeCN 10^{-4} M (RT)	47.2		-	-
	powder	303.8		-	-

[a]Quantum yield is measured against the toluene solution of Yb(TTA)$_3$Phen ($\phi = 1.6\%$). A is the absorption peak in the UV-visible spectrum. Ex is the excitation wavelength.

2.6.4 Proposed Mechanism

In the previous section, we have shown that energy transfer to the lanthanoid centre occurs upon selective excitation of NDI of ligands in a 10^{-5} M solution. The absorption spectrum is analogous to its excitation spectrum when the emission wavelength is selected at the peak corresponding to transitions of lanthanoid emissive state to the ground states. Upon excitation via the NDI of Ln(**L3**) complex, the emission spectrum shows the blue fluorescence from the NDI monomer, the green fluorescence from NDI aggregate and characteristic Ln^{3+} luminescence.

In the case of Eu(**L3**) complex, the emissive states of aggregate and europium lie close in energy. In order to know whether there is energy transfer between them, the emission spectra of Gd^{3+} complex and Eu^{3+} complex as well as the lifetime were measured at room temperature and 77K. The Gd^{3+} complex is used as a model for comparison.

Table 10: The lifetime of the emission from aggregate in the Gd(L3) and Eu(L3) complex in a mixture of DCM/MeCN (10^{-5} M) at room temperature and 77K.

	T_{obs}		
	λ_{em} =410 nm (RT, 77K)	λ_{em} =500 nm ns (RT)	λ_{em} =500 nm ns (77K)
Gd(**L3**)	-	19	25 (45%), 54 (55%)
Eu(**L3**)	-	18	23 (48%), 53 (52%)

At room temperature, the lifetime of the aggregate peak was measured to be 19 ns (Gd^{3+}) and 18 ns (Eu^{3+}) (Table 10). At 77K, the decay was fitted to biexponential function with components of 25 ns (45%) and 54 ns (55%) in the Gd^{3+} complex and 23 ns (48%) and 53 ns (52%) in the Eu^{3+} complex. The values of the lifetime of aggregate peak are similar in the Gd^{3+} or Eu^{3+} complexes, so we rule out the energy transfer between aggregate and Eu^{3+}. The emission spectra and lifetime decay curves can be found in the appendix.

As the energy of the triplet state is lower than the emissive state of Eu^{3+}, energy transfer can not occur from the triplet state of NDI. Therefore, it is possible that the energy transfer to the Eu^{3+} is from the excited singlet state of NDI. The lifetime of peak at 410 nm corresponding to the emission from the excited singlet state of NDI was too short to be measured, even at 77K with our instrumentation. We need further evidence to confirm this sensitisation process.
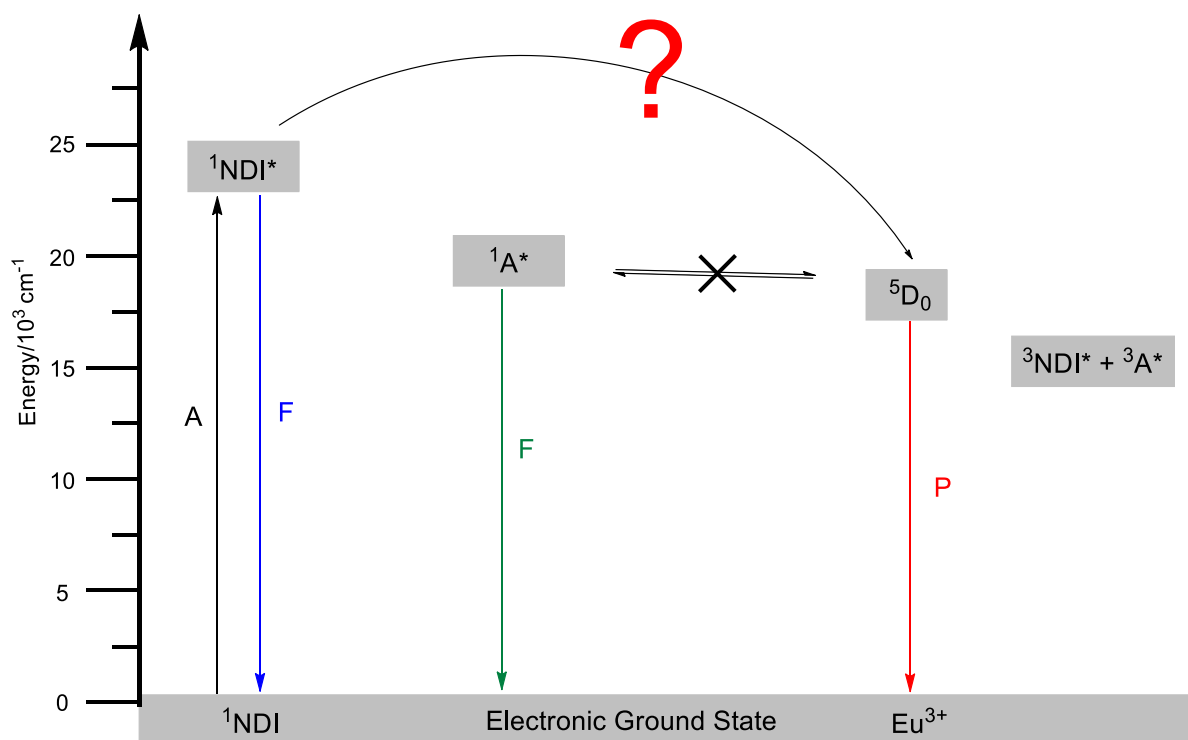
Figure 85: Photophysical state diagram for Eu(L3) complex at room temperature. "A" is absorption. "F" is fluorescence. "P" is phosphorescence.

The energy of the triplet state is higher than the emissive state of Nd^{3+} and Yb^{3+}. It is likely that the triplet state is involved in the sensitization mechanism. The Gd^{3+} complexes provide a heavy atom effect, but the intensity of phosphorescence peak is very low at 77K. In order to further investigate sensitisation mechanism, all of its corresponding complexes were investigated in a mixture of DCM/MeCN/10%EtI (10^{-5} M) at 77K. The Gd(**L3**) complex is again used as a model. The emission spectra of Gd(**L3**), Nd(**L3**) and Yb(**L3**) were recorded.

Upon excitation, the emission spectrum of Gd^{3+} complex shows fluorescence from the NDI monomer (410 nm) and aggregate (500 nm), along with the phosphorescence peaks above 500 nm (Figure 86). The addition of 10%EtI at 77K did not significantly change the lifetime of the aggregate peak and components at 500 nm. The lifetime was calculated to be 21 ns (44%) and 57 ns (56%). The lifetime of phosphorescence peak at 616 nm was calculated to be 3.6 ms (83%) and 878 µs (17%) (Table 11). The fluorescence peak at 410 nm can not be measured because it is shorter than the resolution of our fluorimeter. The emission wavelengths selected at 410 nm, 500 nm and 616 nm result in similar excitation spectra, suggesting the all emission bands are associated with the excitation of NDI monomer.

Table 11: The photophysical data of Ln(L3) complexes in a mixture of DCM/MeCN/10%EtI at 77K were summarised in the table.

	τ_{obs}		
	λ_{em} =410 nm	λ_{em} =500 nm ns	λ_{em} = 616 nm (ms), (µs)
Gd(**L3**)	-	23 (44%), 54 (56%)	3.6 (83%), 878 (17%)
Nd(**L3**)	-	21 (44%), 58 (56%)	3.6 (83%), 878 (17%)
Yb(**L3**)	-	22 (44%), 53 (56%)	2.9 (82%), 624 (18%)

The TCSPC decay of emission from aggregate and triplet state of NDI are shown in appendix.
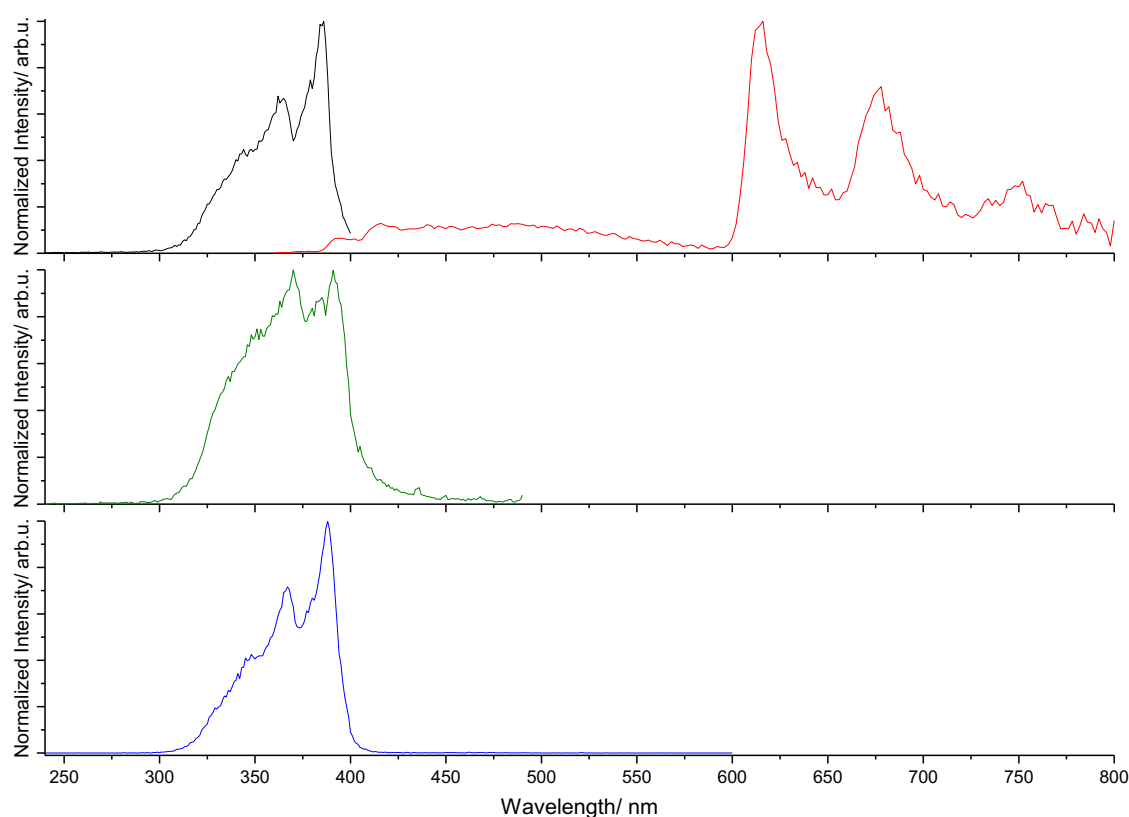
Figure 86: Emission spectrum of Gd(L3) complex in a mixture of DCM/MeCN/10%EtI at 77K (red trace), 10⁻⁵ M. Excitation spectra: λem = 410 nm (black trace); λem = 500 nm (green); λem = 616 nm (blue).

The emission spectrum of Nd(**L3**) complex follows the same trend that presented in the Gd(**L3**) complex in the UV-visible region (Figure 87). A small peak tailing off into NIR region corresponds to phosphorescence from NDI in the NIR region, and the characteristic Nd^{3+} luminescence is also observed. The excitation spectra are similar regardless of selected emission wavelength including emission wavelength at 1060 nm. Therefore, we can conclude that NDI can sensitise Nd^{3+} metal-

centered emission, concurrently generating fluorescence from NDI monomer, aggregate and phosphorescence from NDI.

The values of lifetime of two components at 500 nm do not significantly decrease in comparison to the Gd(**L3**) complex, suggesting that there is no energy transfer taking place between aggregate and Nd^{3+}. The value of lifetime of peak at 616 nm is exactly the same. These results suggest the energy transfer to the Nd^{3+} centre is not from the triplet state of NDI as well. Therefore, the energy transfer to the Nd^{3+} is neither from the aggregate nor from the excited triplet state of NDI. This suggests the energy transfer to Nd^{3+} centre might be from the excited singlet state of NDI. But we still can not draw a definitive conclusion due to the lack of lifetime of the peak at 340 nm.
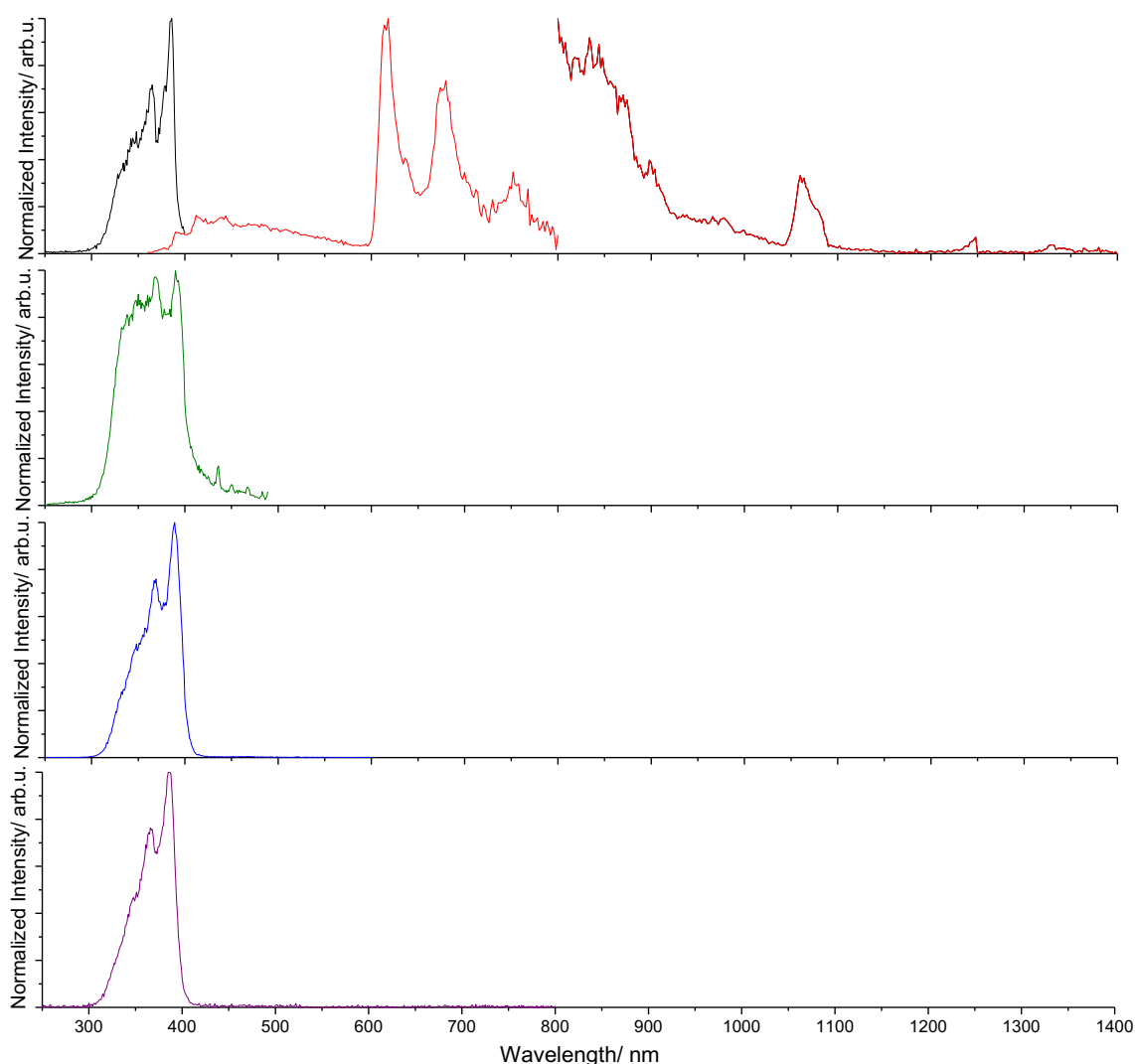
Figure 87: Emission spectrum of Nd(L3) complex in a mixture of DCM/MeCN/10%EtI at 77K (red trace), 10^{-5} M. Excitation spectra: λ_{em} = 410 nm (black trace); λ_{em} = 500 nm (green trace); λ_{em} = 616 nm (blue trace); λ_{em} = 1060 nm (purple trace).
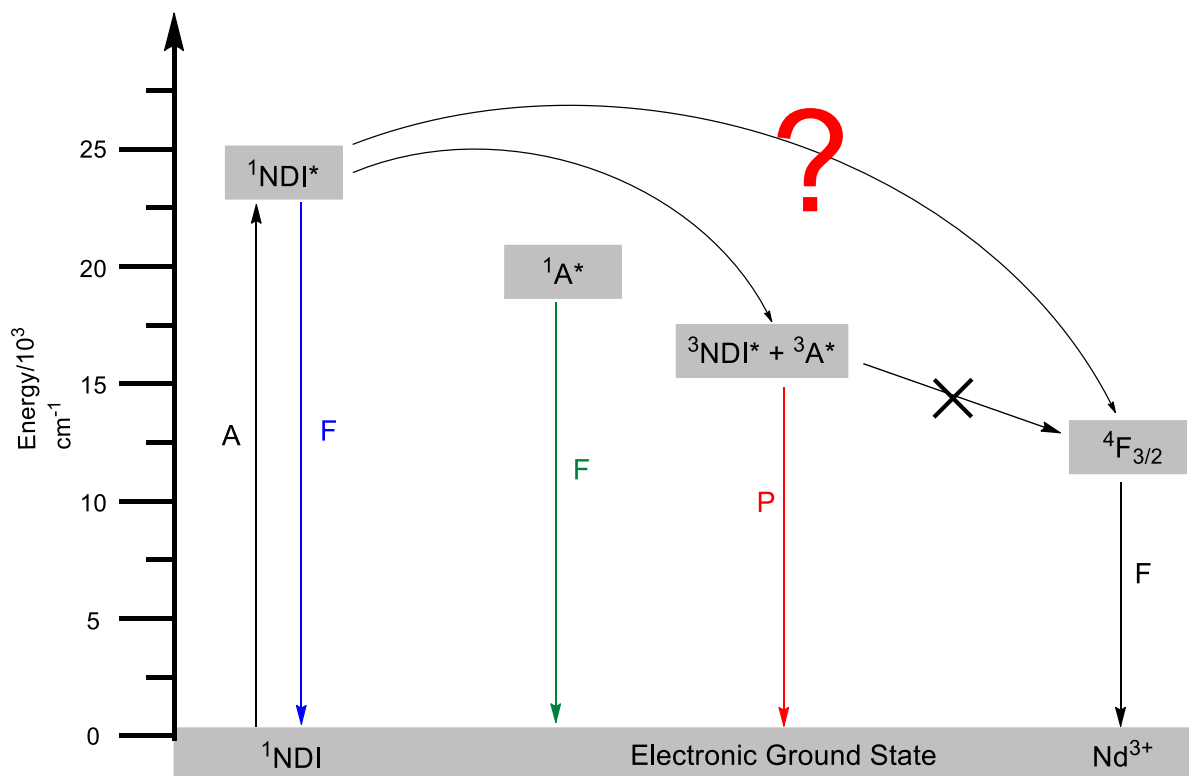
Figure 88: Photophysical state diagram for Nd(L3) complex in a mixture of DCM/MeCN/10EtI at 77K (10^{-5} M). "A" is absorption. "F" is fluorescence. "P" is phosphorescence.

In the case of Yb(**L3**) complex in DCM/MeCN/10%EtI at 77K, the emission spectra show a significant change (Figure 89). The most noticeable difference is that the structureless band around 500 nm is more visible. The value of the lifetime (22 ns, 53ns) and the ratio of these two species (82%, 18%) are similar to those of Gd^{3+} complex, indicating that the aggregate does not transfer to the Yb^{3+} centre. While the lifetime of phosphorescence peak is shortened to 624 μs (18%)/ 2.9 ms (82%) in comparison to that observed for the Nd^{3+} or Gd^{3+} complex. The shorter lifetime in comparison to that observed in Nd^{3+} and Gd^{3+} complex suggests that the energy transfer to the Yb^{3+} centre takes place via the triplet state of NDI.
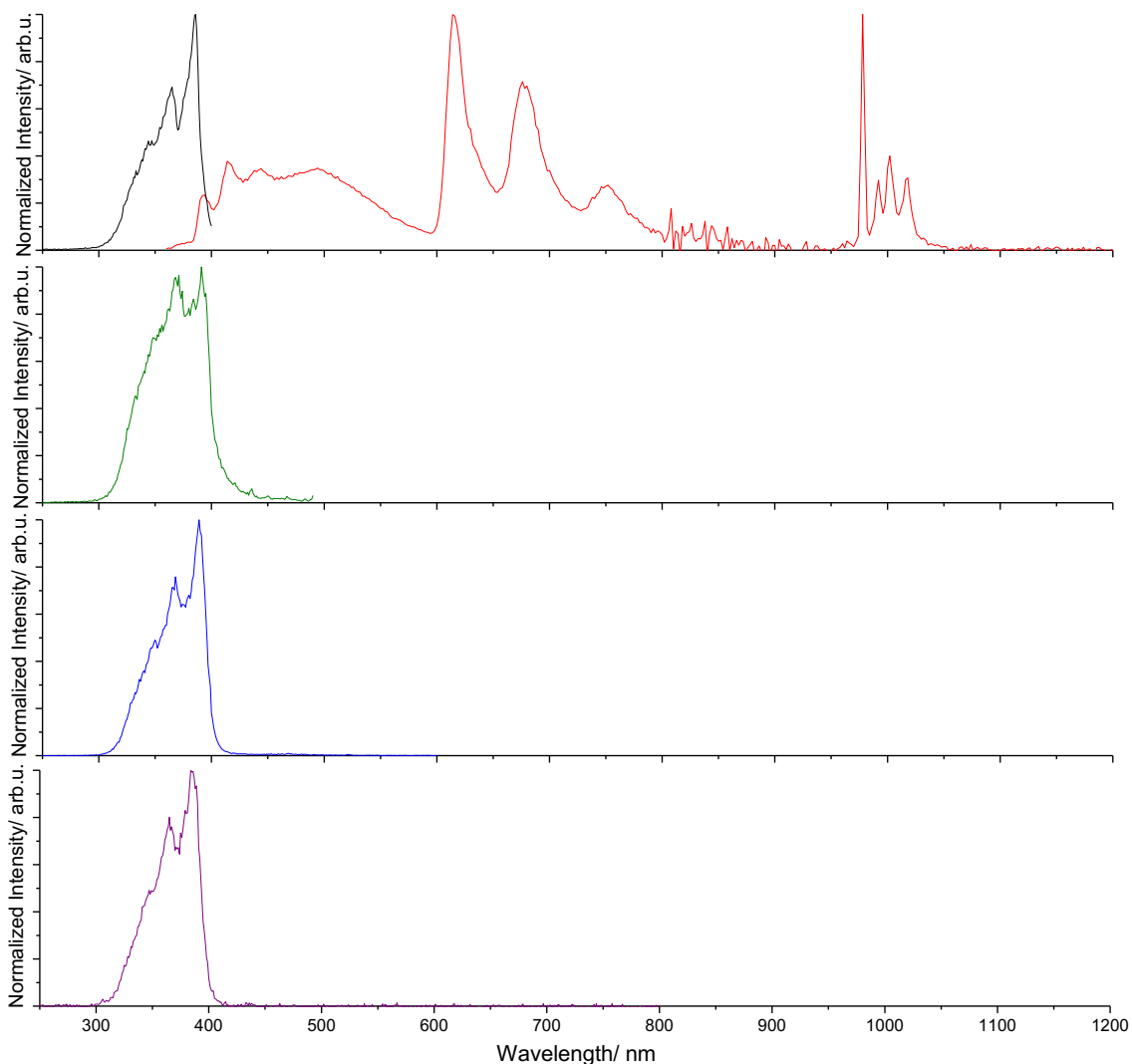
Figure 89: Emission spectrum of Yb(L3) complex in a mixture of DCM/MeCN/10%EtI at 77K (red trace), 10^{-5} M. Excitation spectra: λ_{em} = 410 nm (black trace); λ_{em} = 500 nm (green trace); λ_{em} = 616 nm (blue trace); λ_{em} = 980 nm (purple trace).

We confirmed this result by concentration-controlled experiment and measured the emission spectra of Yb_x(**L3**) complex (x = 0 ~ 1) with a different molar ratio of Yb^{3+} to ligand at 77K (Figure 90). The intensity of the Yb^{3+} luminescence increases with the increasing molar ratio of Yb^{3+}, but the intensity of the phosphorescence decreases.

It is worth mentioning that the intensity increases in the case of $Yb_{0.2}$(**L3**) complex in comparison to the free ligand. It is due to the heavy metal effect of Yb^{3+} inducing extra phosphorescence from NDI. The intensity of peak around 500 nm also increases steadily with increasing molar of Yb^{3+} due to the formation of aggregate. We can not measure the fluorescence lifetime from the NDI monomer, so we can not rule out the energy transfer between the excited singlet state of NDI and the Yb^{3+}.
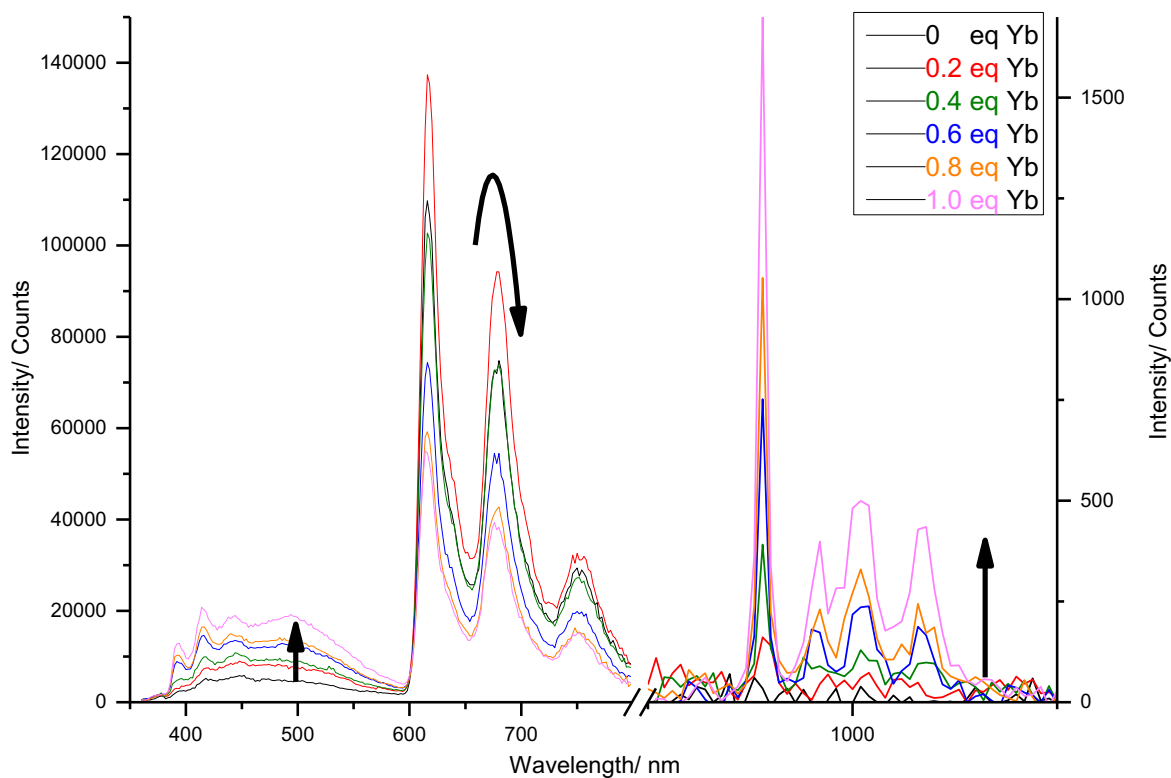
Figure 90: Emission spectra of Yb$_x$(L3) complex (x = 0 ~ 1) in a mixture of DCM/MeCN/10% EtI at 77K (10^{-5} M).
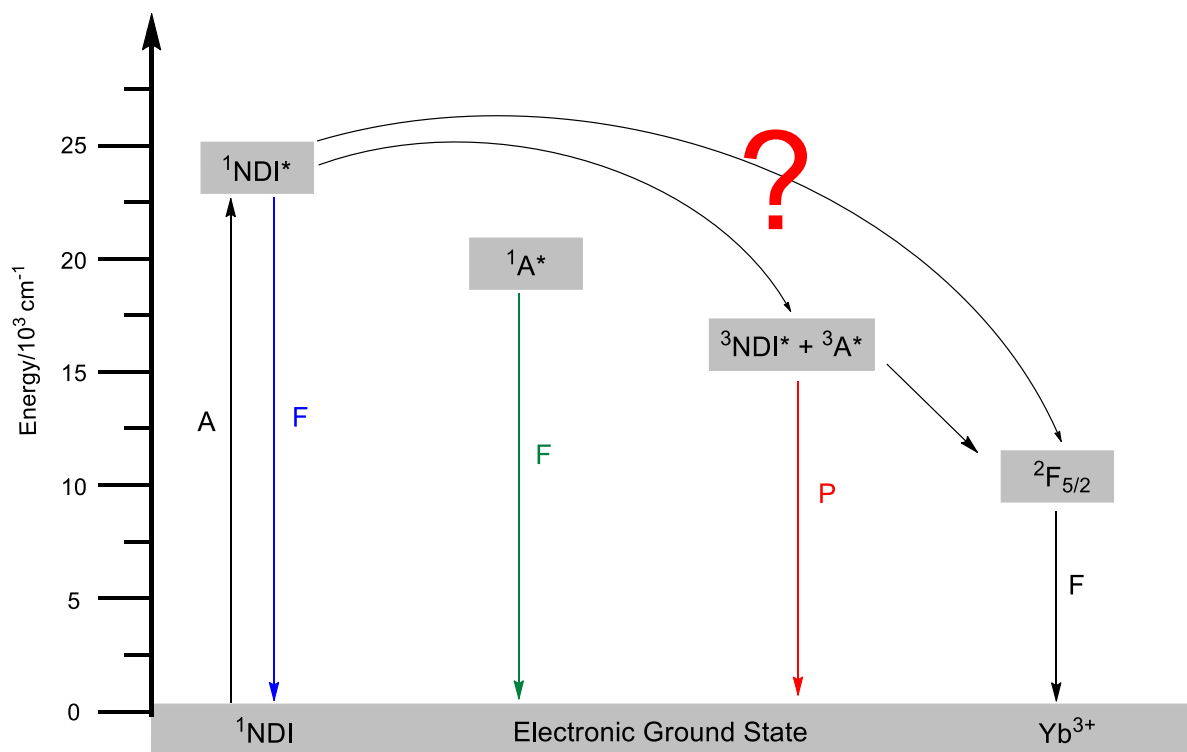
Figure 91: Photophysical state diagram for Yb(L3) complex in a mixture of DCM/MeCN/10EtI at 77K (10^{-5} M). "A" is absorption. "F" is fluorescence. "P" is phosphorescence.

The attempt to measure the emission spectrum of Yb(**L2**-2H)NO$_3$ complex in a mixture of DCM/MeCN/10%EtI was not successful. Nevertheless, we still can partly propose the sensitization mechanism of the complex. Firstly, the lack of phosphorescence peak in the emission spectra of the Gd^{3+} complex (or Gd^{3+} ions in excess) at room temperature and at 77K (Figure 71) indicates the intersystem crossing process is not facilitated and the triplet state is not populated. This is further evidenced by the lack of a peak corresponding to the emission from singlet oxygen in an air-equilibrated solution in the case of the Yb(**L2**-2H)NO$_3$ complex (Figure 75, top). We also tried to measure the photoluminescence quantum yield of the Yb^{3+} complex in N$_2$- and air-equalibrated solutions. The overall PLQY was measured to be <1% in both cases. Secondly, the emission from the aggregate is not observed, making it easier to propose the sensitization mechanism. Therefore, the energy transfer to the Yb^{3+} via the ligand **L2** as an antenna might be only from the singlet state of NDI.
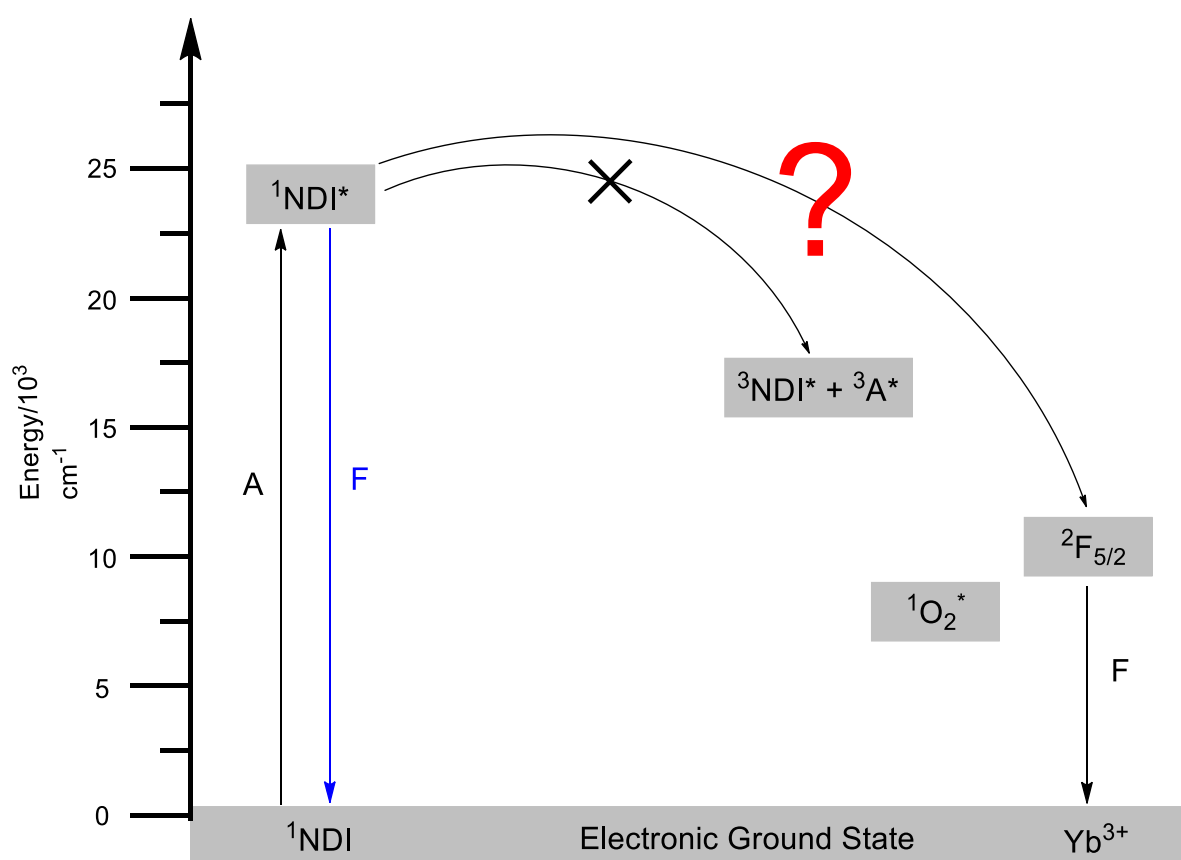
Figure 92: Photophysical state diagram for Yb(L2-2H)NO$_3$ complex in a mixture of DCM/MeCN/10EtI at 77K (10^{-5} M). "A" is absorption. "F" is fluorescence. "P" is phosphorescence.

2.7 Electrochemical Properties

The reduction of neutral naphthalenetetracarboxylic diimide has been studied in an aprotic solvent such as DMF.[106] However, it is discussed above that lanthanoid complexes were not formed in DMF with these calixarenes. The solubility of the ligand **L2** is very low in a MeCN solution. Therefore, the spectroelectrochemical experiments were conducted in a mixture of dichloromethane and acetonitrile

(1:1) containing 0.1 M Et$_4$NClO$_4$ as the electrolyte. Both of the NDI radical anions and dianions are not stable, and acetonitrile is employed to avoid protonation of the radicals. Reduction of NDI in MeCN was carried out using Pt electrodes.

The cyclic voltammogram was recorded, and spectroelectrochemical experiments were conducted (Figure 93). Ligand **L2** consists of two NDI units, and two or four redox processes should be involved theoretically. However, three electrochemically reversible redox processes are observed in cyclic voltammogram with reduction potential at -938 mV, -1044 mV and -1468 mV. All redox systems exhibit ideal reversibility. The first and second reduction process (two, one electron charge transfer process) correspond to the reduction of neutral NDI to NDI radical anions. The separation between these two reduction peaks was large, indicating the interaction or electronic communication between two NDI moieties. The difference between the first reduction process and second reduction process suggests that the second NDI is significantly harder than the first one probably because of intramolecular enhanced coulombic repulsion in the negatively charged ligand. This result is consistent with the previously reported NDI dimer and NDI triangular prism.[102, 170] In the third reduction process, the reduction potential at -1468 mV corresponds to the formation of two dianions. However, these peaks at lower potential are not dramatically split into two or closely spaced and cannot be resolved. This indicates that after generating two dianions, the conformation changes resulting may result in alleviation of negative-negative electron repulsion.

The spectroelectrochemical studies also show increasing absorbance of four vibronically structured absorption peaks in the range from 400 – 800 nm upon gradual decrease of potential from -700 mV to -1200 mV. These peaks are attributed to the $D_o{\rightarrow}D_n$ transition of NDI radical anion.[106] Further lowering the applied potential below -1300 nm shows these absorption peaks are less visible. These peaks are replaced by two new peaks around 550 nm and 609 nm, corresponding to the absorption of NDI radical dianions.[106] Analysis of the absorbance as a function of the applied potential also confirms formation of two NDI radical anions and two radical dianions.

The electrochemical behaviours of the ligand **L3** were investigated under the same conditions as the ligand **L2**. The cyclic voltammogram is similar to the ligand **L2**, and it reveals the three reduction peaks at 949, 1043 and 1486 mv. UV-vis spectra obtained accompanying reduction of ligand **L3** are similar to those observed in the case of ligand **L2** as well. These results suggest the fully alkylated tetraamide does not significantly affect the electrochemical properties. The details are shown in Figure 94.
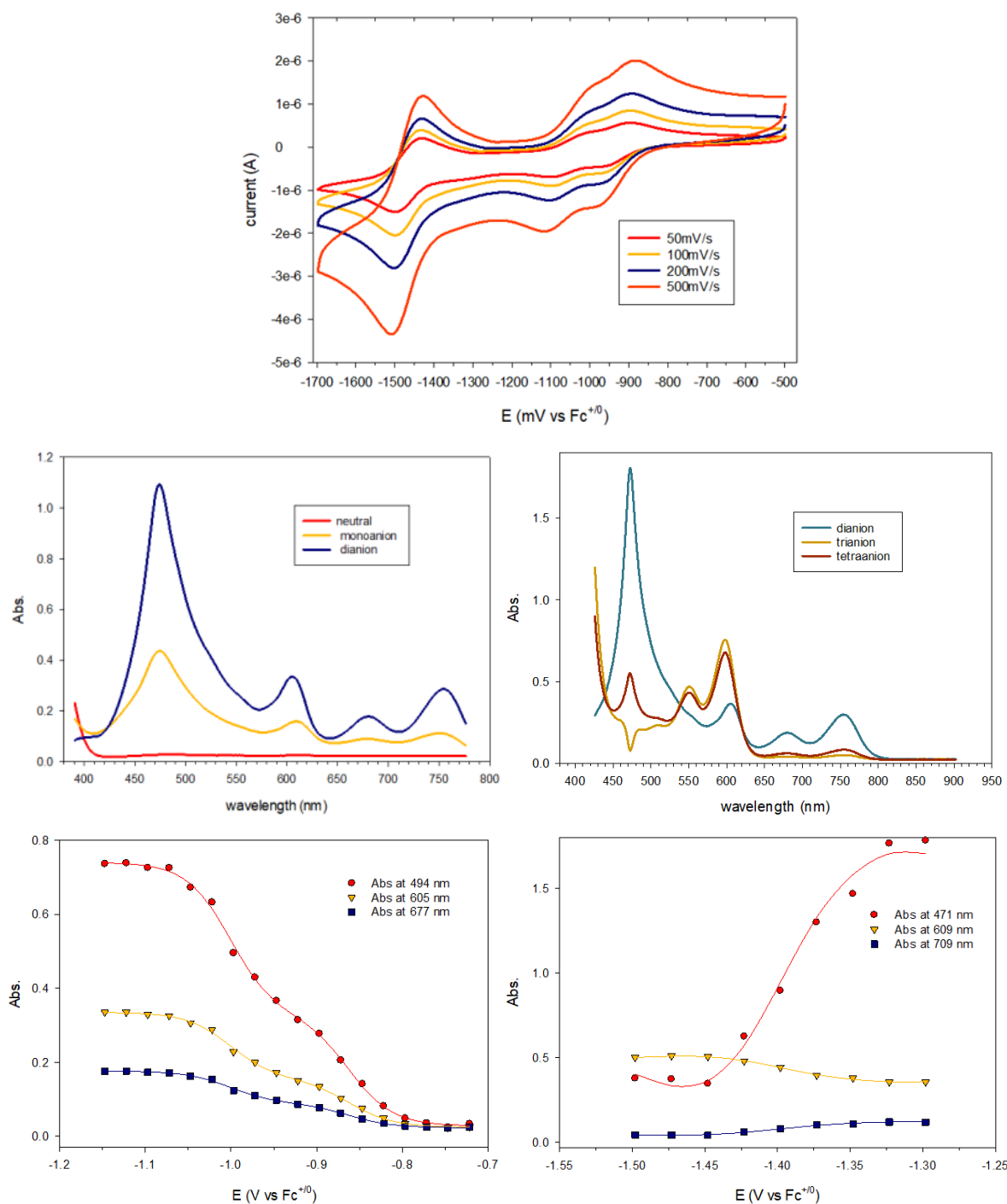
Figure 93: Top: cyclic voltammograms of ligand L2 in a mixture of DCM/MeCN containing 10^{-2} M Et$_4$NClO$_4$. Work electrode: 0.5 mm radius Pt electrode. Middle left: absorption spectrum in a cell in a mixture of DCM/MeCN (1:1) for the neutral ligand L2 (red trace), radical monoanion (yellow trace) and radical dianions (blue). Middle right: absorption spectrum in a cell for the radical dianions (green trace), trianion (yellow trace) and tetraanion (brown trace). Bottom left: absorption during the conversion of ligand L2 and formation of radical dianion observed in the potential range of -0.7 V to -1.05 V. Bottom right: absorption during the conversion of radical dianion and formation of trianion and tetranion observed in the potential range of -1.3 V to -1.5 V.

94
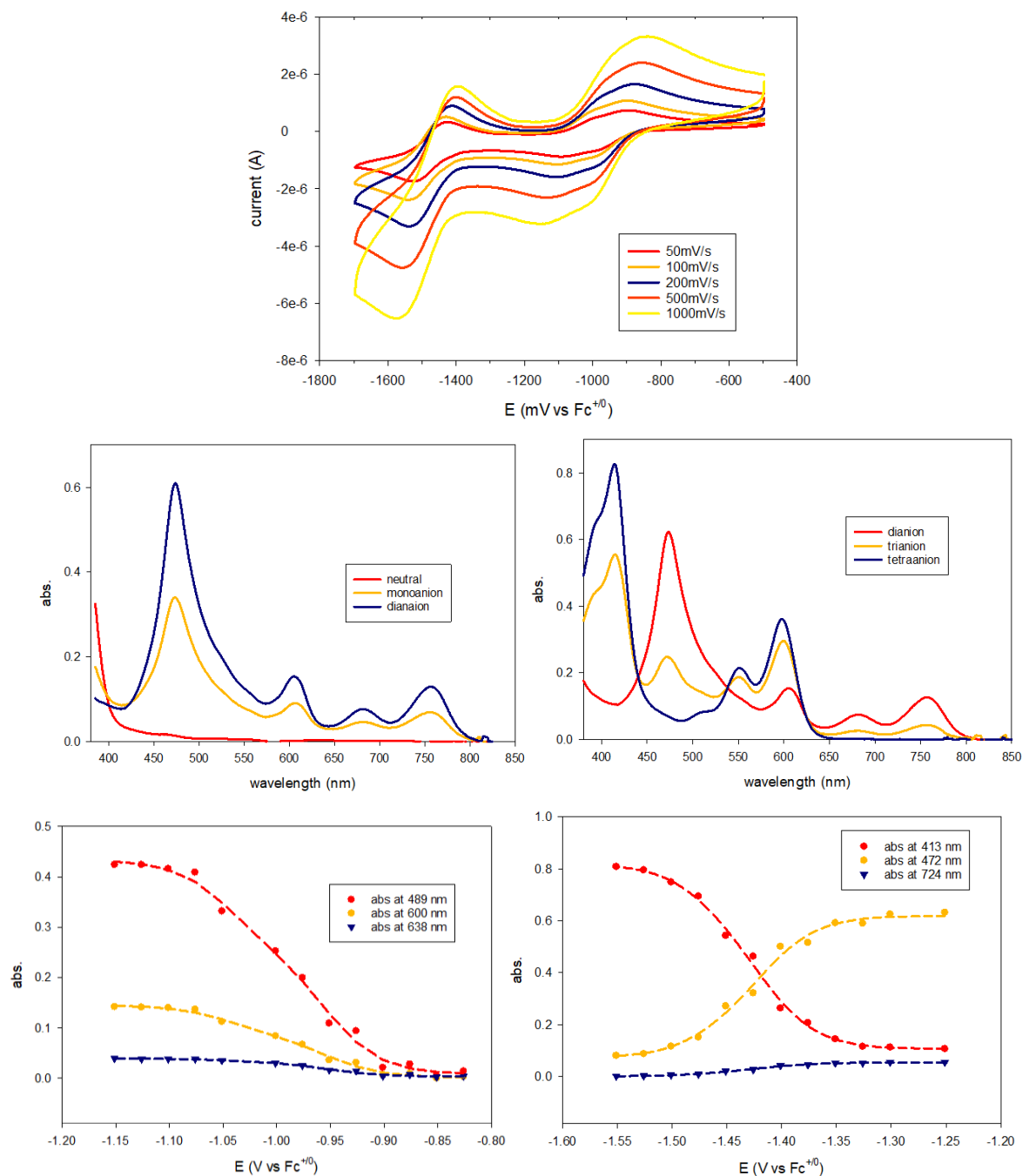
Figure 94: Top: cyclic voltammograms of ligand L3   in a mixture of DCM/MeCN (1:1) containing 10⁻² M Et₄NClO₄. Work electrode: 0.5 mm radius Pt electrode. Middle left: absorption spectrum in a cell in MeCN for the neutral ligand L3(red trace), radical monoanion (yellow trace) and radical dianions (blue). Middle right: absorption spectrum in a cell for the radical dianions (red trace), trianion (yellow trace) and tetraanion (blue trace). Bottom left: absorption during the conversion of ligand L3 and formation of radical dianion observed in the potential range of -0.7 V to -1.05 V. Bottom right: absorption during the conversion of radical dianion and formation of trianion and tetranion observed in the potential range of -1.3 V to -1.5 V.

R = CH$_3$, R' = H, n = 3
R = H, R' = CON(CH$_2$CH$_3$)$_2$, n = 2
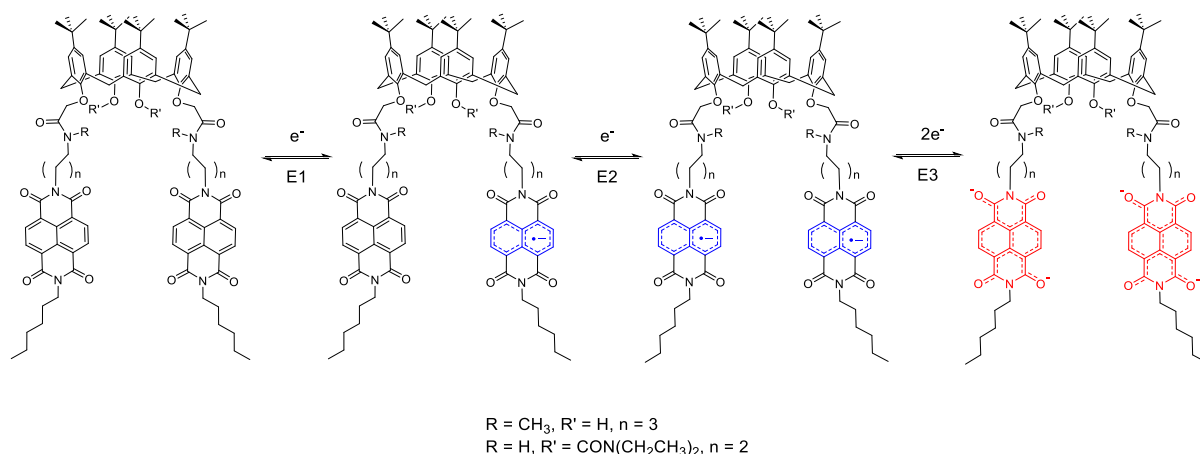
Scheme 17: Sequential reduction of L2 and L3.

2.8 Conclusion

Three bis-NDI substituted calixarene ligands, **L1**, **L2** and **L3**, have been successfully synthesised and fully characterised. In the case of **L1**, complexation did not take place even under basic conditions. Based on single crystal X-ray structure determination and NMR studies, it was proposed that intramolecular hydrogen bonds at the lower rim of the calixarene inhibited metal binding. The combination of the ligand **L3** with lanthanoid precursors [Yb^{3+}(DMSO)$_3$(NO$_3$)$_3$ or Eu^{3+}(DMSO)$_3$(NO$_3$)$_3$] in the presence of triethylamine resulted in the crystallization of mononuclear complexes with a formulation of Ln(**L2-**2H)NO$_3$. The bis-O-alkylation of the phenolic units of **L1** resulted in the fully lower rim alkylated **L3** ligand, which proved to be suitable for lanthanoid coordination.

The photophysical properties of all ligands have been studied, and the photophysical properties of lanthanoid complex with **L2** and **L3** have been also studied. Based on these absorption and emission properties, the energy transfer processes were able to be proposed. In particular, the triplet energy of NDI of **L2** and **L3** ligands was found to be around 16233 cm^{-1}. The energy transfer from the excited state of NDI to the emissive state of Yb^{3+} was successful in the case of Yb(**L2**-2H)NO$_3$ complex. Although the energy of the triplet state was found to be high enough above the emissive state of Yb^{3+}, the triple state is not populated. Therefore, the energy transfer to the Yb^{3+} might be from the excited singlet state of NDI. The overall quantum yield was very low. The characteristic Ln^{3+} metal-centred emission was not observed with the Nd(**L2**-2H)NO$_3$, suggesting the NDI of ligand **L2** can not be used as a sensitizer for Nd^{3+}.

The sensitisation of Eu^{3+}, Yb^{3+} and Nd^{3+} metal-centred emission in the UV-visible and NIR region was successful via the NDI of **L3** ligand, achieving a key aim of the project confirming that the NDI moiety can act as antenna in a molecular lanthanoid complex. The size of the particles in solution increased upon addition of Ln^{3+} ion, and it was concluded that emission from an aggregate was being observed. There was, however, no observable energy transfer between the aggregate and lanthanoid. One of the sensitisation pathways of Yb^{3+} complex has been studied: energy transfer from the excited triplet state of NDI. The use of 10%EtI to induce the phosphorescence of NDI opened up a possibility to better understand the energy transfer processes. More work is needed to be carried out to understand

the energy transfer from the singlet state of NDI and propose the whole sensitization mechanism. In a 10^{-4} M mixture of DCM/MeCN, the inner filter effect and aggregates might make the sensitization mechanism more complicated in both cases. More work can be done to understand the photophysical properties and aggregation behaviours in a concentrated solution.

Electrochemical properties showed three reduction peaks, caused by the electronic communication between two NDI moieties during the reduction to the NDI monoanion. Spectroelectrochemical studies confirmed that the NDI radical anion and dianion could be formed with **L2** and **L3**. There is no significant difference of electrochemical properties between bis-NDI substituted calixarene diamide and tetraamide. Most importantly for the aim of the project, this work confirmed that the radical anion can be accessed in these new calixarene derivatives, leading to the potential to explore the anion as an antenna ligand.

3 Lanthanoid Complexes of Mono-NDI Substituted Calixarene

3.1 Introduction

Bis-NDI substituted calixarene ligands has been discussed in the previous chapter. In this chapter, the aim of this project is to synthesise mono-NDI substituted calixarene ligands, and structural and photophysical properties of mono-NDI-substituted calixarene will also be investigated in comparison to the bis-substituted ligands. Based on the photophysical studies, some energy transfer pathways will be proposed. This chapter first focuses on the synthesis of mono-NDI substituted calixarene derivatives (**L4**, **L5** and **L6**). All these calixarene ligands are fully alkylated tetraamides which should bind more strongly to lanthanoid compared to disubstituted derivatives. Complexation studies are also simplified by the fact that deprotonation of the ligand does not need to be taken into consideration. The structural characterisation of these three new ligands was achieved using the same techniques as those of the previously discussed disubstituted ligands (Chapter 2). Synthesis of their corresponding sodium and yttrium complexes will be discussed. The photophysical properties were studied in detail by absorption and emission spectroscopy. A further goal was to expand the investigation of how the hydrogen bond on the lower rim of calixarene and the methylene spacer influences the photophysical properties of the ligands and their lanthanoid complexes.

Ligand	R	n
L4	$-\xi-H$	2
L5	$-\xi-CH_3$	3
L6	$-\xi-CH_2CH_2CH_3$	6
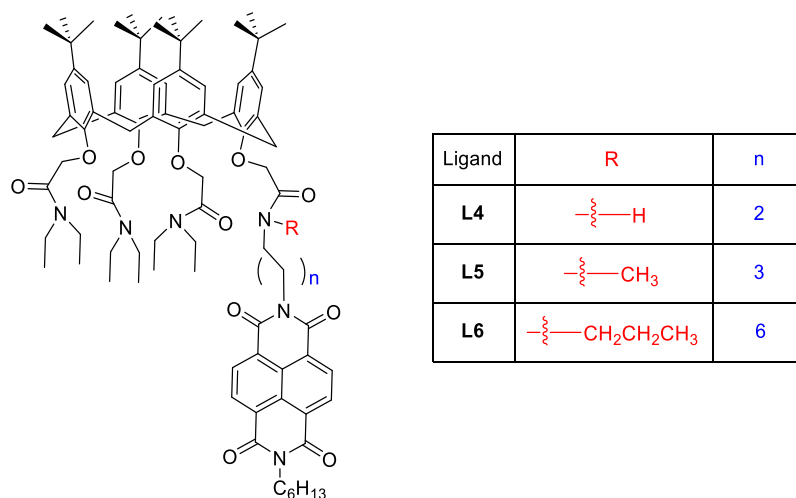
Figure 95: Target tetraamide calixarene derivatives, L4, L5 and L6.

Energy transfer to the Yb^{3+}, Nd^{3+} as well as Eu^{3+} from the NDI moiety was the focus of these investigations. The excited-state lifetime value and quantum yield were calculated. To quantify interaction between lanthanoid and ligand, spectrophotometric titration experiments were carried out. Experiments on the lifetime measurement to determine the number of solvent molecules coordinating to the lanthanoid were conducted by comparing measurements in nondeuterated and deuterated solvents.

3.2 Synthesis

The general synthetic route for the preparation of mono-NDI substituted calixarene derivatives is shown below. The new mono-NDI substituted calixarene derivatives (**L4**, **L5** and **L6**) were synthesised following a similar procedure for the disubstituted ligands. The monocarboxylic acid-functionalised calixarenetrisamide (compound **C4**) was further reacted with amine-functionalised NDI derivatives.
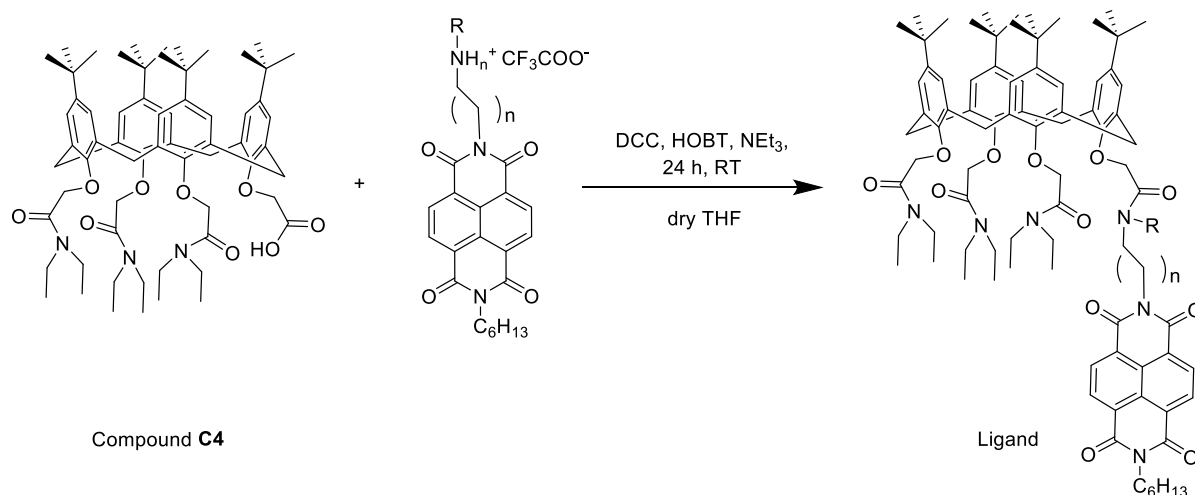
Scheme 18: General procedure for the synthesis of ligands L4-L6 (see Figure 95)

3.2.1 Synthesis of Mono-carboxylic Acid Functionalised Calixarenetriamide

The parent calixarene was reacted with 1 equivalent of ethyl bromoacetate and 1.2 equivalents of cesium fluoride as a base in DMF at 40 $^{\circ}$C under N_2 atmosphere for six hours (Scheme 19). Cesium fluoride is a weak base used to ensure that the singly deprotonated calixarene is the dominant species in solution, although bis-substituted calixarene and the parent calixarene could still be found in the product mixture even after optimisation of reaction conditions. Despite this, these impurities were readily removed by recrystallisation from a DCM/MeOH solvent mixture, and the reaction proceeded in 81% yield.

The reaction between the mono-ester calixarene and 2-chloro-*N,N*-diethylacetamide in a dry acetonitrile solution in the presence of sodium iodide and potassium carbonate resulted in mono-ester functionalised calixarenetrisamide. It was notable that the solvent should not be contaminated by water, as further hydrolysis to carboxylic acid could happen. The reactivity of 2-chloro-*N,N*-diethylacetamide is relatively lower than the equivalent bromo or iodo-functionalized alkylating reagents which are not commercially available. Therefore, an alternative pathway to the nucleophilic substitution reaction was achieved through the addition of sodium iodide to induce the Finkelestein reaction, forming the iodo-functionalised alkylating reagent *in situ*. However, the addition of sodium iodide or potassium iodide was disadvantageous to the isolation of pure ligands because the added metal cations could interact

strongly with the calixarene to form the metal complex. Since mono-ester functionalised calixarenetrisamide was an intermediate, further purification involving removing the Na⁺ ion was planned to be done after hydrolysis of the ester group.
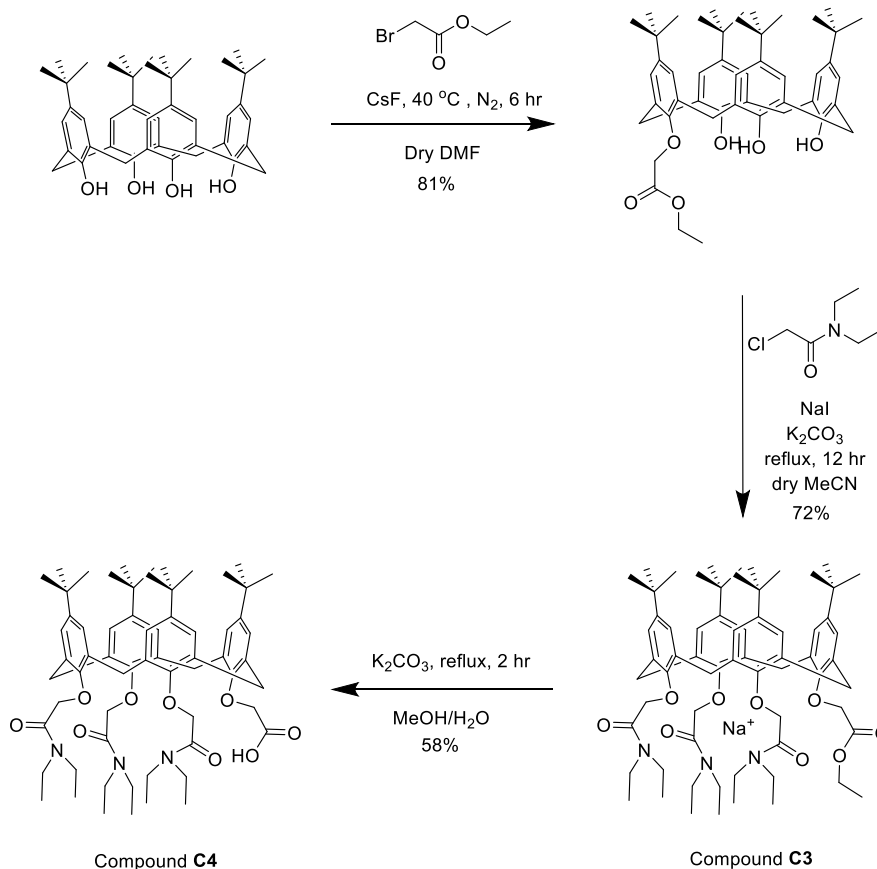
Scheme 19: Synthesis of the compound C4.

Hydrolysis could be achieved using potassium carbonate as a base in a mixture of methanol and water under reflux. The reaction mixture was cooled to room temperature, and after the pH was adjusted to 2, mono-carboxylic acid functionalised calixarenetrisamide was successfully isolated. As mentioned above, the resulting yellow solid was contaminated with metal cations (most likely sodium and possibly some potassium) as shown by the unexpected complexity of the NMR spectra. Removal of metal ions was done through heating the impure material in a mixture of water and methanol at 60 °C. After 2 hours, the methanol was removed at reduced pressure, leaving the metal cations and some highly coloured impurities dissolved in the water. The pure desired product was collected via vacuum filtration. To the best of our knowledge, the compound **C4** has not been reported previously. While characterising the compound by ¹H NMR and ¹³C NMR spectroscopy, it was found that the chemical shift of compound **C4** did not remain constant in CDCl₃. This was likely caused by the trace amount of acid in CDCl₃, leading to peak shifts both in the ¹H NMR spectrum and ¹³C NMR spectrum over time. Therefore, the DMSO-d₆ was used for NMR analysis as it does not contain acid, and the ¹H spectrum was the same before and after 24 hours. It was also found that the compound **C4** decomposed and was not suitable for long-term storage at ambient temperature, based on the change in the chemical shift and presence

of news peaks in the ^{1}H NMR spectrum in comparison with that of the freshly prepared compound. Therefore, it was found best to freshly prepare compound **C4** or refrigerate it under nitrogen.

The peak at 11.42 ppm is assigned to the carboxylic acid proton in the ^{1}H NMR spectrum (Figure 96). There are two singlet peaks (peak *1* and *4*) and two doublet peaks (peak *2* and *3*) with a total integration ratio of 8, which are assigned to protons of aromatic rings. The symmetry gives four hydrogen environments of the OC**H₂** group: multiplet peak (*9a* + *9b*) around 4.8 ppm, singlet peak *9d* at 4.56 ppm and a doublet peak *9c* at 4.50 ppm. The peak *6a* and *8a* correspond to the axial Ar-C**H₂**-Ar protons. Equatorial Ar-C**H₂**-Ar protons have a chemical shift around 3.2 ppm (peak *5e* and *7e*). The multiplet peak labelled *10* and *10'* refers to CON(C**H₂**CH₃)₂ protons with an unexpected integration ratio of 20 due to the presence of water. The peak *11* and *11'* attributed to CON(CH₂C**H₃**)₂ protons situate in the middle of two peaks corresponding to *tert*-butyl protons in the aliphatic region.
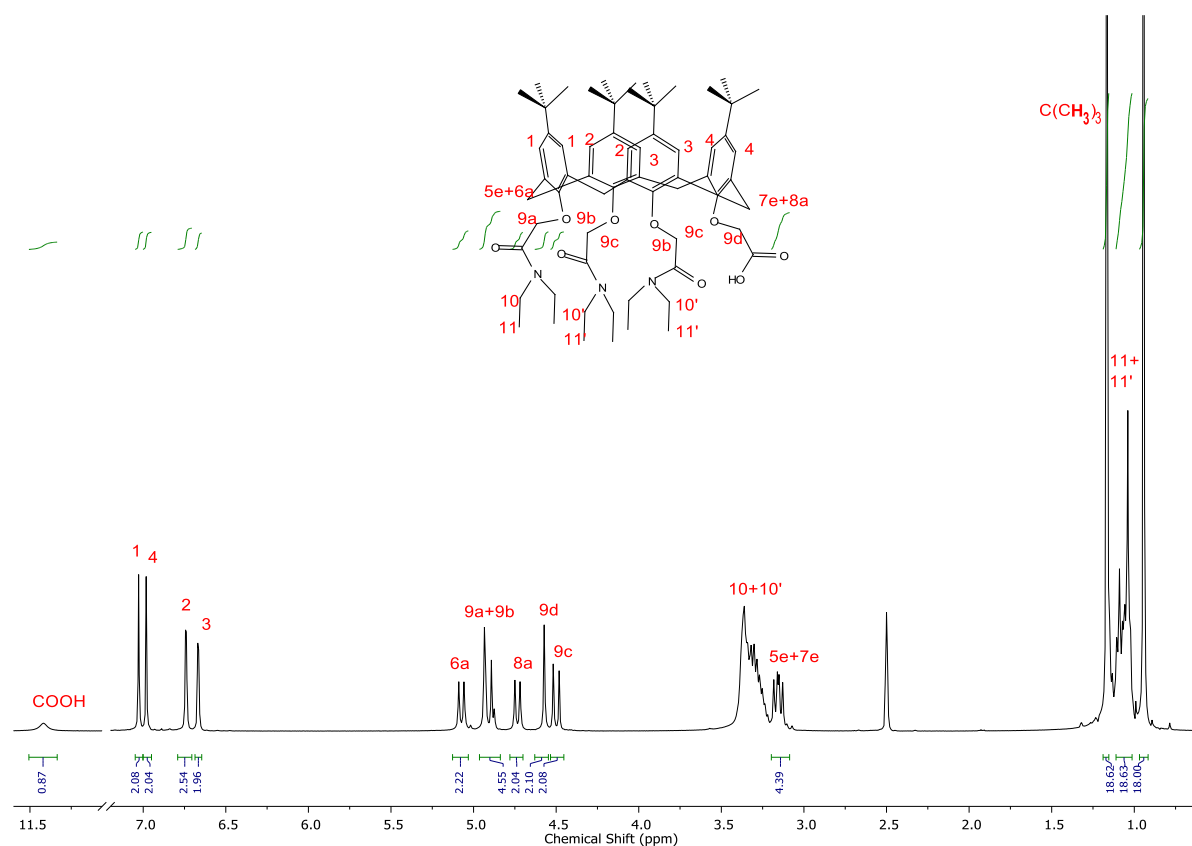
Figure 96: ^{1}H NMR spectrum of the compound C4 in DMSO-d₆ recorded at 400 MHz.
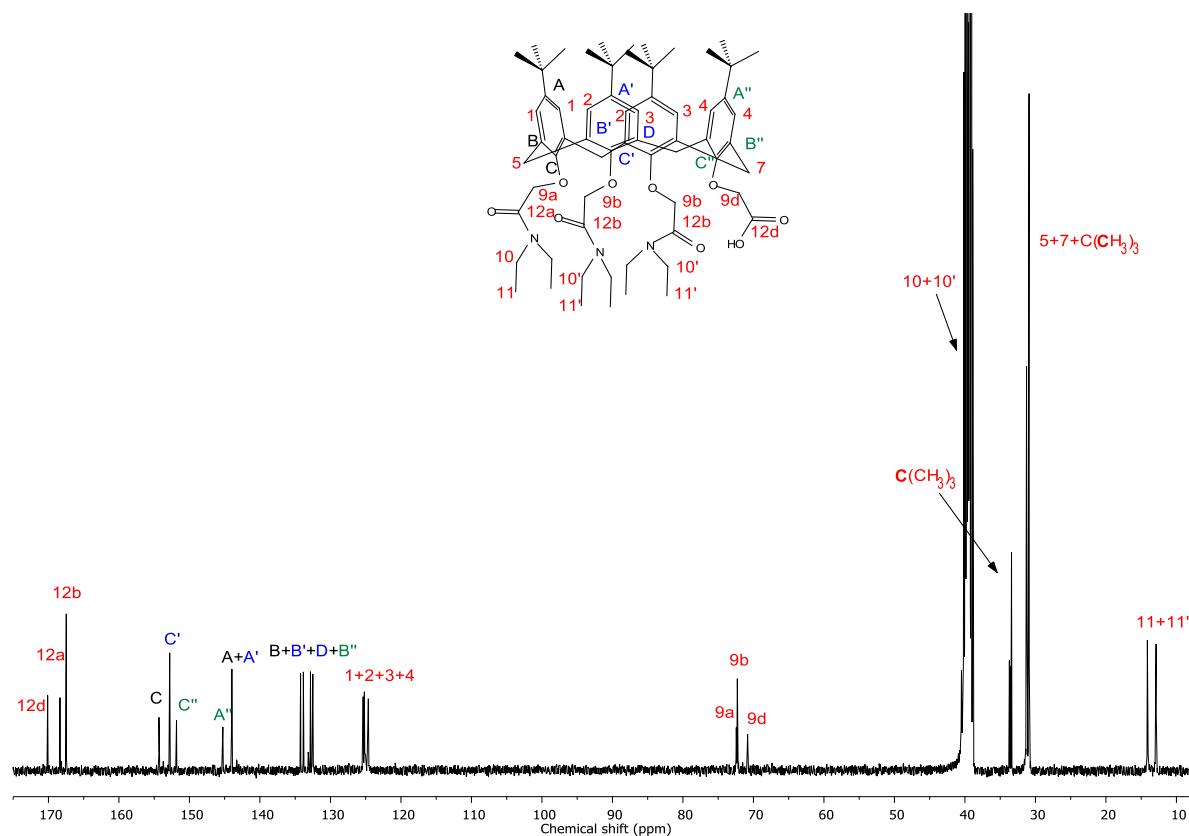
Figure 97: ^{13}C NMR spectrum of the compound C4 in DMSO-d₆ recorded at 100 MHz.

The ^{13}C NMR spectrum reveals three carbon environments of carbonyl groups (peak *12a*, *12b* and *12d*), indicating that there is only one plane of symmetry (Figure 97). Peaks corresponding to the Ar-**C** carbons appear in the range of 155 - 130 ppm. More specifically, the quaternary carbons being close to the "OCH₂" have a chemical shift of 154.33 ppm (peak *C*), 152.80 ppm (peak *C'*) and 151.84 ppm (peak *C''*). Quaternary carbons linking to the *tert*-butyl groups have a chemical shift of 145.26 ppm (peak *A''*), 144.02 ppm (peak *A*) and 143.98 ppm (peak *A'*). There are four carbon environments of quaternary carbon linking to the Ar-CH₂-Ar groups in the range of 135 ppm to 130 ppm (peak *B,B', D* and *B''*), but the specific carbon cannot be assigned due to the low resolution of the HMBC spectrum. The peak *1*, *2*, *3* and *4* correspond to the Ar-**C**H carbons. Three peaks appearing around 72 ppm are attributed to the O**C**H₂. It's notable that the peak *10* and peak *10'* are overlapped with the peak of DMSO, which is supported by the cross peak in the HSQC spectrum. The quaternary carbons of *tert*-butyl groups have a chemical shift around 33 ppm. The peaks of the primary carbon of *tert*-butyl groups are overlapped with peaks of the carbons of methylene bridges, appearing around 31 ppm. The rest of peaks in the upfield are assigned to tertiary carbons of CON(CH₂**C**H₃)₂. The number of all carbon environments cannot be counted due to the overlapped peaks, but the assigned peaks are in the expected range.

3.2.2 Synthesis of Mono-NDI Substituted Calixarene Ligands

The ligand **L4** was synthesised following the procedure used for bis-NDI substituted ligands with some slight modifications (Scheme 20).
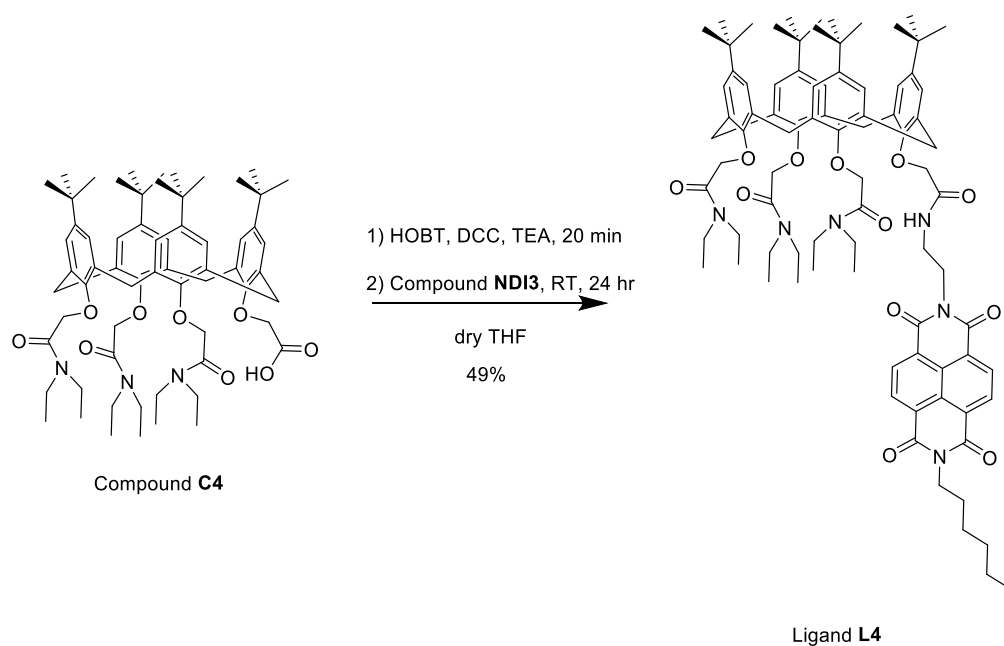
Scheme 20: Synthesis of the ligand L4.

The compound **C4** was made to react with the HOBT, DCC and compound **NDI3** in the presence of triethylamine in dry THF. Attempts to purify the desired product by silica column were unsuccessful. Although the TLC plate displayed the major band with a R_f value of 0.5 in a mixture of DCM/MeOH 20:1, the yellow bands were immobile on the silica column. Increasing the polarity of eluent to 5:1 had no impact, suggesting that the compound might be bound to silica. Using Brockman I Neutral aluminium oxide pretreated by diluted acid instead of silica proved to work well. The ^{1}H NMR analysis suggests the ligand **L4** is isolated with metal cation impurities after purification by column chromatography (Figure 98, bottom). The commercially available neutral aluminium oxide contains small amounts of impurities, such as Na_2O, and Fe_2O_3. These impurities may potentially interact with ligand **L4** as the calixarene tetraamide is a strong ionophore. Nevertheless, the total combined integration ratio matches well with the expected structure of the ligand. This suggests the impurities from the neutral alumina have some interaction with the free ligand, resulting in the change in chemical shift. A final purification step to remove impurities was therefore performed by dissolving the product in a mixture of water and methanol and heating to reflux, followed by precipitation induced by cooling and the addition of water.
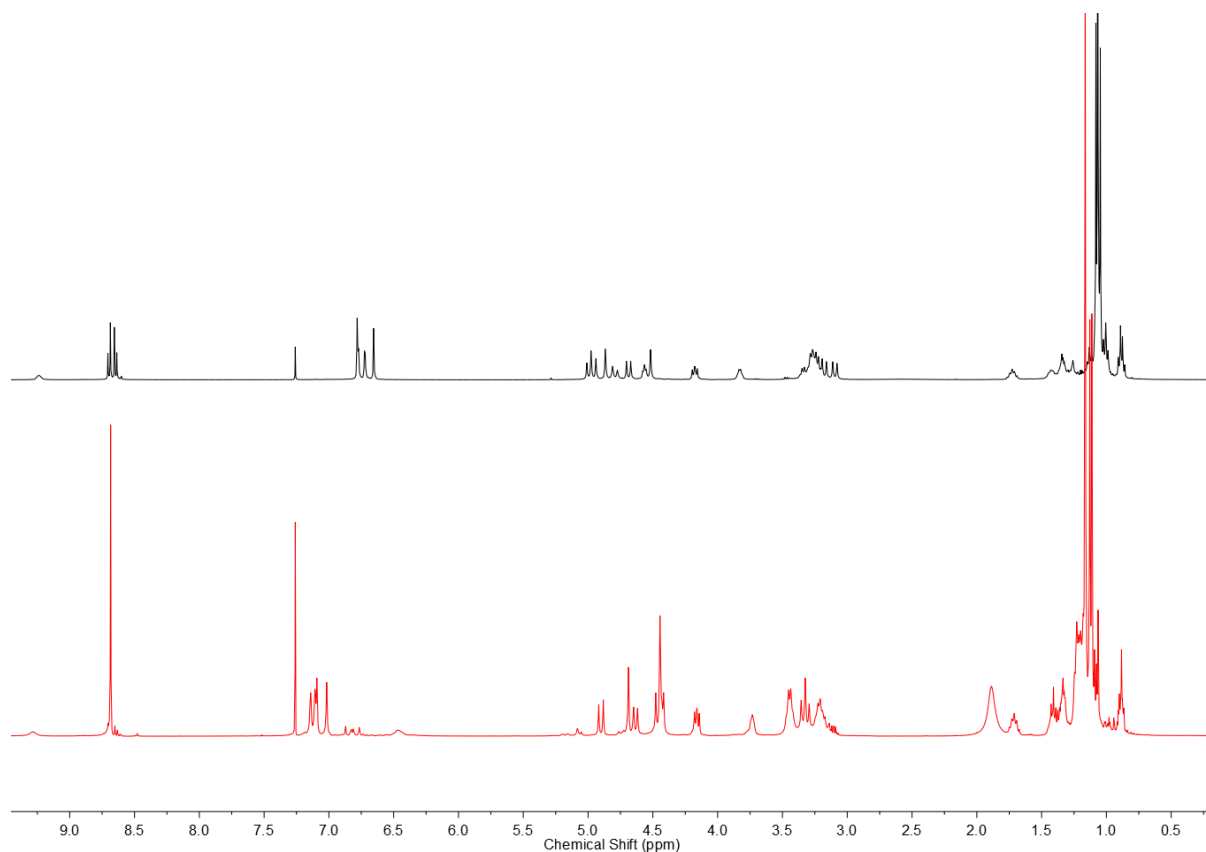
Figure 98: Top: ¹H NMR spectrum of the ligand L4 in CDCl₃ recorded at 400 MHz; Bottom: ¹H NMR spectrum of the ligand L4 with metal cation impurities in CDCl₃ recorded at 400 MHz.

The ^{1}H NMR spectrum matches well with the proposed structure (Figure 99). The ^{1}H NMR spectrum of **L4** shows a pair of doublet peaks (peak *H* and peak *G*) appearing at 8.74 ppm with an integration of four which is expected for the mono-NDI substituted calixarene. The absence of a proton of the carboxylic acid and the appearance of a peak corresponding to the secondary amide group at 9.20 ppm also supports the formation of the **L4** ligand. Three peaks of aryl groups appearing at 6.78 ppm (multiplet peak *1 + 2*), 6.72 ppm (doublet peak *3*) and 6.65 ppm (singlet peak *4*) are observed to be consistent with the asymmetric substitution pattern of this calixarene. The ^{1}H NMR spectrum reveals four expected peaks of OCH₂ group: the peak *9a* and peak *9d* corresponding to OCH₂ groups are two singlet peaks at 4.88 ppm and 4.52 ppm; the splitting pattern of the peak at 4.78 ppm is a doublet (peak *9c*); the peak *9b* is overlapped with the peak of the axial Ar-C**H₂**-Ar hydrogens (peak *6a*) lying around 5 ppm. The peak *8a* at 4.68 ppm indicates another hydrogen environment of axial Ar-C**H₂**-Ar protons. Peaks corresponding to methylene groups of the CON(C**H₂**CH₃)₂ group (peak *10 and 10'*) are together

with the peak of equatorial Ar-C**H₂**-Ar hydrogens (peak *5e* and *7e*). These protons have a chemical shift around 3.3 ppm. The multiple peaks with an integration ratio of 48 (36 + 12) around 1.1 ppm are assigned to protons of *tert*-butyl groups and methyl groups of $CON(CH_2CH_3)_2$ group (peak *11 and 11'*). All protons for the rest of the NDI hydrogens are assigned with reference to the assignment of peaks in the ligand **L1**.
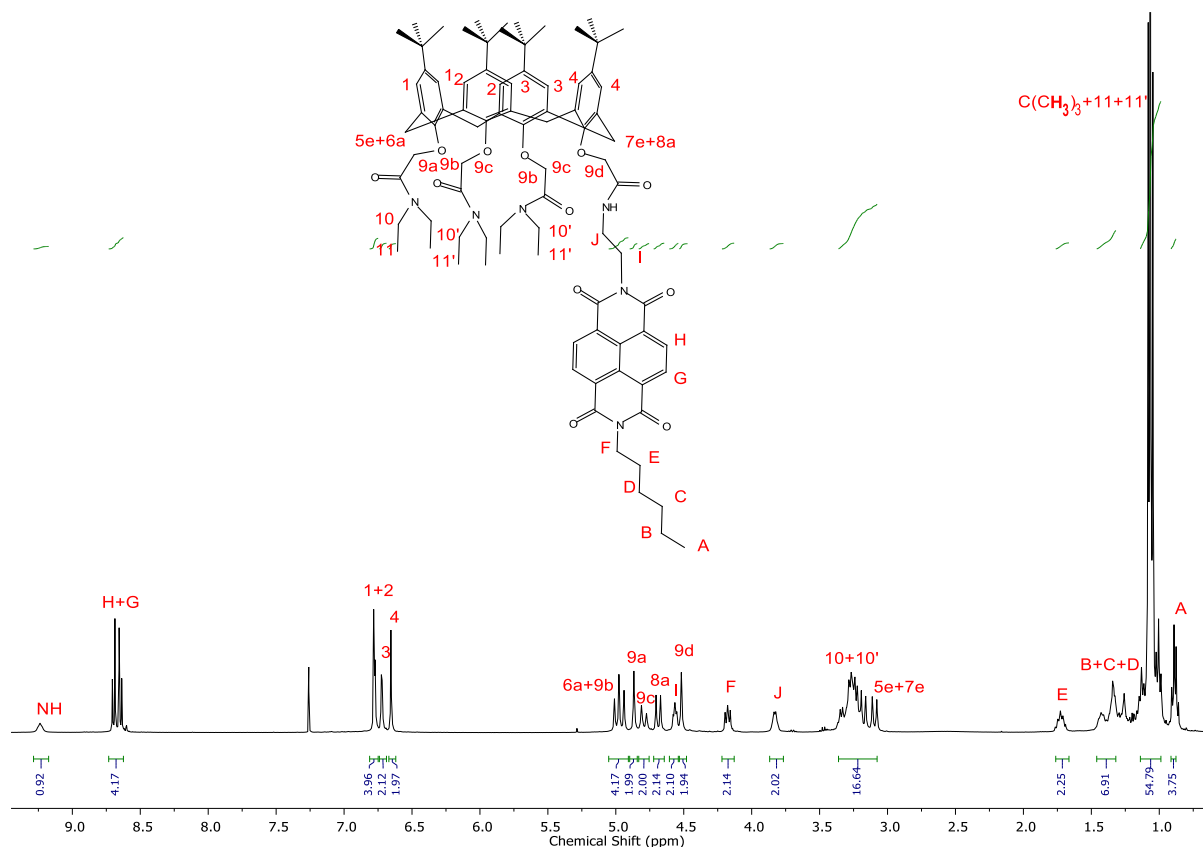
Figure 99: ¹H NMR spectrum of the ligand L4 in CDCl₃ recorded at 400 MHz.

The ligand **L4** was also characterised by ¹³C NMR experiments with the assistance from 2D NMR techniques, including HSQC and HMBC for the assignment of peaks (Figure 100). The quaternary carbon of the secondary amide group resonates at 171.50 ppm (peak *12d*). Quaternary carbons of $\mathbf{C}ON(CH_2C\mathbf{H}_3)_2$ have a chemical shift around 169 ppm (peak *12a* and peak *12b*). The quaternary carbons of NDI-**C**O have a chemical shift around 163 ppm. Peaks appearing in the range of 154-132 ppm are assigned to all carbons of aromatic rings, including NDI-**C**H (peak *H* and peak *G* around 130 ppm), Ar-**C**H (peak *1, 2, 3* and *4* around 126 ppm) and Ar-**C.** The analysis based on the HMBC spectrum can distinguish signals for tertiary carbon environments of aromatic rings, but the peak of the specific tertiary carbon on each ring are overlapped with the carbon in the same position of the other aromatic rings. Tertiary carbons of NDI-**C** have a chemical shift around 127 ppm, but the specific carbon cannot be assigned. There are three carbon environments of O**C**H₂, and the peak *9d*, *9a* and 9b have a similar chemical shift at 74.64 ppm, 71.67 ppm, 71.61ppm, respectively. The peak *9d* is assigned to the carbon of the O**C**H₂ group attached to the secondary amide group. All carbon peaks (*I*, *F*, *J*, 10 and *10'*) of methylene groups linking to nitrogen atoms appear in the range of 41- 38 ppm. The **C**(CH₃)₃ carbons

have the chemical shift of 33.90 ppm and 33.95 ppm. Peaks around 31 ppm relating to carbon environments of Ar-CH_2-Ar (peak *5* and *7*) are overlapped with the peak of C(CH_3)$_3$ and N(CO)$_2$CH$_2$CH$_2$CH$_2$$CH_2CH_2CH_3$ (peak *C*). Carbon peaks in the further upfield correspond to the rest of the hexyl chain (peak *A*, *B*, *D* and *E*) and CON(CH$_2$$CH_3$)$_2$ (peak *11*). Because some peaks overlap each other and some specific carbons cannot be assigned, the total number of carbon environments cannot be counted. All carbon peaks are in the expected range.
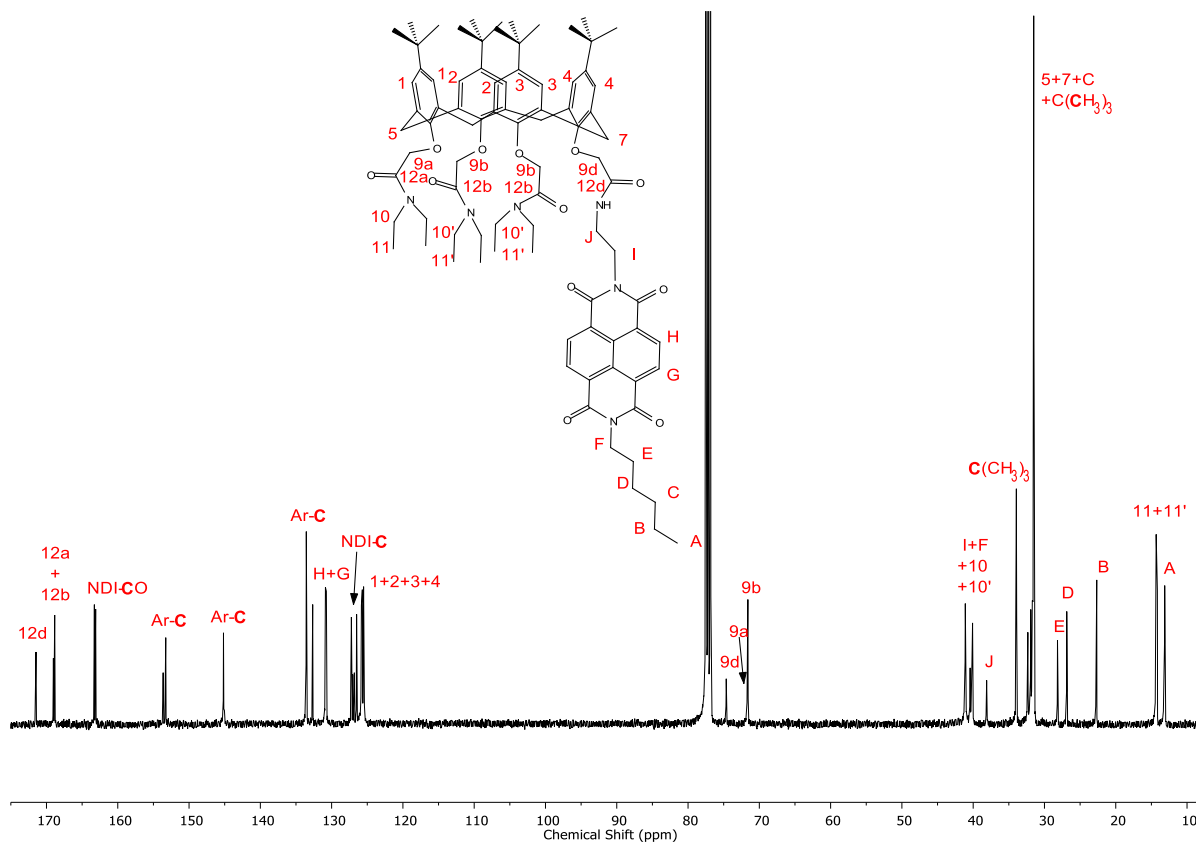
Figure 100: ^{13}C NMR spectrum of the ligand L4 in CDCl$_3$ recorded at 100 MHz.
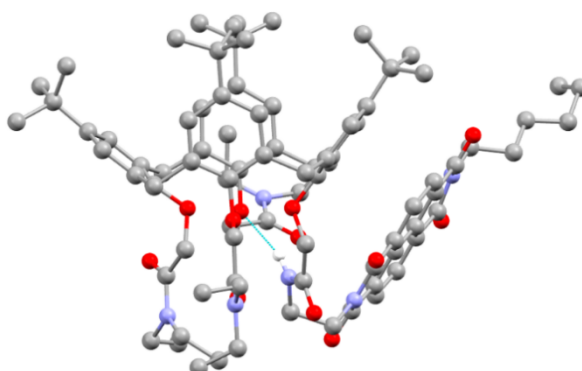
Figure 101: Crystal structure of the ligand L4.

The structure of **L4** was also confirmed by a single crystal X-ray structure determination. The ligand was crystallised in the course of metal complex crystallisation attempts, which were otherwise

unsuccessful. The calixarene crystallised from DMF without any inclusion of solvent molecules. The calixarene assumes a pinched cone conformation (Figure 101). The dihedral angles between the planes of the phenyl rings with the tertiary amide linkers and the methylene C4 plane are 42.7° (ring 1), 86.5° (ring 2) and 85.8° (ring 3), respectively. The dihedral angle between the plane of the phenyl ring 4 with the NDI moiety on the lower rim and the methylene C4 plane is 50.2°. Unlike the previous bis-NDI calixarene structures, the NDI moiety here is not aligned with calixarene aromatic rings, and there are no notable intermolecular interactions in the structure. A key feature is an intramolecular hydrogen bond with a N…O distance of 2.99 Å is observed between the secondary amide N atom and the O atom of the phenyl ring 3.

The ligand **L5** was synthesised following the same procedure used for the ligand **L4** (Scheme 21).
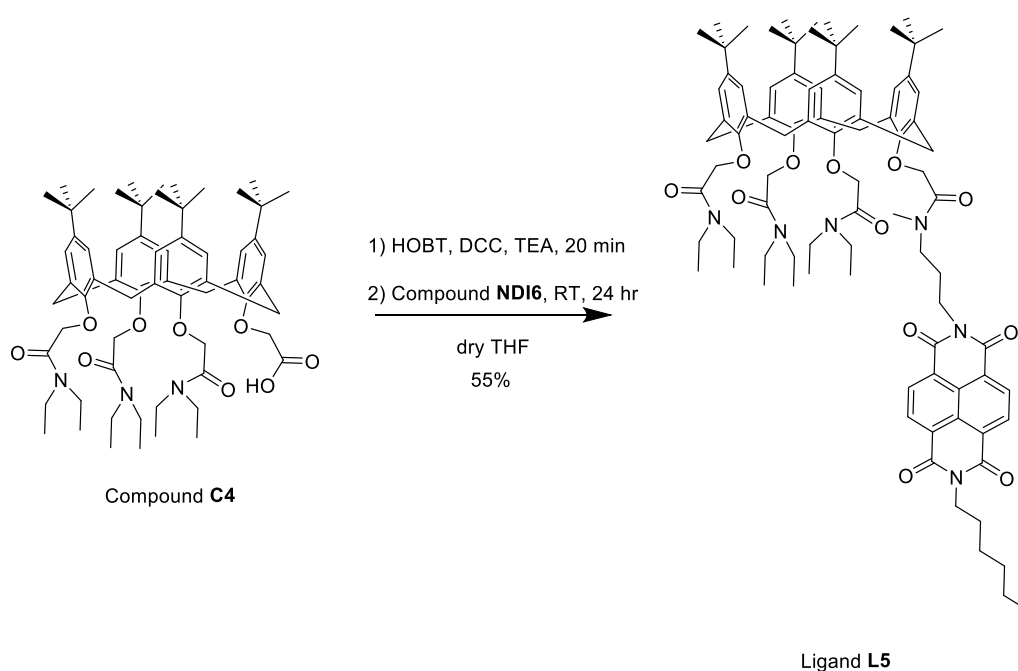
Scheme 21: Synthesis of the ligand L5.

The ligand **L5** was found to be more soluble in a range of common organic solvents. While the compound appeared to decompose on silica TLC plates, the use of neutral alumina as the stationary phase for column chromatography was once again successful, albeit with the apparent incorporation of some impurities into the eluted product based on the NMR spectrum (Figure 102, top). Again the total combined integration ratio matches well with the expected structure of the ligand. Further purification was performed using the same purification procedure used for the ligand **L4**. The amide coupling reaction achieved a moderate yield of 55%.
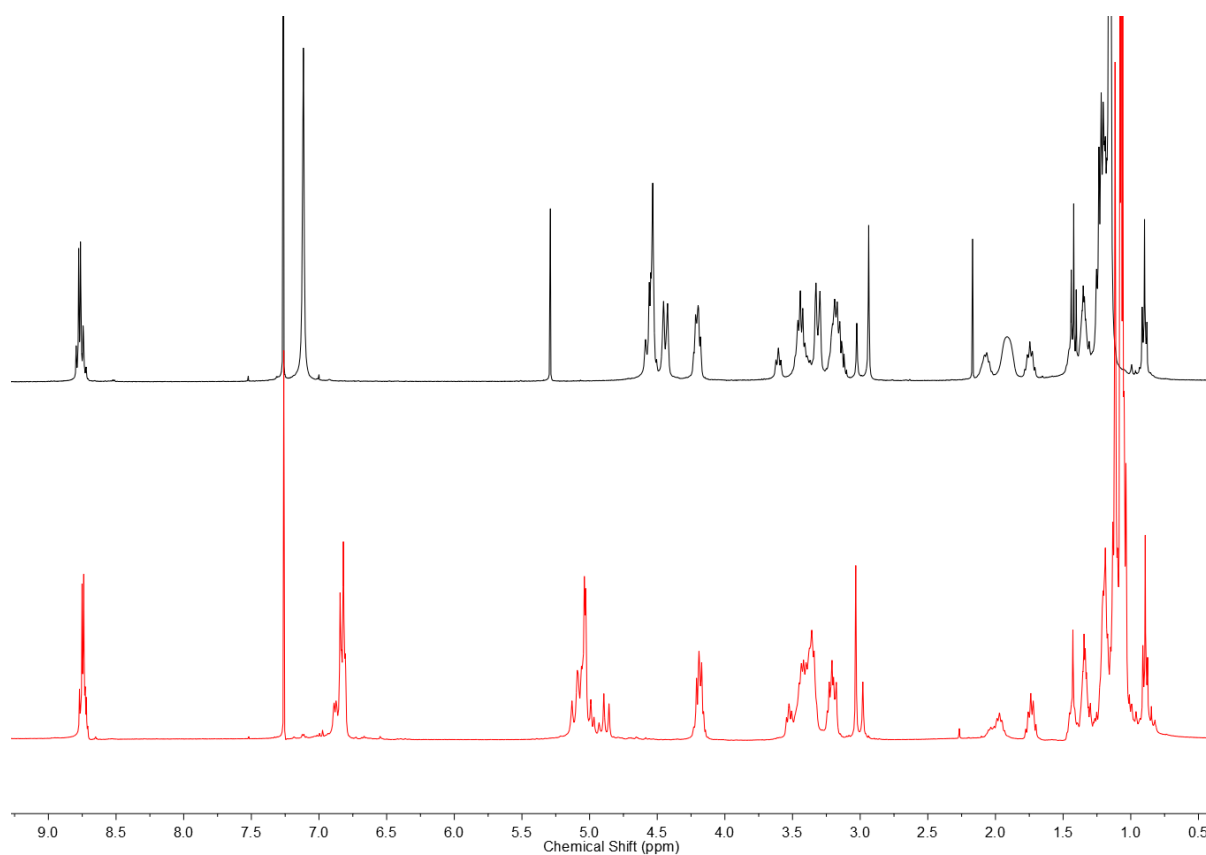
Figure 102: Top: ^{1}H NMR spectrum of the L5 ligand with metal cation impurities in CDCl$_3$ recorded at 400 MHz; Bottom: ^{1}H NMR spectrum of the L5 ligand in CDCl$_3$ recorded at 400 MHz.

Without the amide hydrogen bond, the free ligand **L5** in the ^{1}H NMR looks completely different from the ligand **L4** (Figure 103)**.**
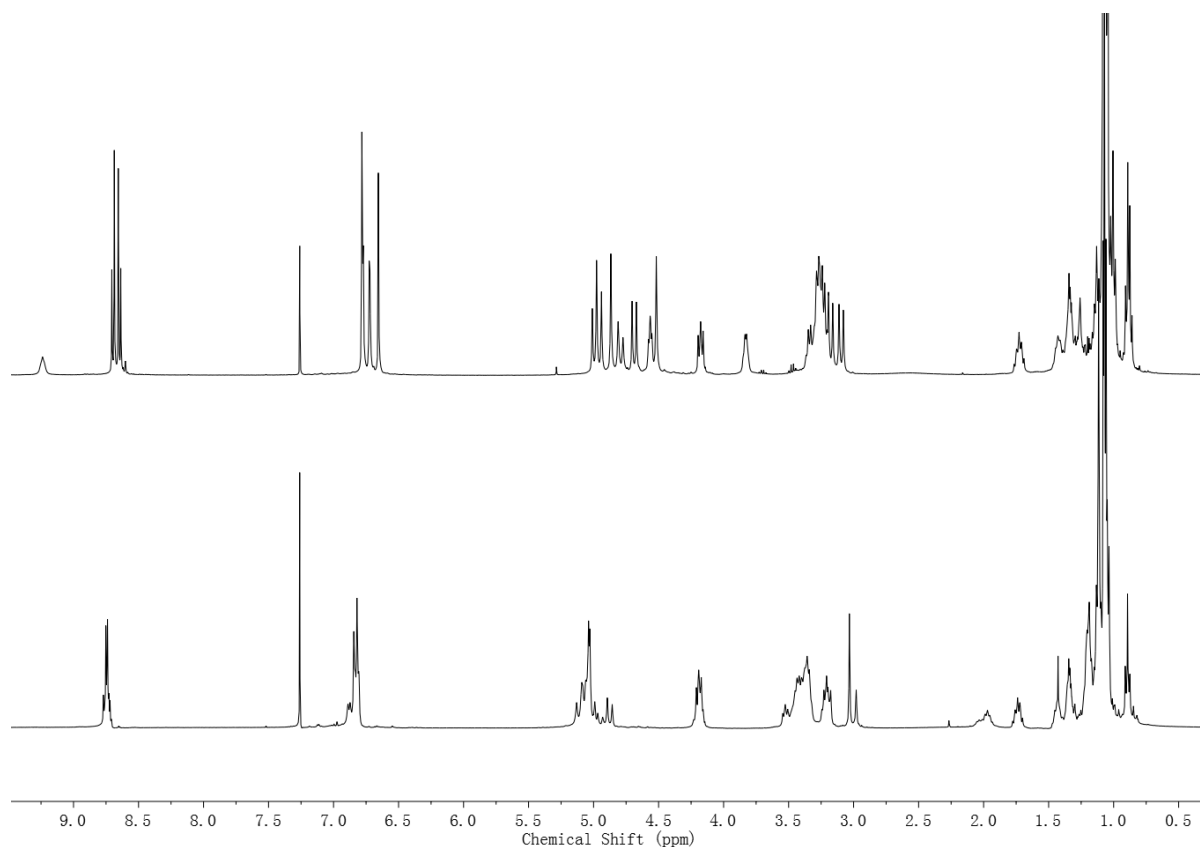
Figure 103: ^{1}H NMR spectrum of the ligand L4 (top) and L5 (bottom) in CDCl$_3$ recorded at 400 MHz.

The 2D COSY experiment was employed for assignments of all proton peaks. The ^{1}H NMR spectrum (Figure 104) in CDCl$_3$ is in agreement with the proposed structure. The splitting pattern of the four hydrogens of the NDI is a multiplet (peak *H* and *G*). The hydrogen assignments of aromatic rings are peaks *1*, *2*, *3* and *4* around 6.9 ppm with an integration ratio of 8. Those peaks with a total integration ratio of 12 around 5.00 ppm are not well separated, corresponding to the axial protons of Ar-C**H$_2$**-Ar (*6a* and *8a*) and the protons of OC**H$_2$** groups (*9a*, *9b*, *9c* and *9d*). The multiplet peak (peak *F* and *I*) at 4.20 ppm is attributed to the protons of methylene groups linking to the NDI moiety. The peaks in the range of 3.56 - 3.30 ppm are associated with twelve protons of the CON(C**H$_2$**CH$_3$)$_2$ group (peak *10* and *10'*) and two protons of CON(CH$_3$)C**H$_2$**CH$_2$CH$_2$N(CO)$_2$ groups (peak *K*). Equatorial protons of Ar-C**H$_2$**-Ar groups have a chemical shift at 3.20 ppm (*5e* and *7e*). Eleven hexyl protons resonat in the aliphatic region (peak *A*, *B*, *C*, *D* and *E*). Compared with the NMR of the **L3** ligand, an additional peak (peak J) is attributed to the proton of CON(CH$_3$)CH$_2$C**H$_2$**CH$_2$N(CO)$_2$. This is further confirmed by the cross peak appearing at (4.2 ppm, 2.0 ppm)/(peak *I*, peak *J*) as well as the cross peak appearing at (3.6 ppm, 1.7 ppm)/(peak *K*, peak *J*) in the COSY NMR spectrum. The COSY NMR spectroscopy was used to assign the peaks of N(CO)$_2$CH$_2$C**H$_2$**(CH$_2$)$_3$CH$_3$ via the cross peak appearing at (4.0 ppm, 1.6 ppm)/(peak *F*, peak *E*). Intense peaks around 1.10 ppm with a total integration ratio of 54 correspond to *tert*-butyl groups and CON(CH$_2$C**H$_3$**)$_2$ (peak *11* and *11'*).

It is notable that the NMR characterisation shows the two singlet peaks (peak *L*) around 3.00 ppm which are assigned to hydrogens of CON(C**H$_3$**)CH$_2$CH$_2$CH$_2$N(CO)$_2$ with an integration ratio of 3. This result is probably associated with the presence of amide rotamers in a ratio of 2:1 based on the

integration ratio of the methyl group. The presence of amide rotamers is also supported by the observation of some less intense peaks next to their prominent peaks (Figure 104 inset).
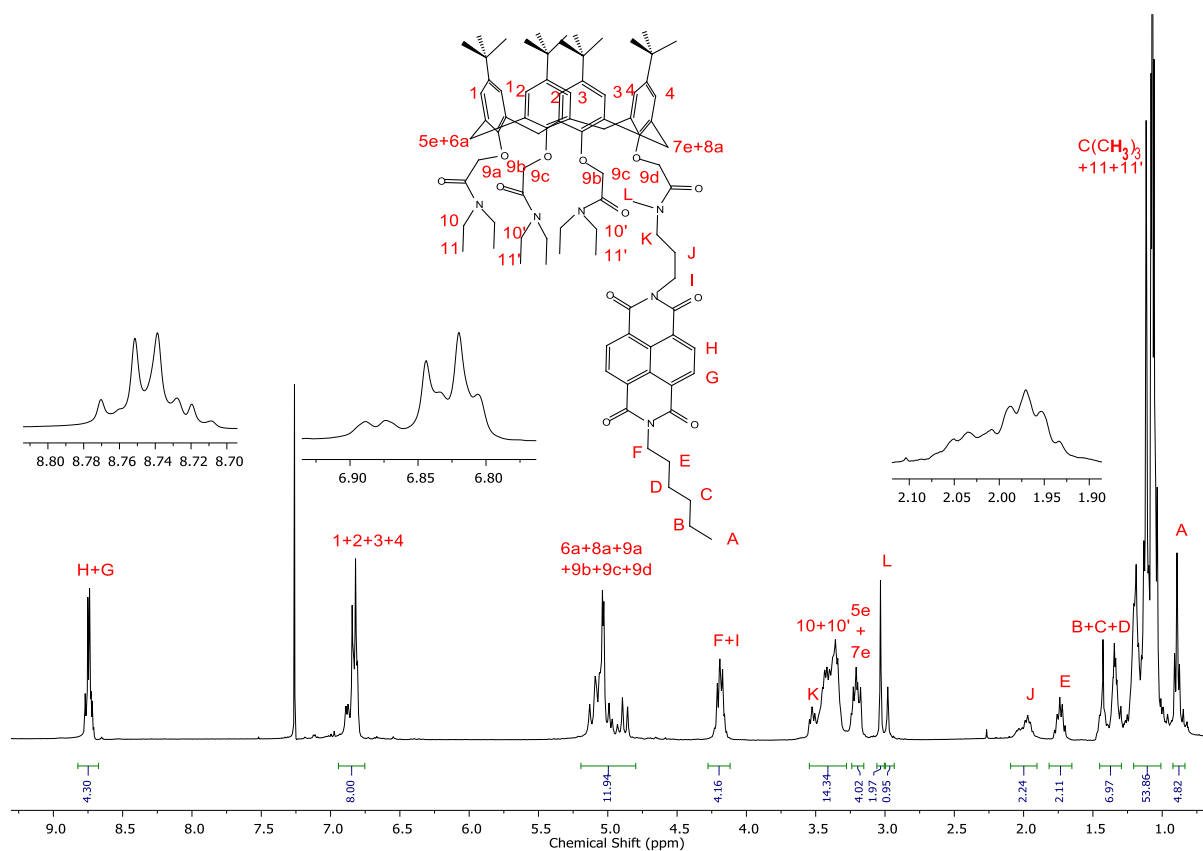
Figure 104: ¹H NMR spectrum of the ligand L5 in CDCl₃ recorded at 400 MHz.

Due to the less intense peaks in the normal ^{13}C NMR spectrum even if a concentrated solution was used, the DEPTQ ^{13}C NMR technique was used to characterise the ligand **L5**. The assignment of the peaks was aided by HSQC and HMBC techniques (Figure 105). Due to the similarity of the structure, most of the peaks have a similar and expected chemical shift as those observed in the case of the ligand **L4**. The observed additional peaks are consistent with the structure of the ligand **L5**. The resonance of CON(**C**H₃)CH₂**C**H₂CH₂N(CO)₂ is visible at 26.01ppm (peak *J*) and 34.09 ppm (peak *L*). Only peak *K* significantly shifts upfield to 45.57 ppm. The ^{13}C NMR spectrum is again consistent with the proposed structure, and all peaks are in their expected region. But many peaks cannot be specifically assigned, especially peaks in the aromatic region.
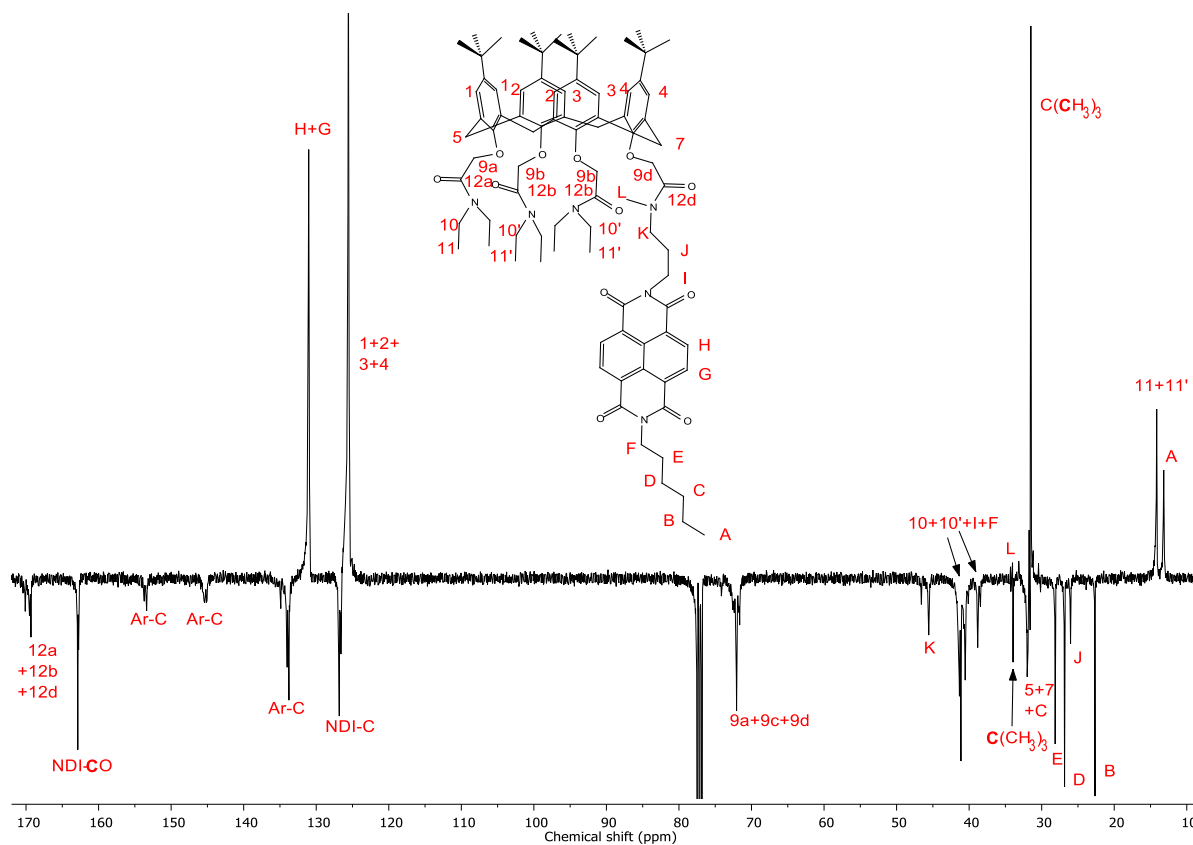
Figure 105: DEPTQ ^{13}C NMR NMR spectrum of the ligand L5 in CDCl$_3$ recorded at 100 MHz.

As mentioned above, the aim of this project was to investigate the energy transfer from NDI to the lanthanoid. The NDI moiety is two methylenes and three methylenes away from the nitrogen atoms of the amide group in the case of **L4** and **L5** ligands. The plan was to make the NDI more distant from the coordination centre, which could be achieved by increasing the number of methylene groups. Thus, the ligand **L6** was used as a comparison with the **L4** and **L5** ligands to further investigate the antenna effect. The ligand **L6** was synthesised following the same procedure for ligand **L4** and **L5**. But there was an important intermediate (compound **NDI9** or its TFA salt compound **NDI11**) that needed to be synthesised before the amide coupling reaction. The synthetic paths for the compounds are displayed in Scheme 22 and Scheme 23.
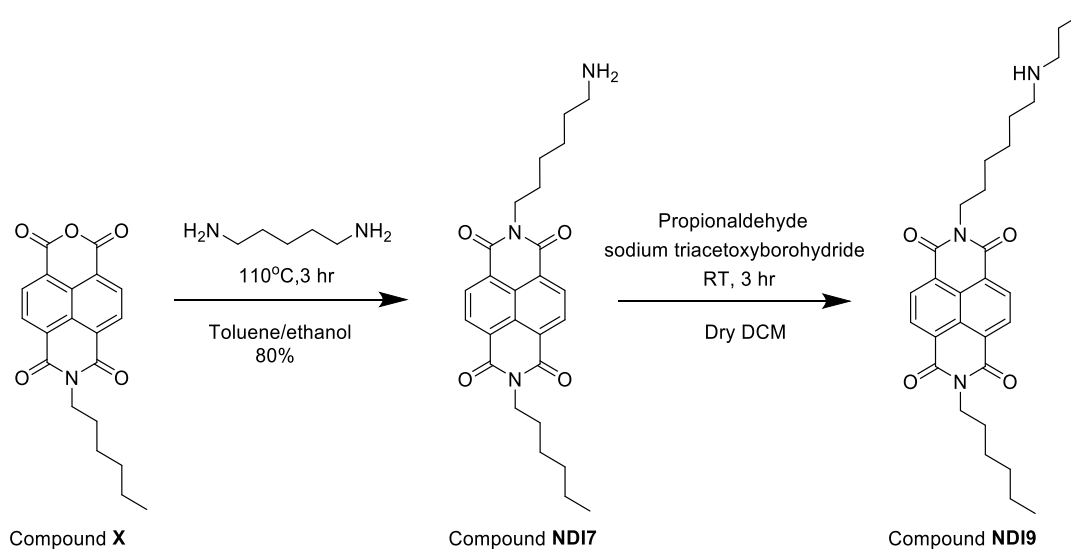
Scheme 22: Synthetic path for the compound NDI9.

The primary amine-functionalised intermediate had to be made first from a condensation reaction between the compound **X** and 1,6-hexanediamine. The employment of the sodium triacetoxyborohydride in a dry dichloroethane is a common way to reduce the imine from a primary amine to secondary amine. However, it was found that the majority of the product was the tertiary amine-functionalised NDI (Compound **NDI 8**) when using this reagent. The remaining minor components were hard to purify by column chromatography or to identify in the NMR spectrum of the crude reaction mixture. The low solubility of the starting material, the primary amine intermediate, probably contributed to these issues. As a result of these issues, an alternative synthetic approach was developed.
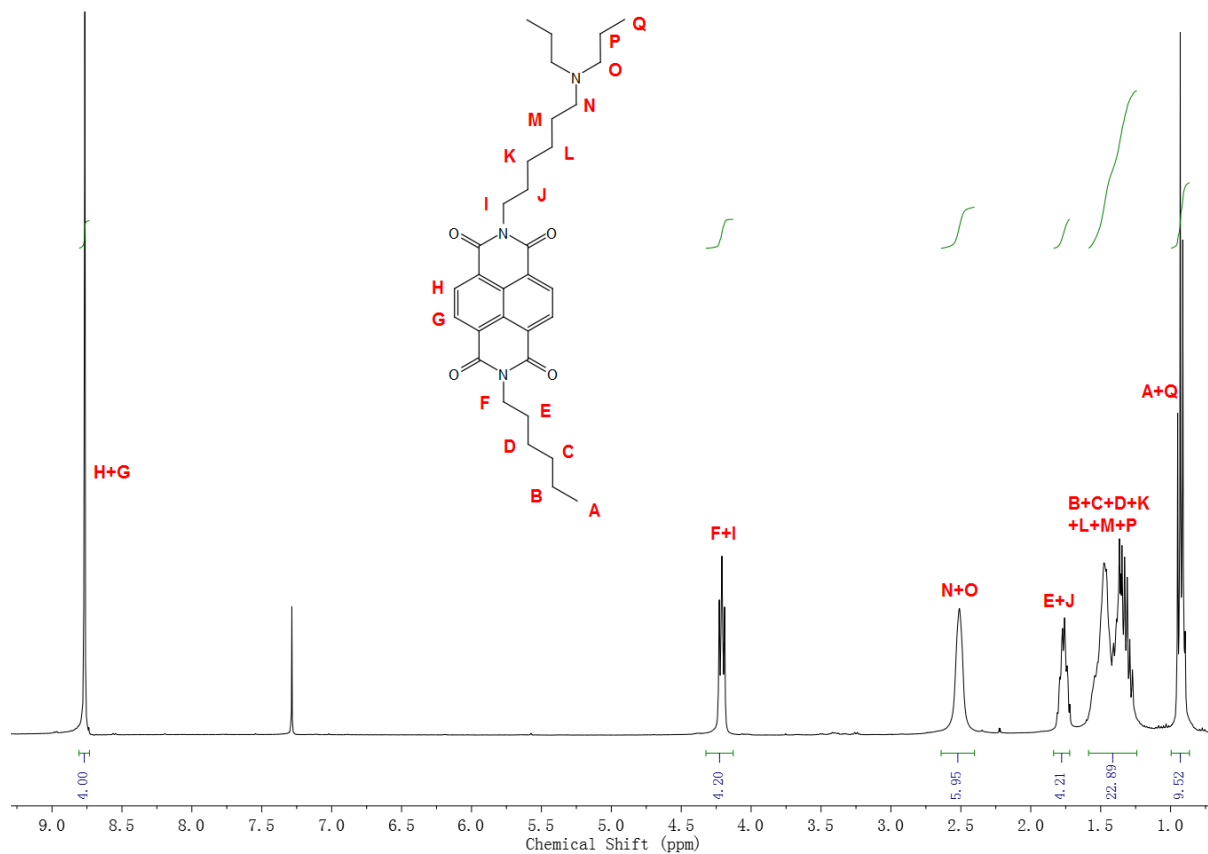
Figure 106: ^{1}H NMR spectrum of the tertiary amine-functionalised NDI8 in CDCl$_3$ recorded at 400 MHz.
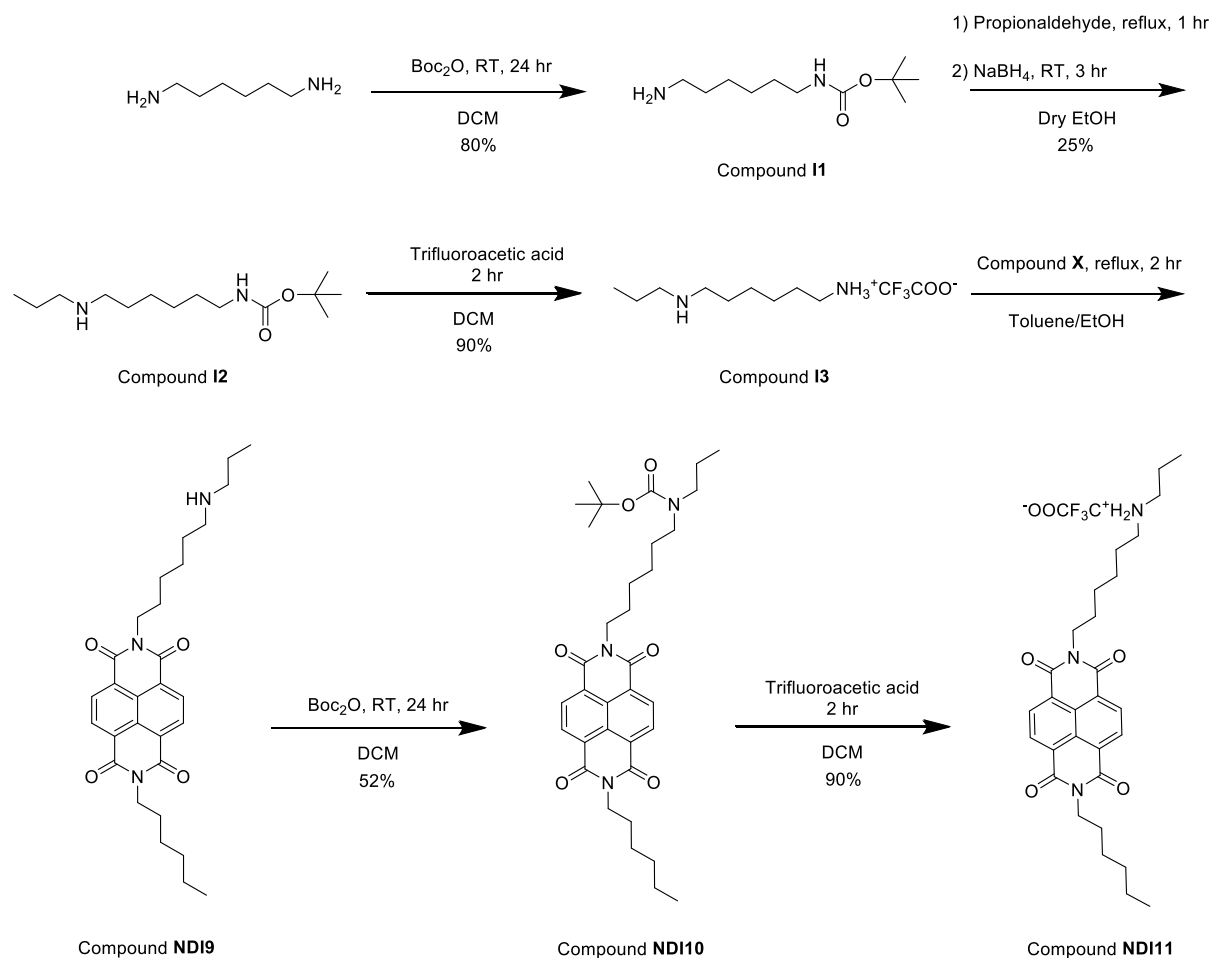
Scheme 23: Synthetic path for compound NDI11.

This alternative synthesis of the compound **NDI11** required six steps. The first step was to make N-Boc-1,6-hexanediamine following standard conditions. The crude product was washed with water eight times to remove the excess 1,6-hexanediamine before the next reaction. The imine intermediate was prepared by treating *N*-Boc-1,6-hexanediamine (compound **I1**) with 1.2 equivalents of propionaldehyde in dry EtOH at reflux. After obtaining the imine intermediate, sodium borohydride was added to generate the monopropylated amine. Column chromatography using silica gel and DCM/MeOH (10:0.8) as eluent was used to purify the intermediate (compound **I2**). The reaction proceeded with a low yield of 25%. The Boc deprotection was accomplished by stirring with trifluoroacetic acid at room temperature in DCM for 2 hours. This TFA salt (compound **I3**) was used directly for the next step without further purification. The condensation reaction between compound **I3** and compound **X** was performed in a mixture of toluene and EtOH (2:1) at 100 °C for 3 hours. In order to avoid a difficult purification of the secondary amine-functionalised NDI (compound **NDI9**) by column chromatography, di-*tert*-butyl dicarbonate was used again to convert it to its *N*-Boc derivative. The desired Boc-protected amine (compound **NDI10**) was purified by column chromatography. The deprotection of the product using trifluoroacetic acid gave the desired compound **NDI11**. Compared with the synthetic path for compound **NDI8**, this path resulted in the desired compound but at the cost

of an increased number of steps and at a very low overall yield (8.6%). The H NMR spectrum is shown in Figure 107.
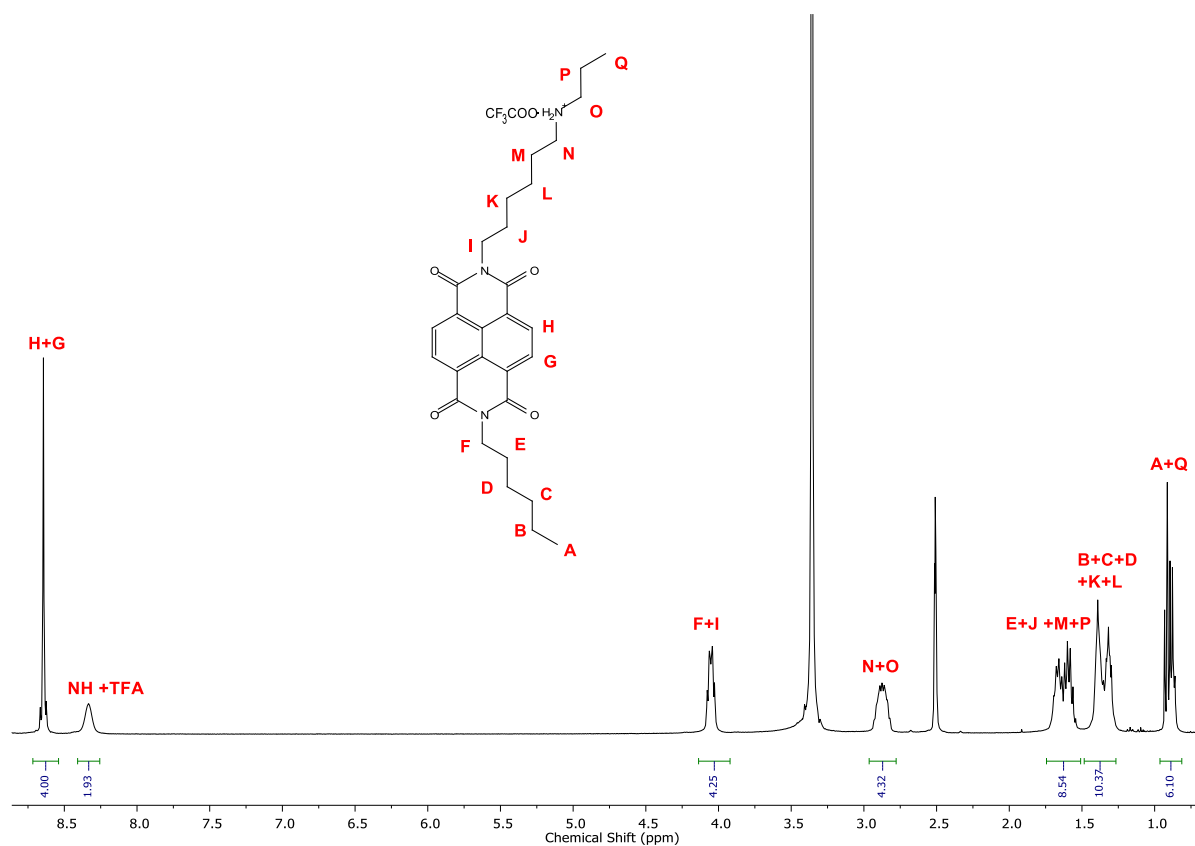
Figure 107: ¹H NMR spectrum of the compound NDI11 in CDCl₃ recorded at 400 MHz.

The ligand **L6** was prepared under the same reaction condition for previously synthesised ligands (Scheme 24). The compound **X**, two equivalents of HOBT and two equivalents of DCC were stirred at room temperature for 20 minutes in the presence of triethylamine. Subsequent amide coupling with compound **X** gave the crude product of the ligand **L6**. Purification of the ligand **L6** was first attempted by recrystallisation. It was found that the ligand **L6** was completely soluble in all common organic solvents, including hexane and petroleum spirit. Therefore, the recrystallisation to purify the free ligand did not work. The free ligand was converted to its corresponding sodium complex due to its relatively lower solubility. However, an attempt to purify the sodium complex by recrystallization was also not successful with impurities co-crystallising out together with the desired product.

Not surprisingly given previous results, the product decomposed on the silica TLC plate. Three dominant spots were displayed on the neutral Al₂O₃ TLC plate: impurities, free ligand and what was assumed to be ligand with metal cation impurities. Therefore, the ligand was converted to its corresponding sodium complex by adding two equivalents of sodium tetrafluoroborate. The product was then purified via neutral Al₂O₃ column chromatography eluted with a mixture of DCM: MeOH (100: 0.2) to yield the metal containing ligand **L6**. The removal of the metal cation following procedure used for the ligand **L4** did not work as the metal cations were not removed completely. The removal was

achieved by dissolving the mixture in minimal acetone, then adding water at 70°C, and filtering to afford the free ligand **L6** in 29% yield.

1) HOBT, DCC, TEA, 20 min

2) Compound **NDI11**, RT, 24 hr

dry THF

29%

Compound **C4**
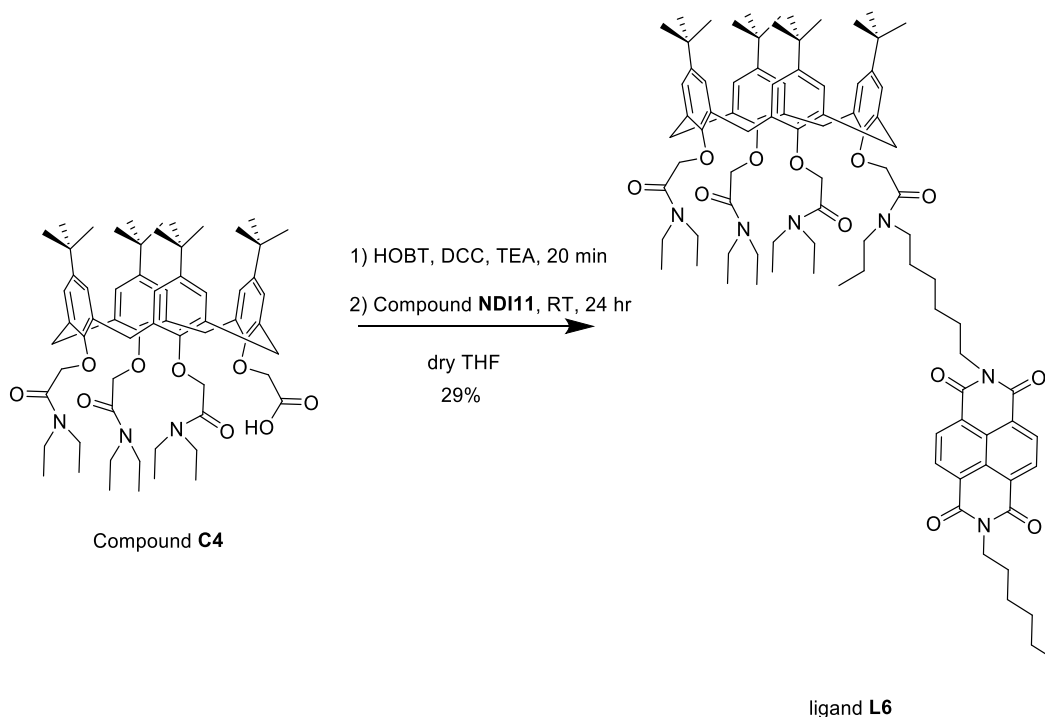
ligand **L6**

Scheme 24: Synthesis of the ligand L6.

The ^{1}H NMR in CDCl$_3$ with the assistance from 2D multinuclear NMR techniques confirmed the successful isolation of the pure ligand **L6** (Figure 108). The peaks are relatively easily assigned as the calixarene shares a similar structure with the **L4** and **L5** ligands. The ^{1}H NMR spectrum reveals a singlet peak associated with four NDI hydrogens at 8.74 ppm with an integration ratio of 4 (peak *G*). Two multiplet peaks (*1*, *2*, *3* and *4*) with an integration ratio of 8 (4+4) in the aromatic region of 6.92 - 6.64 ppm represent aryl components of the calixarene. Three separate multiplet peaks appearing in the range of 5.28-4.82 ppm are assigned to axial Ar-C**H₂**-Ar protons (peak *6a* and *8a*), OC**H₂** protons (peak *9a* and *9b*) and OC**H₂** protons (peak *9c* and *9d*). The apparent multiplet peak centred at 4.18 ppm with an integration ratio of 4 is attributed to two CH$_2$ groups attached to NDI (peak *H* and *F*). These peaks around 3.2 ppm with the integration ratio of 20 protons appear to be the combination of peaks corresponding to CONC**H₂**CH$_2$CH$_3$ protons(peak *N*), CONC**H₂**CH$_2$CH$_2$CH$_2$CH$_2$CH$_2$N(CO)$_2$ protons (peak M), CON(C**H₂**CH$_3$)$_2$ (peak *10* and *10'*) and equatorial Ar-CH$_2$-Ar (peak *5e* and *7e*). The chemical shift and integration ratio of the rest peaks in the further upfield region match well with the proposed structure, and these peaks represent the alkyl chain (peak *I* + *E*, *O* + *L* and *K* + *J* + *B* + *C* + *D*), C(C**H₃**)$_3$ and CON(CH$_2$C**H₃**)$_2$ (peak *11* and *11'*). The peak *A* represents the methyl group of hexyl chain overlapped with the peak *P* of (CONCH$_2$CH$_2$C**H₃**), resonating at a similar frequency around 0.90 ppm.
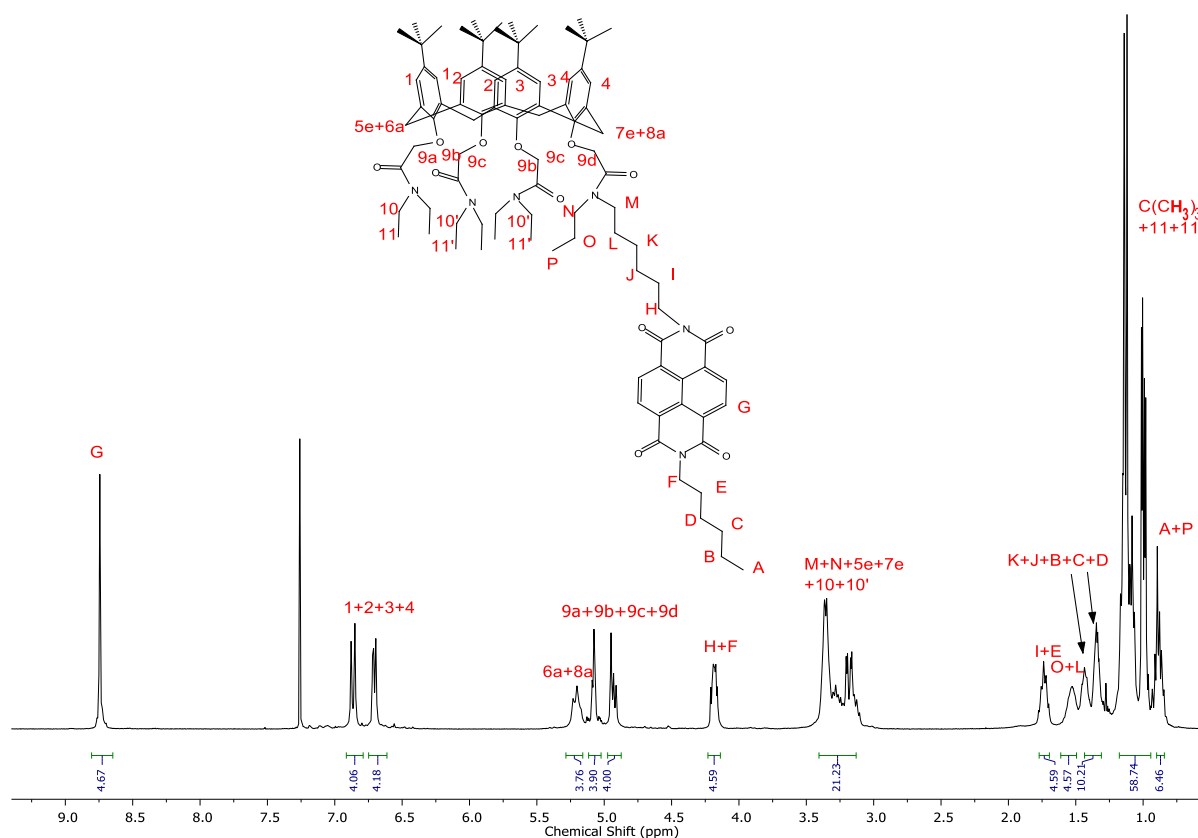
Figure 108: ¹H NMR spectrum of the ligand L6 in CDCl₃ recorded at 400 MHz.

The ligand **L6** was also characterised by ^{13}C NMR experiments with the attribution of 2D NMR spectra, including HSQC and HMBC spectroscopy for the assignment of the peaks (Figure 109). Compared with the spectrum of the ligand **L4**, the symmetry of the NDI is confirmed by the one carbon environment of NDI-**C**H (peak *G*). The number of carbon environments and chemical shift in the aromatic region are similar to those observed in the case of **L4** and **L5** because they share the same calixarenetrisamide moiety. The peaks at 72.49 ppm and 72.57 ppm correspond to O**C**H₂ carbons. The increase of carbon environments in the aliphatic region is attributed to the alkyl chain situated at the amide group of the lower rim of the fourth aromatic ring. More specifically, two resonance (peak *O* and *L*) at 21.07 ppm and 22.17 ppm confirm the presence of two carbon environments of CON(CH₂**C**H₃)₂. The rest of signals corresponds to the carbon of the alkyl chain (*A*, *P*, *K*, *J*, *B* and *D*), but the specific carbon cannot be assigned due to the similar carbon environment. It is notable that there are four carbon environments for carbon *M* and carbon *N* due to the presence of amide rotamers.
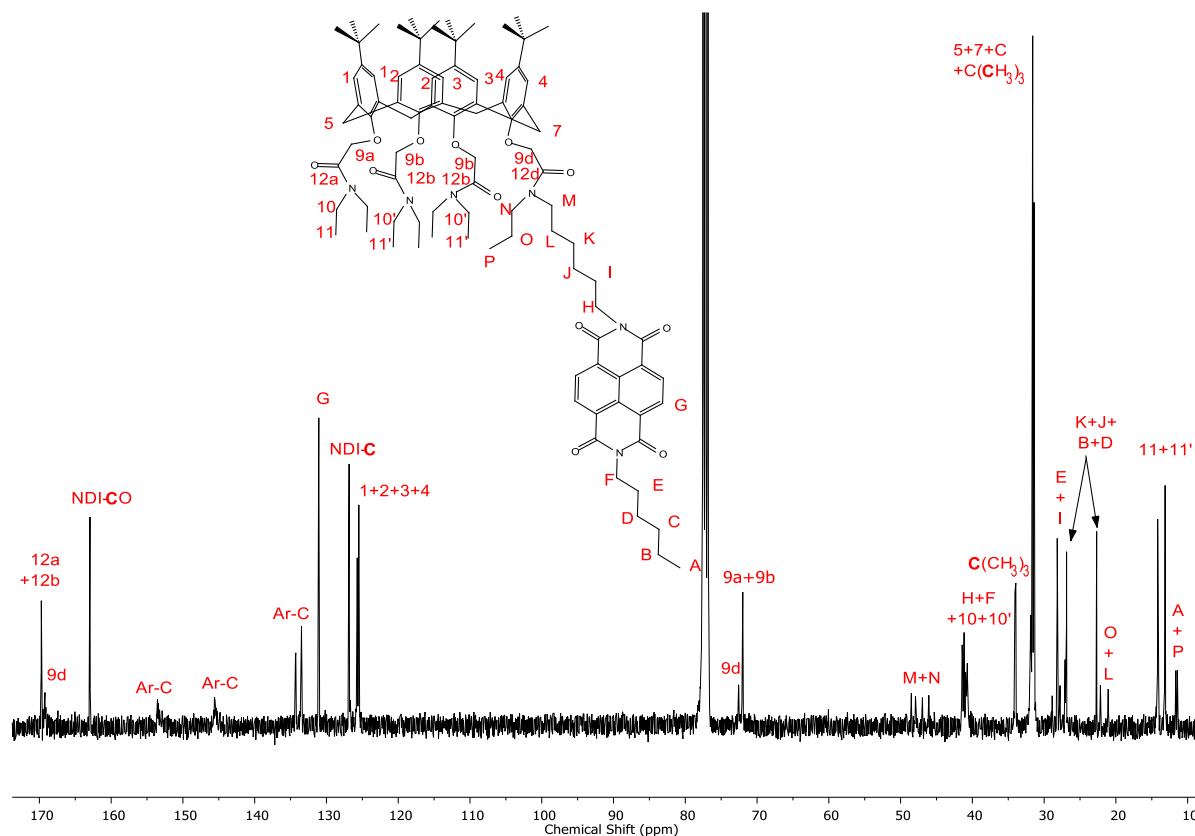
Figure 109: ^{13}C NMR spectrum of the ligand L6 in CDCl$_3$ recorded at 100 MHz.

3.3 NMR Studies of Sodium and Yttrium Complexes

The reaction of the **L4** ligand with sodium tetrafluoroborate results in a significant change in the NMR spectrum (Figure 110, blue). Firstly, the splitting pattern of the NDI peaks is a singlet, not a pair of doublets as observed in the free ligand. All aromatic peaks shift downfield after adding Na(I) ions. The peaks corresponding to OCH$_2$ groups on the lower rim of calixarene shift upfield to some extent. The ^{1}H NMR signals corresponding to the other side of NDI as well as CON(C**H$_2$**CH$_3$)$_2$ shift in response to complexation. The multiplet peaks at 0.7 - 1.3 ppm correspond to protons of C(C**H$_3$**)$_3$ and CON(CH$_2$C**H$_3$**)$_2$. Within this multiplet, three singlet peaks due to the *tert*-butyl groups at 1.18 ppm, 1.10 ppm and 1.08 ppm are visible. The shifts of the hexyl group of the NDI are independent of calixarene coordinating to the sodium centre.

For easier comparison and analysis, the NMR spectrum of the yttrium complex of ligand **L4** was analysed in CDCl$_3$, although the yttrium complex of the ligand **L4** has low solubility in CDCl$_3$. Alternative solvents including deuterated acetone, toluene, and acetonitrile did not give any better results. After adding the Y(DMSO)$_3$(NO$_3$)$_3$ to the ligand **L4** in CDCl$_3$, a solid white precipitate formed immediately. Many peaks become very broad, making it hard to assign. The NMR of the solution that remained after precipitation is shown in Figure 110.
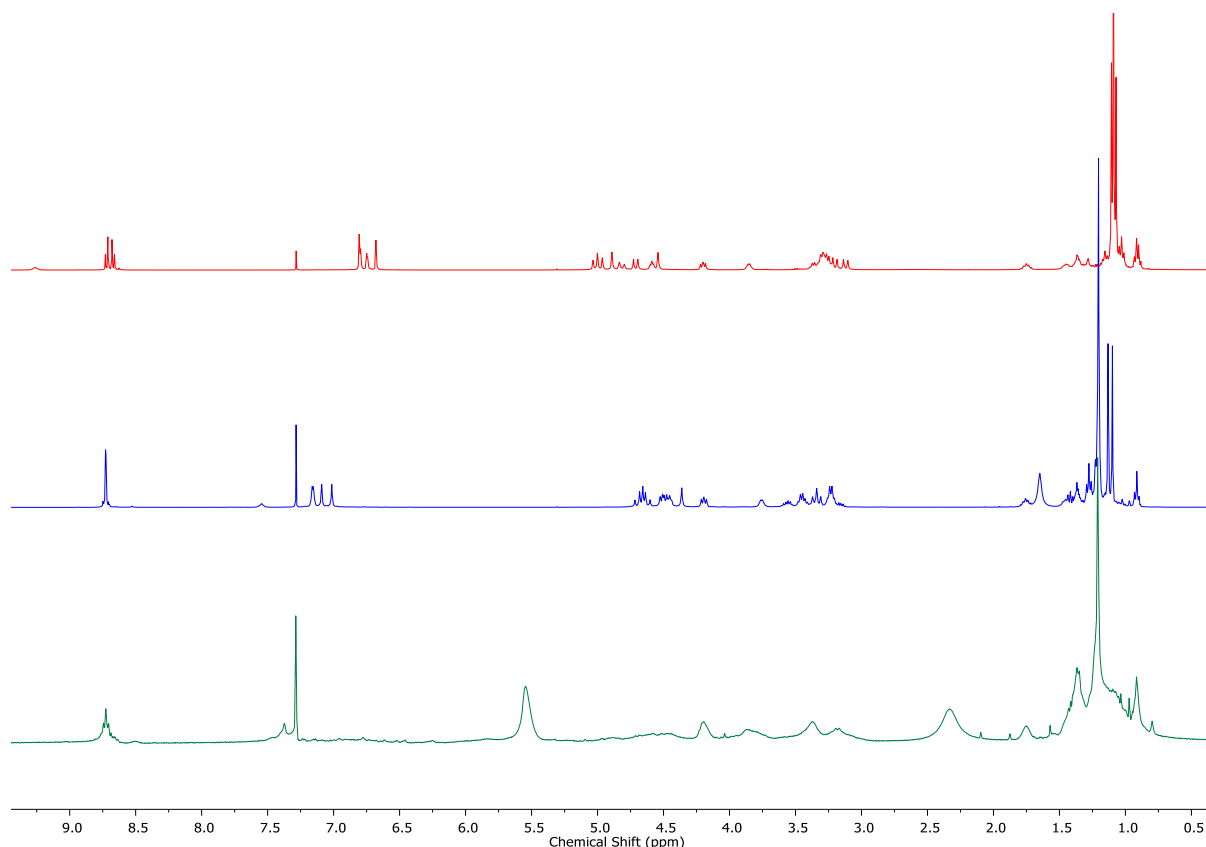
Figure 110: ^{1}H NMR spectra of the free L4 ligand (in red), Na complex of the L4 ligand (in blue) and the soluble material remaining after the addition of Y(III) into L4 ligand (in green) in CDCl$_3$ recorded at 400 Hz.

We also investigated the interaction between **L5** ligand and Na$^+$ by H NMR spectroscopy (Figure 111). After adding excess NaBF$_4$, many changes in the chemical shift of ^{1}H NMR spectrum are observed in comparison to the free ligand: multiplet peaks corresponding to aromatic rings of calixarene shift downfield, and coalesce into a singlet peak; peaks corresponding to OC**H$_2$** group and axial Ar-C**H$_2$**-Ar group shift upfield; peaks in the region of 3.68 - 3.10 ppm are well separated; the separate peaks of the *tert*-butyl groups coalesce into a single peak and have a slight downfield shift from 1.08 ppm to 1.16 ppm, while the chemical shift of peaks assigned to the hexyl chain remains constant. A solid white precipitate was also observed after the addition of Y(DMSO)$_3$(NO$_3$)$_3$ to the **L5** ligand in CDCl$_3$. The NMR of the solution that remained after precipitation is shown in Figure 111.
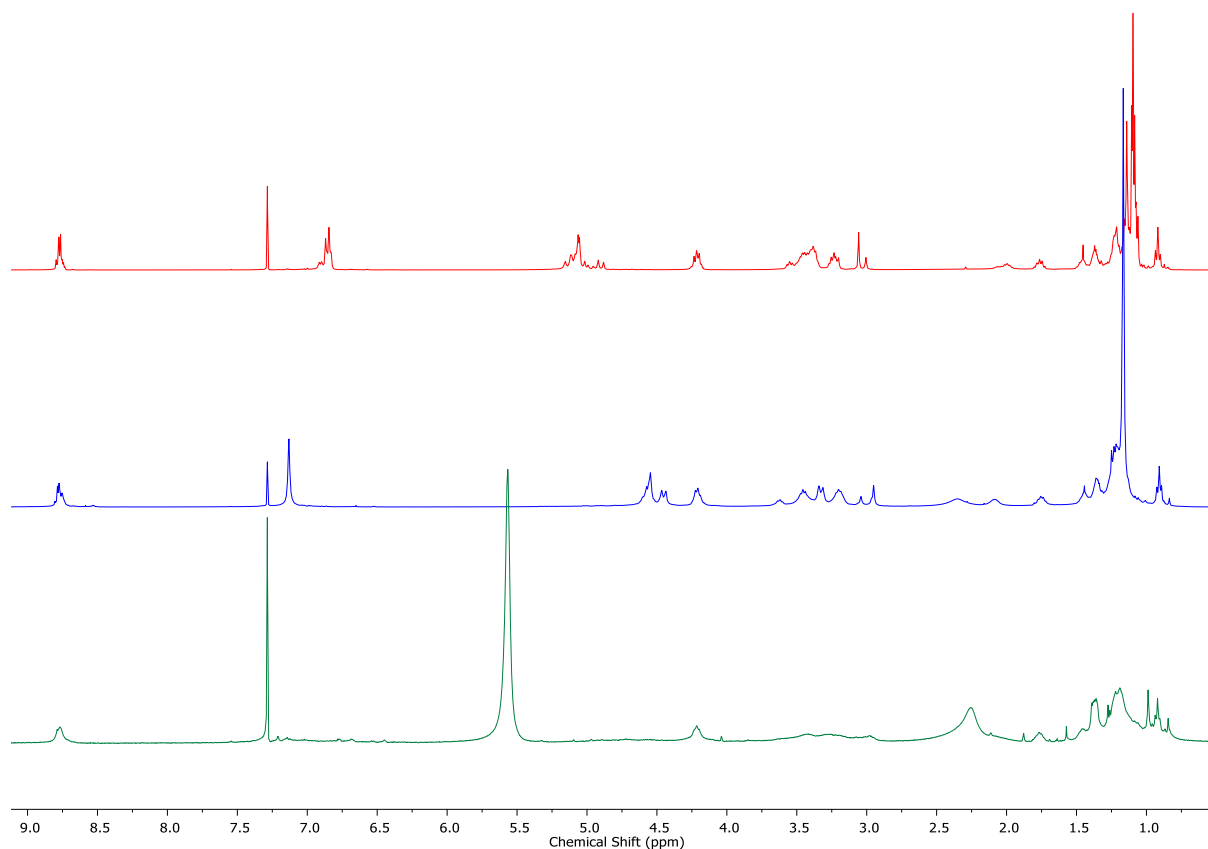
Figure 111: ^{1}H NMR spectra of the free L5 ligand (in red), Na complex of the L5 ligand (in blue) and the soluble material remaining after the addition of Y(III) into L5 ligand (in green) in CDCl$_3$ recorded at 400 Hz.

3.4 Photophysical Properties of Mono-NDI Substituted Ligands

3.4.1 Absorption and Emission Results

The absorption spectra of mono-substituted NDI ligands in 10^{-4} M acetonitrile solutions were recorded. The absorption profiles are shown in Figure 112.
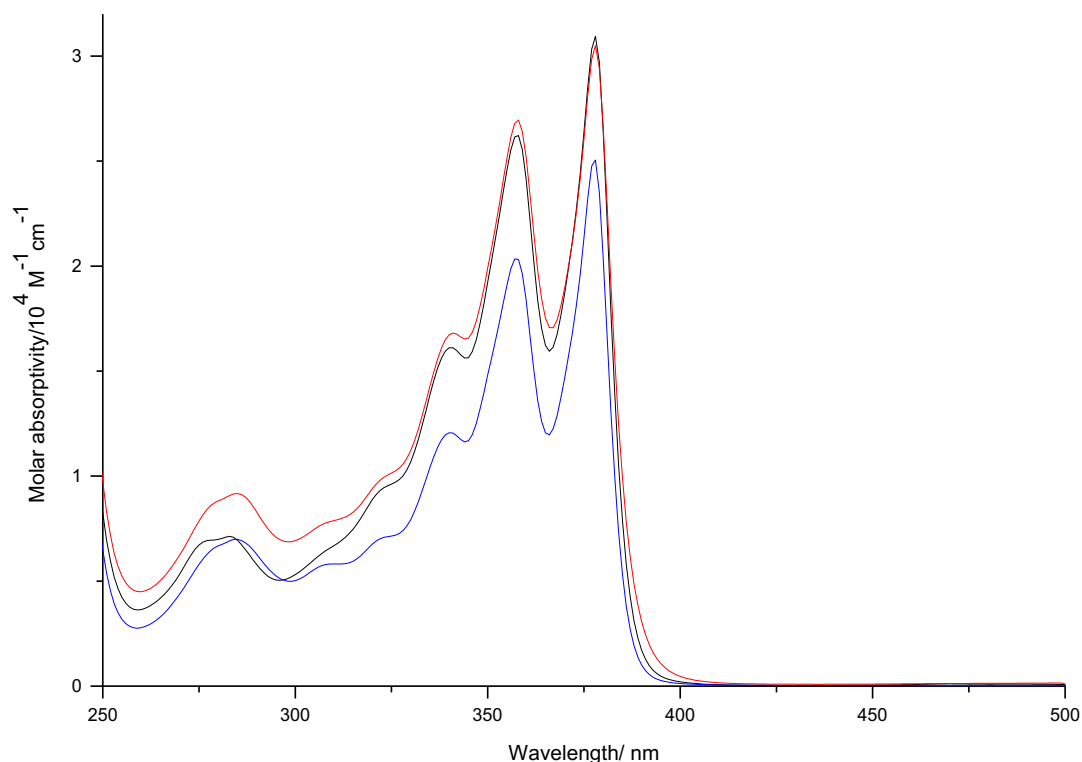
Figure 112: Absorption spectra for 10^{-4} M MeCN solutions of the L4 ligand (black), L5 ligand (red) and L6 ligand (blue).

By referring to the similar absorption spectra of bis-NDI substituted calixarene ligands, the absorption band below 300 nm is attributed to the $\pi \rightarrow \pi^*$ transitions of the calixarene. The band spanning from 300 nm to 400 nm with vibronic progression spaced around 1500 cm^{-1} is assigned to the S_0 to S_1 electronic transition of the NDI moiety.[100-101] Due to the monosubstitution, the value of molar absorptivity of NDI unit of **L4**, **L5** and **L6** ligand is lower than those of bis-substituted ligands (see Chapter 2).

Table 12: Summary of the absorption and emission data of L3, L4 and L6 ligands in 10^{-4} M acetonitrile solutions

Ligand	λ_{abs} [nm] (10^4 ε [M^{-1} cm^{-1}])	λ_{Em} [nm]
L4	277 (0.69), 285 (0.69), 322 (0.93), 340 (1.61), 358 (2.62), 378 (3.09)	406, 525
L5	285 (0.91), 323 (0.99), 340 (1.67), 358 (2.70), 378 (3.05)	500, 650 406, 500, 650
L6	285 (0.70), 309 (0.58), 323 (0.70), 340 (1.20), 358 (2.03), 378 (2.50)	388, 406, 432, 510

Upon excitation at 340 nm, mono-NDI substituted calixarene ligands again show similar emissive behaviour to those of bis-substituted ligands. The luminescent spectra (Figure 113) in a 10^{-5} M MeCN solutions show emission peaks around 400 nm corresponding to the fluorescence from the NDI monomer.[100] In ligand **L6,** the formation of aggregates results in a broad and structureless peak around 500 nm. This is the only ligand that the emission from aggregates can be observed in a 10^{-5} M MeCN solution.[101]
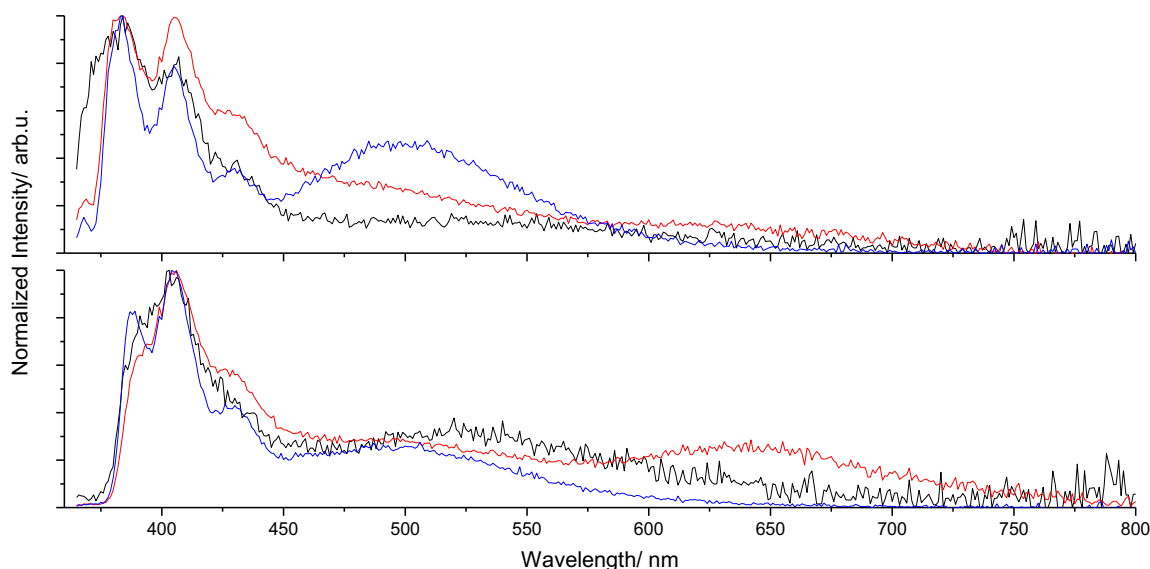
Figure 113: Top: Emission spectra for 10^{-5} M MeCN solutions of the L4 ligand (black), L5 ligand (red) and L6 ligand (blue). Bottom: Emission spectra for 10^{-4} M MeCN solution of the L4 ligand (black), L5 ligand (red) and L6 ligand (blue). Excitation wavelength: 340 nm.

In 10^{-4} M MeCN solutions, both the emission from NDI monomer and aggregate were observed in all cases.

3.4.2 Spectrophotometric Titrations

The stoichiometry of **L4** and **L5** ligands interacting with lanthanoid cations was determined using the same conditions used for the titration of ligand **L2** with europium(III) nitrate hydrate in acetonitrile

solutions. The data was recorded in the UV-visible region from 200 nm to 400 nm. Unlike the ligand **L2**, the spectrophotometric titrations of neutral **L4** ligand and **L5** ligand were performed in the absence of triethylamine because no protons needed to be removed from the ligand. The molar absorptivity of calixarene and NDI decreases with increasing equivalents of Eu^{3+} ions (Figure 114 and Figure 115). This is consistent with previous studies of lanthanoid complexes of calixarene tetraamides, where the molar absorptivity of the peak attributed to aromatic rings was lower in the complex in comparison to that of ligand [84-85, 171]. The spectrum of the molar absorptivity as a function of the molar ratio of the ligand to Eu^{3+} has an inflection point at 1:1 in the case of the **L5** ligand as well as the **L4** ligand, indicating the formation of stable 1:1 Eu complex of the ligand. This result is in agreement with the literature that calixarene tetramide binds strongly to Eu^{3+} ion.[84] Continuing the titration illustrated that no significant changes are observed up to four equivalents.
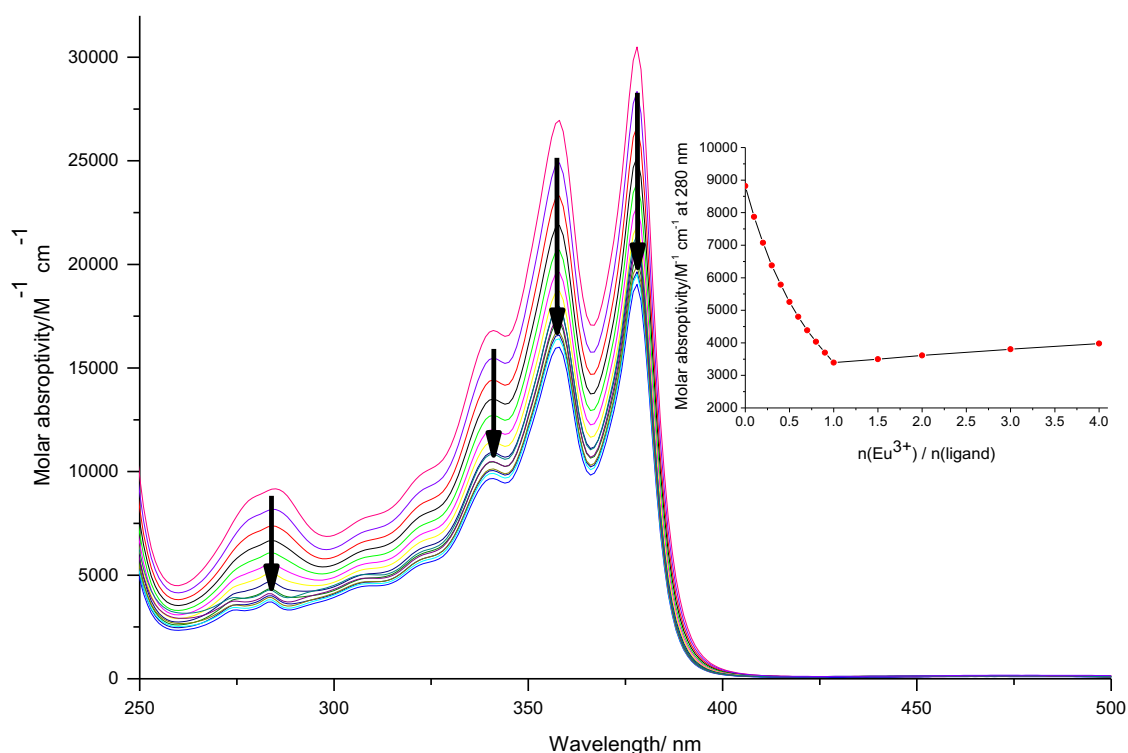
Figure 114: Spectrophotometric titration of the L4 ligand with Eu(NO₃)₃·6H₂O in MeCN at constant ionic strength (10⁻² M NBu₄PF₆) at room temperature. Inset shows the dependence of molar absorptivity at 280 nm versus the Eu³⁺/L5 molar ratio.
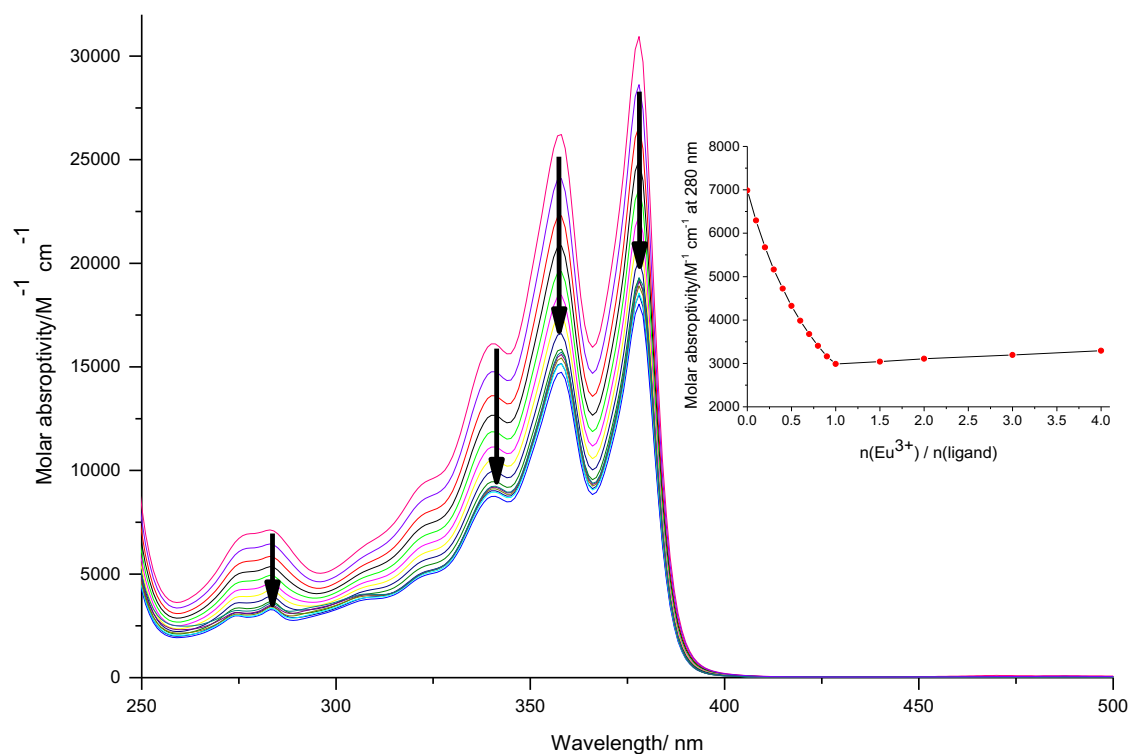
Figure 115: Spectrophotometric titration of the L5 ligand with Eu(NO₃)₃·6H₂O in MeCN at constant ionic strength (10⁻² M NBu₄PF₆) at room temperature. Inset shows the dependence of molar absorptivity at 280 nm versus the Eu³⁺/L5 molar ratio.

The stability constant for these two complexes can only be estimated to be log K ≥ 6.[84] In an attempt to lower the stability constant to a range that could be accurately assessed, the titration of the **L5** ligand was also performed in a DMF solution (Figure 116). The absorption profiles show the same trend after the addition of Eu³⁺ salt. The inset shows no change in molar absorptivity with increasing molar ratio of Eu³⁺ to ligand. These results suggest the Eu³⁺ complex does not form in DMF. While these studies did not allow a comparison of the stability of the complexes formed by **L4** and **L5**, the results were useful in determining the appropriate solvent system to use for photophysical studies.
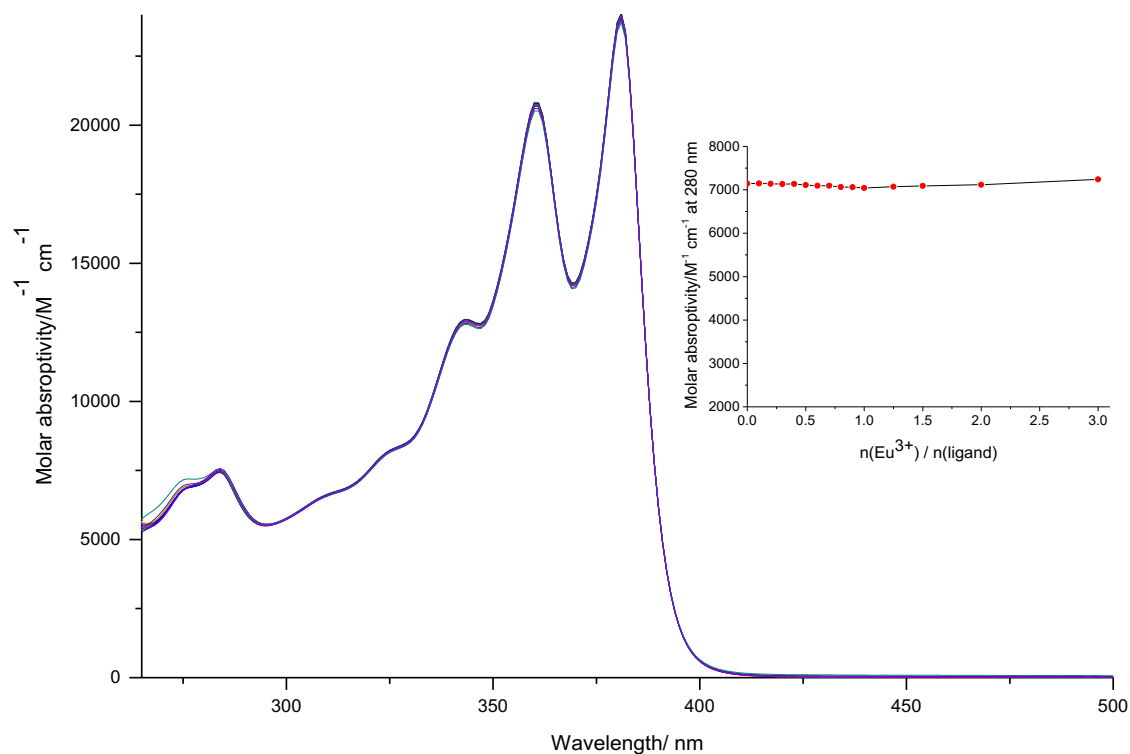
Figure 116: Spectrophotometric titration of the L5 ligand with Eu(NO₃)₃·6H₂O in MeCN at constant ionic strength (10⁻² M NBu₄PF₆) at room temperature. Inset shows the dependence of molar absorptivity at 280 nm versus the Eu³⁺/L5 molar ratio.

3.5 Photophysical Properties of Lanthanoid Complexes

It has been reported that the calixarenetetraamides bind strongly to europium(III),[84] gadolinium(III),[22] neodymium(III)[22] and ytterbium(III)[84]. The attachment of NDI to one of the amide groups should have no significant effect on binding properties. Lanthanoid complexes for photophysical measurements in the solution phase and the solid state were prepared using the same procedure for lanthanoid complexes of bis-NDI substituted ligands.

3.5.1 Energy of Triplet State

In order to find the energy of the triplet state of NDI, the emission spectra of the Gd³⁺ complexes were recorded (Figure 117).
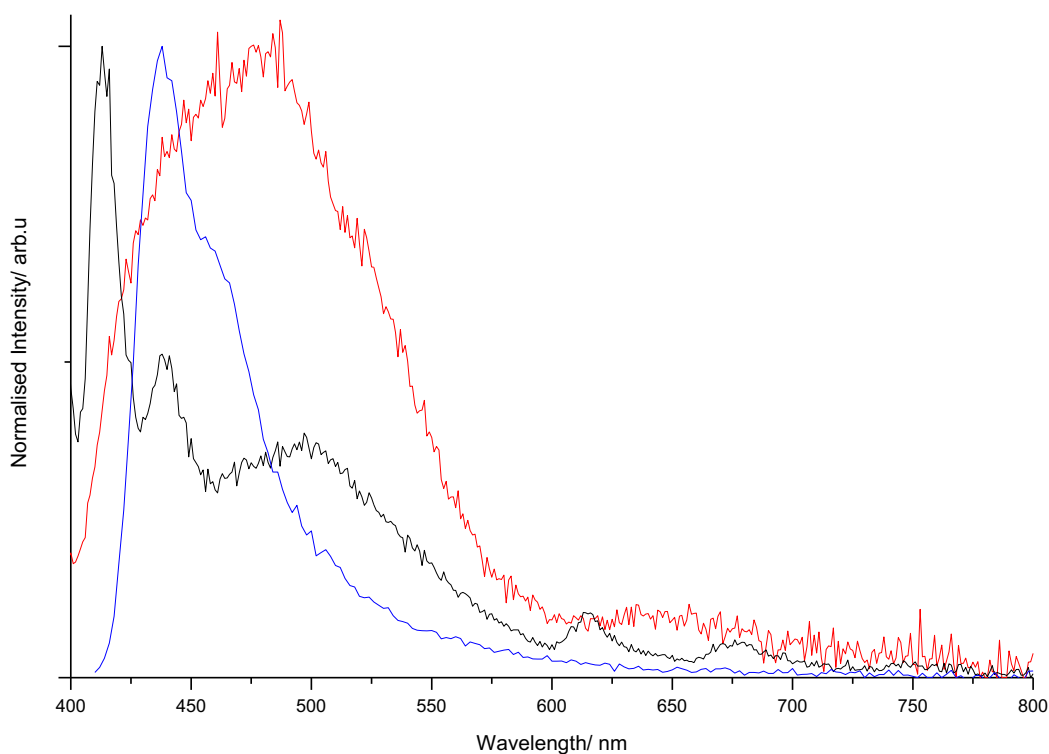
Figure 117: Emission spectra for 10^{-5} M MeCN solutions of the Gd(L4) complex (black trace), Gd(L5) complex (red trace) and Gd(L6) complex (blue trace) at 77K. Excitation wavelength: 340 nm.

By referring to the detailed study of the Gd^{3+} complex of bis-NDI substituted calixarene, the triplet states of NDI and aggregate are estimated to be around 16233 cm^{-1} (616 nm). Despite the weak emission, the phosphorescence peak in the region of 600 – 800 nm is still observed. The phosphorescence peak of NDI in the ligand **L6** was not observed. Therefore, the population of the triplet state of NDI also might depend on the distance between NDI and Gd^{3+}.

As discussed in Chapter Two, the phosphorescence can be induced in the presence of 10% ethyl iodide at 77K. Upon excitation, the several emission bands are observed in the range of 600 - 800 nm in all cases (Figure 118). This result is in agreement with that observed in the case of bis-NDI substituted calixarene ligands. The excited state lifetime decay was fitted to a biexponential function in all cases. However, the lifetimes of both components are shortened in the mono-NDI substituted ligands compared to the bis-NDI derivatives. The values of lifetimes of the peak at 616 nm are 532.9 μs (15%) and 2.5 ms (85%) for **L4** ligand, 687.6 μs (24%) and 2.4 ms (76%) for **L5** ligand, and 684.4 μs (25%) and 2.3 ms (84%) for **L6** ligand, respectively. The major component is assigned to the phosphorescence from NDI monomer, and the minor component is assigned to the phosphorescence from aggregates.
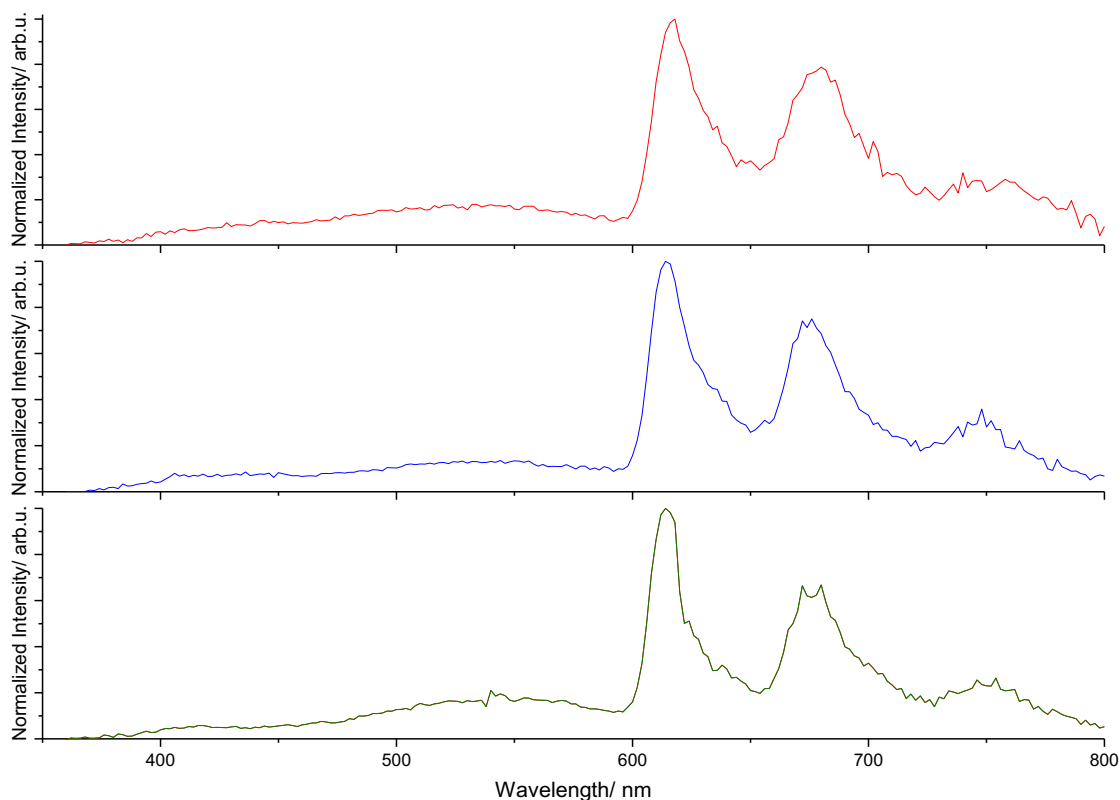
Figure 118: Emission spectra of ligand L4 (red), L5 blue (blue) and L6 (green) in a mixture of MeCN/10%EtI at 77K (10^{-5} M). Excitation wavelength: 340 nm.

3.5.2 Ytterbium(III) Complexes

The emission spectra of the Yb(**L5**) complex in a 10^{-5} M solution, 10^{-4} M MeCN solution and the solid state show one prominent peak at 977 nm with a shoulder centred around 1020 nm (Figure 119). In the excitation spectrum of a 10^{-5} M solution, the prominent peak at 285 nm suggests that the calixarene can work as an antenna to sensitise Yb^{3+} luminescence. The intensity of the peak at 340 nm and 500 nm corresponding to the NDI monomer and aggregate is very low, indicating the poor sensitisation efficiency of NDI. In a 10^{-4} M solution, the excitation spectrum displays an extra broad and structureless band around 490 nm with an identical intensity of peak at 285 nm, indicating that Yb^{3+} luminescence can also be sensitised by aggregated species. In the solid state, the aggregate peak around 500 nm is prominent in the excitation spectrum. The lifetime decay was fitted as a monoexpoential function (Figure 120), and the value was calculated to be 12.4 µs in the 10^{-4} M solution (χ^2= 1.003), 12.0 µs in the 10^{-5} M solution (χ^2= 1.090), and 10.0 µs (χ^2= 1.140) in the solid state, respectively. The overall quantum yield of the Yb(**L5**) complex in a 10^{-4} MeCN solution was measured to be 1.0% after excitation at 285 nm.

Figure 119: Black trace is the excitation spectra, and the red trace is the emission spectra for the Yb(L5) complex. Excitation wavelength: 340 nm. Top: 10^{-5} M MeCN solution; middle: 10^{-4} M MeCN solution; bottom: solid state.
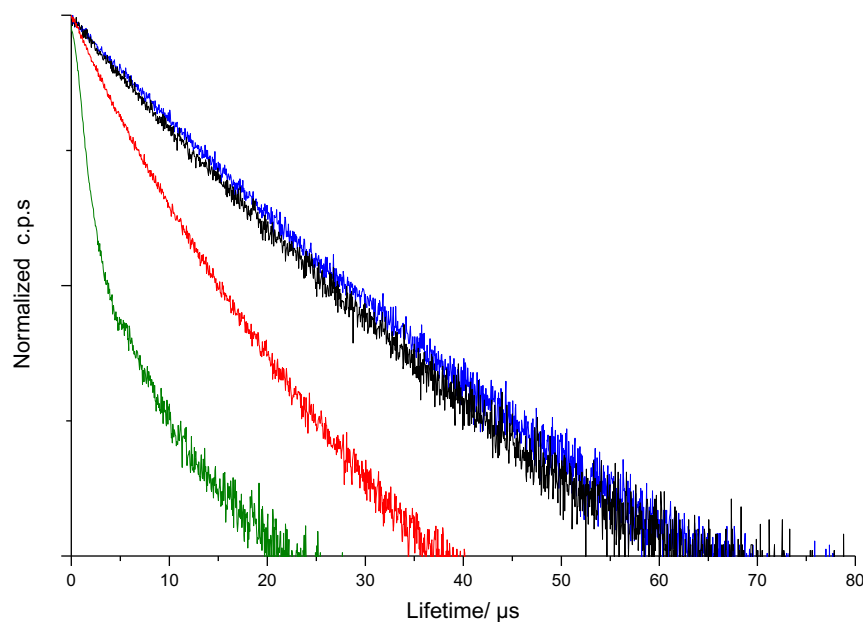
Figure 120: Lifetime decay of the Yb(L5) complex in the 10^{-4} M MeCN (blue trace), 10^{-5} M MeCN (black trace) and the solid state (red trace) at room temperature. The green trace is the instrument response function.

Compared with the ligand **L5**, the ligand **L4** displays less visible NDI and aggregate peaks in the excitation spectra (Figure 121). The excitation spectrum mainly shows one intense peak around 290

nm in a 10^{-5} M solution. The NDI peak at 340 nm is hardly observed due to the poor sensitization efficiency. In 10^{-4} M solution, the excitation spectrum presents a prominent peak at 290 nm and the peak corresponding to the aggregate around 490 nm which is less visible compared with that of ligand **L5**. The emission spectra of the Yb(**L3**)complex in three different conditions are very similar to those of the Yb(**L5**) complex. The observed lifetime decay of the Yb(**L4**)complex was fitted to monoexponential function (Figure 122) and had a value of 10.3 µs in the 10^{-4} M (χ^2= 1.079) and 10^{-5} M MeCN solution (χ^2= 1.086) and 13.2 µs in the solid state (χ^2= 1.062), respectively.

The overall quantum yield of Yb(**L4**) complex in a 10^{-4} MeCN solution was estimated to give a value of 0.5% after excitation at 285 nm. The **L4** and **L5** ligands share a similar structure. The difference between them is that the **L4** ligand is functionalised with secondary amide, while the **L45** ligand is functionalised with tertiary amide. Removal of the hydrogen bond between amide groups on the lower rim has limited effect on the photophysical properties.

Figure 121: Black trace is the excitation spectra, and the red trace is the emission spectra for Yb(L4) complex. Excitation wavelength: 340 nm. Top: 10^{-5} M MeCN solution; middle: 10^{-4} M MeCN solution; bottom: solid state.
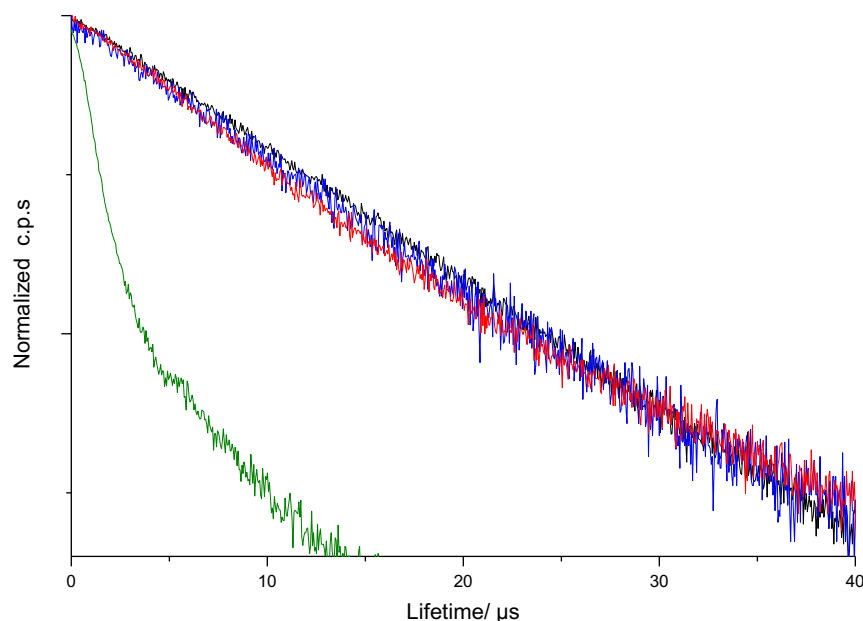
Figure 122: Lifetime decay of the Yb(L4) complex in a 10^{-4} M MeCN (blue trace), 10^{-5} M MeCN (black trace) and the solid state (red trace) at room temperature. The green trace is the instrument response function.

The **L6** ligand links the NDI moiety to the tertiary amide group through six methylene groups, making the NDI further away from the lanthanoid centre. The aggregation behaviours seen in the previous complexes are not observed in the excitation spectrum of the Yb^{3+} complex in a 10^{-4} M solution (Figure 123). The lack of a NDI peak around 340 nm in the excitation spectrum suggests that NDI might be too far away from the Yb^{3+} centre. Therefore, the energy transfer from the NDI to Yb^{3+} does not take place. Increasing the concentration to 10^{-4} M does not improve the sensitisation via the NDI. Only the peak corresponding to the phenol of calixarene is observed below 300 nm. The aggregate peak spanning from 400 to 550 nm can only be observed in the solid state. The emission spectra display characteristic Yb^{3+} emission, which are similar to those of Yb(**L5**) and Yb(**L4**) complexes. The excited-state lifetimes of the Yb(**L6**) complex in a 10^{-4} MeCN solution and solid state were fitted as a monoexponential decay (Figure 124), giving the values of 12.9 μs (χ^2= 1.127) and 9.7 μs (χ^2= 1.082). The overall quantum yield of Yb^{3+} emission in a 10^{-4} M MeCN solution was estimated to be the same as that of the Yb(**L5**) complex, achieving the expected value of 1% after excitation at 285 nm.

Figure 123: Black trace is the excitation spectra, and the red trace is the emission spectra of Yb(L6) complex. Excitation wavelength: 340 nm. Top: 10^{-5} M MeCN solution; middle: 10^{-4} M MeCN solution; bottom: solid state.
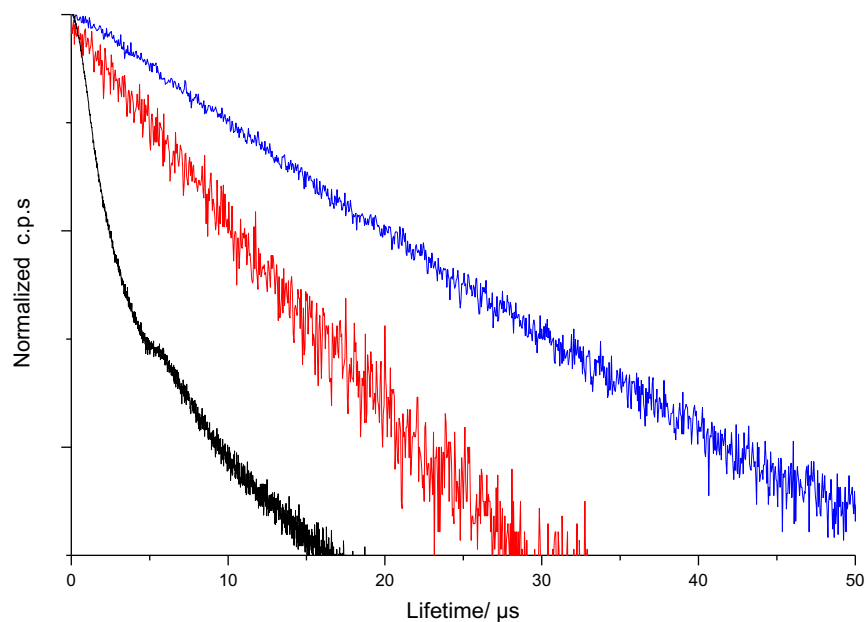
Figure 124: Lifetime decay of Yb(L6) complex in a 10^{-4} M DCM/MeCN (blue trace) and in the solid state (red trace) at room temperature. The black trace is the instrument response function.

131

3.5.3 Neodymium(III) complexes

The combined excitation spectra and emission spectra of the Nd(**L5**) complex are illustrated in
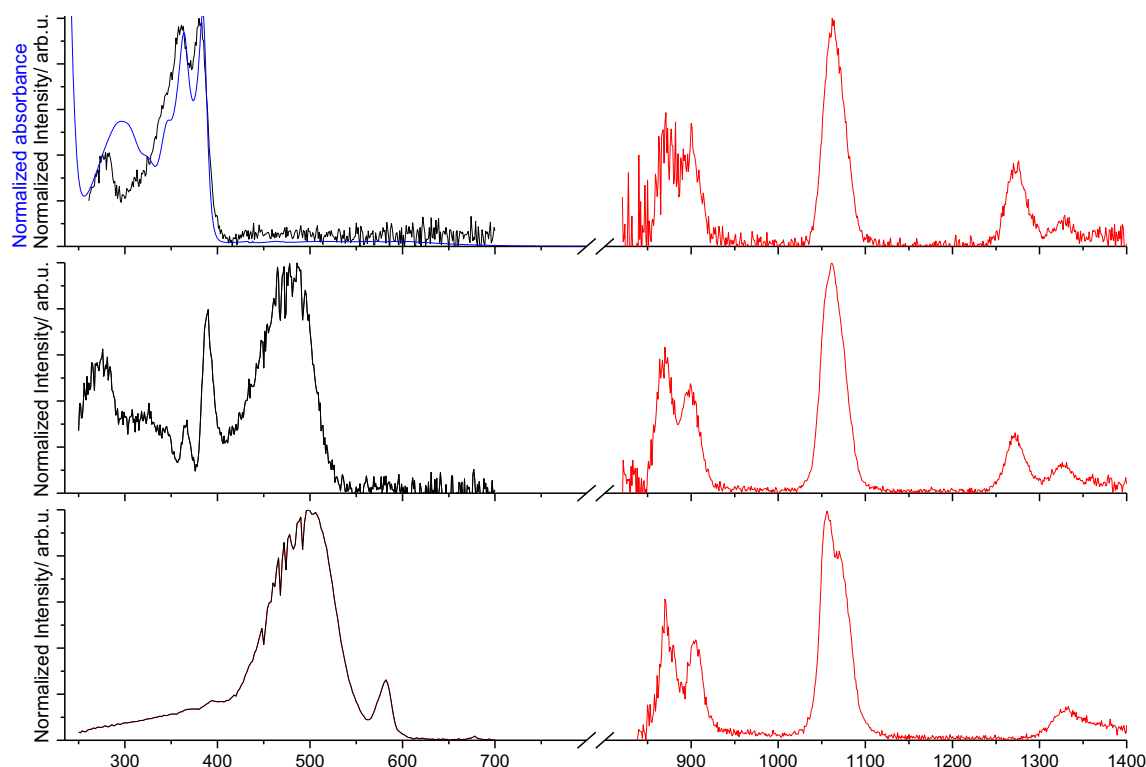
Figure **125**. The emission spectrum of Nd(**L5**) complex shows three emission bands attributed to $^4F_{3/2}$ to $^4I_{9/2}$ transitions at 870 nm, $^4F_{3/2}$ to $^4I_{11/2}$ transition at 1060 nm and $^4F_{3/2}$ to $^4I_{13/2}$ transition at 1320 nm in 10^{-4} M and 10^{-5} M solutions. The emission from the singlet oxygen (1270 nm) is observed as the triplet state of NDI is populated in the solution phase. In the solid state, the peak corresponding to $^4F_{3/2}$ to $^4I_{11/2}$ transition is at 1056 nm and has a shoulder around 1068 nm. The peak corresponding to $^4F_{3/2}$ to $^4I_{13/2}$ transition becomes a broad peak ranging from 1300 nm to 1400 nm.

The intensity of the prominent peak below 400 nm decreases from the 10^{-5} M to 10^{-4} M solution to solid state with increasing intensity of peak around 500 nm in the excitation spectra. This broad and structureless peak around 500 nm is assigned to the aggregate. In a 10^{-5} M solution, this excitation profile is similar to the absorption profile, indicating that the NDI is acting as the antenna moiety resulting in energy transfer to Nd^{3+}.

The peak at 580 nm is visible in the excitation spectrum of complex in the solid state, corresponding to the direct excitation of Nd^{3+} in the solid state. The lifetime of the Nd(**L5**) complex shown in Figure 126 was estimated to be 9.7 μs in a 10^{-4} M MeCN solution (χ^2= 1.037) and 9.9 μs in the solid state (χ^2= 1.067). The lifetime could not be determined in a 10^{-5} M MeCN solution due to the weakness of emission. A deconvolution from the instrumental response function (IRF) was done, and this was done for all lifetime measurements in this project where the decay curve is similar to the IRF.
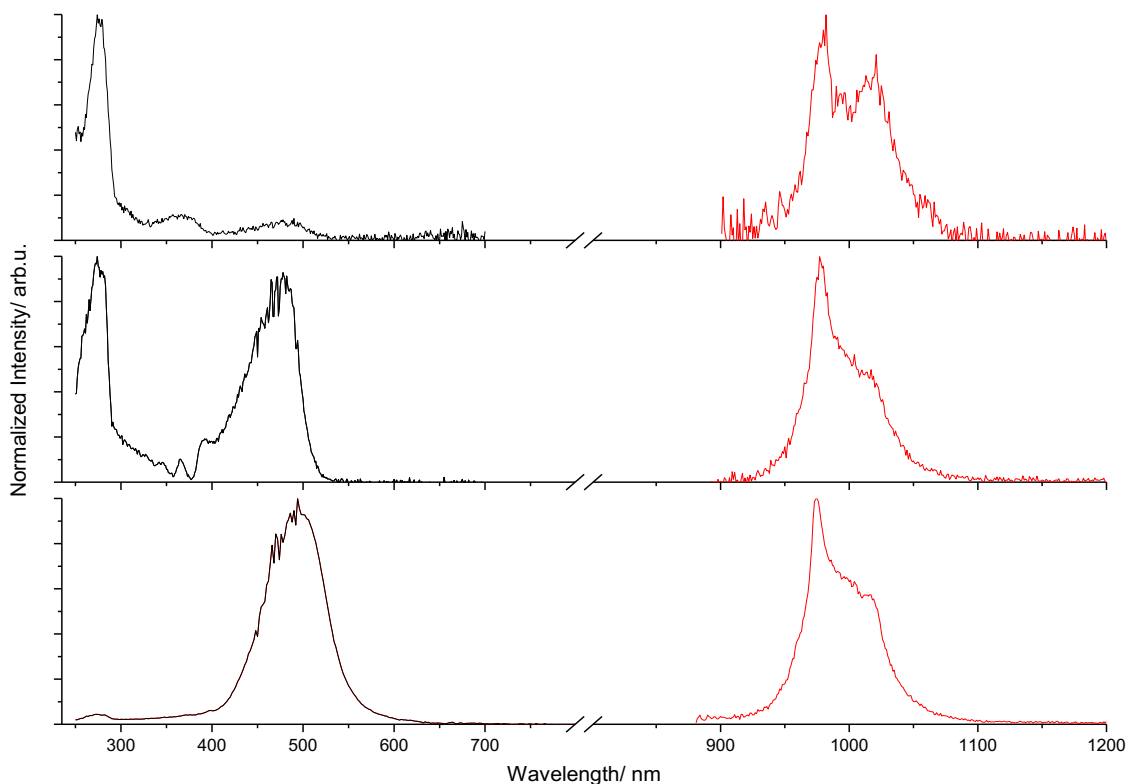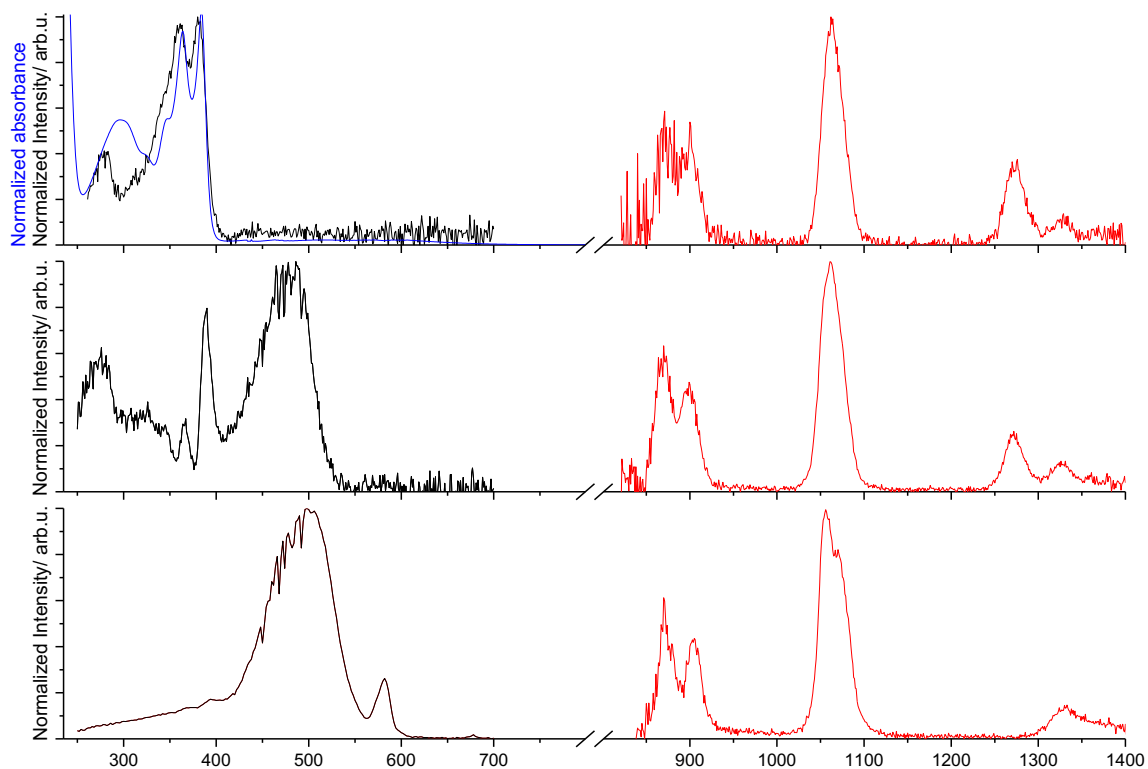
Figure 125: Black trace is the excitation spectra, and the red trace is the emission spectra for the Nd(L5) complex. Excitation wavelength: 340 nm. Blue trace: the normalised absorption spectrum Top: 10^{-5} M MeCN solution; middle: 10^{-4} M MeCN solution; bottom: solid state.
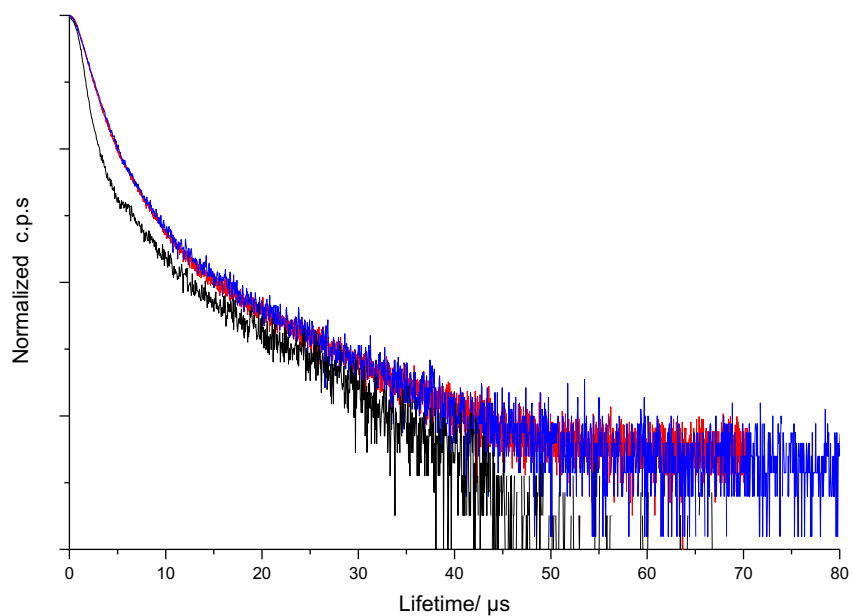
Figure 126: Lifetime decay of the Nd(L5) complex in a 10^{-4} M MeCN (blue trace) and the solid state (red trace) and the instrument response factor (black trace) at room temperature.

An attempt to record the emission spectra of the Nd(**L4**) complex in a 10^{-5} M MeCN solution was unsuccessful due to the weak emission. The emission spectra of the Nd(**L4**)complex display three typical bands associated with $^4F_{3/2}$ to $^4I_{9/2}$ transitions (870 nm), $^4F_{3/2}$ to $^4I_{11/2}$ transition (1060 nm) and $^4F_{3/2}$ to $^4I_{13/2}$ transition (1320 nm) in a 10^{-4} M MeCN solution (Figure 127). Not surprisingly, the peak corresponding to the emission from singlet oxygen is also observed. The excitation spectrum of the Nd(**L4**) complex in a 10^{-4} M solution presents peak at 285 nm, 350 nm, 490 nm and 580 nm corresponding to the phenyl of calixarene, NDI monomer, aggregate and direct excitation of Nd^{3+}. The low intensity of these peaks around 350 nm and 490 nm is suggestive of poor sensitisation efficiency of the NDI monomer and aggregate. In the solid state, both of peaks around 580 nm become more visible with the disappearance of the absorption of phenyl ring. The value of observed lifetime cannot be measured in a 10^{-4} M MeCN solution due to the weakness of emission. Only the observed lifetime in the solid state was measured (Figure 128), giving a value of 9.2 µs (χ^2= 1.136).
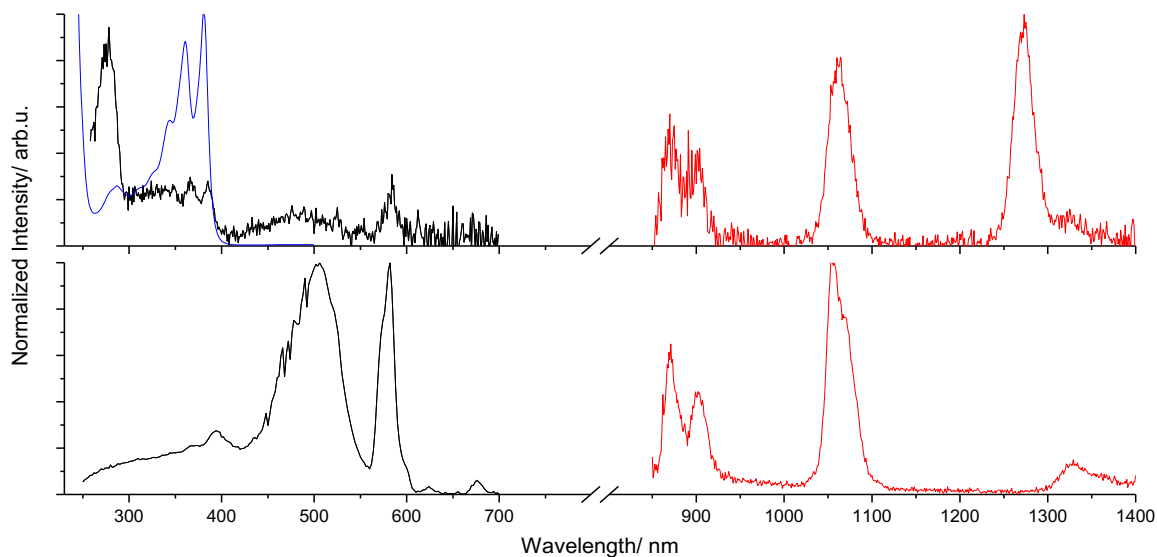
Figure 127: Black trace is the excitation spectra, and the red trace is the emission spectra for the Nd(L4) complex. Excitation wavelength: 340 nm. Top: 10^{-4} M MeCN solution; bottom: solid state.
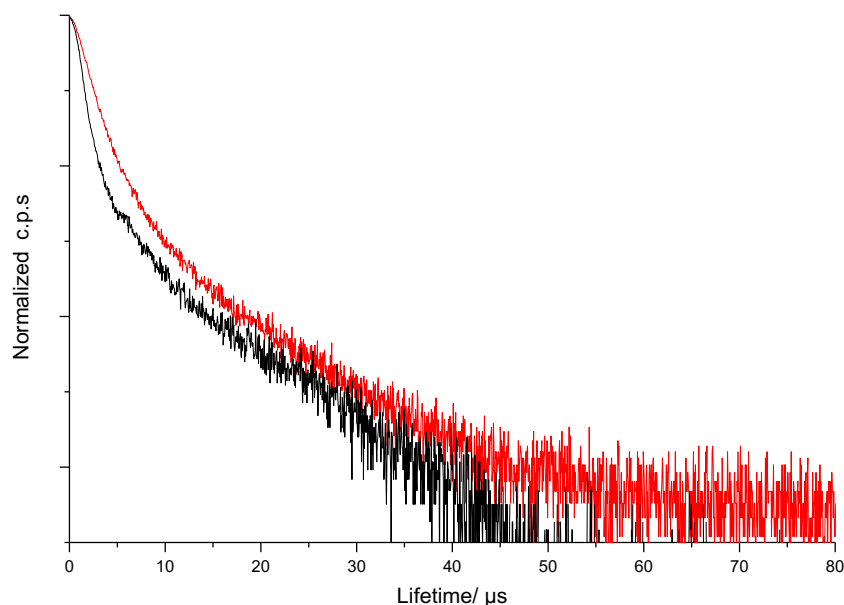
Figure 128: Lifetime decay of the Nd(L4) complex in the solid state (red trace) and the instrument response factor (black trace) at room temperature.

The emission spectra of Nd(**L6**) complex display characteristic Nd^{3+} emission in the NIR region both in a 10^{-4} M solution and the solid state (Figure 129). In a 10^{-4} M solution, the excitation spectrum is analogous to the absorption spectrum, suggesting the Nd^{3+} emission can be sensitized via the phenyl and NDI monomer. This result provides evidence that even if the NDI is far away from the Nd^{3+} centre, the energy can still be transferred to the Nd^{3+}. This contrasts to the results obtained for Yb^{3+} luminescence which was not sensitised by the NDI monomer if it was too distant from the Yb^{3+} centre. In the solid state, the aggregate peak and peak at 580 nm attributed to direct excitation of Nd^{3+} are observed in the excitation spectrum. The excited-state lifetime can only be measured in the solid state, giving the value of 9.3 µs (χ^2= 1.100, Figure 130).
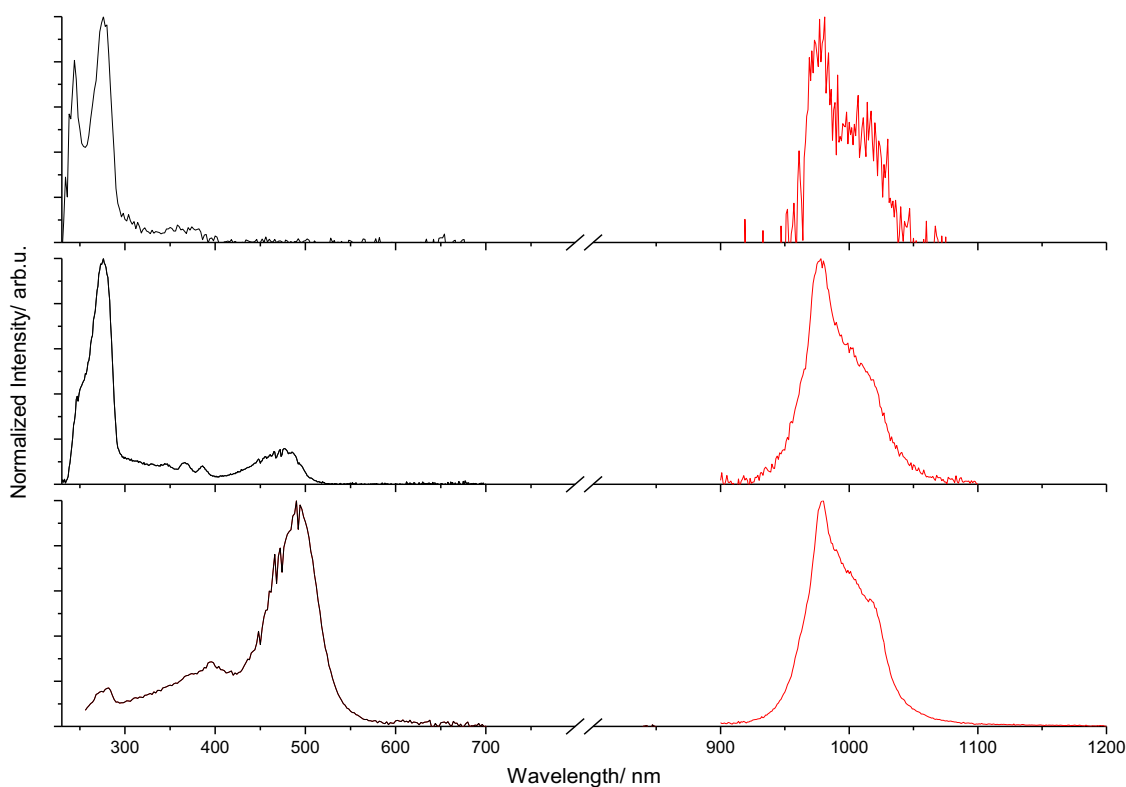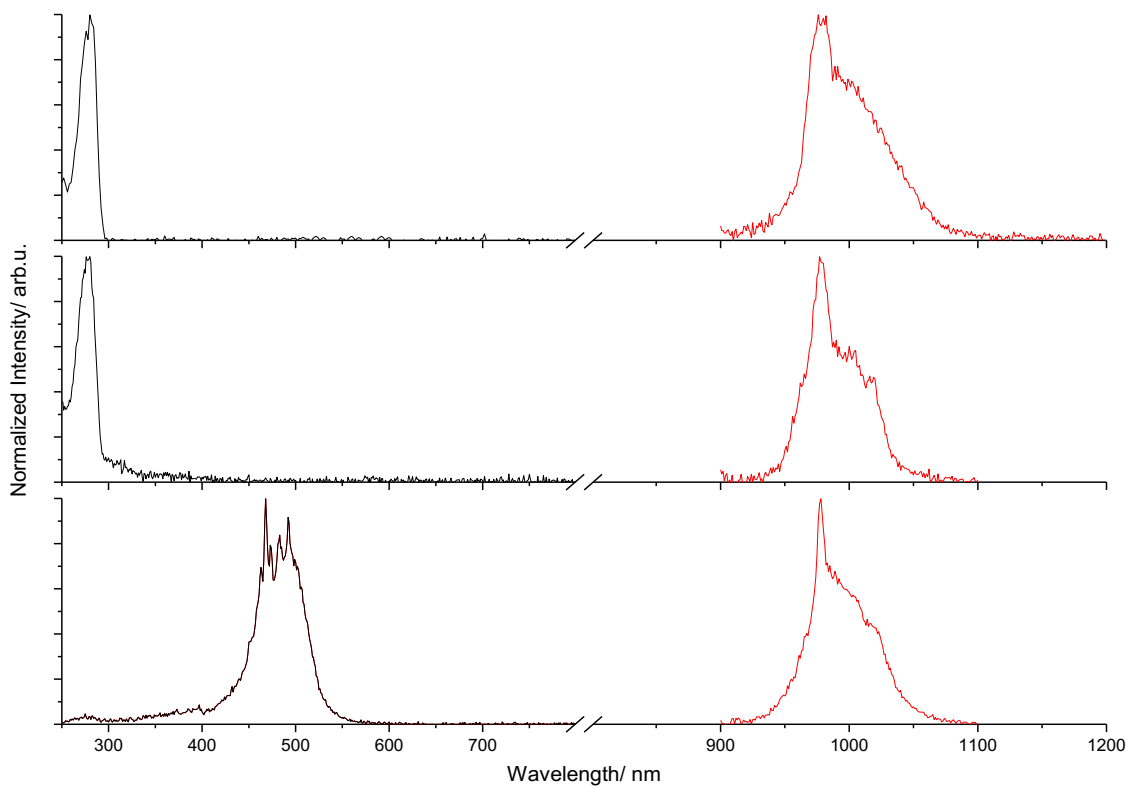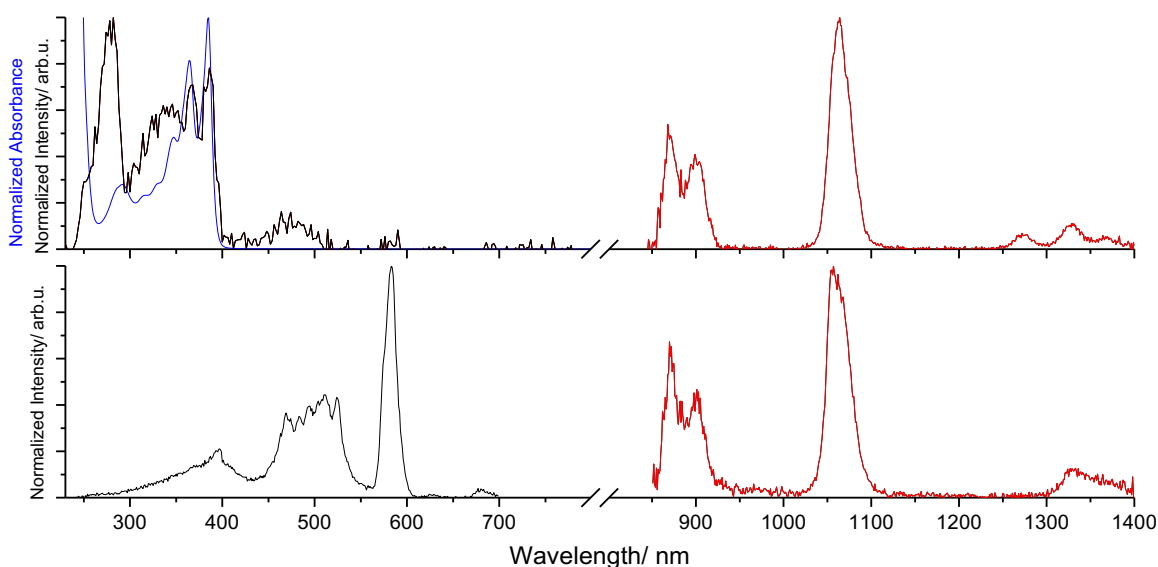
Figure 129: Black trace is the excitation spectra, and the red trace is the emission spectra of the Nd(L6) complex. Excitation wavelength: 340 nm. Blue trace: the normalised absorption spectrum. Top: 10^{-4} M MeCN solution; bottom: solid state.
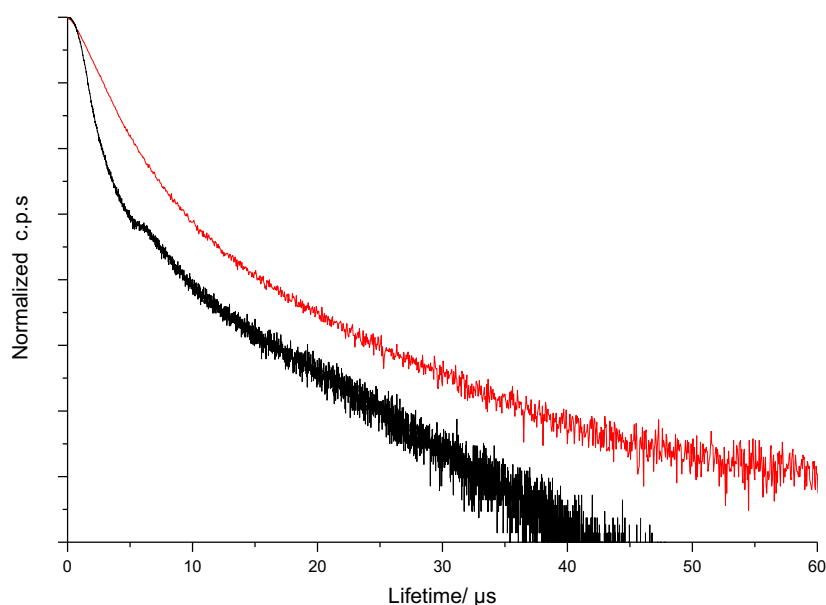
Figure 130: Lifetime decay of the Nd(L6) complex in the solid state (red trace) and the instrument response function (black trace) at room temperature.

3.5.4 Europium(III) Complexes

We have shown that sensitisation of ytterbium(III) and neodymium(III) is achievable by excitation of NDI monomer and aggregate. In this section, investigation of the antenna effect via NDI is extended to Eu^{3+} complexes. The higher energy of the emissive state of Eu^{3+} compared to that of Nd^{3+} and Yb^{3+} was expected to have an impact on the photophysics.

Upon excitation at 340 nm, the emission bands of all Eu^{3+} complex in 10^{-5} M solutions are split into three regions (Figure 131): 1) vibronically structured bands from 350 nm to 450 nm correspond to the fluorescence from the NDI monomer; 2) A broad and structureless band from 450 nm to 580 nm is attributed to the emission from aggregate; 3) The very weak spikes in the remaining bands correspond to emission from the europium(III). The emission spectra of the Eu(**L4**) complex, Eu(**L5**) complex and Eu(**L6**) complex in 10^{-5} M MeCN solutions display two sharp bands centred around 616 nm and 690 nm. These two bands are attributed to the $^5D_0 \rightarrow {}^7F_2$ and $^5D_0 \rightarrow {}^7F_4$ transitions. The $^5D_0 \rightarrow {}^7F_1$ transition at 590 nm is observable only in the case of the Eu(**L5**) complex. The peak at 500 nm corresponding to the aggregate is observed in the Eu(**L5**) complex and Eu(**L6**) complex. The more methylene bridges the ligand has, the more visible the aggregate peak is. The intensity of peak corresponding to Eu^{3+} luminescence is lowest in comparison to that of NDI monomer and aggregate most likely due to the quenching effect of the LMCT state and/or an inefficient NDI sensitisation pathway.[168-169]

136

The excitation spectra were recorded using the emission wavelength at 690 nm to avoid the contribution from aggregates. The absorption spectrum and the excitation spectrum are closely matched in each case, suggesting that the energy transfer to the emissive state of Eu^{3+} is from the NDI. As the energy of the triplet state of NDI is lower than the emissive state of Eu^{3+}, the sensitisation of the Eu^{3+} might be via the singlet state of NDI. The lifetime decay was fitted as monoexponential function in all cases (Figure 132) and observed lifetime is 114.1 µs for the Eu(**L4**) complex (χ^2= 1.734), 633.8 µs for the Eu(**L5**) complex (χ^2= 1.462) and 767.7 µs for the Eu(**L6**) complex (χ^2= 1.758), respectively. The residuals are provided in the appendix.
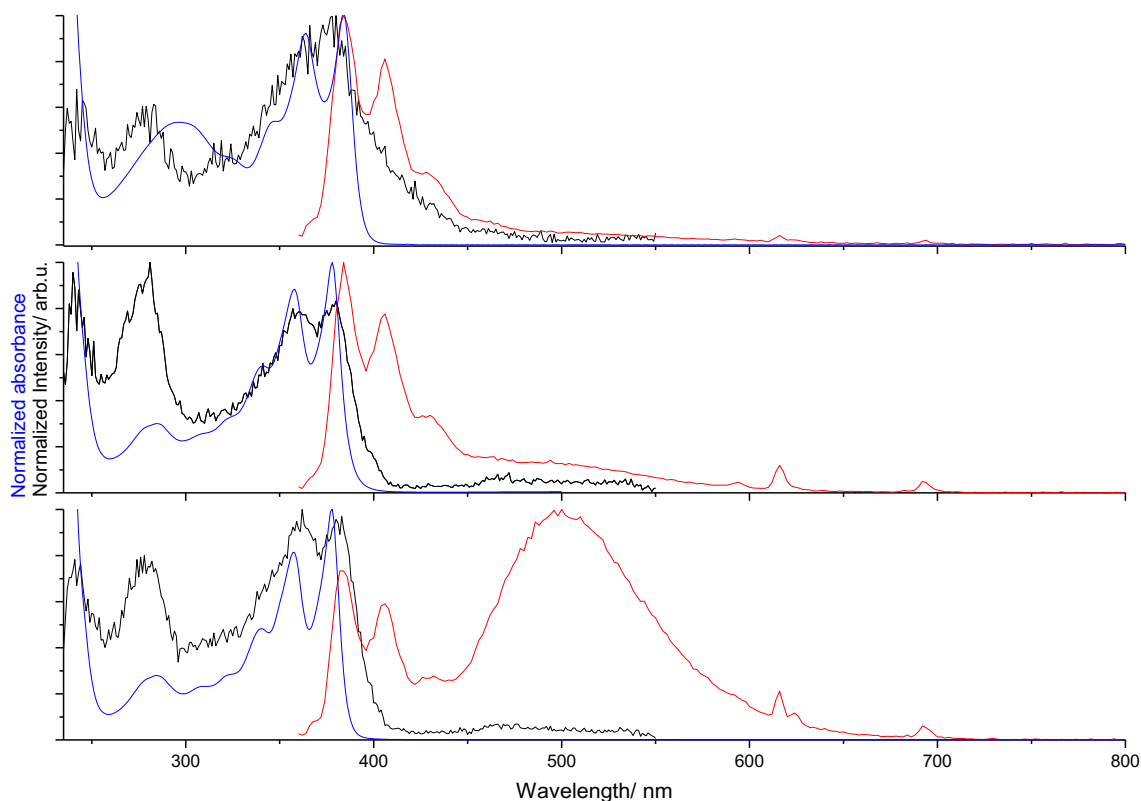
Figure 131: Concentration: 10^{-5} M MeCN solution at room temperature. Black trace: the excitation spectra; red trace: the emission spectra; blue trace: the normalised absorption spectrum. Excitation wavelength: 340 nm. Top: Eu(L4) complex; middle: Eu(L5) complex; bottom: Eu(L6) complex.
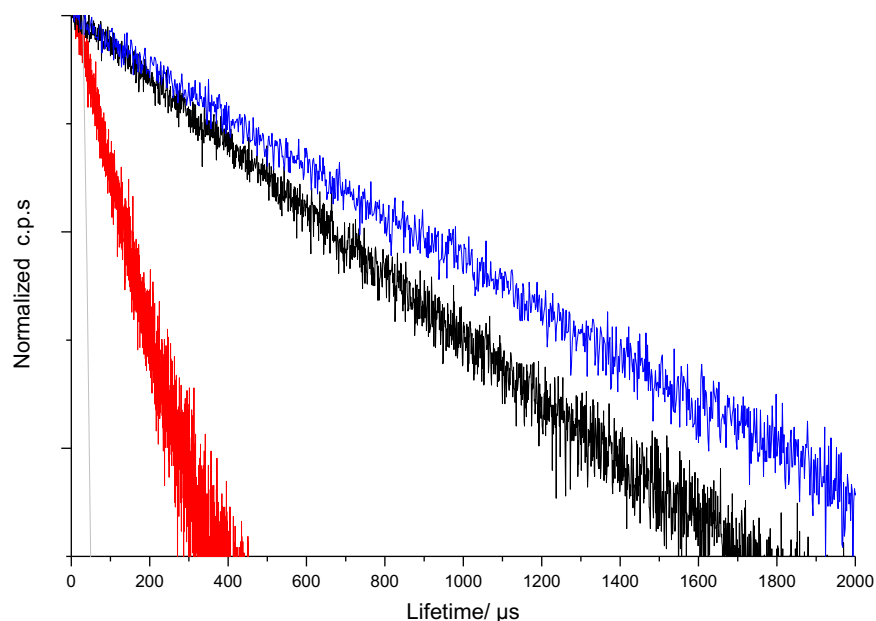
Figure 132: Lifetime decay of Eu^{3+} complexes in 10^{-5} M solutions at room temperature: Eu(L4) complex (red trace), Eu(L5) complex (black trace) and Eu(L6) complex (blue trace). The grey trace is the instrument response function.

In a 10^{-4} M MeCN solution, the emission spectra of these Eu^{3+} complexes display a similar trend to those observed in 10^{-5} M MeCN solutions (Figure 133). In the excitation spectra, a new peak with relatively high intensity with a shoulder around 400 nm is observed, probably caused by inner filter effect or aggregates.[164-165] The observed lifetime was measured in 10^{-4} M MeCN solutions as described previously, giving in all cases a significantly longer lifetime than that measured in 10^{-5} M MeCN solutions. The lifetime decay was fitted as a monoexponential function (Figure 134), giving a value of 121.5 µs for the Eu(**L4**) complex (χ^2= 1.632), 633.8 µs for the Eu(**L5**) complex (χ^2= 1.745),1479.5 µs for the Eu(**L6**) complex (χ^2= 1.800), respectively. The residuals are provided in the appendix.
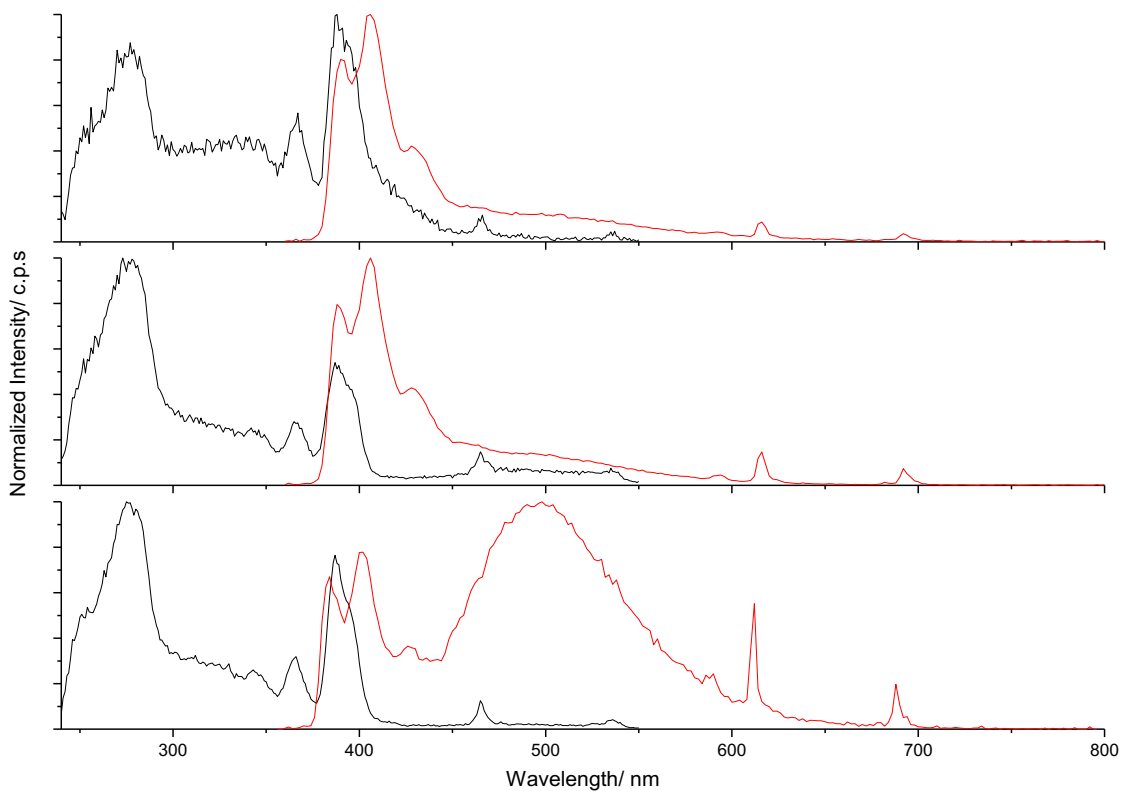
Figure 133: Concentration: 10^{-4} M MeCN solution at room temperature. Black trace: the excitation spectra; red trace: the emission spectra. Excitation wavelength: 340 nm. Top: Eu(L4) complex; middle: Eu(L5) complex; bottom: Eu(L6) complex.
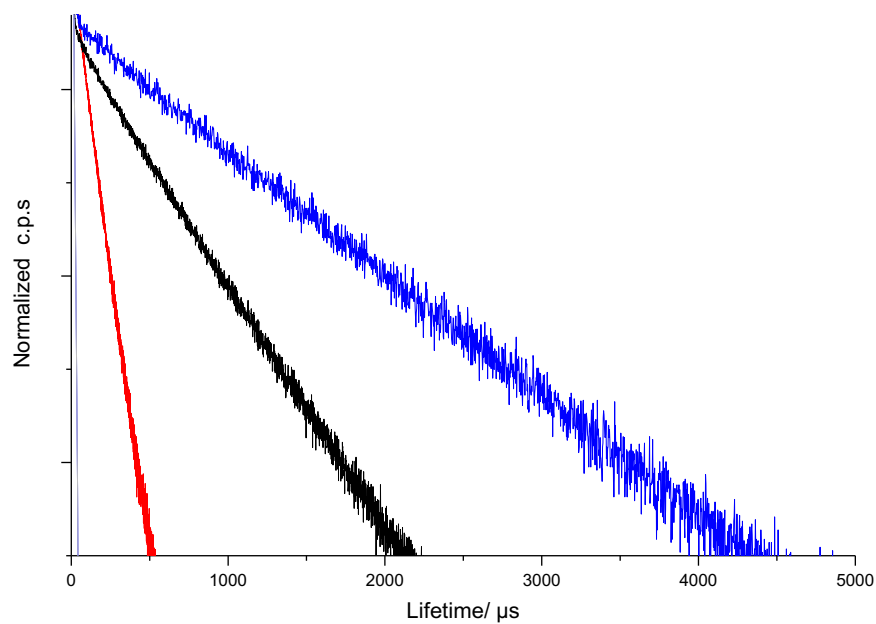
Figure 134: Lifetime decay of Eu^{3+} complexes in 10^{-4} M solutions at room temperature: Eu(L4) complex (red trace), Eu(L5) complex (black trace) and Eu(L6) complex (blue trace). The grey trace is the instrument response factor.

In the solid state, the emission profiles display broad and structureless bands spanning from 400 to 800 nm with a few spikes corresponding to characteristic europium luminescence in all cases (Figure 135). The fluorescent emission from NDI monomer is not observed. The relative intensity of Eu^{3+} spike is significantly higher than the aggregate peak in comparison to those in the solution phase. The excited state lifetime was longer than that of the complexes in the solution phase (Figure 136), giving a value of 515.2 μs for the Eu(**L4**) complex (χ^2= 1.732), 922.7 μs for the Eu(**L5**) complex (χ^2= 1.745), 1479.5 μs for the Eu(**L6**) complex (χ^2= 1.691), respectively. The residuals are provided in the appendix.
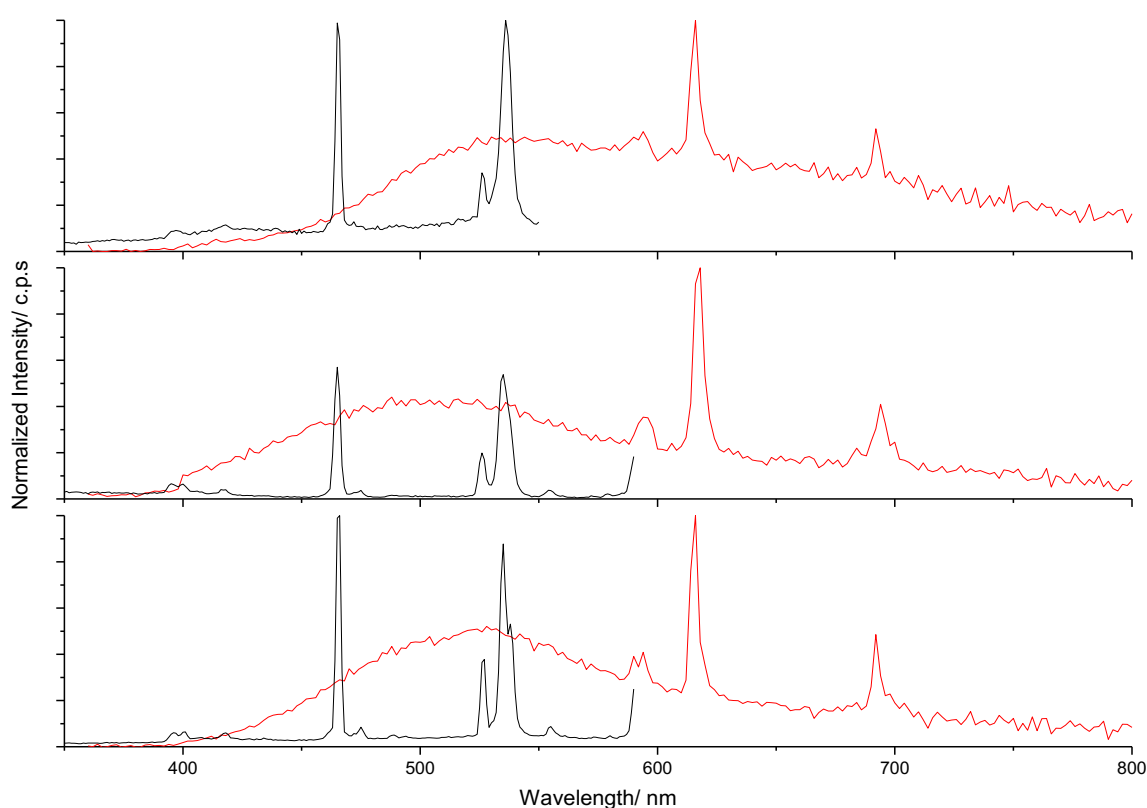
Figure 135: Solid state at room temperature. Black trace: the excitation spectra; red trace: the emission spectra. Excitation wavelength: 340 nm. Top: Eu(L4) complex; middle: Eu(L5) complex; bottom: Eu(L6) complex.
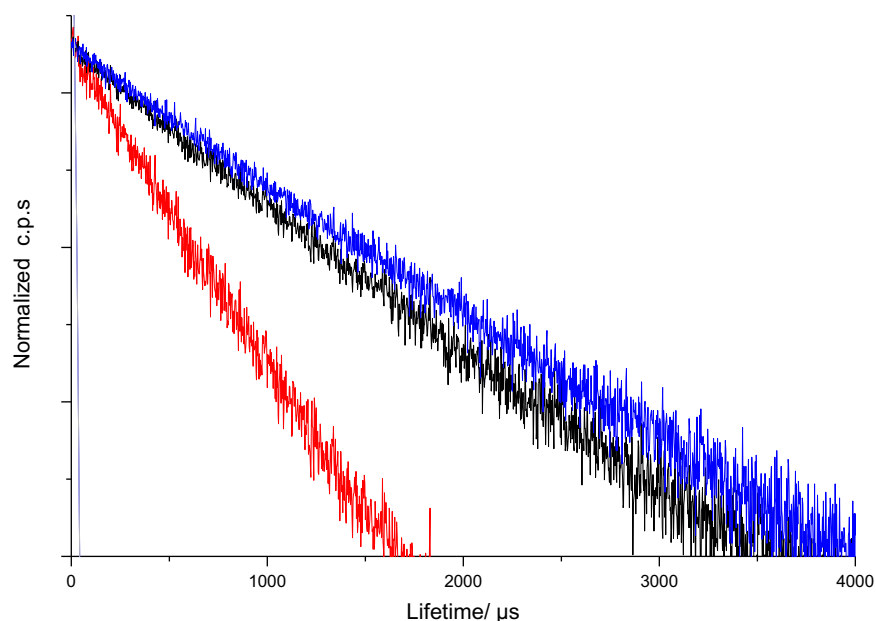
Figure 136: Lifetime decay of Eu^{3+} complexes in the solid state at room temperature: Eu(L4) complex (red trace), Eu(L5) complex (black trace) and Eu(L6) complex (blue trace). The grey trace is the instrument response factor.

The emission from aggregates is in the range from 450 nm to 650 nm, which is overlapped with $^5D_0 \rightarrow {}^7F_0$ (around 580 nm) and $^5D_0 \rightarrow {}^7F_1$ (around 610 nm) emission bands of Eu^{3+}. It could be reasoned that low intensity of the Eu^{3+} bands is due to the back energy transfer process. In order to minimize the back energy transfer and increase the europium(III) luminescence, the emission spectra were recorded at 77K (Figure 137). The emission profiles show that the fluorescence from NDI monomer is not observed. Although the relative intensity of Eu^{3+} spikes is slightly increased in each case in comparison to that observed at room temperature (Figure 131), the aggregate peak is still more visible. The attempt to restrict the back energy transfer to increase the Eu^{3+} luminescence is not successful at 77K. The result is in agreement with the detailed study of Eu(**L3**) complexes that there is no energy transfer between the aggregate state and $^5D_0$ state of europium. The observed lifetime of Eu(**L4**), Eu(**L5**) and Eu(**L6**) complexes (Figure 138) were measured to be 271.3 μs (χ^2= 1.738), 1347.5 μs (χ^2= 1.725) and 1555.5 μs (χ^2= 1.803), respectively when the emission wavelength was selected at 690 nm. The residuals are provided in the appendix.
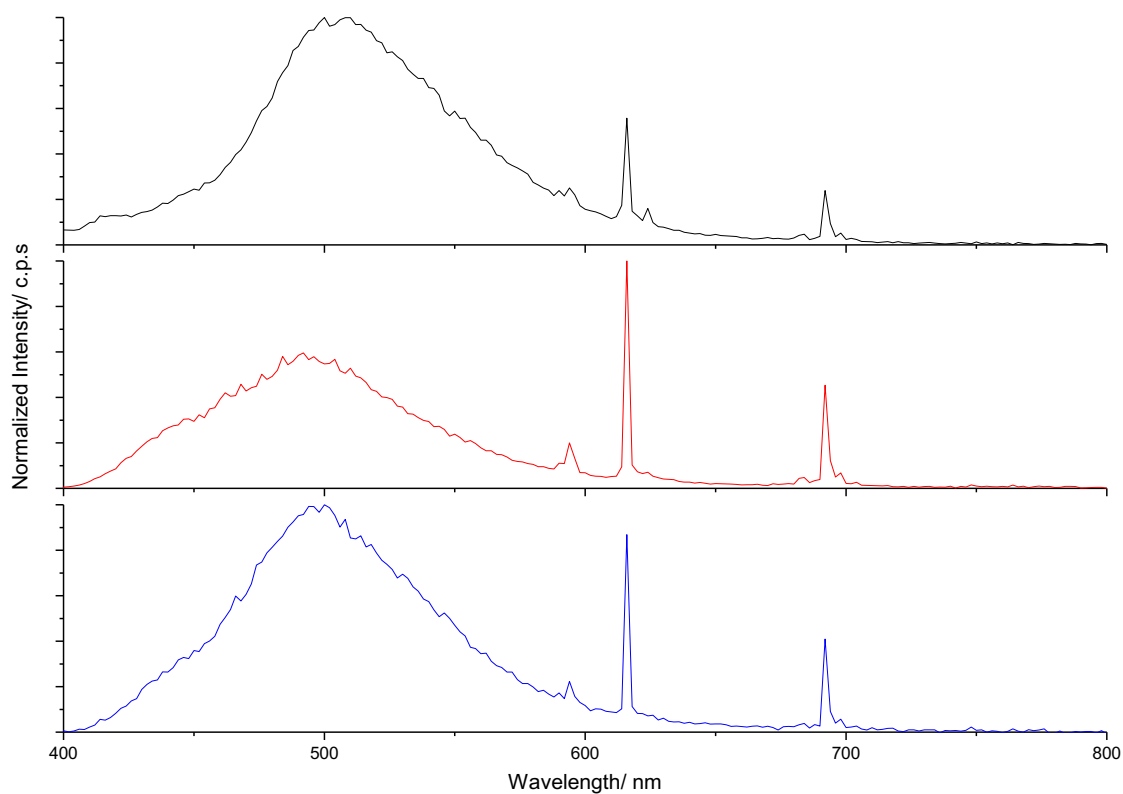
Figure 137: Concentration: 10⁻⁵ M MeCN solution at 77K. Black trace: the excitation spectra; red trace: the emission spectra. Excitation wavelength: 340 nm. Top: Eu(L4) complex; middle: Eu(L5) complex; bottom: Eu(L6) complex.
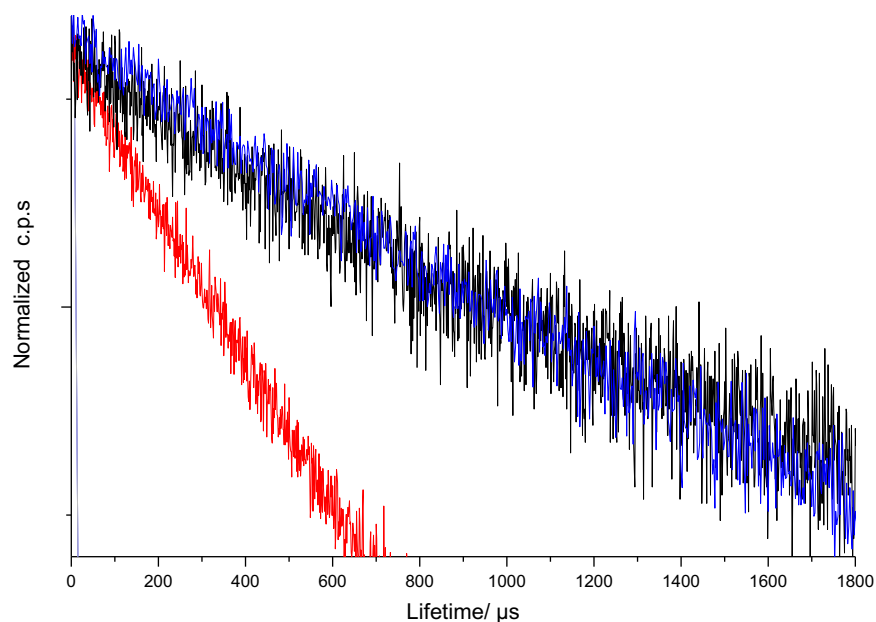
Figure 138: Lifetime decay of Eu³⁺ complexes in 10⁻⁵ M solutions at 77K: Eu(L4) complex (red trace), Eu(L5) complex (black trace) and Eu(L6) complex (blue trace). The grey trace is the instrument response factor.

The frequency of vibration of bonds such as NH plays an important role in quenching the lanthanoid luminescence. Compared with the lifetime (50.1 µs) of Eu(**L3**) complex with two NH groups in 10^{-5} M solution at room temperature, the observed lifetime in the case of Eu(**L4**) complex with one NH group is longer (114.1 µs). While the observed lifetime of Eu(**L5**) complex as well as Eu(**L6**) complex without NH groups is much longer (271.3 µs and 767.7 µs). Although the NH group does not coordinate directly to the europium, it is in the outer coordination sphere which is not far away from the coordination centre. This result is expected because NH group is an efficient quencher which can shorten the excited-state lifetime.

Table 13: A summary of the photophysical properties of Eu(III), Yb(III), and Nd(III) complexes

Complex	Concentration/Media	τ_{obs} (µs)		ϕ_{Ln}^{L}(%)
				Ex = 285 nm
Yb(**L4**)	MeCN 10^{-5} M (RT)	10.3		
	MeCN 10^{-4} M (RT)	10.3	λ_{em} = 980 nm	0.5
	powder	13.2		
Nd(**L4**)	MeCN 10^{-5} M (RT)	-		
	MeCN 10^{-4} M (RT)	-	λ_{em} = 1060 nm	
	powder	9.2		
Eu(**L4**)	MeCN 10^{-5} M (RT)	114.1		-
	MeCN 10^{-5} M (77K)	271.3		-
	MeCN 10^{-4} M (RT)	121.5	λ_{em} = 690 nm	-
	powder	515		-
Yb(**L5**)	MeOH 10^{-4} M (RT)	550.8		
	MeOD 10^{-4} M (RT)	1216.9		
	MeCN 10^{-4} M (RT)	12.4	λ_{em} = 980 nm	1.0

	powder	10.0		-
	MeCN 10^{-5} M (RT)	-		-
Nd(**L5**)	MeCN 10^{-4} M (RT)	9.7	λ_{em} = 1060 nm	-
	powder	9.9		-
Eu(**L5**)	MeCN 10^{-5} M (RT)	571.3		-
	MeCN 10^{-5} M (77K)	1347.5	λ_{em} = 690 nm	-
	MeCN 10^{-4} M (RT)	633.8		-
	powder	922.7		-
Yb(**L6**)	MeCN 10^{-4} M (RT)	12.9	λ_{em} = 980 nm	1.0
	powder	9.7		-
Nd(**L6**)	MeCN 10^{-4} M (RT)	-	λ_{em} = 1060 nm	-
	powder	9.3		-
Eu(**L6**)	MeCN 10^{-5} M (RT)	767.7		-
	MeCN 10^{-5} M (77K)	1555.5	λ_{em} = 690 nm	-
	MeCN 10^{-4} M (RT)	1479.5		-
	powder	1084.1		-

[a]Quantum yield is measured against the toluene solution of Yb(TTA)$_3$Phen (ϕ = 1.6%). Ex is the excitation wavelength.

It was reported that a solvent molecule, such as water, could coordinate to the metal centre in lanthanoid complexes with a tetra-amide functionalised calixarene.[22] We measured the lifetime in nondeuterated and deuterated solvents, and calculated the number of coordinated solvent molecules using a method proposed by Horrocks.[23-24] The emission spectra of Eu(**L4**) complex in MeOD and MeOH solutions at room temperature are similar (Figure 139). The decay curves were found to fit the monoexponential function, giving the value of 1216.9 μs (χ^2= 1.812) and 550.8 μs (χ^2= 1.652), respectively. The residuals are provided in the appendix. Based on the calculation (Eqn 5), these two values suggest there are two MeOH/MeOD molecules coordinating directly to the Eu^{3+} centre.
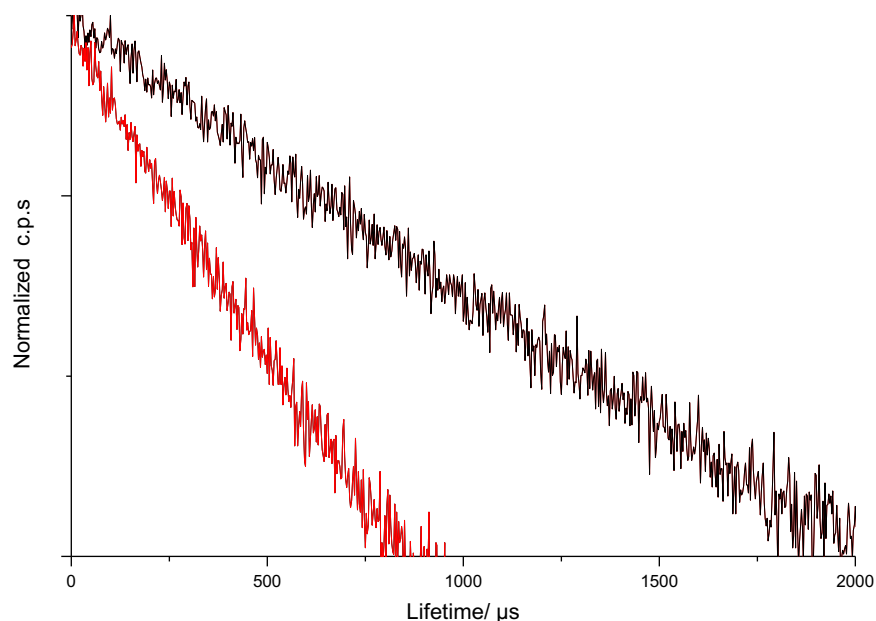
Figure 139: Lifetime decay of the Eu(L4) complex in 10^{-4} M MeOH (black trace) and 10^{-4} M MeOD (red trace) at room temperature.

$$M = 2.1 \times (\tau_{MeOH}^{-1} - \tau_{MeOD}^{-1}) \qquad \textbf{Eqn 5}$$

$$M = 2.1 \times (1/0.551 - 1/1.217)$$

$$M = 2.08 \sim 2 \text{ molecules}$$

3.6 Electrochemical Properties of Ligands

Electrochemical behaviours of the **L4** and **L5** ligand were investigated under the same conditions of bis-NDI substituted calixarene ligands. Cyclic voltammogram shows there are two single electron redox processes in the case of the **L4** ligand (Figure 140). The first one electron charge transfer process corresponds to the reduction of neutral NDI to the NDI radical anion. The second process occurs when the NDI radical anions are further reduced to dianions. Two sequential cathodic peaks at -973 mV and -1450 mv versus Fc+/Fc correspond to the generation of NDI$^{\bullet-}$ and NDI^{2-}.
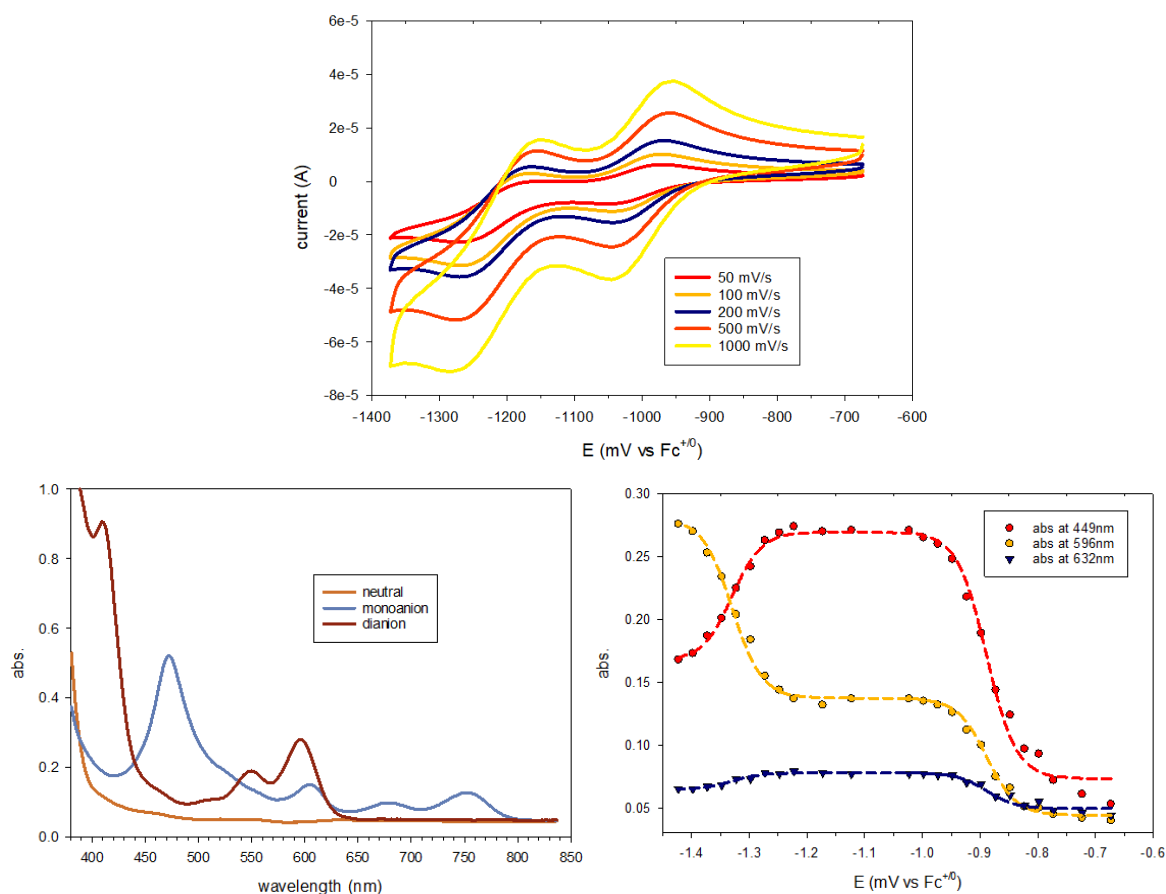
Figure 140: Top: cyclic voltammograms of the ligand L4 in MeCN (0.1 M Et₄NClO₄). Work electrode: 0.5 mm radius Pt electrode. Bottom left: absorption spectrum in a cell in MeCN for the neutral ligand L4 (orange trace), radical anion (blue trace) and dianions (red trace). Bottom right: absorption during the conversion of the ligand L4 and formation of radical anion and dianions observed in the potential range of -0.6 V to -1.5 V.

Spectroelectrochemistry (SEC) analysis was performed under the same conditions for cyclic voltammetry except for the working electrode. The SEC was done with a Pt working electrode while the CVs were done with a glassy carbon electrode, but that should not affect the redox potential. The Cell does not transmit below about 360 nm due to the limitation of the instrument. Therefore, the absorption spectrum can only be reported in the range of 360 to 850 nm. There are no peaks corresponding to the neutral ligand in the range. After reduction of neutral ligand to its corresponding radical anions form, the spectrum displays four peaks in this range of 400 - 800 nm, indicating the electronic transition of D_0 to D_n. After the second electroreduction from radical anion to dianions, these bands disappeared with the emergency of new absorptions peaks at 410 nm with a shoulder at 400 nm, 550 nm and 600 nm. Analysis of the absorbance at 449 nm, 596 nm and 632 nm as a function of the applied potential reveals changes occurring when the potential reaches -0.89 V. These values remains constant until the potential reaches -1.33 V, driving the formation of NDI^{2-} at the expense of $NDI^{\bullet-}$. All these results are consistent with those reported for reduction of NDI.
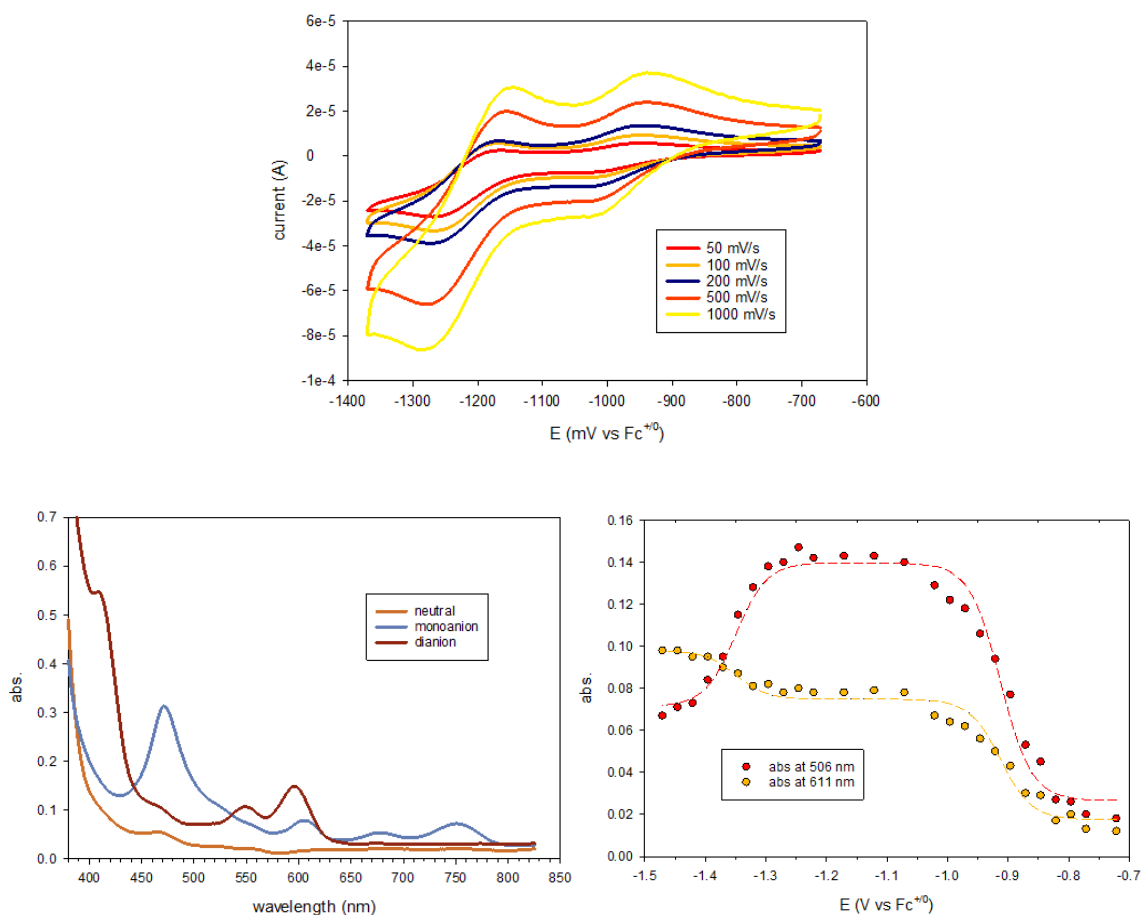
Figure 141: Top: cyclic voltammograms of the L5 ligand in MeCN (0.1 M Et₄NClO₄). Work electrode: 0. 5 mm radius Pt electrode. Bottom left: absorption spectrum in a cell for the neutral the L5 ligand (orange trace), radical anion (blue trace) and dianions (red trace). Bottom right: absorption during the conversion of the L5 ligand and formation of radical anion and dianion observed in the potential range of -0.7 V to -1.5 V.

Similar results were obtained for **L5** (Figure 141). The CV measurements show the reduction potentials of NDI/ NDI $^{•-}$ and NDI $^{•-}$/NDI^{2-} are a little more negatively shifted with the value of -0.91 V and -1.35 V vs Fc$^{+/0}$. The absorption bands are the same as those in the case of the **L4** ligand. The trends of each peak in the spectrum of the absorbance as a function of the applied potential are rather similar.

R = H, n = 2
R = CH₃, n = 3
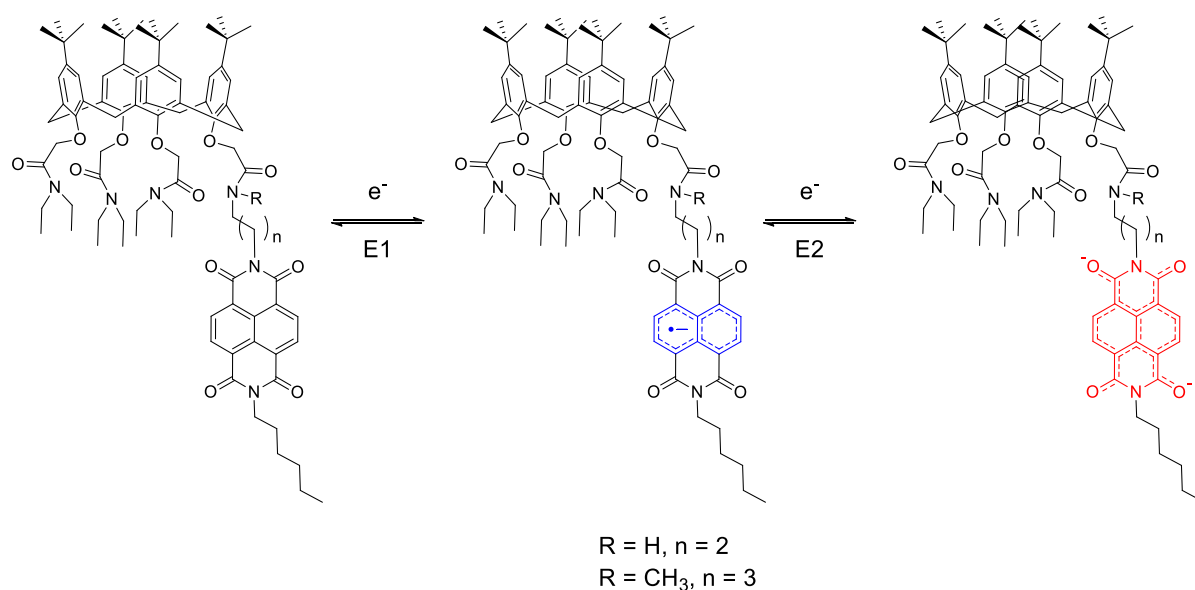
Scheme 25: Sequential reduction of L4 and L5.

3.7 Conclusion

The aims to investigate the structural properties of mono-NDI substituted calixarene ligands have been achieved. Three mono-NDI substituted calixarene ligands, **L4**, **L5** and **L6**, have been successfully synthesised and fully characterised. The ligand **L6** was the only one of these found to form an aggregate in the absence of metal ions. Complexation was confirmed by titration experiment using UV-visible spectroscopy, which shows an inflection point at the 1:1 metal to ligand ratio in acetonitrile solutions. Complexation did not appear to occur in a DMF solution. Two methanol molecules were found to coordinate directly to the lanthanoid centre in methanol solution.

Secondly, the photophysical properties of mono-NDI substituted calixarene ligands and corresponding lanthanoid complexes have been investigated. Despite the poor sensitisation efficiency, the ligand **L4** and **L5**, which have shorter methylene bridges, can still sensitise the Yb^{3+} luminescence in 10^{-5} M solutions. In 10^{-4} M solutions, the energy transfer to the Yb^{3+} is from the calixarene as well as the aggregate. In the case of ligand **L6**, the Yb^{3+} luminescence can only be induced by intramolecular energy transfer from the calixarene aromatic groups. Only the NDI of ligand **L5** can sensitise the Nd^{3+} luminescence in a 10^{-5} M MeCN solution. When the concentration is increased to the 10^{-4} M solution, the inner filter effect and aggregate may lead to the more complex energy transfer processes. But it is unambiguous that even if the NDI is not close to the coordination centre, the sensitisation of Nd^{3+} still takes place via the antenna effect from the NDI.

Spectroelectrochemical studies confirmed that the NDI radical anion, and dianion could be formed with **L4** and **L5**. While time and travel restrictions prevented more detailed studies, the spectroscopic results obtained were sufficient to guide subsequent chemical generation of the radical anion species.

4 Exploring NDI Radical Anion as an Antenna

4.1 Introduction

Most examples of the antenna effect, including the results in Chapter 2 and 3, are assumed to involve excitation of the lanthanoid by energy transfer from the singlet or triplet excited state. Energy transfer from the doublet state has not been reported to our knowledge. Here, it was hypothesized that energy transfer from the doublet state could be explored by taking the NDI functionalized calixarenes reported in the previous Chapters, and reducing these to the radical anions.

The classic method for the preparation of NDI radical anion in solution involves the addition of reductants under a nitrogen atmosphere, such as sodium dithionite,[111] tetrakis(dimethylamino)ethylene (TDAE),[172] cobaltocene,[109, 112] sodium cyanide[173] and hydrazine.[113-114] Alternatively, it can be obtained from bulk electrolysis experiments.[106, 174] After the successful reduction, the resulting photophysical properties of the ligand **L5**$^{\bullet-}$ and Ln(**L5**$^{\bullet-}$) complex were explored using absorption spectroscopy and emission spectroscopy. The possibility of lanthanoid sensitization via the doublet state of NDI radical anion will be discussed.

4.2 Synthesis of Naphthalenetetracarboxylic Diimide Radical Anion

In an attempt to generate NDI radical anion, tetrakis(dimethylamino)ethylene (TDAE) was used to donate the electron to and reduce the neutral NDI. [172] We use TDAE as a reductant for the following reasons: 1) TDAE will not reduce Ln^{3+} to Ln^{2+}. For example, the Nd^{III}/ Nd^{II} couple is around −2.60 V, and the Yb^{III}/ Yb^{II} couple is around −1.05 V,[2] whereas the TDAE/TDAE$^{\bullet+}$ potential and TDAE^{+}/TDAE^{2+} potential are at -0.78 V and -0.61 V repsectively.[175] 2) Compared with cobaltocene, the TDAE does not contain metal ions or chromophores which could have an impact on photophysical results. 3) Compared with the alternative reductants tetrabutylammonium fluoride[116, 176-177] and $Na_2S_2O_4$[111], TDAE can selectively reduce the NDI and form the desired radical anion without the risk of the formation of the radical dianion. 4) Alternative techniques, such as bulk electrolysis, are not needed in the synthetic laboratory.

The synthesis of the NDI radical anion can be achieved following the modified literature procedure for the preparation of the rylenediimide radical anion (Scheme 26).[172, 178] The neutral ligand **L5** or its corresponding Ln(**L5**) complex was dissolved in a dry MeCN solution in a Schlenk flask. The solution was degassed via three freeze-pump-thaw cycles and then was transferred to a prepared Schlenk cuvette purged with nitrogen. The TDAE was added under positive nitrogen flow. The Schlenk cuvette was sealed for the photophysical measurements.

In the photophysical measurements described in the previous Chapters, the lanthanoid complexes were formed *in situ* by adding a metal salt to a solution containing the ligand. Here, to avoid introducing trace amounts of water with lanthanoid salt precursors, which may destabilise the radical anion, the Yb(**L5**) complex was isolated and dried under a nitrogen atmosphere before being used.
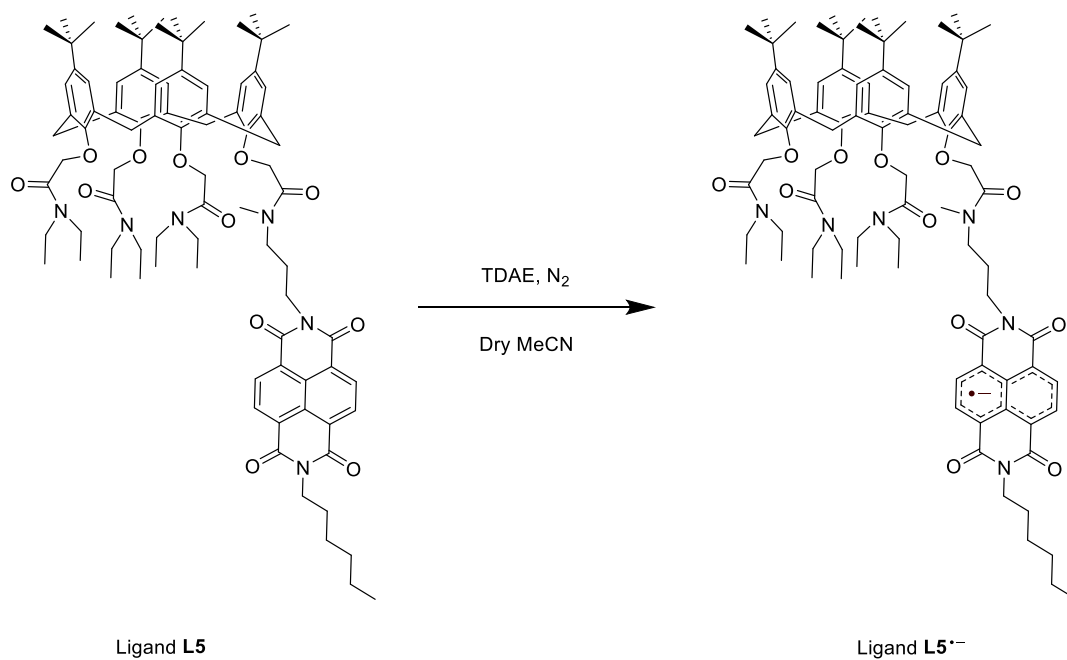
Ligand **L5**   Ligand **L5**·⁻

Scheme 26：Synthesis of L5·⁻ ligand.

4.3 Photophysical Investigation

4.3.1 Absorption Results

The absorption spectra of the neutral ligand **L5** and Yb(**L5**) complex in air-equilibrated MeCN solutions (*ca.* 10^{-4} M), and their corresponding radical anion in N_2-equilibrated MeCN solutions (*ca.* 10^{-4} M) were recorded (Figure 142).
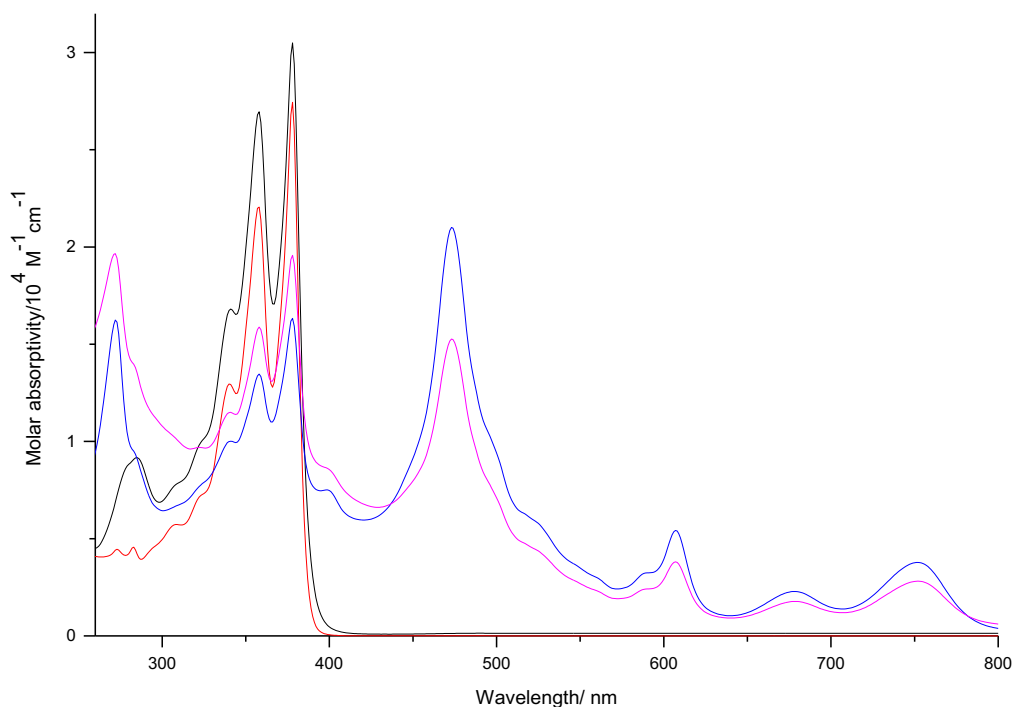
Figure 142: Absorption spectra for 10^{-4} M MeCN solutions of the ligand L5 (black trace), Yb(L5) complex (red trace), ligand L5$^{\bullet-}$ (blue trace) and Yb(L5$^{\bullet-}$) complex (pink trace).

The absorption data have been summarised in Table 14.

Table 14: Summary of the absorption data of the L5, Yb(L5), L5$^{\bullet-}$ and Yb(L5$^{\bullet-}$) in acetonitrile solutions at room temperature.

Compound	λ_{abs} [nm] (10^4 ε [M^{-1} cm^{-1}])
L5	278 (0.8728), 286 (0.9127), 310 (0.1087), 323 (0.9941), 341 (1.6829), 360 (2.641), 378 (3.0498)
Yb(**L5**)	274 (0.2573), 285 (0.3091), 307 (0.4082), 322(0.5122), 339(0.9254), 359 (1.6957), 378 (1.5986)
L5$^{\bullet-}$	273 (1.614), 340 (0.9940), 359 (1.3340), 379 (1.5934), 475 (2.0963), 524 (0.5605), 589 (0.3244), 608 (0.5393), 679 (0.2275), 753(0.3773)
Yb(**L5$^{\bullet-}$**)	273 (2.1754), 342 (1.4828), 359 (2.1558), 377 (2.6774), 402 (0.9454), 475 (2.2783), 524(0.6484), 589(0.3681), 609(0.5883), 678 (0.2561), 753 (0.4162)

The absorption spectra of the ligand **L5$^{\bullet-}$** or the Yb(**L5$^{\bullet-}$**) complex display three regions corresponding to three different chromophores (Figure 142). The absorption band below 300 nm in the ultraviolet region is assigned to the π-π* transition of phenyl rings of calixarene. The band spanning in the visible region from 300 to 400 nm is attributed to the $S_o \rightarrow S_1$ transition of neutral NDI. The ligand **L5$^{\bullet-}$** also also exhibits an absorption peak around 490 nm with a shoulder around 530 nm, a peak around 610 nm with a shoulder around 580 nm and a peak around 675 nm, all of which are assigned to $D_o \rightarrow D_n$

(n>1) transitions. The peak at 750 nm corresponds to the $D_0 \rightarrow D_1$ transition. It has been reported there are no absorption peaks of the radical monoanion in the NIR region (up to 1000 nm). These results are consistent with the previously reported data.[118] There is no significant difference between the ligand **L5**$^{\bullet-}$ and Yb(**L5**$^{\bullet-}$) complex in the absorption spectra. The peaks corresponding to $D_0 \rightarrow D_n$ transitions in the lower energy bands are not observed in the neutral **L5** ligand or Yb(**L5**) complex.

Having obtained the absorption spectrum of ligand **L5**$^{\bullet-}$ and Yb(**L5**$^{\bullet-}$) complex generated by chemical reduction, the attention was turned to compare with the spectra of the ligand generated by electrochemical reduction *in situ* (Figure 143, blue trace). The absorption spectrum of spectroelechemistry shows similar absorption bands in the region of 400 - 800 nm no matter which method is employed. The slight difference is that the peak at 600 nm is a broad peak in SEC, while there is a peak with a shoulder in chemical reduction. This is probably due to the spectral resolution and sensitivity of the instrument. The peaks attributed to the transition of NDI dianion are not observed, which should be observed when the potential moves more negatively. This result confirms the attempt to produce the NDI radical anion by TDAE is successful.
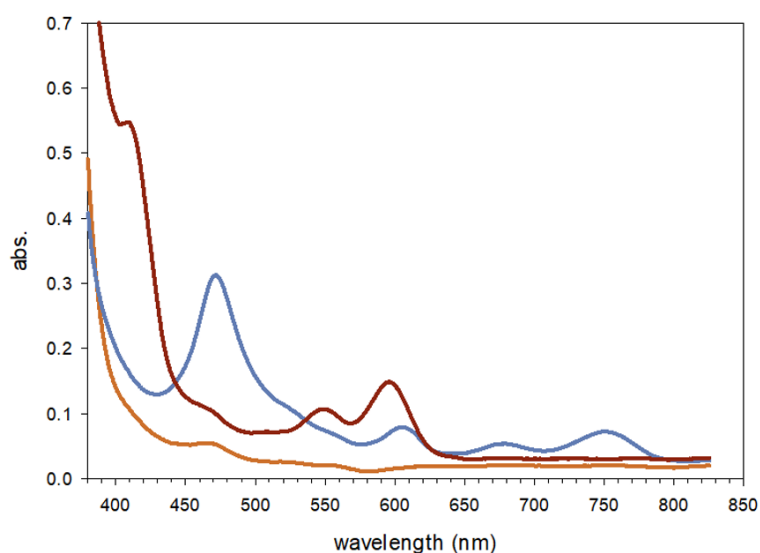
Figure 143: The emission spectrum of ligand L5$^{\bullet-}$ generated by electrochemical reduction. ligand L5, orange trace; ligand L5$^{\bullet-}$, blue trace; ligand L5^{2-}, red trace.

4.3.2 Emission Properties of Ligand Radical Anion

Two equivalents of the TDAE were added for the rest of photophysical measurements. The aim was to stabilise the ligand **L5**$^{\bullet-}$ and its corresponding lanthanoid complexes because photophysical data, such as the lifetime, took some time to collect.

Upon excitation at 460 nm, 510 nm, 600 nm and 690 nm, all emission spectra show a sharp emission peak around 780 nm as well as an emission peak at 860 nm with a shoulder centred at 950 nm in the NIR region. The relative intensity of these peaks can not be compared due to the different detectors. Even if the NDI radical anion was excited to a higher energy state, the molecule still relaxed to its lowest energy excited state via internal conversion following Kasha's law. Therefore, the emission spectrum of ligand **L5**$^{\bullet-}$ is independent of the excitation wavelength (Figure 144). Combined with the

absorption spectrum, this emission is attributed to the radiative emission from the lowest excited doublet state (Figure 145). The energy of the doublet state is obtained from the intersection point of the absorption spectrum and emission spectrum, which is calculated to be 13054 cm^{-1} (766 nm). The emission profiles feature the structured emission band with a vibronic progression around 1320 cm^{-1}. A search of the literature relating to the photophysical data of the NDI radical anion only found the steady-state absorption and transient absorption data.[102, 106, 114-115, 118, 170] To the best of our knowledge, this is the first observation of emission from the excited doublet state of NDI in steady-state measurement. The excited state lifetime is too short to be measured with our instrumentation (TCSPC, 50 ns).
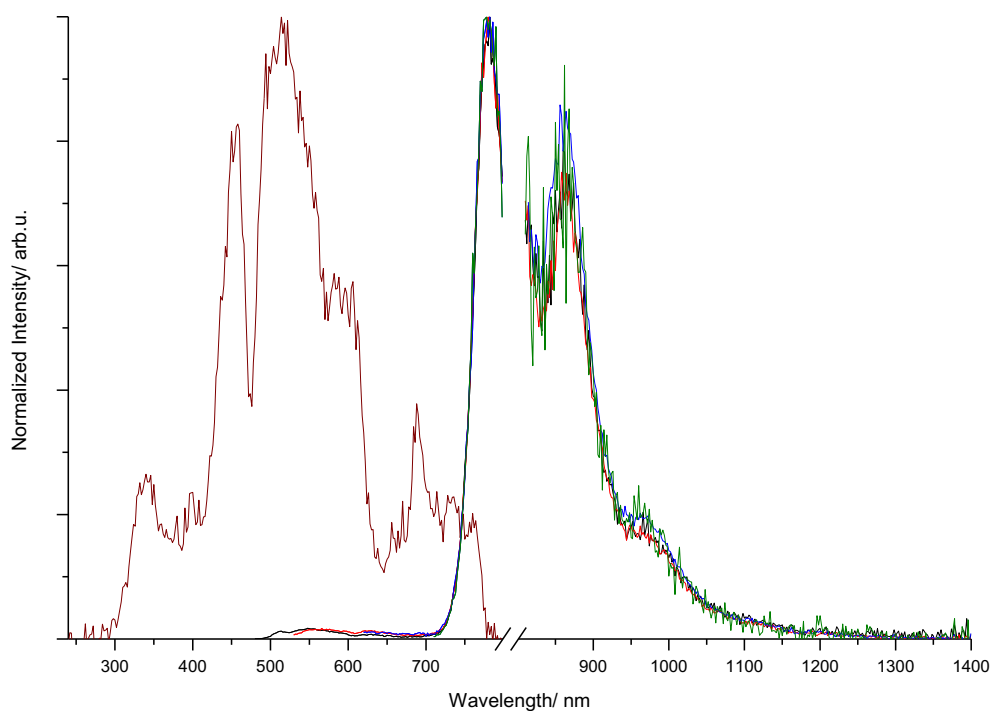
Figure 144: Normalized excitation spectrum of the L5$^{\bullet-}$ (brown trace) and normalized emission spectra, (λ_{exc} = 460 nm, black trace), (λ_{exc} = 510 nm, red trace), (λ_{exc}=600 nm, blue trace) and (λ_{exc} = 690 nm, green trace) in a nitrogen-equilibrated dry MeCN solution (*ca.*10^{-4} M).
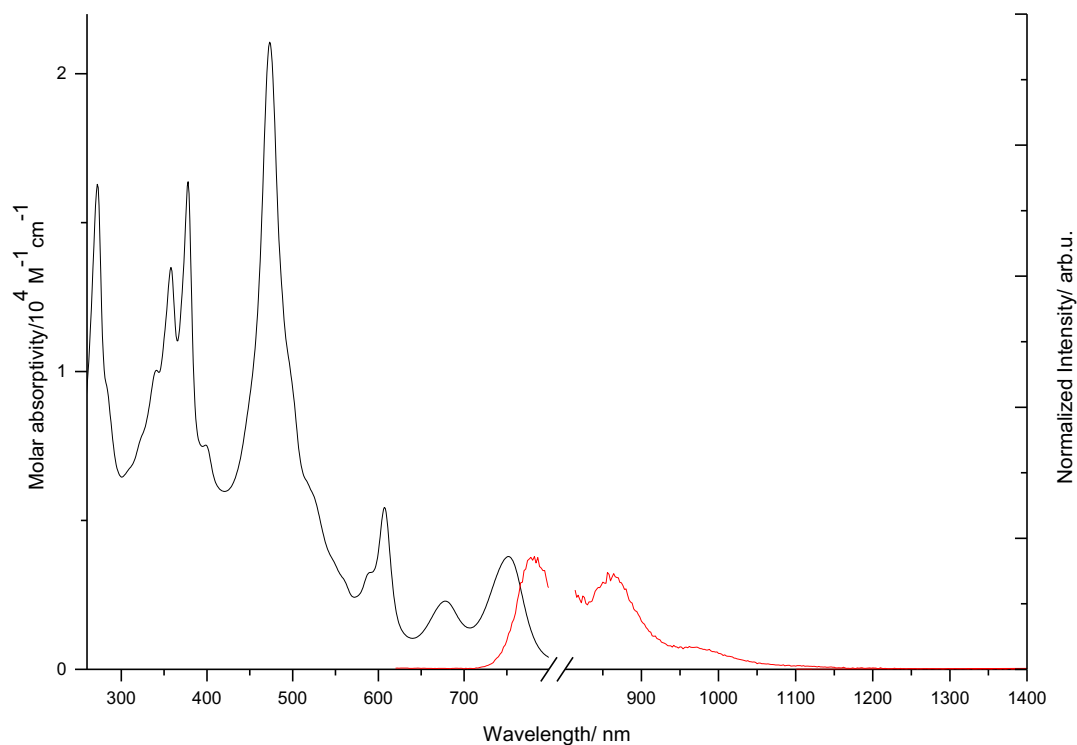
Figure 145: Black trace: absorption spectrum of a 10^{-4} M MeCN solution of ligand $L5^{\bullet-}$; Red trace: emission spectrum of the ligand $L5^{\bullet-}$ (λ_{exc} = 460 nm) in a nitrogen-equilibrated dry MeCN solution (10^{-4} M).

4.3.3 Emission Properties of Ytterbium(III) and Neodynium(III) complex

Yb(III) and Nd(III) precursors are chosen for two reasons: Firstly, NDI/NDI$^{\bullet-}$ redox couple is around -1000 mv, well clear of the Yb$^{III/II}$ or Nd$^{III/II}$ redox couples. Secondly, the energy of emissive state of the Yb(III) and Nd(III) is relatively low, making it possible for the radical anion to sensitise its luminescence. Upon excitation, the emission band of Nd($L5^{\bullet-}$) complex is analogous to that of the ligand $L5^{\bullet-}$ observed in the NIR region. The characteristic Nd^{3+} emission in the NIR region is not observed. This result suggests the emissive state of Nd(III) is not populated by excitation of the NDI radical anion.

However, in the case of the Yb($L5^{\bullet-}$) complex, the emission profiles reveal the vibronically structured emission of the NDI radical anion around 780 nm upon excitation at 460 nm, 510 nm, 600 nm and 690 nm (

Figure **146**). The emission spectrum in the NIR region shows emission from the lowest excited doublet state of NDI radical anion as well as a spike at 980 nm corresponding to the $^2F_{5/2} \rightarrow {}^2F_{7/2}$ transition of Yb^{3+}. Since the peak attributed to direct excitation of Yb^{3+} is in the NIR region, the energy transfer therefore must be concluded to be occurring from the doublet state of the NDI radical anion to the Yb^{3+} centre. The excited-state lifetime of Yb($L5^{\bullet-}$) complex in a 10^{-4} MeCN solution was fitted to a monoexponential decay function, giving a value of 10.8 µs (χ^2= 1.310, Figure 147). The residuals are shown in the appendix. The excitation wavelength used for the lifetime decay measurement was 750 nm, and the deconvolution from the instrumental response function was done.
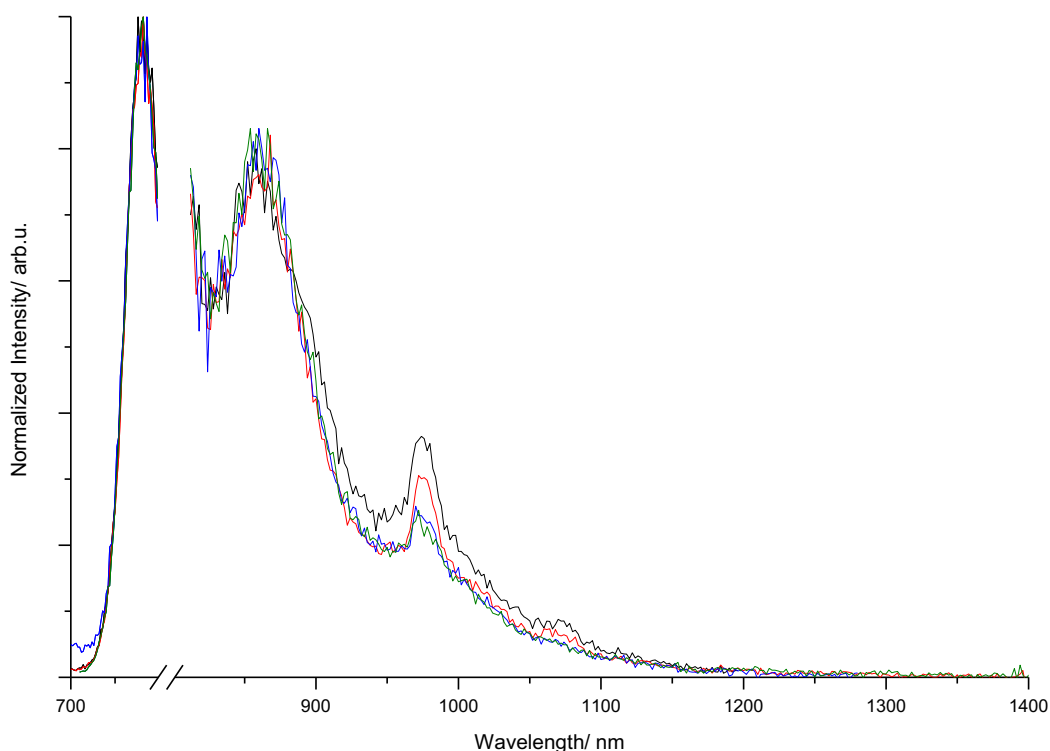
Figure 146: Normalized normalized emission spectra of the Yb(L5$^{\bullet-}$) complex (λ_{exc} = 460 nm, black trace), (λ_{exc} = 510 nm, red trace), (λ_{exc} = 600 nm, blue trace) and (λ_{exc} = 690 nm, green trace) in a nitrogen-equilibrated MeCN solution(ca.10^{-4} M).
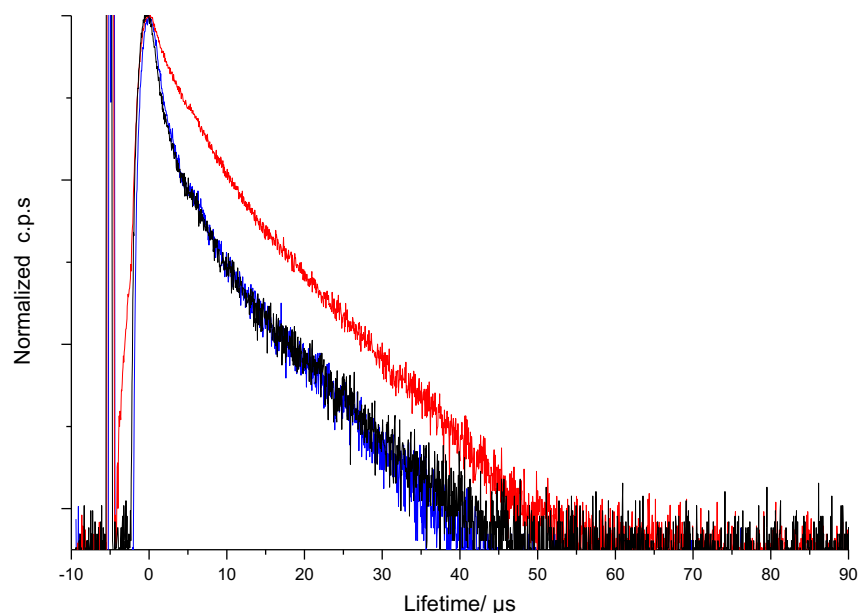
Figure 147: Lifetime decay of the Yb(L5$^{\bullet-}$) complex after dissolution in a nitrogen-equilibrated MeCN solution (*ca.*10^{-4} M) at room temperature. Excitation wavelength: 750 nm. Emission peak at 980 nm, red trace; emission peak at 850 nm, blue trace; instrument respond factor, black trace.

The excitation spectrum of the Yb(**L5**$^{\bullet-}$) complex recorded choosing the emission wavelength at 850 nm was similar to that of ligand **L5**$^{\bullet-}$after normalisation (Figure 148). However, when the emission

155

wavelength was selected at 980 nm, the excitation spectrum revealed a sharp peak at 285 nm corresponding to the π-π* transition of phenyl rings of calixarene. This result was expected as the calixarene macrocycle was still able to work as an antenna to sensitise Yb^{3+} emission after the NDI reduction.
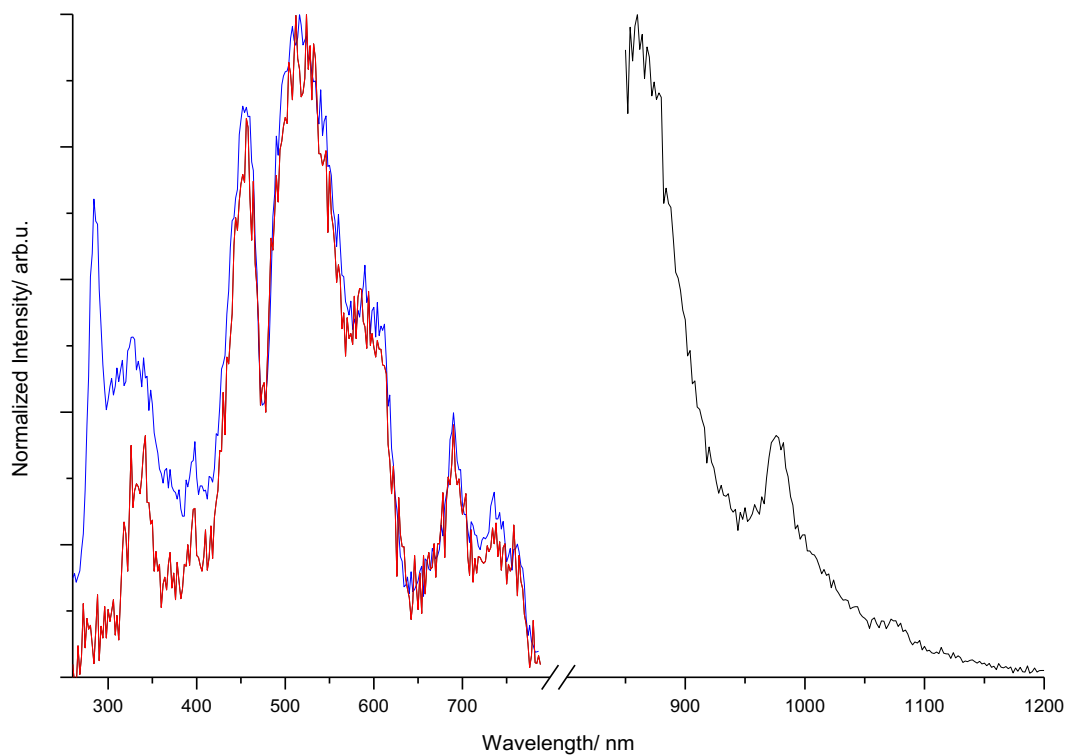
Figure 148: Emission spectrum (black trace). Emission wavelength = 850 nm, excitation spectrum of Yb(L5•⁻) complex, red trace. Emission wavelength = 980 nm, excitation spectra of Yb(L5•⁻) complex, blue trace.

The proposed energy transfer mechanism is shown in Figure 149.
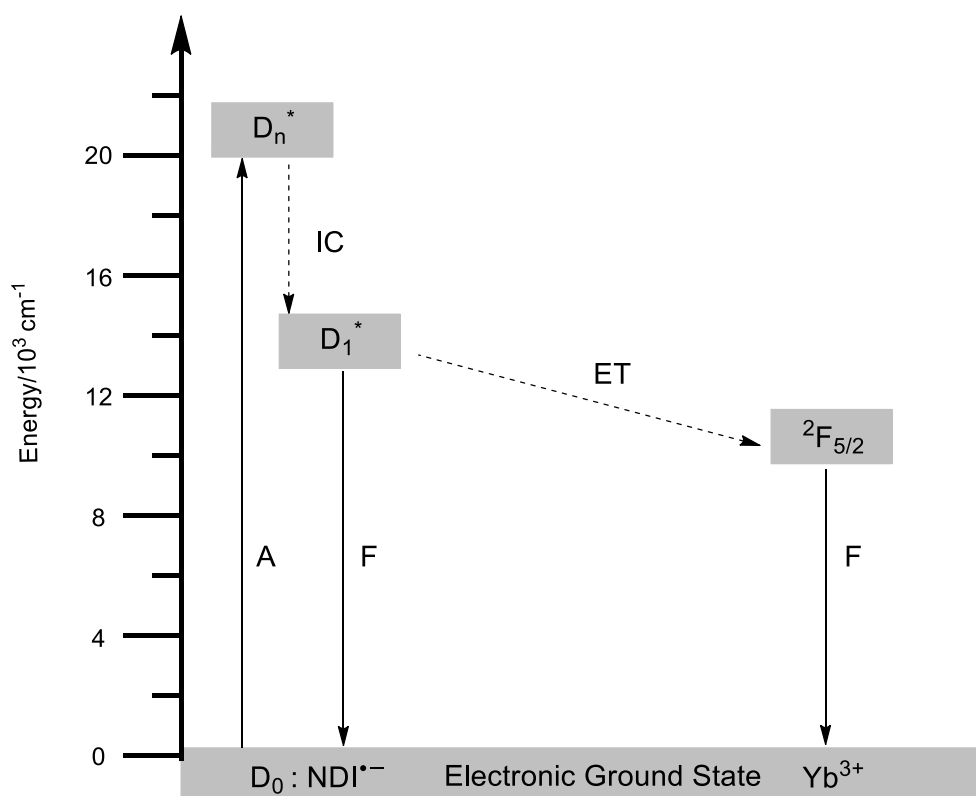
Figure 149：Photophysical state diagram for Yb(L5·⁻) complexat room temperature. "A" is absorption. "F" is fluorescence. "D" is the doublet state of NDI radical anion. "IC" is internal conversion. "D" is doublet state.

4.4 Conclusion

In this chapter, two aims of the project have been achieved. Firstly, the previously synthesised ligand **L5** was successfully reduced to its radical anion form using a chemical reductant. The experimental procedures for chemically generating NDI radical anion were proved to be reproducible. Well-controlled reduction reaction under a nitrogen atmosphere resulted in solutions of the ligand reduced to the NDI radical anion as well as the corresponding Yb^{3+} complex. Secondly, the photophysical properties of ligand **L5·⁻ and** Yb(**L5·⁻**) have been studied, and the energy transfer process has been proposed. This was the first observation of emission from the lowest excited doublet state of a NDI radical anion. A spike in the NIR region was observed in the case of the Yb(**L5·⁻**) complex upon excitation of the NDI radical anion, suggesting the energy transfer from the doublet state to the emissive state of Yb^{3+} took place. This is, to our knowledge, the first example of sensitization of lanthanoid via the excited doublet state of an antenna moiety. This strategy opens up a different sensitisation mechanism by which antenna effect occurs and should be further investigated.

157

5 Conclusion

Prior to the work described in the thesis, there is a lack of detailed photophysical studies on lanthanoid complexes incorporating naphthalenetetracarboxylic diimides. Although several papers reported attaching extra coordination sites at the axial position of NDI showed promising lanthanoid binding properties, detailed photophysical investigations were not carried out. Therefore, we endeavoured here to explore the potential of NDI, also the NDI radical anion, as antenna ligands.

The thesis mainly focuses on exploring the chemistry of NDI-functionalised calixarene ligands. The NDI moiety was successfully attached on the lower rim of the calixarene via amide linkages was successful, and six new NDI-calixarene ligands were synthesised and fully characterised. Five out of six ligands formed complexes with lanthanoid ions and sensitised lanthanoid emission via the antenna effect of the NDI moieties.

The first class of receptor described was bis NDI-substituted calixarene ligands. The synthesis used well-established calixarene derivatisation methodologies, with the NDI linked to the calixarene using standard amide coupling conditions. Studies using NMR spectroscopy and crystal structures showed that intramolecular hydrogen bonds on the lower rim of the calixarene can play a crucial role in inhibiting the formation of lanthanoid complexes. To solve this, both methylation of amide nitrogens or full alkylation of the lower rim to form tetraamide receptors was proven to produce calixarene receptors able to bind the lanthanoid ions. Single crystal structure determinations confirmed that the lanthanoid complex with tertiary amide ligand **L2** was 8-coordinated, with the general formula $Ln(L2-2H)NO_3$, where $Ln = Eu^{3+}$ and Yb^{3+}. The **L2** and **L3** ligands sensitised Yb^{3+} luminescence upon excitation of the NDI moiety. It is clear that NDI of ligand **L3** can act as an antenna to sensitise Eu^{3+}, Nd^{3+} and Yb^{3+}. The energy transfer to the emissive state of Eu^{3+} and Nd^{3+} from the aggregate and the excited triplet state of NDI was ruled out, whereas a possible energy transfer pathway to the Yb^{3+} was proposed to be from the excited triplet state of NDI. The quantum yield was very low in both cases regardless of excitation via the calixarene calixarene aromatic groups or NDI substituents.

A second series of mono NDI-substituted calixarene ligands and their corresponding lanthanoid complexes were synthesised. The synthetic procedure resulted in isolation of the sodium complex, and a purification process was developed to obtain the free ligand. It was confirmed that the lanthanoid complex was formed with calixarene tetraamide functionalised with NDI on the lower rim. Titration experiments confirmed that the complex was formed in a ratio of 1:1 with high stability constants. Photophysical studies on mono-NDI substituted ligands showed the sensitisation of the Yb^{3+} was achieved via the calixarene in all cases. Sensitisation of Yb^{3+} luminescence via NDI is also successful in the case of Yb(**L4**) and Yb(**L5**) complex, albeit with poor sensitisation efficiency. Only the NDI of ligand **L5** can sensitise Nd^{3+} luminescence in a 10^{-5} M solution. Increasing the concentration revealed more complicated photophysical behaviour in all cases. There was evidence that even if the NDI is not close to the coordination centre, it does sensitise Nd^{3+} luminescence in the case of Nd(**L6**) complex. However, Yb^{3+} luminescence can not be sensitised if the NDI is too distant from the Yb^{3+} centre. Furthermore, the emissive state of lanthanoid was effectively quenched by the NH group situated on

the lower rim of the calixarene, as indicated by the shorter lifetime. Solvent molecules were found in the first coordination sphere in our system consistent with other studies of calixarene tetraamides.

Finally, study of the antenna effect of NDI was extended to the NDI radical anion. The conversion of the neutral NDI to its NDI radical anion was successful using the tetrakis(dimethylamino)ethene (TDAE) under nitrogen atmosphere, as confirmed by comparison with the results of spectroelectrochemistry. The first observation of emission from the spin-allowed doublet state of the NDI both in the visible and NIR region was reported. The energy can not be transferred to populate the emissive state of Nd^{3+} via the doublet state, but preliminary results showed that the employment of the NDI radical anion to sensitise Yb^{3+} luminescence via its excited doublet state was successful. Further investigation of these photophysical phenomena is warranted, as to our knowledge this is the first example of excitation of a lanthanoid cation from a doublet state.

6 Experimental

6.1 General procedure

The neutral aluminia (Brockmann I activity) for chromatography was mixed with the desired amount of water. The size of silica gel particle for column chromatography was 60 um. The thin layer chromatography was used to track the progress of the reaction and column chromatography. The UV lamp was used to visualize the thin layer chromatography by incident light with the long wavelength at 365 nm and short wavelength at 254 nm.

All commercially available reagents and chemicals were bought from chemical suppliers with high quality and used without further purification. Only naphthelenetetracarboxylic dianhyhdride was needed to be recyrstalised from a hot DMF to remove a trace amount of impurities before use. The $Ln(DMSO)_x(NO_3)_3$ complexes were prepared by dissolving $Ln(NO_3)_3$ hydrate salt in a minimum amount of water, followed by adding the DMSO and ether (for crystallization).

All procedures relating to synthesis and workup were performed under a normal atmospheric condition. The synthesis of the radical anion and its corresponding lanthanoid complexes was carried out in a dry acetonitrile solution under a N_2 atmosphere. The digital balance used to weigh the chemicals and compounds for synthesis has a readability of 0.01 g, and the analytical balance for photophysical measurement has a readability of 0.01 mg.

Elemental analysis was performed by Dr. Chiara Caporale in the central science laboratory at Curtin University. All samples were dried under the vacuum before the measurement. The measurement was repeated three times. The calculated mean value of the percentage of carbon, nitrogen and oxygen in comparison to the theoretical value was used to characterise the compound.

High resolution liquid chromatography-mass spectrometric spectra were recorded from Dr. Frankie Busetti at the Edith Cowan University on a UHPLC Orbitrap mass spectrometer. The samples decomposed in the column were analysed by infusion. The reported experimental data was used to compare with the theoretical data obtained from the Chemdraw software.

The ^1H and ^{13}C Nuclear Magnetic Resonance spectra, including 2D COSY, NOESY, HSQC and HMBC spectra, were obtained from Bruker Avance 400 spectrometer at 300 Kelvin. The DeptQ135 technique was also used where necessary. The MestreNova software was used to process the data. The solvent signal was calibrated to the chemical shift reported in the literature.[179]

Absorption spectra were recorded at room temperature using Perkin Elmer Lambda 35 UV/Vis spectrophotometer. The absorption spectrum was calibrated following the instruction before use.

All excitation spectra and emission spectra of compounds in the solution phase and the solid state were recorded using Edingburgh FLS980 fluorimeter. The Xenon lamp was used as a source for the steady excitation and emission spectrum. Time-correlated single-photon counting (TCSPC) and microsecond xenon flash lamp were used to estimate the excited-state lifetime. The experimental data was fit to the decay model, and the goodness of fitting and weighted residuals were used to evaluate if the model was rejected or accepted. The instrument response function was measured by using the blank solution. The fluorometer was equipped with double excitation and emission monochromators. The Peltier cooled Hamamatsu R928P photomultiplier tube was the detector for measuring spectra in

the UV-visible region, and this detector should be cooled down to -20 °C before use. The Hamamatsu R5509-42 photomultiplier for measuring spectra in the near-infrared region, and this detector should be cooled down to -80 °C and stabilised at this degree for 2.5 hours before use.

The air-equilibrated sample solutions of neutral ligands and their corresponding complexes were analysed in quartz cuvette at ambient temperature, while the nitrogen-equilibrated sample solution of ligand radical anion and its corresponding complexes was measured in Schlenk cuvette prepurged with nitrogen. The quartz slides were used to measure the dry sample in the solid state and transferred to the sample holder for measurement. In order to estimate the triplet state of the sample, solutions should be pipetted into a quartz tube and frozen at 77K. After putting the cap on to seal the tube, the tube was placed in the special dewar flask filled with liquid nitrogen. The quantum yield was measured according to the reference method. The equation has been previously stated in the chapter.

Crystals were grown at Curtin University Laboratory by the candidate. Dr. Alexandre Sobolev and Associate Professor Stephen Moggach were acknowledged for their help of data collection, refinement and analysis.

Electrochemical measurement was performed by Professor Paul Bernhardt. The cyclic voltrammetry was done with a glassy carbon electrode. Two Ag/Ag+ electrodes (silver wire in a solution of 0.1 M KCl in H_2O) were used as the pseudoreference electrode and counter electrode, respectively. The saturated calomel electrode electrode with the Fc/Fc+ redox couple was used to calibrate as an internal reference. The 0.1M Et_4NClO_4 solution was used as the supporting electrolyte. The spectroelectrochemical (SEC) measurement was done with a Pt working electrode. The UV-visible spectrum of SEC experiment was recorded in the range of 390 nm to 780 nm.

6.2 Synthetic procedure

6.2.1 Compound **C3**

Mono-ester functionalized calixarene (1.1 g, 1.5 mmol) and K_2CO_3 (1.0 g, 7.4 mmol) were suspended in acetonitrile (200 mL). Then excess NaI (0.7 g, 4.5 mmol) and 2-chloro-*N,N*-diethylacetamide (1.3 mL, 4.8 mmol) were added. The mixture was heated at 100°C for eight hours. Upon cooling to room temperature, the acetonitrile was removed under the vacuum via rotary evaporator, and the residue was taken up in DCM (200 mL). The organic layer was washed with water (2 x 100 mL). The organic layer was dried over anhydrous $MgSO_4$ and removed via rotary evaporator. The compound **C3** was used directly for the next step without further purification.

6.2.2 Compound **C4**

Compound **C3** (1.0 g, 0.9 mmol) and potassium carbonate (1.0 g, 1.8 mmol) were combined in a mixture of methanol (100 mL) and water (100 mL). The mixture was stirred at reflux for two hours. After removal of the organic solvent, the pH was adjusted to 2. The residue was added to dichloromethane (100 mL) for extraction. The bottom layer was dried over anhydrous $MgSO_4$and removed via rotary evaporator. After removing the solvent, the solid was redissolved in methanol (20 mL), added dropwise to an aqueous methanolic solution (200 mL, methanol: water 1:1) and heated at 60 °C for 3 hours. The

methanol was removed under the vacuum via rotary evaporator. The white solid was collected via the vacuum filtration. Yield: 84%.

^{1}H NMR (400 MHz, DMSO-d_6) δ 11.42 (s, 1H, COO**H**), 7.02 (s, 2H, Ar-**H**), 6.98 (s, 2H, Ar-**H**), 6.74 (d, J = 2.4 Hz, 2H, Ar-**H**), 6.68 (d, J = 2.4 Hz, 2H, Ar-**H**), 5.06 (d, J = 12.8 Hz, 2H, Ar-C**H$_2$**-Ar), 4.98 – 4.86 (m, 4H, OC**H$_2$**), 4.72 (d, J = 12.8 Hz, 2H, Ar-C**H$_2$**-Ar), 4.56 (s, 2H, OC**H$_2$**), 4.54 – 4.46 (m, 2H, OC**H$_2$**), 3.44 – 3.20 [m, 12H, CON(C**H$_2$**CH$_3$)$_2$ + **H$_2$**O], 3.20 – 3.10 (m, 4H, Ar-C**H$_2$**-Ar), 1.18 [s, 9H, Ar-C(C**H$_3$**)$_3$], 1.13 [s, 9H, Ar-C(C**H$_3$**)$_3$], 1.10 – 1.00 [m, 18H, CON(CH$_2$C**H$_3$**)$_2$], 0.94 [s, 18H, Ar-C(C**H$_3$**)$_3$].

^{13}C NMR (100 MHz, DMSO-d_6) δ [170.11, 168.36, 167.47, **C**ON(CH$_2$CH$_3$)$_2$ +**C**OOH], (154.33, 152.80, 151.84, 145.26, 144.02, 143.98, 134.24, 133.84, 132.83, 132.50, Ar-**C**), (125.36, 125.19, 125.07,124.63, Ar-**C**H), 72.43(O**C**H$_2$), 72.28(O**C**H$_2$), 70.83(O**C**H$_2$), [33.70, 33.56, 33.39, Ar**C**(CH$_3$)$_3$], [31.26, 31.22, 31.14, 30.96, 30.90, (Ar-**C**H$_2$-Ar) + Ar**C**(C**H$_3$**)$_3$], [14.12, 14.05, 12.96, 12.89, CON(CH$_2$**C**H$_3$)$_2$]. CON(**C**H$_2$CH$_3$)$_2$ carbon signals overlap with solvent signals.

HRMS (ESI): calculated for C$_{64}$H$_{91}$N$_3$O$_9$ as [M + H]$^+$: 1046.6828; found: 1046.6821.

Elemental analysis calcd (%) for C$_{64}$H$_{91}$N$_3$O$_9$: C, 73.46; H, 8.77; N, 4.02; found: C, 72.94; H, 8.83; N, 3.95.

6.2.3 Compound **I1**

N-Boc-1,6-diaminoheane ethylenediamine (compound **11**) was synthesised following the literature.[180] The ^{1}H NMR data were in agreement with the literature.

6.2.4 Compound **I2**

Compound **I1** (2.0 g, 9.3 mmol) and propionaldehyde (0.7 g, 12.0 mmol) were dissolved in dry EtOH (100 ml), and the mixture was heated to reflux at 85 ^{o}C for one hour under a nitrogen atmosphere. Upon cooling to room temperature, NaBH$_4$ (0.7 g, 22.2 mmol) was added, and the mixture was further stirred at room temperature for three hours. The reaction was quenched by 1M HCl (5 ml), and the ethanol was removed under the vacuum via rotary evaporator. More water (100 ml) was added, and then the resulting solution was made basic with K$_2$CO$_3$ solution. The mixture was extracted with dichloromethane (100 ml x 3), followed by washing with deionised water (100 mL x 3). The bottom layer was dried over anhydrous Mg$_2$SO$_4$ and removed via rotary evaporator. The compound **I2** was purified via column chromatography (SiO$_2$, dichloromethane: methanol: aqueous 28% ammonia 100: 5: 0.1). Yield: 25% (0.6 g).

^{1}H NMR (400 MHz, acetone-d$_6$) δ = 5.90 (s, 1H, CH$_3$CH$_2$N**H**), 3.05 (td, J = 7.0, 5.8 Hz, 2H, NHCH$_2$CH$_2$CH$_2$CH$_2$CH$_2$C**H$_2$**NH-Boc), 2.54 (dt, J = 14.2, 7.0 Hz, 4H, NHC**H$_2$**CH$_2$CH$_2$CH$_2$CH$_2$CH$_2$NH-Boc + CH$_3$CH$_2$C**H$_2$**NH), 1.56 – 1.26 (m, 19H, CH$_3$C**H$_2$**CH$_2$NH + NHCH$_2$C**H$_2$C**H$_2$**C**H$_2$**C**H$_2$**CH$_2$NH-Boc + Boc-**H**), 0.88 (t, J = 7.4 Hz, 3H, C**H$_3$**CH$_2$CH$_2$NH).

6.2.5 Compound **I3**

To a stirring solution of compound **I2** (0.6 g, 2.3 mmol) in dichloromethane (5 ml), trifluoroacetic acid (1.5 ml) was added. The mixture was stirred at room temperature for about two hours, and the reaction was monitored by TLC until the starting material was consumed. The solvent was removed to afford a pale yellow solid. Yield: 90% (0.6 g).

^{1}H NMR (400 MHz, D$_2$O) δ = 3.08 – 2.90 (m, 6H, NHC**H$_2$**CH$_2$CH$_3$ + NHC**H$_2$**CH$_2$CH$_2$CH$_2$CH$_2$C**H$_2$**NH$_3$$^+$) 1.74 – 1.60 (m, 6H, NHCH$_2$C**H$_2$**CH$_3$ + NHCH$_2$C**H$_2$**CH$_2$CH$_2$C**H$_2$**CH$_2$NH$_3$$^+$), 1.46 – 1.34 (m, 4H, NHCH$_2$CH$_2$C**H$_2$**C**H$_2$**CH$_2$CH$_2$NH$_3$$^+$), 0.96 (t, J = 7.4 Hz, 3H, NHCH$_2$CH$_2$C**H$_3$**).

6.2.6 Compound **NDI2**

Compound **X** (1.5 g, 4.3 mmol) and *N*-Boc-ethylenediamine (0.7 g, 4.3 mmol) were dissolved in a mixture of ethanol/toluene (100 ml, 1:1) and heated at 110 °C for three hours. The organic solvent was removed. The compound **NDI2** was purified via column chromatography (SiO$_2$, dichloromethane: methanol 100: 1). Yield: 70% (1.5 g).

^{1}H NMR (400 MHz, CDCl$_3$) δ =8.78 – 8.72 (m, 4H, NDI-**H**), 4.46 – 4.32 [m, 2H, NHCH$_2$C**H$_2$**N(CO)$_2$], 4.26 – 4.08 [m, 2H, N(CO)$_2$C**H$_2$**CH$_2$(CH$_2$)$_3$CH$_3$], 3.62 – 3.44 [m, 2H, NHC**H$_2$**CH$_2$N(CO)$_2$], 1.80 – 1.70 [m, 2H,N(CO)$_2$CH$_2$C**H$_2$**(CH$_2$)$_3$CH$_3$], 1.46 – 1.08 [m, 15H,N(CO)$_2$CH$_2$CH$_2$(C**H$_2$**)$_3$CH$_3$ + Boc-**H**], 0.88 [t, J = 7.0 Hz, 3H, N(CO)$_2$CH$_2$CH$_2$(CH$_2$)$_3$C**H$_3$**].

6.2.7 Compound **NDI3**

To a stirring solution of compound **NDI2** (1.5 g, 3.0 mmol) in dichloromethane (15 ml), trifluoroacetic acid (3.5 ml) was added. The mixture was stirred at room temperature for about two hours, and the reaction was monitored by TLC until the starting material was consumed. The solvent was removed to afford a pale yellow solid. Yield: 90% (1.4 g).

^{1}H NMR (400 MHz, DMSO-*d$_6$*) δ = 8.68 (s, 4H, NDI-**H**), 7.91 (s, 3H, N**H$_3$**$^+$), 4.34 [t, J = 5.8 Hz, 2H, N(CO)$_2$C**H$_2$**CH$_2$NH$_3$$^+$], 4.06 [t, J = 4 Hz, 2H, N(CO)$_2$C**H$_2$**CH$_2$(CH$_2$)$_3$CH$_3$], 3.26 – 3.14 [m, 2H, N(CO)$_2$CH$_2$C**H$_2$**NH$_3$$^+$], 1.72 – 1.60 [m, 2H, N(CO)$_2$CH$_2$C**H$_2$**(CH$_2$)$_3$CH$_3$], 1.40 – 1.20 [m, 6H, N(CO)$_2$CH$_2$CH$_2$(C**H$_2$**)$_3$CH$_3$], 0.88 [t, J = 6.8 Hz, 3H, N(CO)$_2$CH$_2$CH$_2$(CH$_2$)$_3$C**H$_3$**].

6.2.8 Compound **NDI4**

Compound **X** (1.5 g, 4.3 mmol) and *N*-methyl-1,3-diaminopropane (445.9 µl, 4.3 mmol) were dissolved in a mixture of ethanol/toluene (100 ml, 1:1) and heated at 110 °C for three hours. The organic solvent was removed to afford a black solid. The isolated solid was used directly without further purification.

6.2.9 Compound **NDI5**

Compound **NDI4** (1.6 g, 3.8 mmol) and di-*tert*-butyl dicarbonate (0.8 g, 3.8 mmol) in dichloromethane (20 ml) were stirred at room temperature for two hours. The organic solvent was removed. The desired product was purified via column chromatography (SiO$_2$, dichloromethane: methanol 100: 1). Yield: 50% (1.0 g).

^{1}H NMR (400 MHz, CDCl$_3$) δ = δ 8.68 (s, 4H, NDI-**H**), 4.20 – 4.02 [m, 4H, N(CH$_3$)CH$_2$CH$_2$C**H$_2$**N(CO)$_2$ + N(CO)$_2$C**H$_2$**CH$_2$(CH$_2$)$_3$CH$_3$], 3.38 – 3.22 [m, 2H, N(CH$_3$)C**H$_2$**CH$_2$CH$_2$N(CO)$_2$], 2.84 [s, 3H, N(C**H$_3$**)CH$_2$CH$_2$CH$_2$N(CO)$_2$], 2.00 – 1.84 [m, 2H, N(CH$_3$)CH$_2$C**H$_2$**CH$_2$N(CO)$_2$], 1.74 – 1.54 [m, 2H, N(CO)$_2$CH$_2$C**H$_2$**(CH$_2$)$_3$CH$_3$], 1.42 – 1.16 [s, 15H, N(CO)$_2$CH$_2$CH$_2$(C**H$_2$**)$_3$CH$_3$ + Boc-**H**], 0.80 [t, *J* = 7.2 Hz, 3H, N(CO)$_2$CH$_2$CH$_2$(CH$_2$)$_3$C**H$_3$**].

6.2.10 Compound **NDI6**

To a stirring solution of compound **NDI5** (1.0 g, 1.9 mmol) in dichloromethane (15 ml), trifluoroacetic acid was added (3 ml). The mixture was stirred at room temperature for about two hours, and the reaction was monitored by TLC until the starting material was consumed. The solvent was removed to afford a pale yellow solid.Yield: 90% (0.9 g).

^{1}H NMR (400 MHz, CDCl$_3$) δ = 9.36 [s, 2H, N**H$_2$$^+$**], 8.78 – 8.60 (m, 4H, NDI-**H**), 4.31 [t, *J* = 6.6 Hz, 2H, NH$_2$$^+CH_2CH_2$C**H$_2$**N(CO)$_2$], 4.16 [t, *J* = 7.6 Hz, 2H, N(CO)$_2$C**H$_2$**CH$_2$(CH$_2$)$_3$CH$_3$], 3.22 – 3.02 [m, 2H, NH$_2$$^+$C**H$_2$**CH$_2CH_2$N(CO)$_2$], 2.76 (s, 3H, NH$_2$$^+$C**H$_3$**), 2.30 – 2.22 [m, 2H, NH$_2$$^+CH_2$C**H$_2$**CH$_2$N(CO)$_2$], 1.78 – 1.64 [m, 2H, N(CO)$_2$CH$_2$C**H$_2$**(CH$_2$)$_3$CH$_3$], 1.48 – 1.26 [m, 6H, N(CO)$_2$CH$_2$CH$_2$(C**H$_2$**)$_3$CH$_3$], 0.90 [t, *J* = 7.0 Hz, 3H, N(CO)$_2$CH$_2$CH$_2$(CH$_2$)$_3$C**H$_3$**].

6.2.11 Compound **NDI9**

Compound **X** (0.8 g, 2.2 mmol) and compound **I3** (0.6 g, 2.2 mmol) were dissolved in a mixture of ethanol/toluene (100 ml, 1:1) and heated at 110 °C for 3 hours. The organic solvent was removed to afford a black solid. The isolated solid was used directly without further purification.

6.2.12 Compound **NDI10**

Compound **NDI9** (1.4 g, 2.9 mmol) and di-*tert*-butyl dicarbonate (0.6 g, 2.9 mmol) in dichloromethane (20 ml) were stirred at room temperature for two hours. The organic solvent was removed. The desired product was purified via column chromatography (SiO$_2$, dichloromethane: methanol 100: 1). Yield: 52% (0.9 g).

^{1}H NMR (400 MHz, DMSO-d$_6$) δ = 8.74 (s, 4H, NDI-**H**), 4.26 – 4.12 [m, 4H, Boc-N-CH$_2$CH$_2$CH$_2$CH$_2$CH$_2$C**H$_2$**N(CO)$_2$ + N(CO)$_2$C**H$_2$**CH$_2$(CH$_2$)$_3$CH$_3$], 3.22 – 3.04 [m, 4H, Boc-N-C**H$_2$**CH$_2$CH$_2$CH$_2$CH$_2$CH$_2$N(CO)$_2$ + Boc-N-C**H$_2$**CH$_2$CH$_3$], 1.80 – 1.28 [m, 27H, N(CO)$_2$CH$_2$C**H$_2$**(CH$_2$)$_3$CH$_3$ + Boc-N-CH$_2$C**H$_2$C**H$_2$**C**H$_2$**C**H$_2$**CH$_2$N(CO)$_2$ + Boc-N-CH$_2$C**H$_2$**CH$_3$ + Boc-**H**), 0.94 – 0.78 [m, 6H, N(CO)$_2$CH$_2$CH$_2$(CH$_2$)$_3$C**H$_3$** + NH$_2$$^+CH_2CH_2$C**H$_3$**].

6.2.13 Compound **NDI11**

To a stirring solution of compound **NDI10** (0.9 g, 1.5 mmol) in dichloromethane (15 ml), trifluoroacetic acid (3 ml) was added. The mixture was stirred at room temperature for about two hours, and the reaction was monitored by TLC until the starting material was consumed. The solvent was removed to afford a pale yellow solid. Yield: 90% (700 mg).

^{1}H NMR (400 MHz, DMSO-d_6) δ = 8.62 – 8.66 (m, 4H, NDI-**H**), 8.33 (s, 2H, N**H$_2$**$^+$), 4.10 – 4.00 [m, 4H, NH$_2$$^+CH_2CH_2CH_2CH_2CH_2$C**H$_2$**N(CO)$_2$ + N(CO)$_2$C**H$_2$**CH$_2$(CH$_2$)$_3$CH$_3$], 2.96 – 2.78 [m, 4H, NH$_2$$^+$C**H$_2$**CH$_2CH_2CH_2CH_2CH_2$N(CO)$_2$ + NH$_2$$^+$C**H$_2$**CH$_2CH_3$], 1.74 – 1.52 [m, 8H, N(CO)$_2$CH$_2$C**H$_2$**(CH$_2$)$_3$CH$_3$ + NH$_2$$^+CH_2$C**H$_2$**CH$_2CH_2$C**H$_2$**CH$_2$N(CO)$_2$ + NH$_2$$^+CH_2$C**H$_2$**CH$_3$], 1.46 – 1.24 [m, 10H, NH$_2$$^+CH_2CH_2$C**H$_2$**C**H$_2$**CH$_2CH_2$N(CO)$_2$ + N(CO)$_2$CH$_2$CH$_2$(C**H$_2$**)$_3$CH$_3$], 0.96 – 0.80 [m, 6H, N(CO)$_2$CH$_2$CH$_2$(CH$_2$)$_3$C**H$_3$** + NH$_2$$^+CH_2CH_2$C**H$_3$**].

6.2.14 Ligand **L1**

Compound **C1** (1.0 g, 1.3 mmol) and HOBT (0.4 g, 2.7 mmol) were dissolved in dry THF (40 mL). The 1-Ethyl-3-(3-dimethylaminopropyl)carbodiimide (0.5 g, 2.5 mmol) and triethylamine (1.5 mL, 10.6 mmol) were then added. The mixture was further stirred at room temperature for 20 minutes. The corresponding amine TFA salt, compound **NDI3** (1.3 g, 2.6 mmol), was added. After 24 hours, the solid was filtered, and the solvent was removed via rotary evaporator. The remaining solid was dissolved in DCM (200 mL), followed by washing with deionised water (50mL×3). The bottom layer was dried over anhydrous Mg$_2$SO$_4$and removed via rotary evaporator. The compound was purified via column chromatography (SiO$_2$, dichloromethane: methanol 100: 0.7). Yield: 44%.

^{1}H NMR (400 MHz, CDCl$_3$) δ 8.74 [t, J = 6.0 Hz, 2H, CON**H**CH$_2$CH$_2$N(CO)$_2$], 8.60 (dd, J = 15.6 Hz, 7.8 Hz, 8H, NDI-**H**), 7.50 (s, 2H, Ar-O**H**), 6.74 (s, 4H, Ar-**H**), 6.60 (s, 4H, Ar-**H**), 4.48 [t, J = 6.4, Hz, 4H, CONHCH$_2$C**H$_2$**N(CO)$_2$], 4.40 (s, 4H, OC**H$_2$**), 4.20 – 4.14 [m, 4H, N(CO)$_2$C**H$_2$**CH$_2$(CH$_2$)$_3$CH$_3$], 4.04 – 3.96 [m, 4H, CONHC**H$_2$**CH$_2$N(CO)$_2$], 3.64 (d, J = 13.2 Hz, 4H, Ar-C**H$_2$**-Ar), 2.98 (d, J = 13.2 Hz, 4H, Ar-C**H$_2$**-Ar), 1.82 – 1.68 [m, 4H, N(CO)$_2$CH$_2$C**H$_2$**(CH$_2$)$_3$CH$_3$], 1.50 –1.28 [m, 9H, N(CO)$_2$CH$_2$CH$_2$(C**H$_2$**)$_3$CH$_3$], 1.10 [s, 18H, Ar-C(C**H$_3$**)$_3$], 0.94 [s, 18H, Ar-C(C**H$_3$**)$_3$], 0.90 [t, J = 7.0 Hz, 6H, N(CO)$_2$CH$_2$CH$_2$(CH$_2$)$_3$C**H$_3$**].

^{13}C NMR (100 MHz, CDCl$_3$) δ [168.28, **C**ONHCH$_2$CH$_2$N(CO)$_2$], (163.43, 162.90, NDI-**C**O), (148.65, 148.54, 148.18, 143.14, 132.42, Ar-**C**+ Ar-**C**-O + Ar-**C**-OH), (130.75, NDI-Ar-**C**H), (127.16, 126.77, 126.53, 126.51, 126.49, Ar-**C** + NDI-**C**), (126.14, 125.19, Ar-**C**H), (74.84,O**C**H$_2$), [41.11, CONHCH$_2$**C**H$_2$N(CO)$_2$ + N(CO)$_2$**C**H$_2$CH$_2$(CH$_2$)$_3$CH$_3$)], [36.88, CONH**C**H$_2$CH$_2$N(CO)$_2$], [34.22, 33.79, Ar-**C**(CH$_3$)$_3$], [31.67, 31.60, 31.05, Ar-C(**C**H$_3$)$_3$ + Ar-**C**H$_2$-Ar + N(CO)$_2$CH$_2$CH$_2$CH$_2$**C**H$_2$CH$_2$CH$_3$], [28.21, 26.92, 22.71, N(CO)$_2$CH$_2$**C**H$_2$CH$_2$CH$_2$**C**H$_2$CH$_3$], [14.20, N(CO)$_2$CH$_2$CH$_2$(CH$_2$)$_3$**C**H$_3$].

HRMS (ESI): calculated for C$_{92}$H$_{102}$N$_6$O$_{14}$ as [M + Na]$^+$: 1537.7346; found: 1537.7354.

Elementalanalysis calcd (%) for C$_{92}$H$_{102}$N$_6$O$_{14}$: C, 72.90; H, 6.78; N, 5.54; found: C, 72.94; H, 6.98; N, 5.65.

6.2.15 Ligand **L2**

The same procedure for the ligand **L1** was used to synthesise the ligand **L2**. The amine salt used for the amide coupling reaction was compound **NDI6**. Yield: 35%.

^{1}H NMR (400 MHz, CDCl$_3$) δ 8.74 – 8.52 (m, 8H, NDI-**H**), 7.78 – 7.52 (m, 2H, Ar-O**H**), 6.94 – 6.50 (m, 8H, Ar-**H**), 4.96 – 4.70 (m, 4H, OC**H₂**), 4.44 – 2.80 [m, 26H, N(CO)₂C**H₂**CH₂(CH₂)₃CH₃ + CON(CH₃)C**H₂**CH₂CH₂N(CO)₂ + CON(C**H₃**)CH₂CH₂CH₂N(CO)₂ + Ar-C**H₂**-Ar], 2.28 – 2.02 [m, 4H, CON(CH₃)CH₂C**H₂**CH₂N(CO)₂], 1.80 – 1.64 [m, 4H, N(CO)₂CH₂C**H₂**(CH₂)₃CH₃], 1.52 – 1.28 [m, 12H, N(CO)₂CH₂CH₂(C**H₂**)₃CH₃], 1.14 – 0.98 [m, 36H, Ar-C(C**H₃**)₃], 0.92 – 0.82 [m, 6H, N(CO)₂CH₂CH₂(CH₂)₃C**H₃**].

^{13}C NMR (100 MHz, CDCl$_3$) δ [169.11, 169.01, 168.81, **C**ON(CH₃)CH₂CH₂CH₂N(CO)₂], (163.25, 163.08, 162.95, 162.90, 162.59, NDI-**C**O), (152.32, 151.94, 149.72, 149.23, 148.48, 146.80, 146.54, 141.09, 133.42, 133.34, 133.26, Ar-**C** + Ar-**C**-O + Ar-**C**-OH), (130.92, 130.77, 130.73, 130.46, NDI-Ar-**C**H), (127.60, 127.42, 127.04, 126.86, 126.74, 126.68, 126.61, 126.55, 126.50, 126.42, 126.34, 126.29, 125.57, 124.78, 124.73, 124.40, Ar-**C** + NDI-**C**), (73.49, 73.15, 73.04, 72.48, O**C**H₂), [47.01, 46.63, 45.59, 40.97, 40.87, 38.61, 37.88, 37.59, 34.33, 33.94, 33.87, 33.63, 33.57, 33.44, 33.28, 33.04, 32.04, CON(**C**H₃)**C**H₂CH₂**C**H₂N(CO)₂ + N(CO)₂**C**H₂CH₂(CH₂)₃CH₃) + Ar-**C**(CH₃)₃], [31.54, 31.50, 31.42, 31.28, 31.22, 31.17, Ar-C(**C**H₃)₃ + Ar-**C**H₂-Ar + N(CO)₂CH₂CH₂CH₂**C**H₂CH₂CH₃] (28.06, 28.00, [27.77, 27.54, 26.74, 26.15, 25.99, 22.55, [N(CO)₂CH₂**C**H₂**C**H₂CH₂**C**H₂CH₃ + CON(CH₃)CH₂**C**H₂CH₂N(CO)₂], [14.05, N(CO)₂CH₂CH₂(CH₂)₃**C**H₃].

HRMS (ESI): calcd. for C$_{96}$H$_{110}$N$_6$O$_{14}$ as [M + H]$^+$ 1571.8153; found 1571.8157.

Elementalanalysis calcd (%) for C$_{96}$H$_{110}$N$_6$O$_{14}$: C, 73.35; H, 7.05; N, 5.35; found: C, 73.40; H, 7.12; N, 5.58.

6.2.16 Ligand **L3**

Compound **C2** (0.7 g, 0.7 mmol), 1-hydroxybenzotriazole (0.4 g, 2.8 mmol) and triethylamine (0.9 mL, 7.0 mmol) were dissolved in dry THF (40 mL). The mixture was cooled down to 0°C, *N,N'*-dicyclohexylcarbodiimide (0.6 g, 2.8 mmol) was added under stirring. The mixture was further stirred at room temperature for 20 minutes. The compound **NDI3** (0.8 g, 1.6 mmol) was added. After 24 hours, the precipitate was filtered, and the solvent was removed under reduced pressure. The remaining solid was redissolved in DCM (200 mL), followed by washing with water (100 mL x 2). The organic layer was dried over Na$_2$SO$_4$. The solvent was removed via rotary evaporator. The compound was triturated with ethanol, acetone and ether. The filtered cake was further heated in the mixture of water (100 mL) and methanol (100 mL) at 60°C for 2 hours. The methanol was removed under the vacuum, and the white precipitate was collected to afford the pure desired product was a white solid. Yield: 57%.

^{1}H NMR (400 MHz, CDCl$_3$) δ = 9.02 (s, 2H, CON**H**), 8.66 – 8.54 (dd, J = 16.8 Hz, 7.6 Hz, 8H, NDI-**H**), 6.74 (s, 4H, Ar-**H**), 6.66 (s, 4H, Ar-**H**), 4.76 (s, 4H, OC**H₂**), 4.64 – 4.50 (m, *J* = 12.2 Hz, 8H, Ar-C**H₂**-Ar + OC**H₂**), 4.46 [t, *J* = 5.8 Hz, 4H, CONHCH₂C**H₂**N(CO)₂], 4.16 [t, *J* = 7.6 Hz, 4H, N(CO)₂C**H₂**CH₂(CH₂)₃CH₃], 3.88 – 3.78 (m, 4H, CONHC**H₂**CH₂N(CO)₂], 3.22 [q, *J* = 7.0 Hz, 4H, CON(C**H₂**CH₃)₂], 3.15 – 3.03 [m, 8H, CON(C**H₂**CH₃)₂ +Ar-C**H₂**-Ar], 1.76 – 1.64 (m, 4H,

N(CO)$_2$CH$_2$C**H$_2$**(CH$_2$)$_3$CH$_3$], 1.46 – 1.32 [m, 12H, N(CO)$_2$CH$_2$CH$_2$(C**H$_2$**)$_3$CH$_3$], 1.12 [s, 18H, Ar-C(C**H$_3$**)$_3$], 1.04 – 0.92 (m, 30H, Ar-C(C**H$_3$**)$_3$ + CON(CH$_2$C**H$_3$**)$_2$, 0.92 – 0.86 [m, 6H, N(CO)$_2$CH$_2$CH$_2$(CH$_2$)$_3$C**H$_3$**].

^{13}C NMR (100 MHz, CDCl$_3$) δ = [168.41, **C**ON(CH$_2$CH$_3$)$_2$ + **C**ONHCH$_2$CH$_2$N(CO)$_2$], (163.15, 162.95, NDI-**C**O), (153.39, 152.45, Ar-**C**-O), (145.78, 145.53, 132.89, Ar-**C**), (130.83, 130.76, NDI-**C**H), [127.00, 126.90, 126.68, 126.49, NDI-**C**], (125.92, 125.67, Ar-**C**H), (74.04, 71.53, O**C**H$_2$), [41.49, 41.08, 40.38, 40.07,CONHCH$_2$**C**H$_2$N(CO)$_2$ + N(CO)$_2$**C**H$_2$CH$_2$(CH$_2$)$_3$CH$_3$ + CON(**C**H$_2$CH$_3$)$_2$], [38.44, CONH**C**H$_2$CH$_2$N(CO)$_2$], [34.03, 33.93, Ar**C**(CH$_3$)$_3$], [31.99, 31.64, 31.58, 31.37, (Ar-**C**H$_2$-Ar) + ArC(**C**H$_3$)$_3$ + N(CO)$_2$CH$_2$CH$_2$CH$_2$**C**H$_2$CH$_2$CH$_3$], [28.17, 26.89, 22.69, N(CO)$_2$CH$_2$**C**H$_2$**C**H$_2$CH$_2$**C**H$_2$CH$_3$], [14.33, 14.18, CON(CH$_2$**C**H$_3$)$_2$], [13.07, N(CO)$_2$CH$_2$CH$_2$(CH$_2$)$_3$**C**H$_3$].

Elementalanalysis calcd (%) for C$_{104}$H$_{124}$N$_8$O$_{16}$·H$_2$O: C, 70.97; H, 7.22; N, 6.37; found: C, 70.76; H, 7.16; N, 6.26.

HRMS (ESI): calculated for C$_{104}$H$_{124}$N$_8$O$_{16}$ as [M + H]$^+$: 1741.9208; found: 1741.9189.

6.2.17 Ligand **L4**

Compound **C4** (1.0 g, 0.9 mmol) and 1-hydroxybenzotriazole (0.3 g, 2.2 mmol) were dissolved in dry THF (40 mL). The *N,N'*-Dicyclohexylcarbodiimide (0.5 g, 2.5 mmol) and triethylamine (0.4 mL, 2.9 mmol) were then added. The mixture was further stirred at room temperature for 20 minutes. The corresponding amine TFA salt, compound **NDI3** (0.5 g, 0.9 mmol), was added. After 24 hours, the white solid was filtered. The solvent was removed via rotary evaporator. The remaining solid was redissolved in DCM (200 mL), followed by washing with deionised water (150 mL× 2). The bottom layer was dried over anhydrous MgSO$_4$and removed via rotary evaporator. The compound was purified via column chromatography (Brockmann I, neutral alumina, dichloromethane: methanol 100: 0.5). After removing the solvent, the solid was redissolved in methanol (50 mL), added dropwise to an aqueous methanolic solution (methanol: water 1:1) and heated at 60 °C for 3 hours. The methanol was removed under the vacuum via rotary evaporator. The yellow solid was collected via the vacuum filtration. Yield: 49%.

^{1}H NMR (400 MHz, CDCl$_3$) δ 9.24 (s, 1H, CON**H**), 8.72 – 8.62 (m, 4H, NDI-**H**), 6.80 – 6.74 (m, 4H, Ar-**H**), 6.72 (d, J = 2.4 Hz, 2H, , Ar-**H**), 6.66 (s, 2H, Ar-**H**), 5.04 – 4.90 (m, 4H, Ar-C**H$_2$**-Ar + OC**H$_2$**), 4.88 (s, 2H, OC**H$_2$**), 4.72 – 4.64 (m, 2H, OC**H$_2$**), 4.68 (d, J = 13.0 Hz, 2H, Ar-C**H$_2$**-Ar), 4.60 – 4.54 [m, 2H, CONHCH$_2$C**H$_2$**N(CO)$_2$], 4.52 (s, 2H, OC**H$_2$**), 4.22 – 4.12 [m, 2H, N(CO)$_2$C**H$_2$**CH$_2$(CH$_2$)$_3$CH$_3$], 3.88 – 3.78 [m, J = 5.6 Hz, 2H, CONHC**H$_2$**CH$_2$N(CO)$_2$], 3.36 – 3.08 [m, 16H, CON(C**H$_2$**CH$_3$)$_2$ + Ar-C**H$_2$**-Ar], 1.78 – 1.66 [m, 2H, N(CO)$_2$CH$_2$C**H$_2$**(CH$_2$)$_3$CH$_3$], 1.46 – 1.30 [m, 6H, N(CO)$_2$CH$_2$CH$_2$(C**H$_2$**)$_3$CH$_3$], 1.10 – 1.00 [m , 54H, Ar-C(C**H$_3$**)$_3$ + CON(CH$_2$C**H$_3$**)$_2$], 0.90 – 0.84 [(m, 3H, N(CO)$_2$CH$_2$CH$_2$(CH$_2$)$_3$C**H$_3$**].

^{13}C NMR (100 MHz, CDCl$_3$) δ 171.50[**C**ONHCH$_2$CH$_2$N(CO)$_2$], [169.03, 168.85, **C**ON(CH$_2$CH$_3$)$_2$], [163.29, 163.10, NDI-**C**O], (153.63, 153.59, 153.27, 145.17, 145.08, 145.06, 133.56, 133.51, 132.66, Ar-**C**),(130.87, 130.74, NDI-**C**H), [127.23, 127.05, 126.81, 126.49, NDI-**C**], (125.82, 125.69, 125.51, 125.45, Ar-**C**H) (74.64, 71.67, 71.61, O**C**H$_2$), [41.11, 40.43, 40.18, 40.09, CONHCH$_2$**C**H$_2$N(CO)$_2$ + CON(**C**H$_2$CH$_3$)$_2$], (41.04, N(CO)$_2$**C**H$_2$CH$_2$(CH$_2$)$_3$CH$_3$), [38.11, CONH**C**H$_2$CH$_2$N(CO)$_2$], [33.95, 33.90, Ar**C**(CH$_3$)$_3$], [32.34, 31.93, 31.71, 31.63, 31.55, 31.51, 31.47, (Ar-**C**H$_2$-Ar) + ArC(**C**H$_3$)$_3$ +N(CO)$_2$CH$_2$CH$_2$CH$_2$**C**H$_2$CH$_2$CH$_3$], (28.18, 26.87, 22.67, N(CO)$_2$CH$_2$**C**H$_2$**C**H$_2$CH$_2$**C**H$_2$CH$_3$], [14.33, 14.24, 14.16, 13.22, 13.13, N(CO)$_2$CH$_2$CH$_2$(CH$_2$)$_3$**C**H$_3$+ CON(CH$_2$**C**H$_3$)$_2$].

HRMS (ESI): calculated for $C_{86}H_{112}N_6O_{12}$ as $[M + H]^+$: 1421.8411; found:1421.8374.

Elementalanalysis calcd (%) for $C_{86}H_{112}N_6O_{12}$: C, 72.65; H, 7.94; N, 5.91; found: C, 72.48; H, 8.21; N, 6.32.

6.2.18 Ligand **L5**

The same procedure for the **L5** ligand was used to synthesise the **L4** ligand. The amine salt used for the amide coupling reaction was compound **NDI6**. Yield: 55%.

^{1}H NMR (400 MHz CDCl$_3$) δ 8.82 – 8.66 (m, 4H, NDI-**H**), 6.94 – 6.74 (m, 8H, Ar-**H**), 5.18 – 4.80 (m, 12H, Ar-C**H₂**-Ar + OC**H₂**), 4.26 – 4.12 [m, 4H, N(CO)₂**CH₂**CH₂(CH₂)₃CH₃ + CON(CH₃)CH₂CH₂**CH₂**N(CO)₂], 3.58 – 3.12 [m, 18H, CON(CH₃)**CH₂**CH₂CH₂N(CO)₂ + CON(**CH₂**CH₃)₂ + Ar-C**H₂**-Ar], 3.06 – 2.92 [m, 3H, CON(C**H₃**)CH₂CH₂CH₂N(CO)₂], 2.08 – 1.90 [m, CON(CH₃)CH₂C**H₂**CH₂N(CO)₂], 1.82 – 1.64 [m, 2H, N(CO)₂CH₂C**H₂**(CH₂)₃CH₃], 1.46 – 1.28 [m, 6H, N(CO)₂CH₂CH₂(C**H₂**)₃CH₃], 1.24 – 0.94 [m, 54H, [Ar-C(C**H₃**)₃+ [CON(CH₂C**H₃**)₂], 0.91 – 0.85 [m, 3H, N(CO)₂CH₂CH₂(CH₂)₃C**H₃**].

^{13}C DEPTQ 135 NMR (100 MHz, CDCl₃) δ [170.08, 169.53, 169.44, 169.32, **C**ON(CH₂CH₃)₂ + **C**ON(CH₃)CH₂CH₂CH₂N(CO)₂)], (162.86, 162.76, NDI-**C**O), (153.71, 153.37, 145.40, 145.10, 134.87, 134.08, 134, 133.80, 133.76, 133.67, 133.48, Ar-**C**), (131.07,131.03, 130.96, NDI-**C**H), (126.90, 126.81, 126.59, Ar-**C**), (125.57, 125.48, 125.39, Ar-**C**H + NDI-**C**), (72.06, 71.74, 71.63, O**C**H₂), [45.57, CON(CH₃)**C**H₂CH₂CH₂N(CO)₂)], [41.34, 41.12, 40.54, 38.82, 38.45, CON(CH₃)CH₂CH₂**C**H₂N(CO)₂ + N(CO)₂**C**H₂CH₂(CH₂)₃CH₃ + CON(**C**H₂CH₃)₂], [34.29, 34.01, CON(**C**H₃)CH₂CH₂CH₂N(CO)₂], [33.95, Ar-**C**(CH₃)₃], [32.01, 31.87, 31.50, Ar-**C**H₂-Ar + N(CO)₂CH₂CH₂CH₂**C**H₂CH₂CH₃ + Ar-C(**C**H₃)₃], [26.85, 26.01, 22.65, N(CO)₂CH₂**C**H₂**C**H₂CH₂**C**H₂CH₃], [14.15, 14.11, 13.19, 13.11, N(CO)₂CH₂CH₂(CH₂)₃**C**H₃ + CON(CH₂**C**H₃)₂].

Elementalanalysis calcd (%) for $C_{88}H_{116}N_6O_{12}$: C, 72.90; H, 8.06; N, 5.80; found: C, 72.57; H, 8.05, N; 6.04.

HRMS (ESI): calculated for $C_{88}H_{116}N_6O_{12}$ as $[M + H]^+$: 1449.8724; found: 1449.8679.

6.2.19 Ligand **L6**

Compound **C4** (1.2 g, 1.2 mmol), 1-hydroxybenzotriazole (0.3 g, 2.3 mmol) and triethylamine (0.8 mL, 5.7 mmol) were dissolved in dry THF (60 mL). The mixture was cooled down to 0°C, and the *N, N'*-dicyclohexylcarbodiimide (0.5 g, 2.4 mmol) was added under stirring. The mixture was further stirred at room temperature for 20 minutes. The secondary amine TFA salt, compound **NDI11** (0.7 g, 1.2 mmol), was added. After 24 hours, the precipitate was filtered, and the solvent was removed under reduced pressure. The remaining solid was redissolved in DCM (200 mL), followed by washing with water (100 mL x 2). The organic layer was dried over Na₂SO₄. The solvent was removed via rotary evaporator. The residue was redissolved in acetonitrile (50 mL), and sodium tetrafluoroborate (0.2 g, 1.9 mmol) was added. The solvent was removed, and the desired sodium product was purified via column chromatography (Brockmann I, neutral alumina, dichloromethane: methanol 100: 0.2). After removing

the solvent, the solid was redissolved in acetone (10 mL), added dropwise to the H_2O (100 mL) and stirred at 70 °C for 1 hour. The precipitate was filtered to afford an orange solid (0.4 g, yield 23%).

^{1}H NMR (400 MHz, CDCl$_3$) δ 8.74 (s, 4H, NDI-**H**), 6.86 (d, *J* = 11.2 Hz, 4H, Ar-**H**), 6.76 – 6.62 (m, 4H, Ar-**H**), 5.28 – 5.14 (m, 4H, Ar-C**H$_2$**-Ar), 5.12 – 5.02 (m, 4H, OC**H$_2$**), 4.96 – 4.82 (m, 4H, OC**H$_2$**), 4.24 – 4.10 [m, 4H,CONCH$_2$CH$_2$CH$_2$CH$_2$CH$_2$C**H$_2$**N(CO)$_2$ + N(CO)$_2$**CH$_2$**CH$_2$(CH$_2$)$_3$CH$_3$], 3.42 – 3.10 [m, 20H, (CONC**H$_2$**CH$_2$CH$_3$) + CONC**H$_2$**CH$_2$CH$_2$CH$_2$CH$_2$CH$_2$N(CO)$_2$ + ArC**H$_2$**Ar + CON(C**H$_2$**CH$_3$)$_2$], 1.80 – 1.66 [m, 4H, CONCH$_2$CH$_2$CH$_2$CH$_2$C**H$_2$**CH$_2$ N(CO)$_2$ + N(CO)$_2$CH$_2$C**H$_2$**(CH$_2$)$_3$CH$_3$], 1.60 – 1.48 [m, 4H, (CONCH$_2$C**H$_2$**CH$_3$) + CONCH$_2$C**H$_2$**CH$_2$CH$_2$CH$_2$CH$_2$N(CO)$_2$], 1.46 – 1.30 [m, 10H, CONCH$_2$CH$_2$C**H$_2$**C**H$_2$**CH$_2$CH$_2$N(CO)$_2$ +N(CO)$_2$CH$_2$CH$_2$(C**H$_2$**)$_3$CH$_3$], 1.20 – 1.04 [m, 54H, Ar-C(C**H$_3$**)$_3$ + CON(CH$_2$C**H$_3$**)$_2$], 0.92 – 0.82 [m, 6H, N(CO)$_2$CH$_2$C**H$_2$**(CH$_2$)$_3$C**H$_3$**+ CONCH$_2$CH$_2$C**H$_3$**].

^{13}C NMR (100 MHz, CDCl$_3$) δ [169.73, 169.22, **C**ON(CH$_2$CH$_3$)$_2$ + (**C**ONCH$_2$CH$_2$CH$_3$)], (162.95, 162.93, NDI-**C**O), (153.56, 145.53, 134.38, 134.27, 133.55, 133.48, Ar-**C**), (131.08, NDI-**C**H), (126.84, 126.70, NDI-**C**),(125.76, 125.71, 125.49, Ar-**C**H), (72.57, OC**H$_2$**), [48.50, 47.93, 46.96, 46.07, CON**C**H$_2$CH$_2$CH$_2$CH$_2$CH$_2$CH$_2$N(CO)$_2$ + (CON**C**H$_2$CH$_2$CH$_3$)], [41.41, 41.15, 40.94, 40.85, 40.73, 40.70, 40.61, N(CO)$_2$**C**H$_2$CH$_2$(CH$_2$)$_3$CH$_3$ + CONCH$_2$CH$_2$CH$_2$CH$_2$CH$_2$**C**H$_2$N(CO)$_2$ + CON(**C**H$_2$CH$_3$)$_2$], [34.07, 34.05, 33.95, 33.92, Ar**C**(CH$_3$)$_3$], [31.87, 31.63, 31.59, 31.42, (Ar-**C**H$_2$-Ar) + ArC(**C**H$_3$)$_3$ +N(CO)$_2$CH$_2$CH$_2$CH$_2$**C**H$_2$CH$_2$CH$_3$], [28.17, 27.78, 27.08, 27.00, 26.88, 26.75, 22.68, 22.17, 21.07, N(CO)$_2$CH$_2$**C**H$_2$**C**H$_2$CH$_2$**C**H$_2$CH$_3$+ (CONCH$_2$**C**H$_2$CH$_3$) + CONCH$_2$**C**H$_2$**C**H$_2$**C**H$_2$**C**H$_2$CH$_2$N(CO)$_2$], [14.18, 14.12, 13.14, 11.66, 11.44, N(CO)$_2$CH$_2$CH$_2$(CH$_2$)$_3$**C**H$_3$ + CONCH$_2$CH$_2$**C**H$_3$ + CON(CH$_2$**C**H$_3$)$_2$].

HRMS (ESI): calculated for C$_{93}$H$_{126}$N$_6$O$_{12}$ as [M + H]$^+$: 1519.9506; found: 1519.9443.

Elementalanalysis calcd (%) for C$_{93}$H$_{126}$N$_6$O$_{12}$·H$_2$O: C, 72.62; H, 8.39; N, 5.46; found: C, 72.90; H, 8.52; N, 5.39.

6.2.20 Chemical Reduction of NDI

Ligand **L5** (14.5 mg, 9.6 µmol) and Yb(DMSO)$_3$(NO$_3$)$_3$ (5.7 mg, 9.6 µmol) were dissolved in a dry MeCN (10.0 mL). The resulting mixture was stirred at room temperature for 5 minutes. The solvent was removed under a stream of N$_2$ overnight. The Yb(**L5**) complex was stored under N$_2$ for further use. The Nd(**L5**) complex was synthesised following the same procedure.

Ligand **L5** (1.5 mg, 1.0 µmol) was dissolved in a dry MeCN solution (10.0 mL). The solution was degassed via freeze-pump-thaw in schlenk cuvette until no bubbles were observed. The clear solution was transferred to the schlenk cuvette purged with the N$_2$ via a syringe. The Tetrakis(dimethylamino)ethylene (0.5 µL, 2.0 µmol) was added. After mixing, the clear solution changes to brown. The schlenk cuvette was sealed for photophysical measurement. If trace amounts of oxygen were left in the schlenk cuvette, the colour would change to bright yellow, then to colourless.

The Yb(**L5$^{•-}$**) and Nd(**L5$^{•-}$**) complexes were synthesised using the same procedure.

6.3 Preparation of Lanthanoid Complex

A 10^{-3} M DCM/MeCN (1:1) solution of ligand **L2** (1ml) was added to 10^{-3} M DCM/MeCN(1:1) solution (1ml) of Ln(DMSO)$_x$(NO$_3$)$_3$ (where Ln = Eu^{3+}, Gd^{3+}, Nd^{3+} and Yb^{3+}). The trimethylamine was then added to ensure the calixarene was fully deprotonated. The combined mixture solution was further diluted to 10^{-4} M and 10^{-5} M. For the **L3** ligand, the trimethylamine was not needed before dilution because no phenolic units were present to be deprotonated. To prepare the solid samples, one equivalent of the ligand and one equivalent of Ln(DMSO)$_x$(NO$_3$)$_3$ were dissolved in a DCM/MeCN solution in the presence of triethylamine(**L2**) or in the absence of triethylamine(**L3**). The mixture was sonicated in the water bath for five minutes to achieve dissolution. The solvent was removed to afford the lanthanoid complex of ligand **L2** as a green solid and ligand **L3** as a yellow solid. The complexes were used for the measurement without further purification. The procedure for preparing lanthanoid complexes with ligand **L4**, **L5** and **L6** is the same as that used for Ln(L3) complex in acetonitrile solutions and solid state.

6.4 X- Ray Crystallography

Ligand **L1**

Empirical formula C$_{137}$H$_{197}$Eu$_2$N$_{11}$O$_{19}$,formula weight = 2605.96, yellow needle, 0.243 × 0.201 × 0.140 mm^3, triclinic, space group P-1 (No. 2), a = 12.9282(2), b = 13.9847(2), c = 21.2223(3) Å, α = 73.377(1), β = 89.778(1),γ= 64.370(2)°, V = 3282.76(10) Å^3, Z = 1, D_c = 1.318 g cm^{-3},μ= 1.015 mm^{-1}. F_{000} = 1374, MoKα radiation, λ = 0.71073 Å, T = 100(2) K, $2\theta_{max}$ = 64.5°, 70022 reflections collected, 21568 unique (R_{int} = 0.0319). Final $GooF$ = 1.001, R1 = 0.0431, wR2 = 0.1113, R indices based on 19220 reflections with I> 2σ(I) (refinement on F^2), |$\Delta\rho$|$_{max}$= 1.8(1) e Å^{-3}, 804 parameters, 79 restraints. Lp and absorption corrections applied.

Eu(**L2**-2H)(NO$_3$)$_3$

Empirical formula: C$_{108}$H$_{126}$EuN$_{13}$O$_{17}$, formula weight = 2030.17, light blue block crystals, 0.29 × 0.17 × 0.08 mm^3, triclinic, space group P-1 (No. 2), a = 12.780 Å, b = 16.674 Å, c = 24.069 Å, α = 82.76°, β = 84.79°, γ = 88.03°, V = 5065.5 Å^3, T = 293(2) K, Z = 2, Z' = 1, μ(Cu K$_\alpha$) = 5.023, 51579 reflections measured, 17867 unique (R$_{int}$ = 0.0651) which were used in all calculations. The final wR_2 was 0.1404 (all data) and R_1 was 0.0522 (I≥2σ(I)).

Yb(L**2**-2H)(NO$_3$)$_3$

Empirical formula: C$_{108}$H$_{126}$N$_{13}$O$_{17}$Yb, formula weight = 2051.25, dark green block crystals, 0.26 × 0.17 × 0.09 mm^3, triclinic, space group P-1 (No. 2), a = 12.7325(3) Å, b = 16.6893(4) Å, c = 24.0569(5) Å, α = 82.658(2)°, β = 84.804(2)°, γ = 87.775(2)°, V = 5047.3(2) Å^3, T = 94.6(9) K, Z = 2, Z' = 1, μ(Cu K$_\alpha$) = 2.307, 91019 reflections measured, 17998 unique (R$_{int}$ = 0.0821) which were used in all calculations. The final wR_2 was 0.1414 (all data) and R_1 was 0.0540 (I≥2σ(I)).

Ligand **L3**

Empirical formula: $C_{104}H_{124}N_8O_{16}$, formula weight= 1742.10, triclinic, light orange block crystals, 0.45 × 0.13 × 0.09 mm^3, space group P-1 (No. 2), a = 11.8919(4) Å, b = 12.2982(3) Å, c = 35.8870(6) Å, α = 83.103(2)°, β= 89.537(2)°, γ= 88.908(2)°, V = 5209.4(2) Å^3, T = 150.00(10) K, Z = 2, Z' = 1, μ(Cu K$_\alpha$) = 0.602, 95650 reflections measured, 20768 unique (R_{int} = 0.0820) which were used in all calculations. The final wR_2 was 0.4001 (all data) and R_1 was 0.1294 (I≥2σ(I)).

Ligand **L4**

Empirical formula: $C_{86}H_{112}N_6O_{12}$, formula weight = 1421.81, monoclinic, light green block crystals, 0.34 × 0.26 × 0.17 mm^3, space group $P2_1/n$ (No. 14), a = 16.42540(10) Å, b = 15.88100(10) Å, c = 30.2099(3) Å, β= 97.2590(10)°, α= γ = 90°, V = 7817.15(10) Å^3, T = 172(100) K, Z = 4, Z' = 1, μ(Cu K$_\alpha$) = 0.639, 117989 reflections measured, 13829 unique (R_{int} = 0.0564) which were used in all calculations. The final wR_2 was 0.2361 (all data) and R_1 was 0.0779 (I≥2σ(I)).

7 Reference

1.   Cotton, F.; Wilkinson, G., *Advanced Inorganic Chemistry*. 4th ed.; Wiley & Sons, 1980.

2. The Lanthanides - Principles and Energetics. In *Lanthanide and Actinide Chemistry*, 2006; pp 9-22.

3.   Coordination Chemistry of the Lanthanides. In *Lanthanide and Actinide Chemistry*, 2006; pp 35-60.

4.   Bünzli, J.-C. G.; Piguet, C., Lanthanide-Containing Molecular and Supramolecular Polymetallic Functional Assemblies. *Chem. Rev. (Washington, DC, U. S.)* **2002,***102* (6), 1897-1928.

5.   Semenova, L.; Skelton, B.; White, A., The Rare Earth(III) Nitrate Dimethyl Sulfoxide Adducts [(dmso)$_n$Ln(O$_2$(NO)$_3$]. *Aust. J. Chem.* **1996,***49* (9), 997-1004.

6.   Kaltsoyannis, N.; Scott, P., *The f Elements*. Oxford University Press: Oxford, 1999.

7.   Bünzli, J.-C. G.; Piguet, C., Taking advantage of luminescent lanthanide ions. *Chem. Soc. Rev.* **2005,***34* (12), 1048-1077.

8.   Uh, H.; Petoud, S., Novel antennae for the sensitization of near infrared luminescent lanthanide cations. *C. R. Chim.* **2010,***13* (6), 668-680.

9.   Pavia, D. L.; Lampman, G. M.; Kriz, G. S.; Vyvyan, J. A., *Introduction to Spectroscopy*. Cengage Learning: 2008.

10.   Weissman, S. I., Intramolecular Energy Transfer The Fluorescence of Complexes of Europium. *J. Chem. Phys.* **1942,***10* (4), 214-217.

11.   Förster, T., Zwischenmolekulare Energiewanderung und Fluoreszenz. *Annalen der Physik* **1948,***437* (1-2), 55-75.

12.   Dexter, D. L., A Theory of Sensitized Luminescence in Solids. *J. Chem. Phys.* **1953,***21* (5), 836-850.

13.   Kasha, M., Characterization of electronic transitions in complex molecules. *Discussions of the Faraday Society* **1950,***9* (0), 14-19.

14.   Steemers, F. J.; Verboom, W.; Reinhoudt, D. N.; van der Tol, E. B.; Verhoeven, J. W., New Sensitizer-Modified Calix[4]arenes Enabling Near-UV Excitation of Complexed Luminescent Lanthanide Ions. *J. Am. Chem. Soc.* **1995,***117* (37), 9408-9414.

15.   Kleinerman, M., Energy Migration in Lanthanide Chelates. *J. Chem. Phys.* **1969,***51* (6), 2370-2381.

16.   Lazarides, T.; Alamiry, M. A. H.; Adams, H.; Pope, S. J. A.; Faulkner, S.; Weinstein, J. A.; Ward, M. D., Anthracene as a sensitiser for near-infrared luminescence in complexes of Nd(iii), Er(iii) and Yb(iii): an unexpected sensitisation mechanism based on electron transfer. *Dalton Trans.* **2007,** (15), 1484-1491.

17.   Melhuish, W. H., Nomenclature, symbols, units and their usage in spectrochemical analysis-Part VI: molecular luminescence spectroscopy. *Pure Appl. Chem.* **1984,***56* (2), 231-245.

18.   Lakowicz, J. R., *Principles of Fluorescence Spectroscopy*. 2006.

19.   Crosby, G. A.; Demas, J. N., Measurement of photoluminescence quantum yields. Review. *J. Phys. Chem.* **1971,***75* (8), 991-1024.

20.   McPherson, J. N.; Abad Galan, L.; Iranmanesh, H.; Massi, M.; Colbran, S. B., Synthesis and structural, redox and photophysical properties of tris-(2,5-di(2-pyridyl)pyrrolide) lanthanide complexes. *Dalton Trans.* **2019,***48* (25), 9365-9375.

21.   Sato, S.; Wada, M., Relations between Intramolecular Energy Transfer Efficiencies and Triplet State Energies in Rare Earth β-diketone Chelates. *Bull. Chem. Soc. Jpn.* **1970,***43* (7), 1955-1962.

22.   Driscoll, C. R.; Skelton, B. W.; Massi, M.; Ogden, M. I., Structural characterisation and photophysical properties of lanthanoid complexes of a tetra-amide functionalised calix[4]arene. *Supramol. Chem.* **2016,***28* (5-6), 567-574.

23.   Horrocks, W. D.; Sudnick, D. R., Lanthanide ion probes of structure in biology. Laser-induced luminescence decay constants provide a direct measure of the number of metal-coordinated water molecules. *J. Am. Chem. Soc.* **1979,***101* (2), 334-340.

24.   Horrocks, W. D.; Sudnick, D. R., Lanthanide ion luminescence probes of the structure of biological macromolecules. *Acc. Chem. Res.* **1981,***14* (12), 384-392.

25.   Bunzli, J. C. G.; Froidevaux, P.; Harrowfield, J. M., Complexes of lanthanoid salts with macrocyclic ligands. 41. Photophysical properties of lanthanide dinuclear complexes with p-tert-butylcalix[8]arene. *Inorg. Chem.* **1993,***32* (15), 3306-3311.

26.   Fu, L.-M.; Ai, X.-C.; Li, M.-Y.; Wen, X.-F.; Hao, R.; Wu, Y.-S.; Wang, Y.; Zhang, J.-P., Role of Ligand-to-Metal Charge Transfer State in Nontriplet Photosensitization of Luminescent Europium Complex. *J. Phys. Chem. A* **2010,***114* (13), 4494-4500.

27.   Horrocks, W. D.; Bolender, J. P.; Smith, W. D.; Supkowski, R. M., Photosensitized Near Infrared Luminescence of Ytterbium(III) in Proteins and Complexes Occurs via an Internal Redox Process. *J. Am. Chem. Soc.* **1997,***119* (25), 5972-5973.

28.   Liu, G. K.; Jensen, M. P.; Almond, P. M., Systematic Behavior of Charge-Transfer Transitions and Energy Level Variation in Soft Donor Complexes of the Trivalent Lanthanides. *J. Phys. Chem. A* **2006,***110* (6), 2081-2088.

29.   Zhong, Y.; Si, L.; He, H.; Sykes, A. G., BODIPY chromophores as efficient green light sensitizers for lanthanide-induced near-infrared emission. *Dalton Trans.* **2011,***40* (43), 11389-11395.

30.   Massi, M.; Ogden, M. I., Luminescent Lanthanoid Calixarene Complexes and Materials. *Materials* **2017,***10* (12), 1369.

31.   Goh, C. Y.; Fu, D.-Y.; Duncan, C. L.; Tinker, A.; Li, F.; Mocerino, M.; Ogden, M. I.; Wu, Y., The inhibitory properties of acidic functionalised calix[4]arenes on human papillomavirus pentamer formation. *Supramol. Chem.* **2020,***32* (5), 345-353.

32.   Fu, D.-Y.; Lu, T.; Liu, Y.-X.; Li, F.; Ogden, M. I.; Wang, Y.; Wu, Y.; Mocerino, M., Enantioselective Inhibition of Human Papillomavirus L1 Pentamer Formation by Chiral-Proline Modified Calix[4]arenes: Targeting the Protein Interface. *ChemistrySelect* **2016,***1* (19), 6243-6249.

33.   Peer Reviewed: Calixarenes: Designer Ligands for Chemical Sensors. *Anal. Chem.* **2001,***73* (1), 22 A-29 A.

34.   Diamond, D.; McKervey, M. A., Calixarene-based sensing agents. *Chem. Soc. Rev.* **1996,***25* (1), 15-24.

35.   Bouvier-Capely, C.; Manoury, A.; Legrand, A.; Bonthonneau, J. P.; Cuenot, F.; Rebière, F., The use of calix[6]arene molecules for actinides analysis in urine and drinking water: an alternative to current procedures. *J. Radioanal. Nucl. Chem.* **2009,** *282* (2), 611.

36.   Zhang, A.; Wei, Y.; Hoshi, H.; Koma, Y.; Kamiya, M., Partitioning of Cesium from a Simulated High Level Liquid Waste by Extraction Chromatography Utilizing a Macroporous Silica-Based Supramolecular Calix[4]arene-Crown Impregnated Polymeric Composite. *Solvent Extr. Ion Exch.* **2007,** *25* (3), 389-405.

37.   Morohashi, N.; Hattori, T.; Yokomakura, K.; Kabuto, C.; Miyano, S., Dinuclear titanium(IV) complex of p-tert-butylthiacalix[4]arene as a novel bidentate Lewis acid catalyst. *Tetrahedron Lett.* **2002,** *43* (43), 7769-7772.

38.   Tsukahara, Y.; Hirotsu, M.; Hattori, S.-i.; Usuki, Y.; Kinoshita, I., A Thiacalix[3]pyridine Copper(I) Complex as a Highly Active Catalyst for the Olefin Aziridination Reaction. *Chem. Lett.* **2008,** *37* (4), 452-453.

39.   Gutsche, C. D.; Chemistry, R. S. o., *Calixarenes: An Introduction*. RSC Publishing: 2008.

40.   Zinke, A.; Ziegler, E., *Ber.* **1941,** *B74*, 1729.

41.   Zinke, A.; Ziegler, E., *Ber.* **1944,** *77*, 264.

42.   Niederl, J. B.; Vogel, H. J., Aldehyde—Resorcinol Condensations1. *J. Am. Chem. Soc.* **1940,** *62* (9), 2512-2514.

43.   Hayes, B. T.; Hunter, R. F., Phenol-formaldehyde and allied resins VI: Rational synthesis of a 'cyclic' tetranuclear p-cresol novolak. *J. Appl. Chem.* **1958,** *8* (11), 743-748.

44.   J. W. Cornforth; P. D'Arcy Hart; G.A. Nicholls; Rees, R. J. W.; Stock, J. A., *Br. J. Pharmacol.* **1955,** *10*, 73.

45.   Gutsche, C. D.; Muthukrishnan, R., Calixarenes. 1. Analysis of the product mixtures produced by the base-catalyzed condensation of formaldehyde with para-substituted phenols. *J. Org. Chem.* **1978,** *43* (25), 4905-4906.

46.   Zinke, A.; Zigeuner, G.; ssinger, K. H., *Monatsh.* **1948,** (79), 438

47.   Patterson, A. M.; Capell, L. T.; Walker, D. F., *The Ring Index,* **1960**, 2nd ed, American Chemical Society, Washington, DC, Ring Index No. 6485.

48.   Guérineau, V.; Rollet, M.; Viel, S.; Lepoittevin, B.; Costa, L.; Saint-Aguet, P.; Laurent, R.; Roger, P.; Gigmes, D.; Martini, C.; Huc, V., The synthesis and characterization of giant Calixarenes. *Nat. Commun.* **2019,** *10* (1), 113.

49.   Nealon, G. L.; McIldowie, M. J.; Skelton, B. W.; Mocerino, M.; Massi, M.; Ogden, M. I., Structural Variations in the Complete Series of Lanthanoid Complexes of a Calix[4]arene Trisamide. *Aust. J. Chem.* **2017**, *73* (6), 424-433.

50.   Furphy, B. M.; Harrowfield, J. M.; Ogden, M. I.; Skelton, B. W.; White, A. H.; Wilner, F. R., Lanthanide ion complexes of the calixarenes. Part 4. Double inclusion by p-t-butylcalix[4]arene (H4L). Crystal structures of [Eu2(HL)2(dmf)4].7dmf (dmf = dimethylformamide) and H4L.dmso (dmso = dimethyl sulphoxide). *J. Chem. Soc., Dalton Trans.* **1989,** (11), 2217-2221.

51.   Guillemot, G.; Castellano, B.; Prangé, T.; Solari, E.; Floriani, C., Use of Calix[4]arenes in the Redox Chemistry of Lanthanides: the Reduction of Dinitrogen by a Calix[4]arene−Samarium Complex. *Inorg. Chem.* **2007,** *46* (13), 5152-5154.

52.   Gutsche, C. D.; Dhawan, B.; Levine, J. A.; Hyun No, K.; Bauer, L. J., Calixarenes 9: Conformational isomers of the ethers and esters of calix[4]arenes. *Tetrahedron* **1983,** *39* (3), 409-426.

53.   Iwamoto, K.; Ikeda, A.; Araki, K.; Harada, T.; Shinkai, S., "Cone" - "Partial-cone" Isomerism in Tetramethoxycalix[4]arenes. Influence of Solvent Polarity and Metal Ions. *Tetrahedron* **1993,** *49* (44), 9937-9946.

54.   Gutsche, C. D.; Bauer, L. J., Calixarenes. 5. Dynamic NMR characteristics of p-tert-butylcalix[4]-arene and p-tert-butylcalix[8]arene. *Tetrahedron Lett.* **1981,** *22* (48), 4763-4766.

55.   Arduini, A.; Fabbi, M.; Mantovani, M.; Mirone, L.; Pochini, A.; Secchi, A.; Ungaro, R., Calix[4]arenes Blocked in a Rigid Cone Conformation by Selective Functionalization at the Lower Rim. *J. Org. Chem.* **1995,** *60* (5), 1454-1457.

56.   Seiji, S.; Koji, A.; Hiroshi, K.; Takayuki, T.; Osamu, M., On the Acidity of the Hydroxyl Groups in Calix[4]arenes and the Dissociation-dependent Conformational Change. *Chem. Lett.* **1986,** *15* (8), 1351-1354.

57.   Koji, A.; Koji, I.; Seiji, S.; Tsutomu, M., "pKa" of Calixarenes and Analogs in Nonaqueous Solvents. *Bull. Chem. Soc. Jpn.* **1990,** *63* (12), 3480-3485.

58.   Grootenhuis, P. D. J.; Kollman, P. A.; Groenen, L. C.; Reinhoudt, D. N.; Van Hummel, G. J.; Ugozzoli, F.; Andreetti, G. D., Computational study of the structural, energetic, and acid-base properties of calix[4]arenes. *J. Am. Chem. Soc.* **1990,** *112* (11), 4165-4176.

59.   Zeng, C.-C.; Becker, J. Y., Synthesis, electrochemical and intramolecular charge-transfer properties of 'calix[4]arene-acceptor' diad and triad derivatives. *Tetrahedron* **2004,** *60* (7), 1643-1650.

60.   Bauer, D.; Stipurin, S.; Köckerling, M.; Mamat, C., Formation of calix[4]arenes with acyloxycarboxylate functions. *Tetrahedron* **2020,** *76* (34), 131395.

61.   Ogden, M. I.; Skelton, B. W.; White, A. H., Syntheses, structural studies and solution properties of iron complexes of some amide-substituted calixarenes. *J. Chem. Soc., Dalton Trans.* **2001,** (20), 3073-3077.

62.   D'Alessio, D.; Krause-Heuer, A. M.; Skelton, B. W.; Fraser, B. H.; Massi, M.; Ogden, M. I., Synthesis, structure and conformational mobility of tetra-substituted cyanomethoxy p-tert-butylcalix[4]arenes. *RSC Adv.* **2016,** *6* (43), 37006-37011.

63.   Arena, G.; Cali, R.; Lombardo, G. G.; Rizzarelli, E.; Sciotto, D.; Ungaro, R.; Casnati, A., Water soluble calix[4]arenes. A thermodynamic investigation of proton complex formation. *Supramol. Chem.* **1992,** *1* (1), 19-24.

64.   Isao, Y.; Nobuhiro, Y.; Fumio, S.; Daido, I.; Keihei, U.; Seiji, S., Re-evaluation of the Acid Dissociation Constants of the Hydroxyl Groups in Tetrasodium 25,26,27,28-Tetrahydroxycalix[4]arene-5,11,17,23-tetrasulfonate. *Bull. Chem. Soc. Jpn.* **1992,** *65* (4), 1012-1015.

65.   Shinkai, S.; Araki, K.; Grootenhuis, P. D. J.; Reinhoudt, D. N., pKa determination of water-soluble calix[4]arenes. *J. Chem. Soc., Perkin Trans. 2* **1991,** (12), 1883-1886.

66.   Shinkai, S., Calixarenes - the third generation of supramolecules. *Tetrahedron* **1993,***49* (40), 8933-8968.

67.   Groenen, L. C.; Ruël, B. H. M.; Casnati, A.; Verboom, W.; Pochini, A.; Ungaro, R.; Reinhoudt, D. N., Synthesis of monoalkylated calix[4]arenes via direct alkylation. *Tetrahedron* **1991,***47* (39), 8379-8384.

68.   Adhikari, B. B.; Roshandel, S.; Fujii, A.; Schramm, M. P., Calixarene-Mediated Liquid Membrane Transport of Choline Conjugates 2: Transport of Drug-Choline Conjugates and Neurotransmitters. *Eur. J. Org. Chem.* **2015,***2015* (12), 2683-2690.

69.   Wolbers, M. P.; van Veggel, F. C. J. M.; Heeringa, R. H. M.; Hofstraat, J. W.; Geurts, A. J.; van Hummel, G. J.; Harkema, S.; Reinhoudt, D. N., Biscalix[4]arene Ligands for Dinuclear Lanthanide Ion Complexation. *Liebigs Ann.* **1997,***1997* (12), 2587-2600.

70.   McIldowie, M. J.; Skelton, B. W.; Mocerino, M.; Ogden, M. I., A lanthanum picrate complex of a 1,2-bisamide substituted calix[4]arene. *J. Inclusion Phenom. Macrocyclic Chem.* **2015,***82* (1), 43-46.

71.   Collins, E. M.; McKervey, M. A.; Madigan, E.; Moran, M. B.; Owens, M.; Ferguson, G.; Harris, S. J., Chemically modified calix[4]arenes. Regioselective synthesis of 1,3-(distal) derivatives and related compounds. X-Ray crystal structure of a diphenol-dinitrile. *J. Chem. Soc. Perkin Trans. I* **1991,** (12), 3137-3142.

72.   Beer, P. D.; Drew, M. G. B.; Kan, M.; Leeson, P. B.; Ogden, M. I.; Williams, G., Lanthanide Structures, Coordination, and Extraction Investigations of a 1,3-Bis(diethylamide)-Substituted Calix[4]arene Ligand. *Inorg. Chem.* **1996,***35* (8), 2202-2211.

73.   Beer, P. D.; Drew, M. G. B.; Grieve, A.; Ogden, M. I., Lanthanide picrate complexes and picric acid adduct of a calix[4]arene diamide. Syntheses and structures of [Tm(LH–2)A], [Ce(LH–2)(MeOH)2A]·HA, [PrLA3] and L·2HA {L = 5,11,17,23-tetra-tert-butyl-25,27-bis(diethylcarbamoylmethoxy)-26,28-dihydroxycalix[4]arene, HA = picric acid}. *J. Chem. Soc., Dalton Trans.* **1995,** (21), 3455-3466.

74.   Marcos, P. M.; Fonseca, J. D.; Proença, C. S.; Ascenso, J. R.; Bernardino, R. J.; Kulesza, J.; Bochenska, M., Experimental and computational studies of the binding properties of lower rim tetra- and di-substituted calix[4]arene amide derivatives with metal ions. *Supramol. Chem.* **2016,***28* (5-6), 367-376.

75.   Noamane, M. H.; Ben Othmen, A.; Al-Ayed, A. S.; Kim, Y.; Hayami, S.; Hamdi, A., Interaction of 2-furanylmethyl- and 2-thienylmethyl-amide derivatives of 1,3-di(carboxymethyl)calix[4]arene with metal salts. *J. Inclusion Phenom. Macrocyclic Chem.* **2019,***94* (3), 249-256.

76.   Casnati, A.; Sansone, F.; Sartori, A.; Prodi, L.; Montalti, M.; Zaccheroni, N.; Ugozzoli, F.; Ungaro, R., Quinoline-Containing Calixarene Fluoroionophores: A Combined NMR, Photophysical and Modeling Study. *Eur. J. Org. Chem.* **2003,***2003* (8), 1475-1485.

77.   Ogden, M. I.; Skelton, B. W.; White, A. H., Synthesis and structural studies of a lanthanide complex of a calix[4]arene tris-amide. *C. R. Chim.* **2005,***8* (2), 181-187.

78.   Calestani, G.; Ugozzoli, F.; Arduini, A.; Ghidini, E.; Ungaro, R., Encapsulated potassium cation in a new calix[4]arene neutral ligand: synthesis and X-ray crystal structure. *J. Chem. Soc., Chem. Commun.* **1987,** (5), 344-346.

79.   Arduini, A.; Ghidini, E.; Pochini, A.; Ungaro, R.; Andreetti, G. D.; Calestani, G.; Ugozzoli, F., p-t-Butylcalix[4]arene tetra-acetamide: a new strong receptor for alkali cations [1]. *J. Incl. Phenom.* **1988,***6* (2), 119-134.

80.   Sabbatini, N.; Guardigli, M.; Mecati, A.; Balzani, V.; Ungaro, R.; Ghidini, E.; Casnati, A.; Pochini, A., Encapsulation of lanthanide ions in calixarene receptors. A strongly luminescent terbium(3+) complex. *J. Chem. Soc., Chem. Commun.* **1990,** (12), 878-879.

81.   Marcos, P. M.; Ascenso, J. R.; Segurado, M. A. P.; Cragg, P. J.; Michel, S.; Hubscher-Bruder, V.; Arnaud-Neu, F., Lanthanide cation binding properties of homooxacalixarene diethylamide derivatives. *Supramol. Chem.* **2011,***23* (1-2), 93-101.

82.   Danil de Namor, A. F.; Baron, K.; Chahine, S.; Jafou, O., Complexation of Calix[4]arene Derivatives and Trivalent Cations in Dipolar Aprotic Media. *J. Phys. Chem. A* **2004,***108* (6), 1082-1089.

83.   Danil de Namor, A. F.; Jafou, O., Complexation of Calixarene Derivatives and Lanthanide Cations in Nonaqueous Media. *J. Phys. Chem. B* **2001,***105* (33), 8018-8027.

84.   Tranfić Bakić, M.; Espinosa, M.; Cindro, N.; Frkanec, L.; Babay, P.; Galić, N., UV-Vis and ESI MS/MS study of calix[4]arene derivatives and their lanthanide complexes. *Croat. Chem. Acta* **2017,***90*.

85.   Lincheneau, C.; Quinlan, E.; Kitchen, J. A.; McCabe, T.; Matthews, S. E.; Gunnlaugsson, T., Delayed lanthanide luminescent Tb(III) complexes formed from lower rim amide functionalised calix[4]arenes. *Supramol. Chem.* **2013,***25* (12), 869-880.

86.   Georgiev, E. M.; Clymire, J.; McPherson, G. L.; Max Roundhill, D., Luminescent europium(III) and terbium(III) ions encapsulated in a 2-aminoethoxy or carbamoyloxy substituted calixarene host. *Inorg. Chim. Acta* **1994,***227* (2), 293-296.

87.   Oude Wolbers, M. P.; van Veggel, F. C. J. M.; Peters, F. G. A.; van Beelen, E. S. E.; Hofstraat, J. W.; Geurts, F. A. J.; Reinhoudt, D. N., Sensitized Near-Infrared Emission from Nd3+ and Er3+ Complexes of Fluorescein-Bearing Calix[4]arene Cages. *Chem. - Eur. J.* **1998,***4* (5), 772-780.

88.   Röhrscheid, F., Carboxylic Acids, Aromatic. In *Ullmann's Encyclopedia of Industrial Chemistry*.

89.   Wang, C.-L. J., *Org. React* **1985,***34*, 319-400.

90.   Hahn, R.; Bohle, F.; Fang, W.; Walther, A.; Grimme, S.; Esser, B., Raising the Bar in Aromatic Donor–Acceptor Interactions with Cyclic Trinuclear Gold(I) Complexes as Strong π-Donors. *J. Am. Chem. Soc.* **2018,***140* (51), 17932-17944.

91.   Suseela, Y. V.; Das, S.; Pati, S. K.; Govindaraju, T., Imidazolyl-Naphthalenediimide-Based Threading Intercalators of DNA. *ChemBioChem* **2016,***17* (22), 2162-2171.

92.   Pfeiffer, C. R.; Biggins, N.; Lewis, W.; Champness, N. R., Nickel(ii) metal–organic frameworks with N,N′-di(4-pyridyl)-naphthalenediimide ligands: influence of secondary building unit geometry on dimensionality and framework dimensions. *CrystEngComm* **2017,***19* (37), 5558-5564.

93.   Brochsztain, S.; Rodrigues, M. A.; Demets, G. J. F.; Politi, M. J., Stabilization of naphthalene-1,8:4,5-dicarboximide radicals in zirconium phosphonate solid materials and thin films. *J. Mater. Chem.* **2002,***12* (5), 1250-1255.

94.   Garai, B.; Mallick, A.; Banerjee, R., Photochromic metal–organic frameworks for inkless and erasable printing. *Chem. Sci.* **2016,***7* (3), 2195-2200.

95. Ganesan, P.; Baggerman, J.; Zhang, H.; Sudhölter, E. J. R.; Zuilhof, H., Femtosecond Time-Resolved Photophysics of 1,4,5,8-Naphthalene Diimides. *J. Phys. Chem. A* **2007,***111* (28), 6151-6156.

96. Frath, D.; Nguyen, V. Q.; Lafolet, F.; Martin, P.; Lacroix, J.-C., Electrografted monolayer based on a naphthalene diimide–ruthenium terpyridine complex dyad: efficient creation of large-area molecular junctions with high current densities. *Chem. Commun. (Cambridge, U. K.)* **2017,***53* (80), 10997-11000.

97. Jones, B. A.; Facchetti, A.; Marks, T. J.; Wasielewski, M. R., Cyanonaphthalene Diimide Semiconductors for Air-Stable, Flexible, and Optically Transparent n-Channel Field-Effect Transistors. *Chem. Mater.* **2007,***19* (11), 2703-2705.

98. Mamada, M.; Pérez-Bolívar, C.; Anzenbacher, P., Green Synthesis of Polycyclic Benzimidazole Derivatives and Organic Semiconductors. *Org. Lett.* **2011,***13* (18), 4882-4885.

99. Keshri, S. K.; Asthana, D.; Chorol, S.; Kumar, Y.; Mukhopadhyay, P., Frontispiece: Appending Diverse π-Extended Acceptors with Tetrathiafulvalene/Dithiafulvalene Donors: Multistate Redox Properties, Radical Ion Generation, and Mid-IR-Absorbing Mixed-Valence States. *Chem. - Eur. J.* **2018,***24* (8).

100. Rogers, J. E.; Kelly, L. A., Nucleic Acid Oxidation Mediated by Naphthalene and Benzophenone Imide and Diimide Derivatives: Consequences for DNA Redox Chemistry. *J. Am. Chem. Soc.* **1999,***121* (16), 3854-3861.

101. Barros, T. C.; Brochsztain, S.; Toscano, V. G.; Filho, P. B.; Politi, M. J., Photophysical characterization of a 1,4,5,8-naphthalenediimide derivative. *J. Photochem. Photobiol., A* **1997,***111* (1), 97-104.

102. Wu, Y.; Frasconi, M.; Gardner, D. M.; McGonigal, P. R.; Schneebeli, S. T.; Wasielewski, M. R.; Stoddart, J. F., Electron Delocalization in a Rigid Cofacial Naphthalene-1,8:4,5-bis(dicarboximide) Dimer. *Angew. Chem., Int. Ed.* **2014,***53* (36), 9476-9481.

103. Flamigni, L.; Wyrostek, D.; Voloshchuk, R.; Gryko, D. T., Solvent polarity effect on intramolecular electron transfer in a corrole–naphthalene bisimide dyad. *Phys. Chem. Chem. Phys.* **2010,***12* (2), 474-483.

104. Molla, M. R.; Ghosh, S., Hydrogen-Bonding-Mediated J-Aggregation and White-Light Emission from a Remarkably Simple, Single-Component, Naphthalenediimide Chromophore. *Chem. - Eur. J.* **2012,***18* (5), 1290-1294.

105. He, T.; Stolte, M.; Burschka, C.; Hansen, N. H.; Musiol, T.; Kälblein, D.; Pflaum, J.; Tao, X.; Brill, J.; Würthner, F., Single-crystal field-effect transistors of new Cl 2 -NDI polymorph processed by sublimation in air. *Nat. Commun.* **2015,***6* (1), 5954.

106. Andric, G.; Boas, J. F.; Bond, A. M.; Fallon, G. D.; Ghiggino, K. P.; Hogan, C. F.; Hutchison, J. A.; Lee, M. A.-P.; Langford, S. J.; Pilbrow, J. R.; Troup, G. J.; Woodward, C. P., Spectroscopy of Naphthalene Diimides and Their Anion Radicals. *Aust. J. Chem.* **2004,***57* (10), 1011-1019.

107. Takahashi, E.; Takaya, H.; Naota, T., Dynamic Vapochromic Behaviors of Organic Crystals Based on the Open–Close Motions of S-Shaped Donor–Acceptor Folding Units. *Chem. - Eur. J.* **2010,***16* (16), 4793-4802.

108.   Parker, M. P.; Murray, C. A.; Hart, L. R.; Greenland, B. W.; Hayes, W.; Cardin, C. J.; Colquhoun, H. M., Mutual Complexation between π–π Stacked Molecular Tweezers. *Cryst. Growth Des.* **2018,***18* (1), 386-392.

109.   Schneebeli, S. T.; Frasconi, M.; Liu, Z.; Wu, Y.; Gardner, D. M.; Strutt, N. L.; Cheng, C.; Carmieli, R.; Wasielewski, M. R.; Stoddart, J. F., Electron Sharing and Anion–π Recognition in Molecular Triangular Prisms. *Angew. Chem., Int. Ed.* **2013,***52* (49), 13100-13104.

110.   Nelsen, S. F., Heterocyclic radical anions. II. Naphthalic and 1,4,5,8-naphthalenetetracarboxylic acid derivatives. *J. Am. Chem. Soc.* **1967,***89* (23), 5925-5931.

111.   Chakraborty, S.; Ray, D.; Aswal, V. K.; Ghosh, S., Multi-Stimuli-Responsive Directional Assembly of an Amphiphilic Donor–Acceptor Alternating Supramolecular Copolymer. *Chem. - Eur. J.* **2018,***24* (61), 16379-16387.

112.   Lu, Z.; Lavendomme, R.; Burghaus, O.; Nitschke, J. R., A Zn4L6 Capsule with Enhanced Catalytic C−C Bond Formation Activity upon C60 Binding. *Angew. Chem., Int. Ed.* **2019,***58* (27), 9073-9077.

113.   Zhou, D.; Wang, Y.; Jia, J.; Yu, W.; Qu, B.; Li, X.; Sun, X., H-Bonding and charging mediated aggregation and emission for fluorescence turn-on detection of hydrazine hydrate. *Chem. Commun. (Cambridge, U. K.)* **2015,***51* (53), 10656-10659.

114.   Lasitha, P., Radical anion formation exhibiting "turn-on" fluorescence sensing of hydrazine using a naphthalene diimide (NDI) derivative with a donor–acceptor–donor (D–A–D) molecular structure. *Photochem. Photobiol. Sci.* **2020,***19* (11), 1603-1612.

115.   Kumar, Y.; Kumar, S.; Mandal, K.; Mukhopadhyay, P., Isolation of Tetracyano-Naphthalenediimide and Its Stable Planar Radical Anion. *Angew. Chem., Int. Ed.* **2018,***57* (50), 16318-16322.

116.   Guha, S.; Goodson, F. S.; Corson, L. J.; Saha, S., Boundaries of Anion/Naphthalenediimide Interactions: From Anion−π Interactions to Anion-Induced Charge-Transfer and Electron-Transfer Phenomena. *J. Am. Chem. Soc.* **2012,***134* (33), 13679-13691.

117.   Kumar, S.; Mukhopadhyay, P., Ambient stable naphthalenediimide radical ions: synthesis by solvent-free, sonication, mechanical grinding or milling protocols. *Green Chem.* **2018,***20* (20), 4620-4628.

118.   Gosztola, D.; Niemczyk, M. P.; Svec, W.; Lukas, A. S.; Wasielewski, M. R., Excited Doublet States of Electrochemically Generated Aromatic Imide and Diimide Radical Anions. *J. Phys. Chem. A* **2000,***104* (28), 6545-6551.

119.   Jana, P.; Maity, S. K.; Bera, S.; Ghorai, P. K.; Haldar, D., Hierarchical self-assembly of naphthalene bisimides to fluorescent microspheres and fluoride sensing. *CrystEngComm* **2013,***15* (13), 2512-2518.

120.   Bhosale, S. V.; Bhosale, S. V.; Kalyankar, M. B.; Langford, S. J., A Core-Substituted Naphthalene Diimide Fluoride Sensor. *Org. Lett.* **2009,***11* (23), 5418-5421.

121.   Pal, S.; Hatai, J.; Samanta, M.; Shaurya, A.; Bandyopadhyay, S., A highly selective chemodosimeter for fast detection and intracellular imaging of Hg2+ ions based on a dithiocarbamate–isothiocyanate conversion in aqueous ethanol. *Org. Biomol. Chem.* **2014,***12* (7), 1072-1078.

122.   Martínez-Quiroz, M.; Ochoa-Terán, A.; Pina-Luis, G.; Santacruz Ortega, H., Photoinduced electron transfer in N,N-bis(pyridylmethyl)naphthalenediimides: study of their potential as pH chemosensors. *Supramol. Chem.* **2017,***29* (1), 32-39.

123.   Doria, F.; Folini, M.; Grande, V.; Cimino-Reale, G.; Zaffaroni, N.; Freccero, M., Naphthalene diimides as red fluorescent pH sensors for functional cell imaging. *Org. Biomol. Chem.* **2015,***13* (2), 570-576.

124.   Sato, S.; Takenaka, S., Linker effect of ferrocenylnaphthalene diimide ligands in the interaction with double stranded DNA. *J. Organomet. Chem.* **2008,***693* (7), 1177-1185.

125.   Collie, G. W.; Promontorio, R.; Hampel, S. M.; Micco, M.; Neidle, S.; Parkinson, G. N., Structural Basis for Telomeric G-Quadruplex Targeting by Naphthalene Diimide Ligands. *J. Am. Chem. Soc.* **2012,***134* (5), 2723-2731.

126.   Marchetti, C.; Minarini, A.; Tumiatti, V.; Moraca, F.; Parrotta, L.; Alcaro, S.; Rigo, R.; Sissi, C.; Gunaratnam, M.; Ohnmacht, S. A.; Neidle, S.; Milelli, A., Macrocyclic naphthalene diimides as G-quadruplex binders. *Bioorg. Med. Chem.* **2015,***23* (13), 3819-3830.

127.   Zhao, Y.; Sakai, N.; Matile, S., Enolate chemistry with anion–π interactions. *Nat. Commun.* **2014,***5* (1), 3911.

128.   Reiß, B.; Wagenknecht, H.-A., Naphthalene diimides with improved solubility for visible light photoredox catalysis. *Beilstein J. Org. Chem.* **2019,***15*, 2043-2051.

129.   Mareda, J.; Matile, S., Anion–π Slides for Transmembrane Transport. *Chem. - Eur. J.* **2009,***15* (1), 28-37.

130.   Dawson, R. E.; Hennig, A.; Weimann, D. P.; Emery, D.; Ravikumar, V.; Montenegro, J.; Takeuchi, T.; Gabutti, S.; Mayor, M.; Mareda, J.; Schalley, C. A.; Matile, S., Experimental evidence for the functional relevance of anion-pi interactions. *Nat. Commun.* **2010,***2* (7), 533-8.

131.   Shukla, D.; Nelson, S. F.; Freeman, D. C.; Rajeswaran, M.; Ahearn, W. G.; Meyer, D. M.; Carey, J. T., Thin-Film Morphology Control in Naphthalene-Diimide-Based Semiconductors: High Mobility n-Type Semiconductor for Organic Thin-Film Transistors. *Chem. Mater.* **2008,***20* (24), 7486-7491.

132.   Chen, W.; Zhang, J.; Long, G.; Liu, Y.; Zhang, Q., From non-detectable to decent: replacement of oxygen with sulfur in naphthalene diimide boosts electron transport in organic thin-film transistors (OTFT). *J. Mater. Chem. C* **2015,***3* (31), 8219-8224.

133.   Kalita, A.; Subbarao, N. V. V.; Iyer, P. K., Large-Scale Molecular Packing and Morphology-Dependent High Performance Organic Field-Effect Transistor by Symmetrical Naphthalene Diimide Appended with Methyl Cyclohexane. *J. Phys. Chem. C* **2015,***119* (22), 12772-12779.

134.   Li, G.-B.; He, J.-R.; Pan, M.; Deng, H.-Y.; Liu, J.-M.; Su, C.-Y., Construction of 0D to 3D cadmium complexes from different pyridyl diimide ligands. *Dalton Trans.* **2012,***41* (15), 4626-4633.

135.   Li, G.-B.; Liu, J.-M.; Cai, Y.-P.; Su, C.-Y., Structural Diversity of a Series of Mn(II), Cd(II), and Co(II) Complexes with Pyridine Donor Diimide Ligands. *Cryst. Growth Des.* **2011,***11* (7), 2763-2772.

136.   Liao, C.; Yarnell, J. E.; Glusac, K. D.; Schanze, K. S., Photoinduced Charge Separation in Platinum Acetylide Oligomers. *J. Phys. Chem. B* **2010,***114* (45), 14763-14771.

137.	Iengo, E.; Pantoş, G. D.; Sanders, J. K. M.; Orlandi, M.; Chiorboli, C.; Fracasso, S.; Scandola, F., A fully self-assembled non-symmetric triad for photoinduced charge separation. *Chem. Sci.* **2011,** *2* (4), 676-685.

138.	Ji, Z.; Wu, Y., Photoinduced Electron Transfer Dynamics of Cyclometalated Ruthenium (II)–Naphthalenediimide Dyad at NiO Photocathode. *J. Phys. Chem. C* **2013,** *117* (36), 18315-18324.

139.	Das, A.; Ghosh, S., H-bonding directed programmed supramolecular assembly of naphthalene-diimide (NDI) derivatives. *Chem. Commun. (Cambridge, U. K.)* **2016,** *52* (42), 6860-6872.

140.	Kar, H.; Gehrig, D. W.; Allampally, N. K.; Fernández, G.; Laquai, F.; Ghosh, S., Cooperative supramolecular polymerization of an amine-substituted naphthalene-diimide and its impact on excited state photophysical properties. *Chem. Sci.* **2016,** *7* (2), 1115-1120.

141.	Opina, A. C. L.; Ghaghada, K. B.; Zhao, P.; Kiefer, G.; Annapragada, A.; Sherry, A. D., TmDOTA-Tetraglycinate Encapsulated Liposomes as pH-Sensitive LipoCEST Agents. *PLoS One* **2011,** *6* (11), e27370.

142.	Durand, S.; Dognon, J.-P.; Guilbaud, P.; Rabbe, C.; Wipff, G., Lanthanide and alkaline-earth complexes of EDTA in water: a molecular dynamics study of structures and binding selectivities. *J. Chem. Soc., Perkin Trans. 2* **2000,** (4), 705-714.

143.	Fusaro, L.; Mocci, F.; Muller, R. N.; Luhmer, M., Insight into the Dynamics of Lanthanide-DTPA Complexes As Revealed by Oxygen-17 NMR. *Inorg. Chem.* **2012,** *51* (15), 8455-8461.

144.	Arora, H.; Mukherjee, R., Coordination polymers using (2-pyridyl)alkylamine-appended carboxylates: magnetic properties. *New J. Chem.* **2010,** *34* (11), 2357-2365.

145.	Chen, C.; Li, H., Synthesis and Crystal Structure of Amino Acid Modified NDI Lanthanide Coordination Complex. *Z. Anorg. Allg. Chem.* **2019,** *645* (13), 888-892.

146.	Chen, C.; Wu, Y.; Li, H., Fine-Tuning Aromatic Stacking and Single-Crystal Photoluminescence Through Coordination Chemistry. *Eur. J. Org. Chem.* **2019,** *2019* (8), 1778-1783.

147.	Xiang, Z.; Shan, Y.-B.; Li, T.; Huang, C.-C.; Huang, X.-H.; Lin, M.-J., Four isostructural lanthanide(III) coordination compounds based on a new N-oxydic pyridyl naphthalenediimide ligand: synthesis and characterization. *Acta Crystallogr. C* **2019,** *75* (1), 38-45.

148.	Nojima, T.; Kondoh, Y.; Takenaka, S.; Ichihara, T.; Takagi, M.; Tashiro, H.; Matsumoto, K., Detection of DNA hybridization by use of a lanthanide fluorescent intercalator that specifically binds to double stranded DNA. *Nucleic Acids Res. Suppl.* **2001,** (1), 105-6.

149.	Wang, X.; Wang, Y.; Wang, X.; Lu, K.; Jiang, W.; Cui, P.-P.; Hao, H.; Dai, F., Two series of Ln-MOFs by solvent induced self-assembly demonstrating the rapid selective sensing of Mg2+ and Fe3+ cations. *Dalton Trans.* **2020,** *49* (43), 15473-15480.

150.	Xiang, Z.; Shan, Y. B.; Li, T.; Huang, C. C.; Huang, X. H.; Lin, M. J., Four isostructural lanthanide(III) coordination compounds based on a new N-oxydic pyridyl naphthalenediimide ligand: synthesis and characterization. *Acta Crystallogr. C Struct. Chem.* **2019,** *75* (Pt 1), 38-45.

151.	Martinez, J. F.; La Porte, N. T.; Chaudhuri, S.; Sinopoli, A.; Bae, Y. J.; Sohail, M.; Batista, V. S.; Wasielewski, M. R., Effect of Electronic Coupling on Electron Transfer Rates from Photoexcited Naphthalenediimide Radical Anion to Re(bpy)(CO)3X. *J. Phys. Chem. C* **2019,** *123* (16), 10178-10190.

152.	Johansson, O.; Borgström, M.; Lomoth, R.; Palmblad, M.; Bergquist, J.; Hammarström, L.; Sun, L.; Åkermark, B., Electron Donor−Acceptor Dyads Based on Ruthenium(II) Bipyridine and Terpyridine Complexes Bound to Naphthalenediimide. *Inorg. Chem.* **2003,***42* (9), 2908-2918.

153.	Zhang, H.-L.; Liao, J.-Z.; Yang, W.; Wu, X.-Y.; Lu, C.-Z., A novel naphthalenediimide-based lanthanide–organic framework with polyoxometalate templates exhibiting reversible photochromism. *Dalton Trans.* **2017,***46* (15), 4898-4901.

154.	Shaikh, D. B.; Bhosale, R. S.; La, D. D.; Al Kobaisi, M.; Bhosale, S. V.; Bhosale, S. V., Chiral Supramolecular Assemblies from an Achiral Naphthalene Diimide Bearing a Urea Moiety. *Chem. Asian J.* **2018,***13* (21), 3268-3273.

155.	Sato, S.; Umeda, Y.; Fujii, S.; Takenaka, S., Cooperative Binding of Ferrocenylnaphthalene Diimide Carrying β-Cyclodextrin Converts Double-Stranded DNA to a Rod-Like Structure. *Bioconjugate Chem.* **2015,***26* (3), 379-382.

156.	Gutsche, C. D.; Dhawan, B.; No, K. H.; Muthukrishnan, R., Calixarenes. 4. The synthesis, characterization, and properties of the calixarenes from p-tert-butylphenol. *J. Am. Chem. Soc.* **1981,***103* (13), 3782-3792.

157.	Hosseini, A.; Taylor, S.; Accorsi, G.; Armaroli, N.; Reed, C. A.; Boyd, P. D. W., Calix[4]arene-Linked Bisporphyrin Hosts for Fullerenes: Binding Strength, Solvation Effects, and Porphyrin−Fullerene Charge Transfer Bands. *J. Am. Chem. Soc.* **2006,***128* (49), 15903-15913.

158.	Arnaud-Neu, F.; Barboso, S.; Casnati, A.; Pinalli, A.; Schwing-Weill, M.-J.; Ungaro, R., Synthesis and binding properties of calix[4]arene diamide dicarboxylic acids. *New J. Chem.* **2000,***24* (12), 967-972.

159.	Maity, D.; Bhatt, M.; Desai, M. L.; Suresh, E.; Si, M. K.; Boricha, V. P.; Ganguly, B.; Paul, P., Effect of conformation, flexibility and intramolecular interaction on ion selectivity of calix[4]arene-based anion sensors: experimental and computational studies. *Supramol. Chem.* **2017,***29* (8), 600-615.

160.	Joseph, R.; Ramanujam, B.; Acharya, A.; Khutia, A.; Rao, C. P., Experimental and Computational Studies of Selective Recognition of Hg2+ by Amide Linked Lower Rim 1,3-Dibenzimidazole Derivative of Calix[4]arene: Species Characterization in Solution and that in the Isolated Complex, Including the Delineation of the Nanostructures. *J. Org. Chem.* **2008,***73* (15), 5745-5758.

161.	Beer, P. D.; Drew, M. G. B.; Gradwell, K., Synthesis and anion coordination chemistry of new calix[4]arene pyridinium receptors. *J. Chem. Soc., Perkin Trans. 2* **2000,** (3), 511-519.

162.	D'Alessio, D.; Skelton, B. W.; Sobolev, A. N.; Krause-Heuer, A. M.; Fraser, B. H.; Massi, M.; Ogden, M. I., Lanthanoid Complexation by a Tris-Tetrazole-Functionalised Calix[4]arene. *Eur. J. Inorg. Chem.* **2016,***2016* (34), 5366-5372.

163.	Cameron, L.; Rajagopalan, A.; Abad Galan, L.; Phe, R. Z. H.; Skelton, B. W.; Massi, M.; Ogden, M. I., Lanthanoid coordination with a tetrazole-substituted calix[4]diquinone and calix[4]dihydroquinone. *Supramol. Chem.* **2019,***31* (7), 466-472.

164.	Chen, S.; Yu, Y.-L.; Wang, J.-H., Inner filter effect-based fluorescent sensing systems: A review. *Anal. Chim. Acta* **2018,***999*, 13-26.

165.   Dannenbauer, N.; Matthes, P. R.; Scheller, T. P.; Nitsch, J.; Zottnick, S. H.; Gernert, M. S.; Steffen, A.; Lambert, C.; Müller-Buschbaum, K., Near-Infrared Luminescence and Inner Filter Effects of Lanthanide Coordination Polymers with 1,2-Di(4-pyridyl)ethylene. *Inorg. Chem.* **2016,** *55* (15), 7396-7406.

166.   Ha-Thi, M.-H.; Delaire, J. A.; Michelet, V.; Leray, I., Sensitized Emission of Luminescent Lanthanide Complexes Based on a Phosphane Oxide Derivative. *J. Phys. Chem. A* **2010,** *114* (9), 3264-3269.

167.   Yang, C.; Fu, L.-M.; Wang, Y.; Zhang, J.-P.; Wong, W.-T.; Ai, X.-C.; Qiao, Y.-F.; Zou, B.-S.; Gui, L.-L., A Highly Luminescent Europium Complex Showing Visible-Light-Sensitized Red Emission: Direct Observation of the Singlet Pathway. *Angew. Chem., Int. Ed.* **2004,** *43* (38), 5010-5013.

168.   D'Alessio, D.; Muzzioli, S.; Skelton, B. W.; Stagni, S.; Massi, M.; Ogden, M. I., Luminescent lanthanoid complexes of a tetrazole-functionalised calix[4]arene. *Dalton Trans.* **2012,** *41* (16), 4736-4739.

169.   Sato, N.; Shinkai, S., Energy-transfer luminescence of lanthanide ions encapsulated in sensitizer-modified calix[4]arenes. *J. Chem. Soc., Perkin Trans. 2* **1993,** (4), 621-624.

170.   Wu, Y.; Krzyaniak, M. D.; Stoddart, J. F.; Wasielewski, M. R., Spin Frustration in the Triradical Trianion of a Naphthalenediimide Molecular Triangle. *J. Am. Chem. Soc.* **2017,** *139* (8), 2948-2951.

171.   Benković, T.; Tomišić, V.; Frkanec, L.; Galić, N., ESI MS/MS Study of Calix[4]arene Derivatives and their Metal Complexes. *Croat. Chem. Acta* **2012,** *85*, 469-477.

172.   La Porte, N. T.; Martinez, J. F.; Hedström, S.; Rudshteyn, B.; Phelan, B. T.; Mauck, C. M.; Young, R. M.; Batista, V. S.; Wasielewski, M. R., Photoinduced electron transfer from rylenediimide radical anions and dianions to Re(bpy)(CO)3 using red and near-infrared light. *Chem. Sci.* **2017,** *8* (5), 3821-3831.

173.   Ajayakumar, M. R.; Mukhopadhyay, P.; Yadav, S.; Ghosh, S., Single-Electron Transfer Driven Cyanide Sensing: A New Multimodal Approach. *Org. Lett.* **2010,** *12* (11), 2646-2649.

174.   Pan, M.; Lin, X.-M.; Li, G.-B.; Su, C.-Y., Progress in the study of metal–organic materials applying naphthalene diimide (NDI) ligands. *Coord. Chem. Rev.* **2011,** *255* (15), 1921-1936.

175.   Burkholder, C.; Dolbier, W. R.; Médebielle, M., Reaction of the 2-(bromodifluoromethyl)benzoxazole with tetrakis(dimethylamino)ethylene (TDAE) in the presence of aldehydes. A convenient synthesis of 2-(difluoromethyl)benzoxazole alcohols. *Tetrahedron Lett.* **1997,** *38* (5), 821-824.

176.   Guha, S.; Goodson, F. S.; Roy, S.; Corson, L. J.; Gravenmier, C. A.; Saha, S., Electronically Regulated Thermally and Light-Gated Electron Transfer from Anions to Naphthalenediimides. *J. Am. Chem. Soc.* **2011,** *133* (39), 15256-15259.

177.   Ajayakumar, M. R.; Hundal, G.; Mukhopadhyay, P., A tetrastable naphthalenediimide: anion induced charge transfer, single and double electron transfer for combinational logic gates. *Chem. Commun. (Cambridge, U. K.)* **2013,** *49* (70), 7684-7686.

178.   Zeman, C. J.; Kim, S.; Zhang, F.; Schanze, K. S., Direct Observation of the Reduction of Aryl Halides by a Photoexcited Perylene Diimide Radical Anion. *J. Am. Chem. Soc.* **2020,** *142* (5), 2204-2207.

179.   Fulmer, G. R.; Miller, A. J. M.; Sherden, N. H.; Gottlieb, H. E.; Nudelman, A.; Stoltz, B. M.; Bercaw, J. E.; Goldberg, K. I., NMR Chemical Shifts of Trace Impurities: Common Laboratory Solvents, Organics, and Gases in Deuterated Solvents Relevant to the Organometallic Chemist. *Organometallics* **2010,**29 (9), 2176-2179.

180.   Ling, X.; Samuel, E. L.; Patchell, D. L.; Masson, E., Cucurbituril Slippage: Translation is a Complex Motion. *Org. Lett.* **2010**, *12* (12), 2730-2722.

Appendix
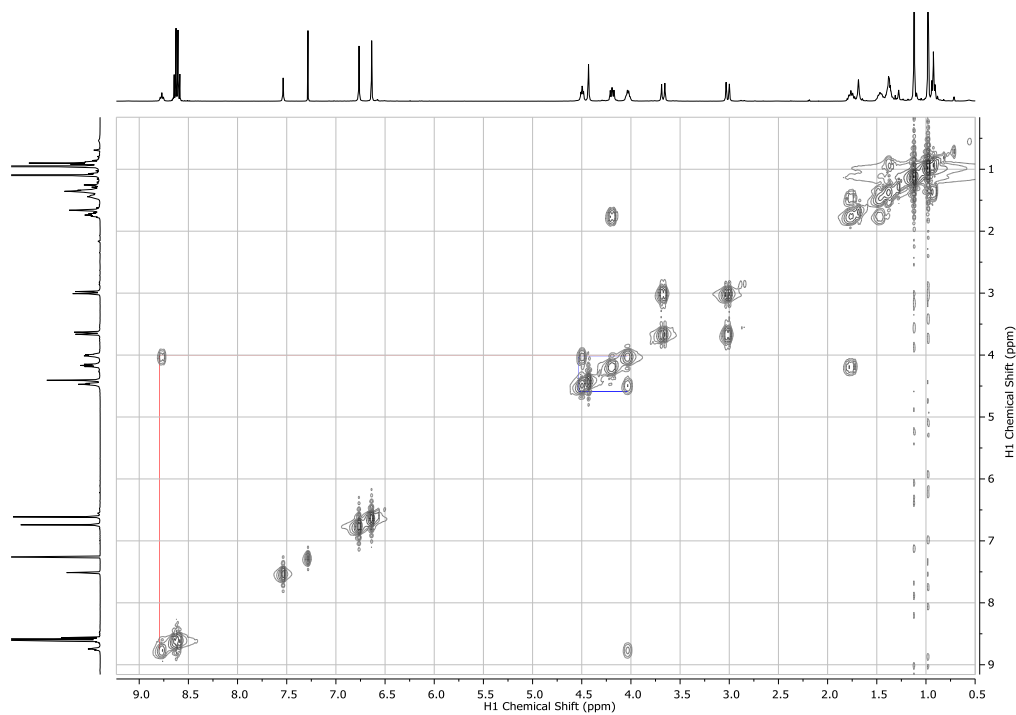
2D NMR Spectra

Figure A1：2D COSY NMR spectrum of the ligand L1.
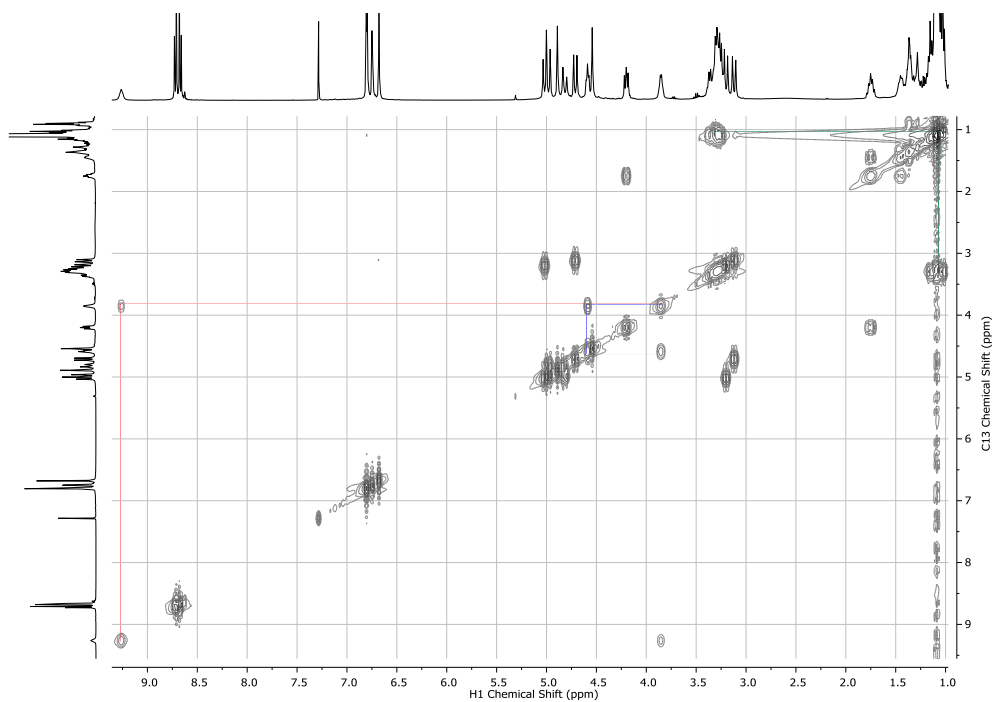
Figure A2: 2D COSY NMR spectrum of the ligand L4.
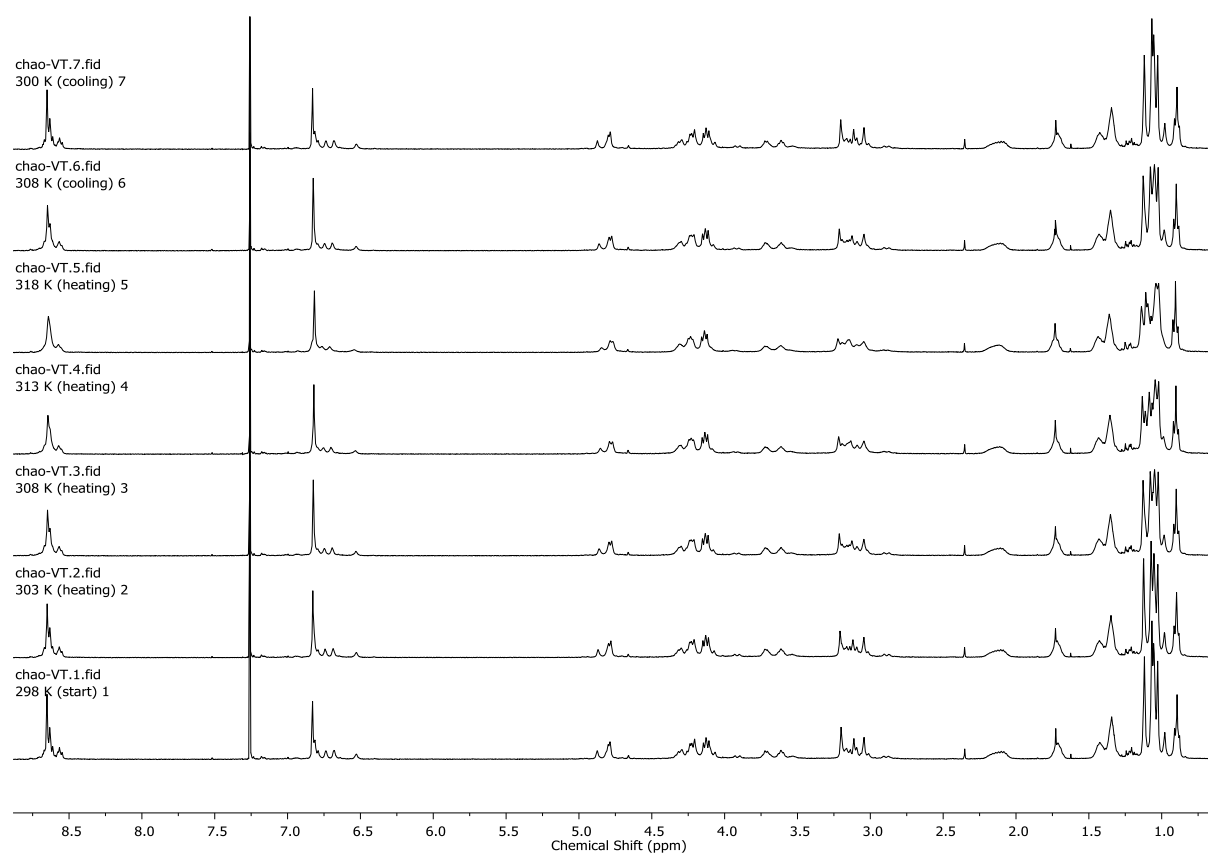
Figure A3: Variable temperature ¹H NMR of ligand L2 in CDCl₃.
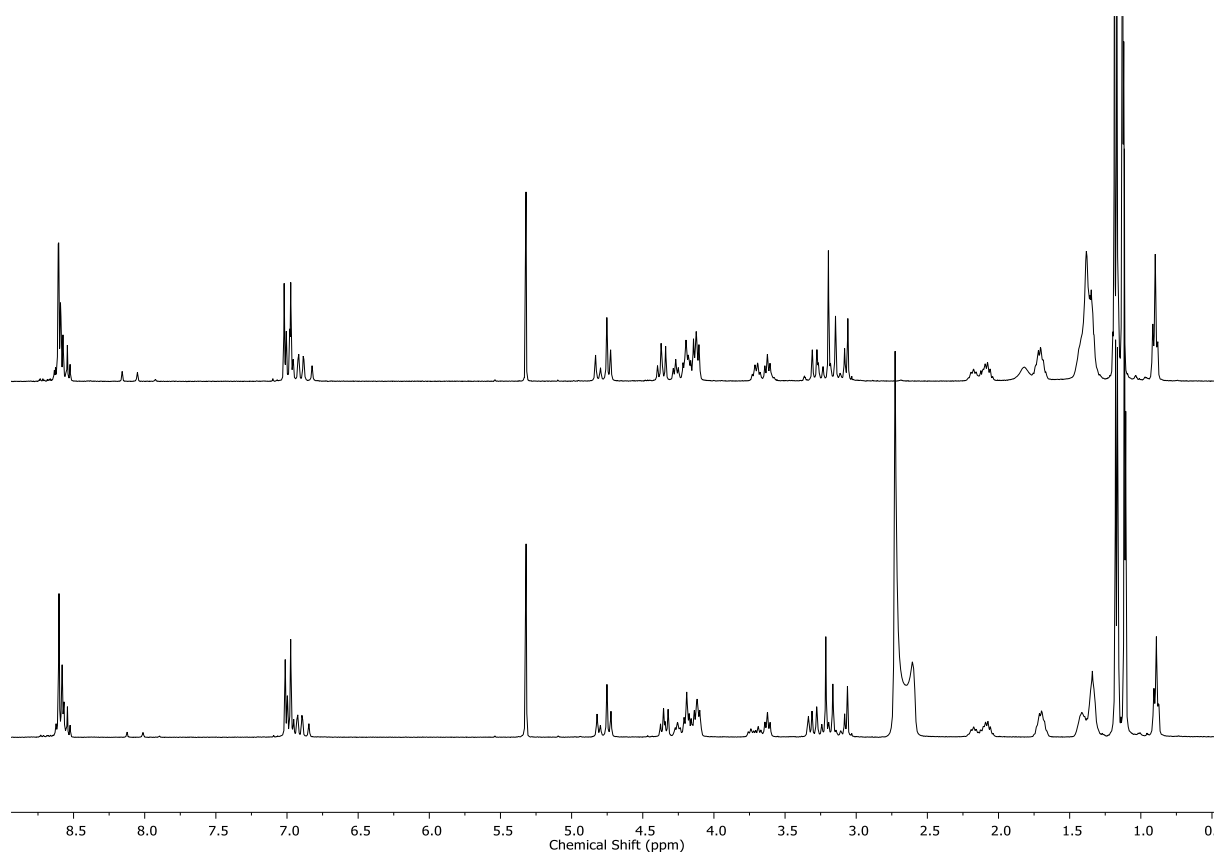
Figure A4: ^{1}H NMR of ligand L2 in CD$_2$Cl$_2$ (top) ^{1}H NMR of ligand L2 + 1 drop of MeOD in CD$_2$Cl$_2$ (bottom).

Lifetime Decay of Phosphorescence
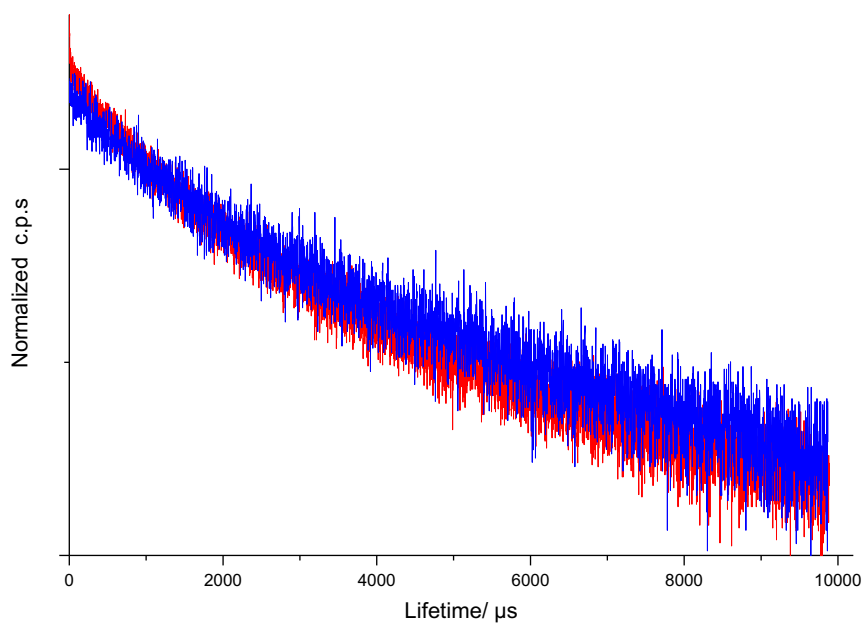
Figure A5: Lifetime decay of phosphorescence in a mixture of DCM/MeCN/10%EtI at 77K: L2 ligand, red trace; L3 ligand, blue trace. λ_{em} = 616 nm.
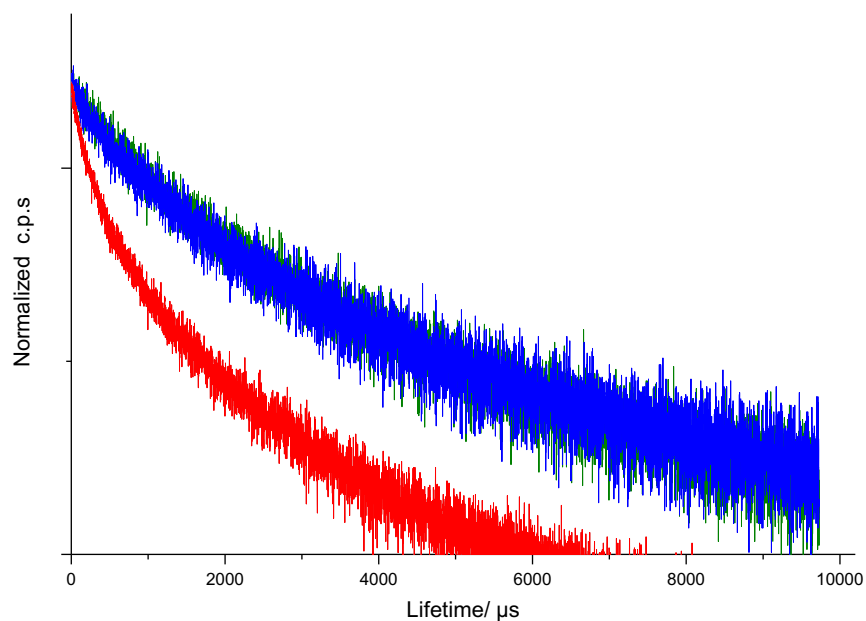
Figure A6: Lifetime decay of phosphorescence in a mixture of DCM/MeCN/10%EtI at 77K: Gd(L3), blue trace; Nd(L3), green trace; Yb(L3), red trace. λ_{em} = 616 nm.
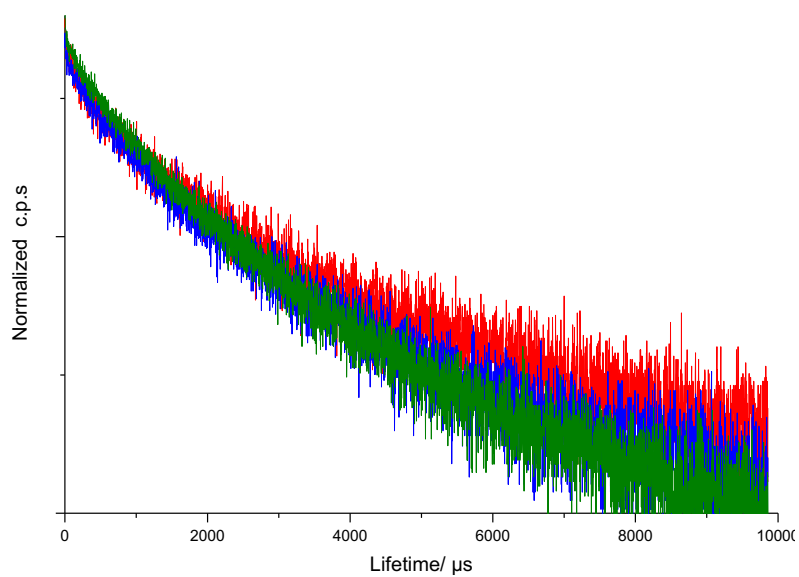
Figure A7: Lifetime decay of ligand L4 (red), L5 blue (blue) and L6 (green) in a mixture of MeCN/10%EtI (10^{-5} M) at 77K. λ_{em} = 616 nm.
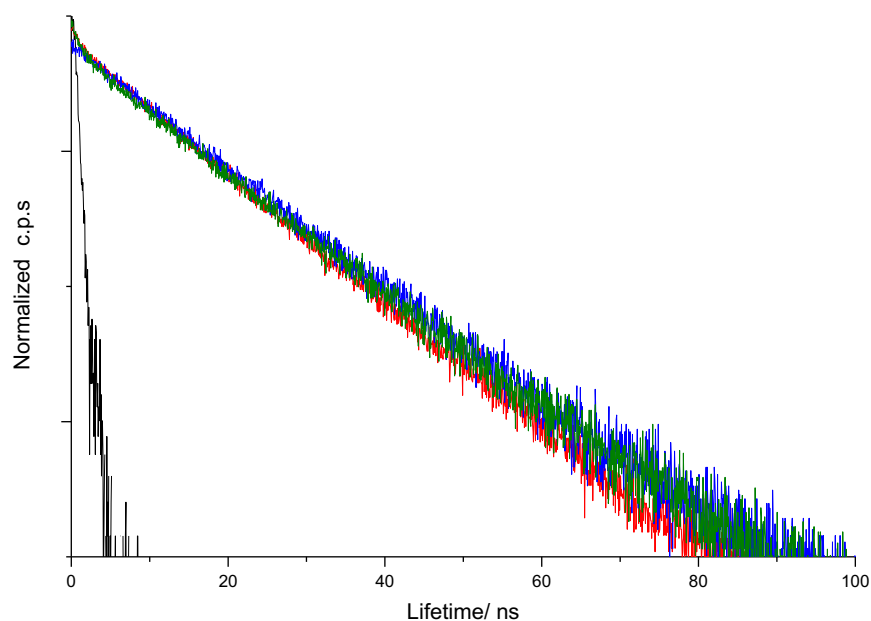
Lifetime Decay of Emission from Aggregates

Figure A8: Lifetime decay of emission from aggregate in a mixture of DCM/MeCN (1:1) at room temperature: Eu(L3), red trace; Gd(L3), blue trace; Yb(L3), green trace, Nd. λ$_{em}$ = 500 nm. Black trace is the instrument response function.
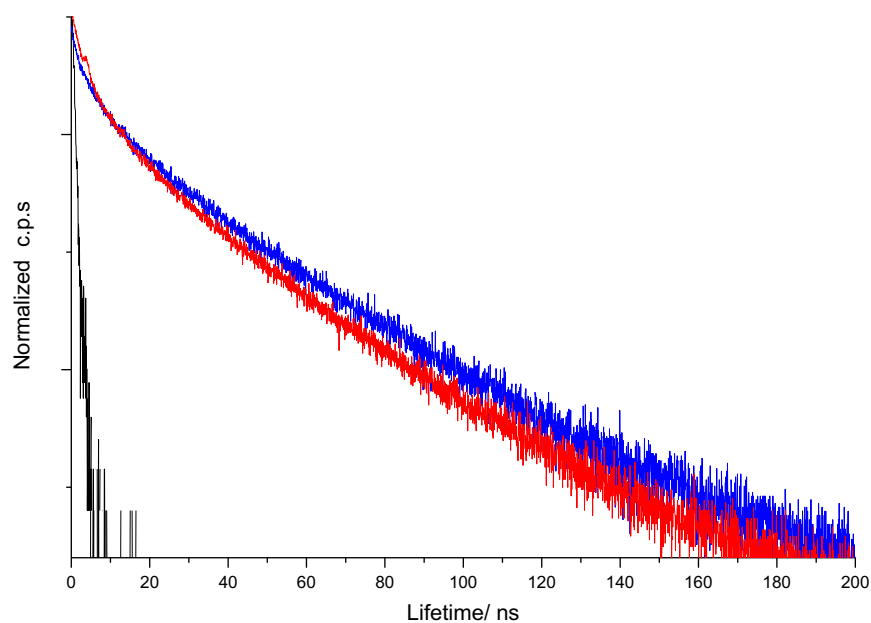

Figure A9: Lifetime decay of emission from aggregate of Eu(L3) complex (red trace) and Gd(L3) complex (red trace) in a mixture of DCM/MeCN (1:1) at 77K. λ$_{em}$ = 500 nm. Black trace is the instrument response function.
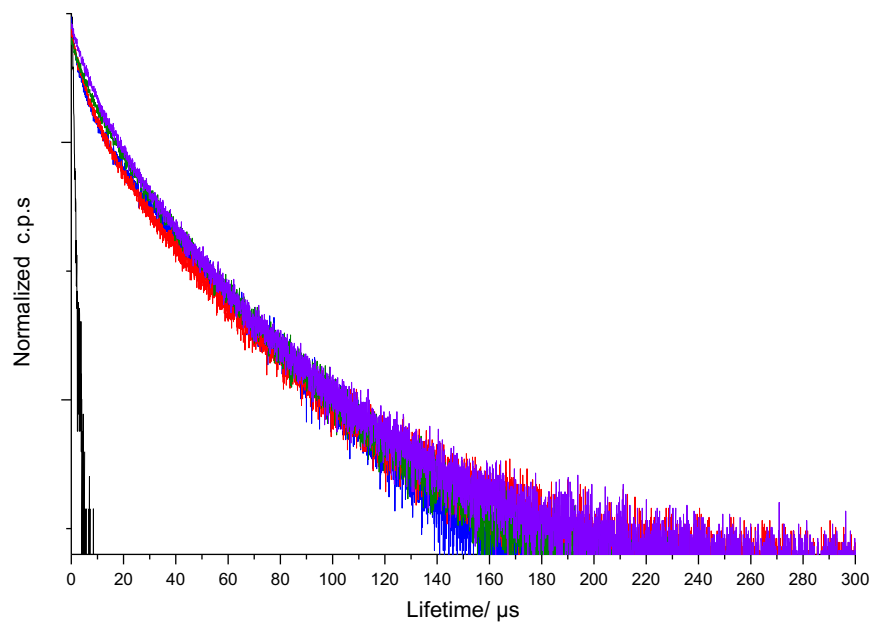
Figure A10: Lifetime decay of emission from aggregate in a mixture of DCM/MeCN/10%EtI at 77K: ligand L5, violet trace; Gd(L3), blue trace; Nd(L3), green trace; Yb(L3), red trace. λ_{em} = 500 nm. Black trace is the instrument response function.
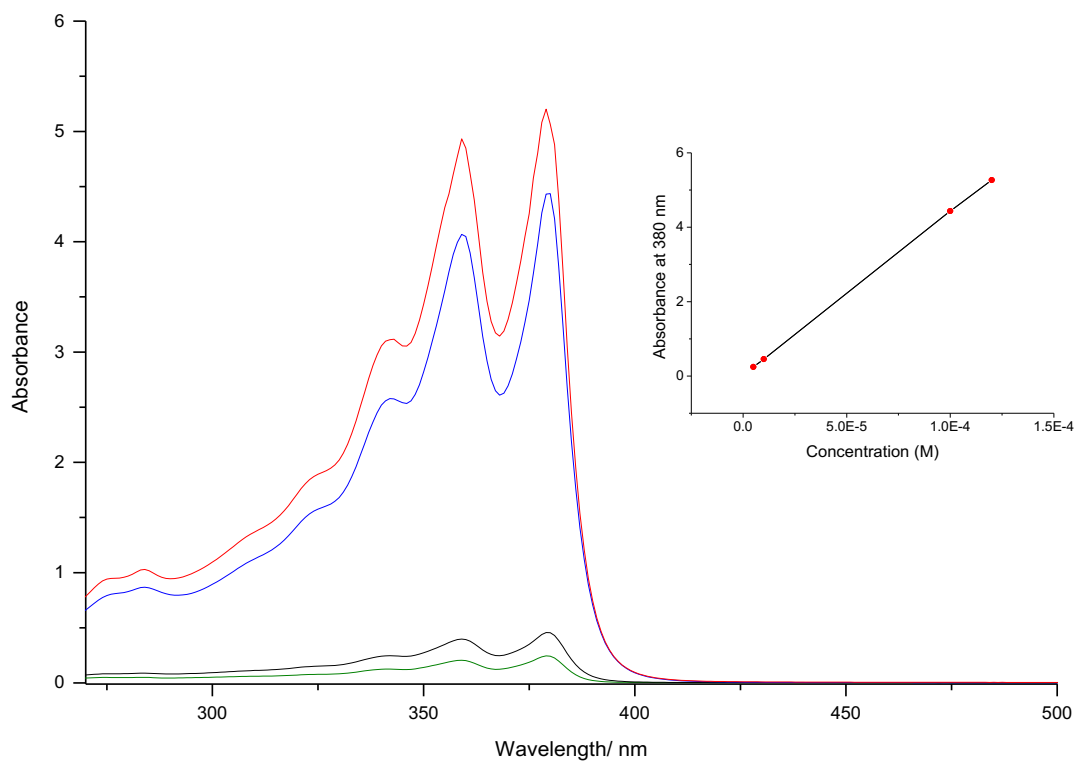
Absorption Spectrum

Figure A11: The UV-visible spectra of ligand L3 in a mixture of DCM/MeCN (1:1) at the concentration of 0.5 x 10^{-5} M (green), 10^{-5} M (black), 10^{-4} M (blue), and 1.2 x 10^{-4} M (red). Inset shows the dependence of absorbance at 380 nm versus concentration.